Microparticle Dynamics in the Presence of Externally Imposed, Ordered Structures in a Magnetized Low-Temperature Plasma

by

Taylor Howard Hall

A dissertation submitted to the Graduate Faculty of
Auburn University
in partial fulfillment of the
requirements for the Degree of
Doctor of Philosophy

Auburn, Alabama
December 14th, 2019

Keywords: Dusty Plasma, Low-temperature Plasma, Radio-frequency Plasma, Plasma Sheath, Plasma Magnetization, Plasma Diagnostics

Approved by

Edward Thomas, Jr., Chair, Charles W. Barkley Endowed Professor of Physics and Associate Dean for Research and Graduate Studies
Joseph Perez, Professor of Physics
Uwe Konopka, Associate Professor of Physics
Marcelo Kuroda, Assistant Professor of Physics

Abstract

Dusty plasmas are a type of plasma which consists of charged microparticles suspended in a background plasma. In the presence of a strong magnetic field, dusty plasmas have been observed to develop new patterned formations in which the pattern corresponds to the shape of a conducting element within the plasma. These formations are given the name imposed, ordered structures. Originally discovered in the Magnetized Dusty Plasma Experiment (MDPX), dust particles were shown to take on the pattern of a conducting wire mesh present in one of the experiments bounding electrodes. This dissertation presents new results from the examination of these imposed, ordered structures in more depth. A two-parameter method for describing the particle organization will be introduced. Using these methods, it will be shown how various types of particle dynamics associated with the onset of imposed, ordered structures are correlated to the increasing magnetization of the background plasma.

In order to better understand the physical mechanism behind the imposed, ordered structures three separate experiments are performed using a new "waffle"-shaped electrode which consists of a large conducting surface with a series of holes through the electrode. When using this electrode, dust particles are observed to become confined to regions beneath the holes in the electrode. Additionally, plasma probe diagnostics show electron density and electric field structures beneath the hole regions of the electrode. A comparison of effective electric potential profiles within the plasma, calculated from three independent experiments, provide strong evidence of magnetically modified plasma sheaths within the plasma.

Acknowledgment

To Dr. Edward Thomas, Jr., Charles W. Barkley Endowed Professor and Associate Dean for Research and Graduate Studies, I cannot thank you enough. Thank you for all the opportunities to travel, to meet new people, and to learn, that you provided. Your guidance has helped me grow not only as a scientist but as a person. The example that you set as a researcher, teacher, and leader has set a standard that I can only hope to live up to in my own career.

To my committee members, thank you for your help during my time here at Auburn. Thank you to Dr. Uwe Konopka, your fresh perspective on so many research tasks always helped me to think of things in a new way. Thank you to Dr. Joseph Perez, you took the time to meet with me as a prospective high school senior which played a great part in my coming to Auburn and pursing this degree, and for that I am forever grateful. Thank you to Dr. Marcelo Kuroda, I'll always appreciate the time you took to help us prepare for our doctoral exams. Thank you to Dr Monika Raj for her time and effort serving as my University Reader.

Thank you to all my friends that have helped me along the way. To James Kring, Ben Schoenek, Ellie Williamson, Omar Lopez Ortiz, thank you for all the long hours studying for classes and the qualifying exams. Thank you to all the members of the PSL/MPRL, past and present, with a special thanks to Misha McKinlay, Lori Scott, Steve Williams, Dr. Jeremiah Williams, Dr. Ami DuBois, and Dr. Brian Lynch. Thank you to Darrick Artis, for always keeping things running smoothly around the lab and for never being bothered when I asked where something was for the hundredth time in a week. Thank you to Dr Ivan Arnold, your constant positivity, friendship, and assistance for the past seven years means more to me than you could

know. And to Dr Spencer LeBlanc, the best officemate I could have asked for, you helped fill these last few years with so many laughs and stories, in and out of the office, for which I cannot thank you enough.

Thank you to my family, my mom Kelly, my dad Brian and his wife Dawn, and my sister Hayden. You all have been there for me since the beginning. I could not have made it this far if not for you being there to help me. Finally, thank you to my incredible wife Elise. Your love and support over the years has meant so much to me and I would not be where I am today if not for you. Your dedication to me and your work inspires me to be the best that I can for you. All the effort that went into this work would not have been possible without you by my side. Thank you.

Table of Contents

List of Figures

List of Tables

List of Abbreviations

MDPX	Magnetized Dusty Plasma Experiment
FTO	Fluorine-doped tin oxide
PIV	Particle Image Velocimetry
ROI	Region of interest
e	Elementary charge (1.6022×10^{-19} C)
k_B	Boltzmann constant (1.381×10^{-23} J $\cdot$ K^{-1}, 8.617×10^{-5} eV $\cdot$ K^{-1})
m_s	Mass of plasma species *s* [kg]
q_s	Charge of plasma species *s* [C]
T_s	Temperature of plasma species *s* [K]
n_s	Number density of plasma species *s* [m^{-3}]
$v_{th,s}$	Thermal speed of plasma species *s* [m/s]
λ_{mfp}^{sn}	Mean free path of the plasma species s with neutral particles [m]
r_{Ls}	Larmor radius of plasma species *s* [m]
σ_{sn}	Collision cross section of a plasma species with neutrals [m^2]
Z_d	Number of charges on a dust grain [e]
a_d	Radius of a dust grain [m]
$\vec{E}$	Electric field [V/m]
$\vec{B}$	Magnetic field [T]
ID/OD	Inner/outer diameter [m, inches]

Chapter 1 Introduction

A complex, or dusty, plasma consists of ion, electrons, neutral gas atoms, and macroscopic particles, commonly called dust. These solid macroscopic particles often range from a few nanometers to tens of micrometers in diameter and can be composed of various materials. In a typical laboratory plasma these dust particles gain a net charge through the collection of ions and electrons. Because of their large size, compared to other plasma components, the dust particles can be illuminated by visible laser light and recorded with basic camera systems. An example of such a cloud of dust particles is shown in Figure 1-1.

In laboratory dusty plasmas dust particles are suspended in the plasma by balancing electric and gravitational forces on the particle. Recently, experimenters have become interested in the role of large, external magnetic fields in dusty plasmas. In experiments at Auburn University, researchers discovered the presence of ordered structures within a dusty plasma at high magnetic fields ($B > 1$ T). [1] This phenomenon of imposed, ordered structures can be seen in Figure 1-2. These structures are a new kind of pattern formation within a dusty plasma which takes its structure from some external conducting element, such as a wire mesh, as was the case in the initial observations.

This dissertation will provide new research which expands on those initial observations. This research will consist of first developing a new method to parameterize the experimental conditions at which these imposed, ordered structures occur. Second, plasma probe measurements beneath a specially designed electrode will be made in order to examine potential structures which confine dust particles. Finally, observations of a dusty plasma system beneath this new electrode

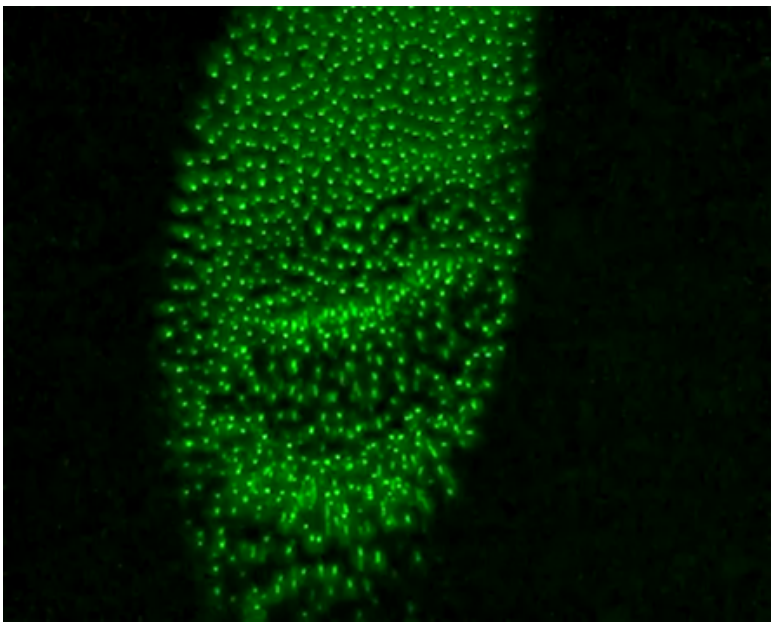

Figure 1-1 A dust cloud illuminated by green laser light.

will be presented and a comparison of those observations to the results of the probe measurements will be discussed.

1.1 Dust Particle Charging in a Dusty Plasma

For a dusty plasma a fundamental property of a dust particle is its charge. This charge is what allows it to be suspended within the plasma and what couples the particle to the other charged plasma components: electrons, ions, and other charged dust grains. Within a laboratory plasma, the electrons are often much more energetic than the ions, leading to a higher flux of electrons onto the dust particle surface. This causes the dust particles to acquire a net negative charge of a few dozen to several thousand electron charges depending on the size of the grain. Eventually, once the particle has acquired enough charge, the dust grain reaches an electrically floating state where the flux of electrons and ions is balanced. This charging process couples the dust to the background plasma and allows the dust to act as an additional plasma component. [2,3]

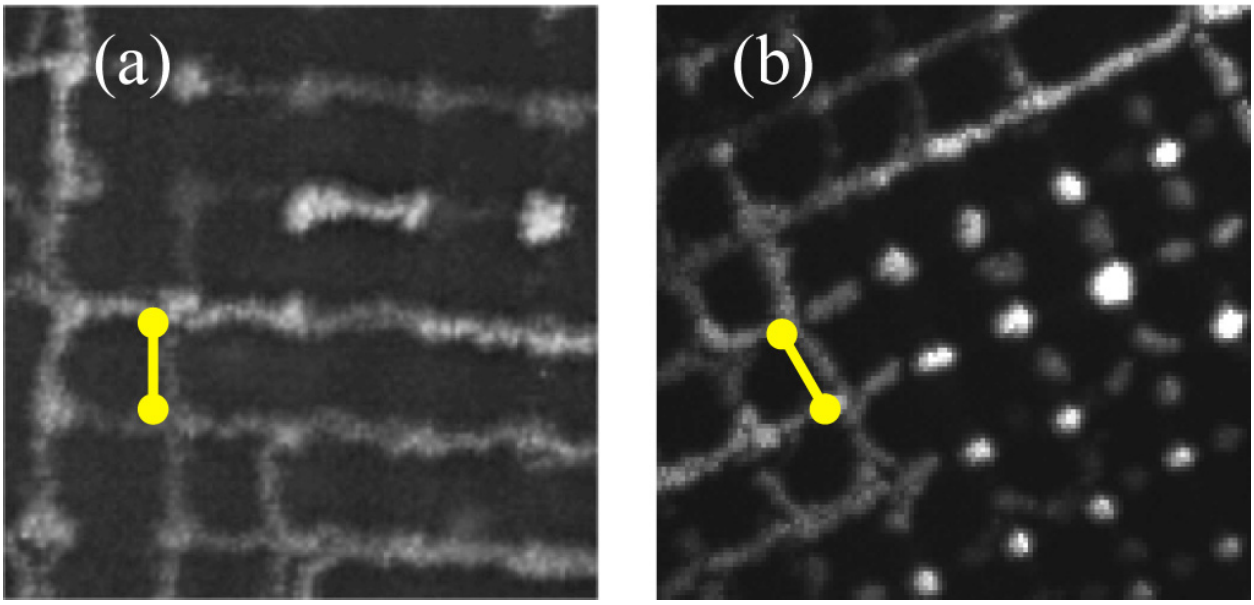

Figure 1-2 Close-up of the first observations of the imposed, ordered structures. Yellow bars show the scale of the titanium wire mesh relative to the dust particle spacing. The field of view is 125 × 125 pixels (3.94 × 3.94 mm) (a) 2 μm diameter particles at $B = 2.0$ T, $P = 145$ mTorr (19.3 Pa). (b) 0.5 μm diameter particles at $B = 1.5$ T, $P = 53$ mTorr (7.1 Pa). From Thomas, et al., Phys. Plasmas 22, 030701 (2015), Fig. 3.

An estimate of the dust charge is made using *orbit-motion-limited* (OML) theory. This model is based on Langmuir probe theory and whose derivation is found in a variety of textbooks. [2,4,5] To determine the charge, it is assumed that the dust particle is electrically floating within the plasma, meaning that the flux, or current, of ions and electrons onto its surface has reached a steady state such that:

$$I_e + I_i = 0 \tag{1-1}$$

If both the electron and ion populations within the plasma are each assumed to be at some thermal equilibrium, and the ions are taken to be cold such that $k_b T_i \ll e|\Phi_d|$, then their respective currents, I_e and I_i, to the surface of the negatively charged grain can be expressed as:

$$I_e = I_{0,e} \exp\left(-\frac{e|\Phi_d|}{k_B T_e}\right)$$
$$I_i = I_{0,i}\left(1 + \frac{e|\Phi_d|}{k_B T_i}\right). \tag{1-2}$$

Here, e is the elementary electron charge, T_e and T_i are the electron and ion temperatures, k_B is the Boltzmann constant, and Φ_d is the grain surface potential relative to ground. The coefficients, $I_{0,e}$ and $I_{0,i}$, are

$$I_{0,s} = 4\pi a^2 n_{0,s} q_s \sqrt{\frac{k_B T_s}{2\pi m_s}} \tag{1-3}$$

where a is the dust grain radius, $n_{0,s}$ is the density of the given plasma species, electrons or ions, and m_s is the mass of the given plasma species. Substituting these currents in to Equation 1-1 and then simplifying, we arrive at the result

$$\sqrt{\frac{m_e T_i}{m_i T_e}}\left(1 + \frac{e|\Phi_d|}{k_B T_i}\right) - \exp\left(-\frac{e|\Phi_d|}{k_B T_e}\right) = 0 \tag{1-4}$$

which can then be solved numerically for Φ_d.

Once this floating potential of the dust grain is found, the dust charge, q_d, is calculated by assuming the grain to be a spherical capacitor such that

$$q_d = C\Phi_d. \tag{1-5}$$

The capacitance, *C,* of a conducting sphere with radius a is given as

$$C = 4\pi\epsilon_0 a. \tag{1-6}$$

where ϵ_0 is the permittivity of free space.

In a plasma which has electrons with a thermal energy of 3 eV and Argon ions with a temperature of 300 K (~ 1/40 eV), a silica dust grain with $a = 1$ μm would have an estimated dust charge of

$$q_d = -Z_d e \cong -4900e \cong -7.85 \times 10^{-16}\ \mathrm{C} \tag{1-7}$$

where Z_d is the number of electrons attached to the surface of the dust grain.

While the dust grain can have a charge several thousand times larger than either the ions or electrons in the plasma, its mass is considerably larger. With the density of silica being $\rho = 2200\ \mathrm{kg/m^3}$, the 1 μm radius dust grain in this example would have a mass of $m_d = 9.2 \times 10^{-15}$ kg. Such a particle would then have a charge-to-mass ratio, $|q_d|/m_d \sim 0.085\ \mathrm{C/kg}$, which is incredibly small compared to an argon ions charge-to-mass ratio of $|q_i|/m_i = 2.42 \times 10^6\ \mathrm{C/kg}$, or the electron charge-to-mass ratio of $|q_e|/m_e = 1.76 \times 10^{11}\ \mathrm{C/kg}$. This very low charge-to-mass ratio means that many phenomena in a dusty plasma occur over time scales that can be easily observed in the laboratory.

Another important aspect of dusty plasmas is their ability to self-organize into various structures. Two-dimensional plasma crystals [6–11] or three-dimensional Coulomb balls [12–14] are examples of self-organization in dusty plasma systems. The self-ordering of a dusty plasma is described by the screened Coulomb coupling parameter, which is the ratio of the electrostatic

potential energy to the dust thermal energy. [2] For a screened Coulomb interaction, the coupling parameter is given by the equation:

$$\Gamma = \frac{Q_d^2}{4\pi\epsilon_0 k_b T_d \Delta} e^{-\frac{\Delta}{\lambda_d}} \tag{1-8}$$

where Q_d is the dust charge, T_d is the dust kinetic temperature, Δ is the dust interparticle spacing, and λ_d is the dust screening length, which is given in terms of the electron and ion Debye lengths

$$\frac{1}{\lambda_d^2} = \frac{1}{\lambda_e^2} + \frac{1}{\lambda_i^2} \tag{1-9}$$

The Debye length for either species of electrons or ions is

$$\lambda_s = \sqrt{\frac{\epsilon_0 k_B T_s}{n_{0,s} e^2}} \tag{1-10}$$

When the Coulomb coupling parameter is very small ($\Gamma \ll 1$), this represents a weakly-coupled, or gas-like, state. Larger values of the coupling parameter ($0.1 \lesssim \Gamma \lesssim 10$) correspond to liquid-like states. For $\Gamma > 10$, a system can be described as making a transition to a strongly coupled state. For large values of $\Gamma \geq 170$ the system can self-organize into a crystalline state, called a plasma crystal.

Other examples of organized structures in dusty plasmas are electrorheological dusty plasmas. [15–19] In these systems long chains of dust particles form as an oscillating flow of background ions create wake structures that trap the dust particles. While these structures have provided significant insights into the physics of dusty plasmas through studies of ion wakes [20–24] and screening effects, all these experiments were performed without the presence of a

significant magnetic field in which both electron and ion magnetization could play a role in the dust charging and dynamics.

1.2 Plasma Magnetization

In this section the details of several important physical concepts, often discussed in many standard plasma physics textbooks such as Chen [25] or Piel [4], will be introduced which will be useful for later discussions on different experimental results. The first of these concepts will be detailed in Section 1.2.1 and present the derivation of *gyromotion* of charged particles in the presence of magnetic fields. Since plasmas are composed of charged particles, it is critical to understand how the presence of magnetic fields, of any magnitude, can alter the particle dynamics. The second derivation presented for the *mean free path,* is introduced in Section 1.2.2. The plasmas used in experiments described in this dissertation are weakly ionized, meaning their ionization fraction is quite low, typically on the order of one ion-electron pair per million neutral atoms. Due to this low ionization fraction, the ions and electrons have a higher probability of colliding with background neutral atoms than with charged species. The mean free path is the statistically average distance that these particles will travel before making such a collision. How this distance is determined will be the focus of this subsection.

By combining the concepts of gyromotion and particle collisions into a single dimensionless parameter, it is possible to quantify the degree of magnetization within a plasma, or rather if the single particle motion within the plasma is dominated by magnetic gyromotion or collisions with neutral particles. This parameter is called the *Hall parameter*, named after physicist Edwin Hall – no relation – and is presented in Section 1.2.3.

1.2.1 Gyromotion/Gyrofrequency

This section outlines the derivation of the *gyrofrequency* and *Larmor radius*. A charged particle of mass m and charge q in the presence of a magnetic field $\boldsymbol{B}$ experiences a force $\boldsymbol{F}$ of the form

$$\boldsymbol{F} = m\boldsymbol{a} = m\frac{d\boldsymbol{v}}{dt} = q\boldsymbol{v} \times \boldsymbol{B} \tag{1-11}$$

If the magnetic field is in the $\hat{z}$ direction such that $\boldsymbol{B} = B\hat{z}$, the components of this equation of motion are written as:

$$\begin{aligned} m\dot{v}_x &= qBv_y \\ m\dot{v}_y &= -qBv_x \\ m\dot{v}_z &= 0 \end{aligned} \tag{1-12}$$

Taking the derivative with respect to time of the first two of these equations gives

$$\begin{aligned} \ddot{v}_x &= \frac{qB}{m}\dot{v}_y = -\left(\frac{qB}{m}\right)^2 v_x \\ \ddot{v}_y &= -\frac{qB}{m}\dot{v}_x = -\left(\frac{qB}{m}\right)^2 v_y \end{aligned} \tag{1-13}$$

These two equations describe a simple harmonic oscillator with a frequency ω_c defined as

$$\omega_c \equiv \frac{|q|B}{m} \tag{1-14}$$

called the *cyclotron frequency*, or *gyrofrequency*. The solution to Equation 1-13 can now be written as:

$$v_{x,y} = v_{\perp} \exp\left(\pm i\omega_c t + i\delta_{x,y}\right) \tag{1-15}$$

where $v_{\perp}$ is a positive constant representing the speed in the plane perpendicular to the magnetic field, $\boldsymbol{B}$. Choosing the phase δ_x to be zero gives:

$$v_x = v_{\perp} e^{i\omega_c t} = \dot{x} \tag{1-16}$$

Which then allows for the velocity in the *y*-direction to be determined by Equations 1-12 and 1-16:

$$v_y = \frac{m}{qB}\dot{v_x} = \pm\frac{1}{\omega_c}\dot{v_x} = \pm i v_{\perp} e^{i\omega_c t} = \dot{y} \tag{1-17}$$

Integrating Equations 1-16 and 1-17 a final time, the position of the particle relative to a fixed point (x_0, y_0) is given by:

$$\begin{aligned} x - x_0 &= -i\frac{v_{\perp}}{\omega_c} e^{i\omega_c t} \\ y - y_0 &= \pm\frac{v_{\perp}}{\omega_c} e^{i\omega_c t} \end{aligned} \tag{1-18}$$

In a plasma which has reached steady state and whose velocities follow a Maxwell-Boltzmann distribution the perpendicular velocity can be taken to be the expected thermal velocity v_{th} of the species of interest. A new property of the gyromotion can then be defined, the *Larmor radius,*

$$r_L \equiv \frac{v_{\perp}}{\omega_c} = \frac{v_{th}}{\omega_c} = \frac{m v_{th}}{|q|B} = \frac{m}{|q|B}\sqrt{\frac{8k_B T}{\pi m}} \tag{1-19}$$

where $k_B T$ is the thermal energy of the species. [25]

1.2.2 Mean Free Path/Collision Frequency

This section will provide the details for the second important parameter that will be required to discuss the magnetization of particles: the *mean free path* and *collision frequency,* the derivation of which follows from that provided by Chen. [25] Consider a small volume of incident area A, and thickness dx. The gas in this volume has a density of n_n so that the total number of atoms in the volume is

$$N = n_n A dx \tag{1-20}$$

If each of the atoms has an effective area σ (formally called the "collision cross section") then the fraction of the volume occupied by these atoms will be

$$\frac{N\sigma}{A} = \frac{n_n A \sigma dx}{A} = n_n \sigma dx \tag{1-21}$$

If a flux Γ of plasma particles is incident on the volume of gas atoms, then the portion of the flux, Γ', which can pass through this volume is given by

$$\Gamma' = \Gamma(1 - n_n \sigma dx) \tag{1-22}$$

From Equation 1-21, the fractional change in the flux can be shown to be dependent on the thickness of the volume, *dx*, and can be written as:

$$\frac{d\Gamma}{dx} = -\Gamma n_n \sigma \tag{1-23}$$

Equation 1-22 is then integrated to obtain an expression for the spatial modulation of the flux:

$$\Gamma = \Gamma_0 e^{(-n_n \sigma x)} \equiv \Gamma_0 e^{x/\lambda_{mfp}} \tag{1-24}$$

The quantity λ_{mfp} is identified as the *mean free path*, representing the characteristic distance between collisions of two gas atoms, and is defined as:

$$\lambda_{mfp} \equiv \frac{1}{n_n \sigma} \tag{1-25}$$

The time between collisions is determined by the velocity of the incident particle and is given by

$$\tau = \frac{\lambda_{mfp}}{v} \tag{1-26}$$

Making the frequency of the collisions equal to

$$\nu = \tau^{-1} = \frac{v}{\lambda_{mfp}} = n_n \sigma v \tag{1-27}$$

If the velocities of the incident particles are represented by a Maxwell-Boltzmann distribution, then the *collision frequency* with neutrals is:

$$\nu = n_n \sigma v_{th} = n_n \sigma \sqrt{\frac{8k_B T}{\pi m}} = \left(\frac{P}{k_B T_n}\right) \sigma \sqrt{\frac{8k_B T}{\pi m}} \tag{1-28}$$

Here, the ideal gas law is used to re-express the neutral density in terms of the gas pressure, *P*.

1.2.3 Hall Parameter

Using the definitions of gyrofrequency and collision frequency, a dimensionless parameter can be derived from them. This parameter, called the *Hall parameter* [4], describes the magnetization for a given plasma species and is parameterized by the ratio of the gyrofrequency to the neutral collision frequency, given by

$$h_s = \frac{\omega_{cs}}{\nu_{sn}} \tag{1-29}$$

where $\omega_s = \frac{|q_s|B}{m_s}$ and $\nu_{sn} = n_n \sigma v_{th,s}$. For the ions, the collision cross section is calculated to be $\sigma_{in} = 3.27 \times 10^{-18}\ m^{-2}$ from the method described by Khrapak [26] by assuming that the ions present in the experiment have a temperature of $T_i = 300$ K. When $h_s \gg 1$ then the plasma species *s* is said to be magnetized. The standard definition of the Hall parameter, given in Equation 1-28, considers the ratio of an angular frequency (gyrofrequency) to a temporal frequency (collision frequency). For this work, a modification to the Hall parameter is used which is believed to have more physical meaning. [27] Here, the modified Hall parameter is computed from the gyrofrequency normalized by 2π divided by the collision frequency as shown in Equation 1-29. The result of this calculation is shown in Equation 1-30:

$$h_s' = \frac{\omega_{cs}}{2\pi\nu_{sn}} = \frac{1}{2\pi}\left(\frac{|q_s|B}{m_s}\right)\left(\frac{1}{n_n\sigma_{sn}v_{th,s}}\right) = \frac{1}{2\pi}\left(\frac{|q_s|B}{m_s v_{th,s}}\right)\left(\frac{1}{n_n\sigma_{sn}}\right) \tag{1-30}$$

$$h_s' = \frac{\lambda_{mfp}^{sn}}{2\pi r_{Ls}} \tag{1-31}$$

Now in Equation 1-30 the modified Hall parameter, h_s', is shown to be the ratio of the mean free path to 2π times the gryoradius which is the circumference of the gryo-orbit. Physically this quantity is meaningful because it considers the modified trajectories of the charged particles as the circulate around the magnetic field lines. Ultimately, both versions of the Hall parameter scale with the magnetic field and neutral pressure – the two primary experimental variables explored in this work – in the same manner, as shown in Equation 1-31:

$$h_s \sim h_s' \sim \frac{B}{P} \tag{1-32}$$

1.3 Plasma Sheaths

This section will introduce the concept of *plasma sheaths* and discuss the effects magnetic fields can have on them. Much of plasma physics is concerned with the properties of the plasma far removed from boundaries. Laboratory plasmas are contained in vacuum vessels and therefore have an interaction with the "cold" chamber walls. For most of these experiments, where the vacuum chamber walls are grounded and held at a fixed potential, and where the electrons are typically more thermally energetic than the ions and tend to exit the system faster, the bulk of the plasma acquires a net positive potential relative to the wall. The boundary plasma near the wall is called the *plasma sheath* and acts as a transition region between the bulk plasma and the wall. [4,25,28,29]

The properties of the sheath region are important to dusty plasma research. In the majority of dusty plasma experiments, the dust particles become suspended in the plasma in the sheath region due to the presence of the electric field that forms between the bulk plasma and the

surrounding wall. [2,4,5] Therefore, understanding how a plasma sheath is formed, and how it may become modified in the presence of a magnetic field, is of critical importance to this work.

The derivation provided here follows the structure presented in texts by Piel [4], as well as Lieberman and Lichtenberg [29]. To derive the properties of the plasma sheath, consider a small region near the wall. Within this region, ions will be assumed to be cold ($k_B T_i \propto 0$ eV) with some drift velocity u_0 and electrons will be assumed to be warm with some finite electron temperature, T_e. The bulk plasma is assumed to have the reference potential $\phi = 0\ V$. While in the laboratory plasma the bulk develops a positive potential relative to the grounded wall, here it is more convenient to let the bulk plasma be at zero potential and the wall develop some negative potential. They are still physically the same system. Within the sheath region, the velocity of the ions will then be given by $u(x)$ as:

$$\frac{1}{2} m_i u(x)^2 = \frac{1}{2} m_i u_0^2 - e\phi(x) \tag{1-33}$$

$$u(x) = \left(u_0^2 - \frac{2e\phi(x)}{m_i} \right)^{1/2} \tag{1-34}$$

where m_i is the ion mass. The equation of continuity for the ion density n_i in terms of the bulk plasma n_0 is then:

$$n_0 u_0 = n_i(x) u(x) \tag{1-35}$$

$$n_i(x) = n_0\left(1 - \frac{2e\phi(x)}{m_i u_0^2}\right)^{-1/2} \tag{1-36}$$

Taking the electrons to be in a thermal equilibrium such that

$$n_e(x) = n_0 \exp\left(\frac{e\phi}{k_B T_e}\right) \tag{1-37}$$

Poisson's equation then takes the form

$$\epsilon_0 \frac{d^2\phi}{dx^2} = e(n_e - n_i) = en_0\left[\exp\left(\frac{e\phi}{k_B T_e}\right) - \left(1 - \frac{2e\phi}{m_i u_0^2}\right)^{-1/2}\right] \tag{1-38}$$

This is the final nonlinear equation which gives the sheath potential and can be solved numerically for the potential ϕ. An example plot, taken from Lieberman [29] (pg. 167), is shown in Figure 1-3. A discussion of the stability condition for this non-linear differential equation is provided in Appendix A.

So far in this discussion of the plasma sheath the presence of magnetic fields has been neglected. In recent decades interest in the effects of magnetic fields on the plasma sheath have steadily grown. [30,31] Much of this focus is primarily on the theoretical application to fusion-like conditions. [32–34]. Only recently have magnetic field effects been incorporated into models of plasma sheaths. [35–37] However, even these theories are only one dimensional and not fully applicable to the three-dimensional system we have in MDPX. Some experimental work has been done on measuring sheaths in a magnetized plasma. [38] These experiments were only carried out with magnetized electrons however, and the magnetic fields do not reach the conditions which are typical for this dissertation. While the work being done on plasma sheaths in highly magnetized environments continues to evolve, they are still poorly understood.

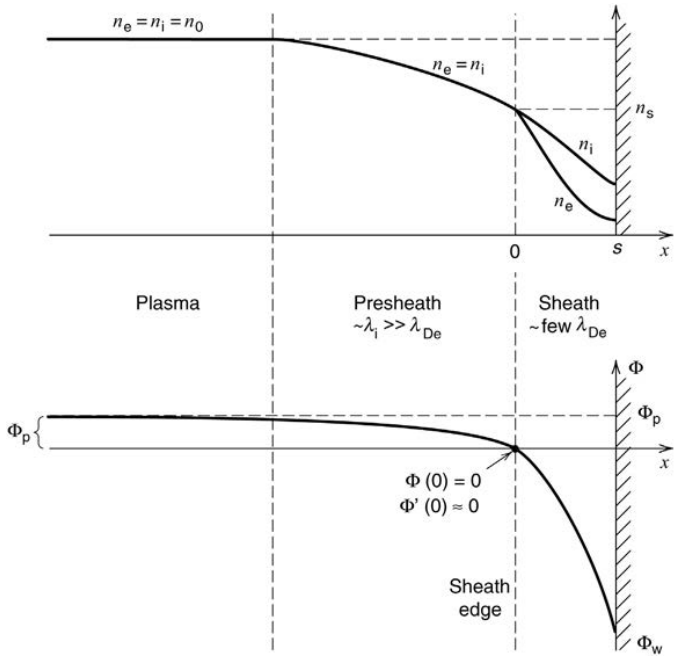

Figure 1-3 Plasma sheath diagram taken from the text by Lieberman (pg. 167). The top plot shows the electrons and ion densities within the sheath, pre-sheath, and bulk plasma regions. The bottom plot shows the plasma potential.

Ultimately the experimental study of plasma sheaths in low-temperature plasmas in the presence of high magnetic fields, of a magnitude which are relevant to the work presented in this dissertation, has not been significantly explored. This dissertation will focus on using measurements of the dust particles and the plasma to gain new insight into the physical properties of the plasma sheath under the influence of strong magnetic fields.

1.4 Outline of Dissertation

This dissertation is organized into 6 chapters and 3 appendices. Chapter 2 discusses various aspects of the research hardware and instrumentation used to perform experiments and collect data, as well background on the imposed, ordered structure phenomenon. Section 2.1 describes the Magnetized Dusty Plasma Experiment (MPDX) and its components. Section 2.2 describes the original observations of the imposed, ordered structures which is the motiving work for this

dissertation. Section 2.3 consists of three subsections and contains descriptions of several diagnostic systems, as well as the background theory on each of those components. Finally, two different primary experimental configurations are presented in Section 2.4.

In Chapter 3, experiments to determine a means of characterizing the imposed, ordered structures are presented. Section 3.1 describes the set of experimental parameters used as well as a scheme to account for data taken with different cameras. The initial experimental observations and data processing methods are presented in Section 3.2. Finally, a discussion on the results of these experiments and their application to understanding the imposed, ordered structures is given in Section 3.3.

Chapter 4 provides the details of initial tests which look to probe the plasma beneath a large "waffle"-shaped electrode. Section 4.1 describes the results of experiments which use a double Langmuir probe to measure electron temperatures and densities across the plasma. Calculations of effective electric potential structures determined by applying Poisson's equation to the electron density measurements is given in Section 4.2. Measurements from another device, which uses two ring shaped probes to measure electric fields, is presented in Section 4.3. Section 4.4 then follows up those measurements by calculating and discussing effective electric potentials resulting from those electric fields.

Experiments which observe the behavior of dust particles beneath the aforementioned "waffle" electrode are presented in Chapter 5. This chapter is made up of several parts which examine the change in dust confinement with increasing magnetic field and how dust behavior reveals the presence of the confining potential. Section 5.1 presents the necessary experimental parameters which are significant to the results presented. A description of the process through which the video data is processed to be used for measurements is given in Section 5.2. The next

part, Section 5.3, presents and discusses measurements of an effective electric potential which is determined from the dust dynamics. Finally, Section 5.4 combines the results of Chapter 4 and Chapter 5 and discusses those results in the broader context of the imposed, ordered structures and plasma sheaths.

Finally, Chapter 6 summarizes the major goals and observations discussed in this dissertation. Possible applications of the observed phenomena as well as avenues for future work are also discussed.

Chapter 2 Experimental Hardware and Configurations

In the previous chapter several important physical concepts relevant to this dissertation were introduced. This chapter introduces the principle experimental device, the Magnetized Dusty Plasma Experiment (MDPX) and gives more details on the original observations of the imposed, ordered structures and the motivation behind this dissertation. Discussion on the various experiments performed for this work, describing the various pieces of hardware, as well as the different configurations that were used, are then be provided. Later chapters focus only on the methods used to analyze the data, as well as the results of that analysis.

Section 2.1 will give the details of the Magnetized Dusty Plasma Experiment (MDPX). This device is at the heart of the experiments presented in this work and so a thorough discussion of its workings will be provided. Section 2.2 will provide background into the original observations of the imposed, ordered structures, highlighting various analysis techniques which will be important for later chapters. Section 2.3 consists of three parts and details the various diagnostic tools which were used to collect the data presented here. Section 2.3.1 contains details on the various scientific cameras and lenses which were used to record videos of the dust particles. Section 2.3.2 provides details on one of the plasma diagnostics used, the double Langmuir probe. A brief summary of the theory used to determine plasma parameters such as electron temperatures and densities is given. Finally, Section 2.3.3 introduces a new probe which was designed and constructed to study the electric fields present in the imposed, ordered structures.

The last section of this chapter, Section 2.4, provides an overview of two different configurations of MDPX which were used to carry out experiments. The first of these experiments

were carried out in the presence of a conducting mesh, similar to that used in the work discussed in Section 2.2, and is described in Section 2.4.1. The next set of experiments were performed using a large grid-like, "waffle" electrode whose details make up Section 2.4.2.

2.1 The Magnetized Dusty Plasma Experiment

The Magnetized Dusty Plasma Experiment (MDPX) (Figure 2-1) is a superconducting magnet device, capable of producing up to 4 T magnetic fields at its center. The magnetic field is created from four coils of superconducting niobium-titanium strands embedded in 1.1 mm (0.043") diameter copper wire. There are two large coils (673.3 mm/26.5" ID, 913.0 mm/36" OD, 12430 turns) and two smaller coils (560.5 mm/22.1" ID, 692.2 mm/27.3" OD, 7068 turns) that are housed in a thermally insulated cryostat. A complete technical description of the design, construction, and initial testing of the MDPX magnet and vacuum system is given in references by Thomas, et al. [39,40]

The cryostats feature a split-bore design, meaning that there is a hollow bore through the center and the upper and lower halves which house the coils are separated by a gap. The bore through the central axis has a 50 cm (19.7") diameter, and the gap which separates the two halves has a diameter of 157 cm (61.8") and a spacing of 19 cm (7.5"). The magnet system consists of four magnet coils, two in each of the halves, which are cooled to around 4-5 K. The magnet coils are cooled by cryostats on the top and bottom which exchange heat with a helium gas line, which is then pumped back to heat exchange with chilled water, the temperature of which is usually between 7-10 °C. A drawing of the body of the cryostat is shown in Figure 2-2.

Figure 2-1 The Magnetized Dusty Plasma Experiment (MDPX). Two magnet coils reside in each of the black cylinders. Cryostats above and below the magnet (just out of frame) pull heat out of the coil cooling them to 4-5 K. The octagonal vacuum vessel can also be seen in the center. This split-bore design allows for greater optical and diagnostic access to experiments. [38,39]

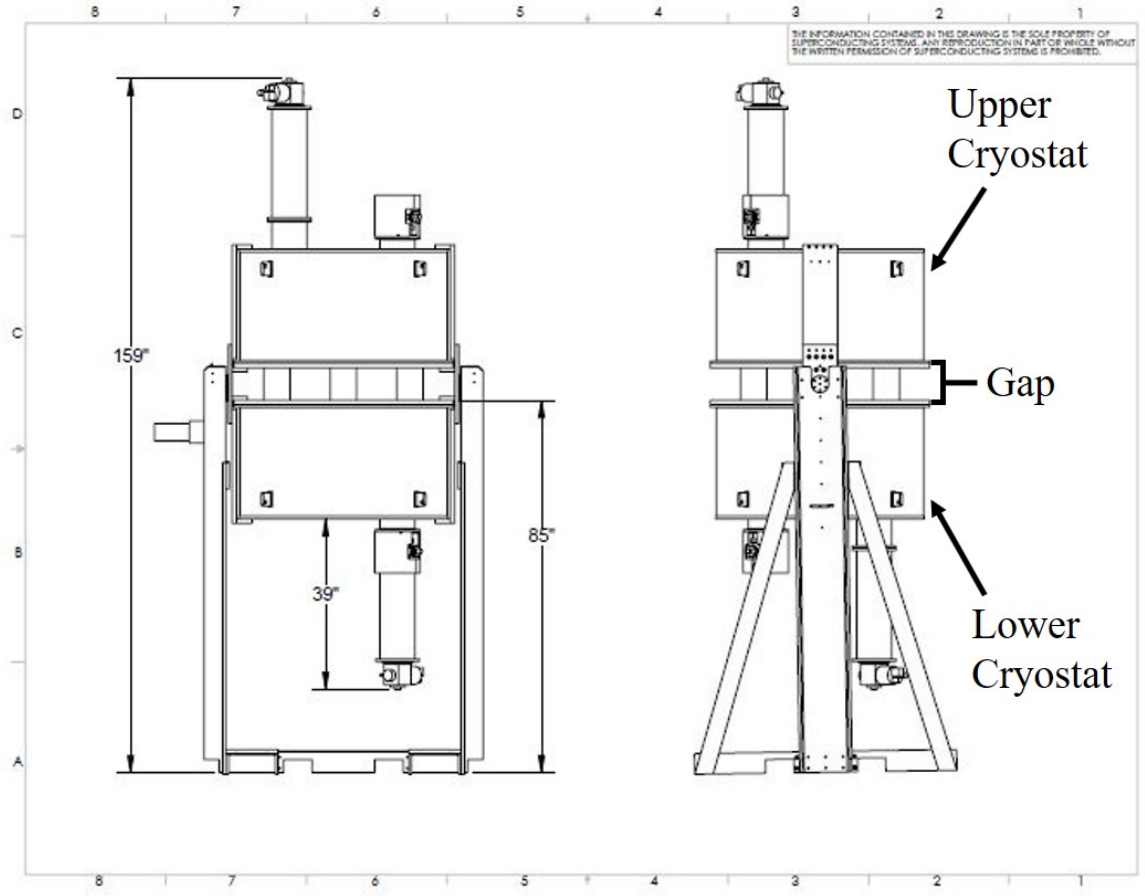

Figure 2-2 Technical drawing of the MPDX cryostat and support stand. All dimensions are given in inches. Drawing from Superconducting Systems, Inc.

Plasma experiments are performed by inserting a vacuum chamber into the central bore of the cryostat. There are currently several vacuum chamber designs that can be accommodated into the magnet, but all of the experiments performed for this work were performed using the primary MDPX octagonal chamber, shown in Figure 2-3. The MDPX vacuum chamber is comprised of an octagonal aluminum frame and two flanges on the top and bottom. The octagonal frame has a maximum outer diameter of 43.2 cm (17”), a circular inner diameter of 35.5 cm (14”), and a height of 17.8 cm (7”). Each of the eight faces has a rectangular through-hole of 12.7 cm tall × 10.2 cm

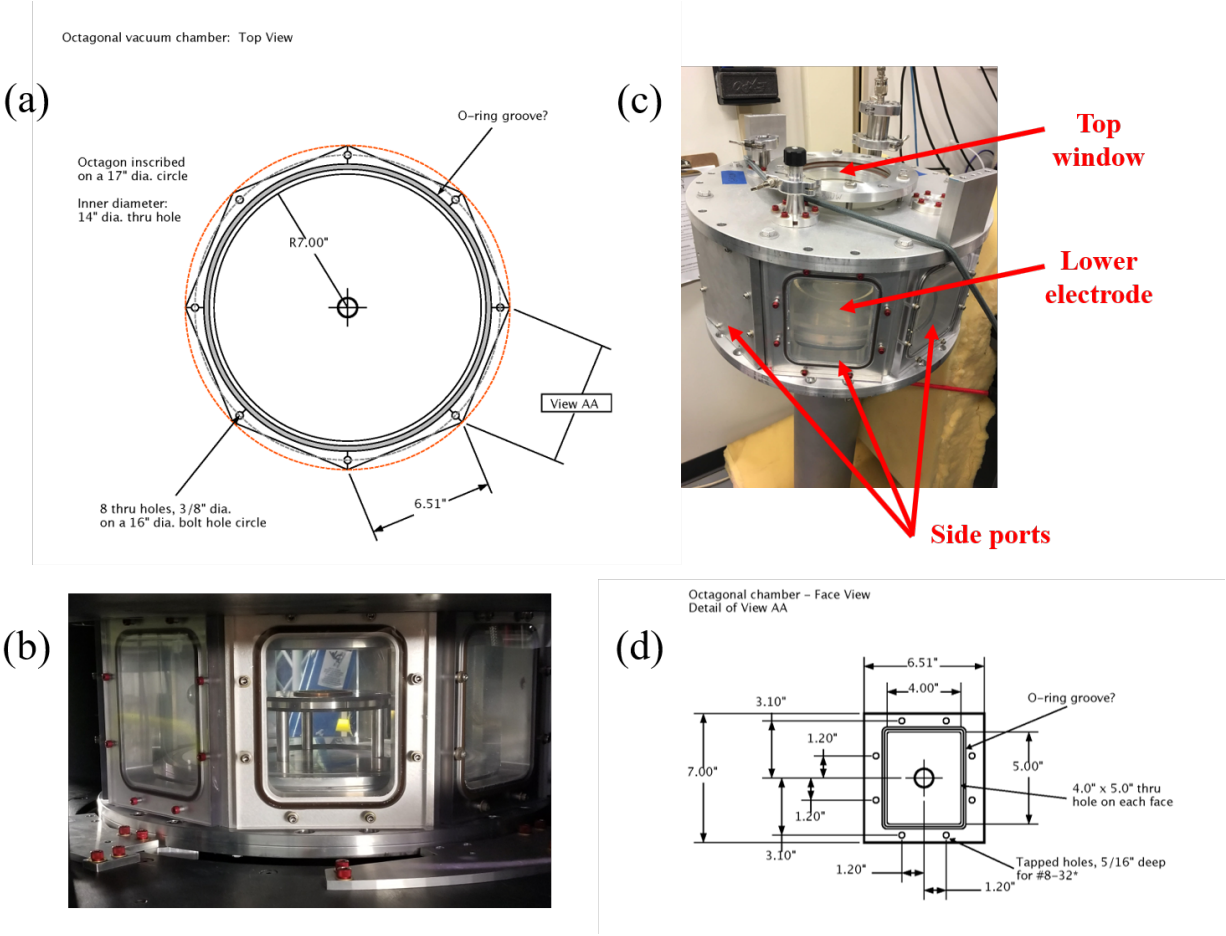

Figure 2-3 (a) Top down schematics of the primary MDPX vacuum chamber. (b) Side image of the vacuum chamber installed in the center of MDPX with a stand used to levitate particles closer to the top electrode. (c) The full vacuum vessel with side ports, the lower electrode, and the top window which allows views into the chamber along the magnetic axis. (d) Schematic of the side port windows seen in (b) and (c).

wide (5" × 4"). The top and bottom flange have an outer diameter of 45.7 cm (18") and a thickness of 2.54 cm (1"). The top flange also has a 14 cm (5.5") diameter through-hole at the center, which allows for a window to be mounted to view the interior of the chamber along the magnetic axis.

Plasma is generated within the vacuum vessel using a pair of capacitively-coupled radio frequency (cc-rf) electrodes of 34.2 cm (13.5") diameter in the top and bottom of the chamber. The electrodes are spaced 11 cm (4.33") apart. The bottom electrode has a 15.2 cm (6") diameter, 0.3 cm (1/8") deep depression in the center. The top electrode has a 14.6 cm (5.75") diameter through-

hole so that experiments can be viewed from the top of the magnets. [40] Plasmas are generated using radio frequency heating at 13.56 MHz. Due to hardware upgrades in the time separating the different experiments presented in this dissertation, two different rf networks were used. The first of these is a RF-VII, Model RF-3-XIII, power supply connected to a Model ATN-5 autotuning matching network, which was used in experiments presented in Chapter 3, as well as some early data taken in Section 4.3. This system can deliver power levels up to 100 W to the system. Recently a new rf network was installed in the MDPX system, a T&C Power Conversion Inc., Model AG 0313, power supply which was paired with a Model AIT-600 autotuning matching network. This rf network was used for the experiments presented in Chapter 4 and Chapter 5. For all the experiments reported here, rf-generated plasmas were generated with an output power of 5 W.

2.2 Initial Observations of Imposed, Ordered Structures

Dust particles within the plasma are very useful for revealing the potential structures present in the background plasma. Puttscher, et al. [41], used dust particle trajectories to study the effect of crossed electric and magnetic fields in the sheath of a radio frequency discharge, gaining insight into the various forces and potentials present. Subsequently, Hall and Thomas were able to make use of similar techniques to calculate the electric fields acting on a dust cloud which experienced an asymmetric response to an electric potential perturbation within the plasma. [42] Even the initial observations of the imposed, ordered structures, the study of which is at the heart of this dissertation, makes use of particle trajectories to calculate an effective trapping potential for dust particles [43] which was then followed up by an suggested formulation for the potential structures. [44]

These original observations of the imposed, ordered structures were some of the earliest published experiments from the MDPX device and form the core motivation for this work. In these

experiments clouds of dust particles were observed organizing into square lattice patterns in which the spatial ordering of the particles within the cloud corresponded to the dimensions of a conducting wire mesh in one of the experimental electrodes. These patterns were dubbed imposed, ordered structures since the organization of the dust particles has a very well-defined square ordering, but this ordering comes from an external source and was not due to the natural interparticle interaction that results in a plasma crystal.

The first experiments were performed in an argon plasma generated using a capacitively-coupled radio frequency (cc-rf) power supply at f = 13.56 MHz and 2.5 W of power. A piece of titanium wire cloth was used to cover the through-hole in the top electrode with the intent of maintaining a mostly uniform conducting boundary while still allowing for recording of the dust cloud to be taken through the top port of the vacuum vessel. The wire cloth was a size 40 × 40 mesh with wire diameter of 0.0098" (0.25 mm) and center-to-center spacing of 0.0246" (0.625 mm) between parallel wires. Silica microspheres of 2 μm diameter were used as the dust component.

By examining sums of several frames of video, traces of particle movement would reveal the structure within the background plasma being imposed by the conducting mesh. These ordered structures were observed to depend highly on both the magnetic field present and the neutral gas pressure within the chamber. In those experiments, it was found that the ordering occurred at high magnetic fields ($B \geq 1$ T) and low neutral gas pressure ($P \leq 100$ mTorr). Under those conditions the square lattice is clearly visible, and some particles even appear to be spatially trapped, as was shown in Figure 1-2.

It was also observed that covering part of the mesh with FTO (fluorine-doped tin oxide)-coated glass, or increasing the neutral pressure, would suppress or even nullify the pattern from

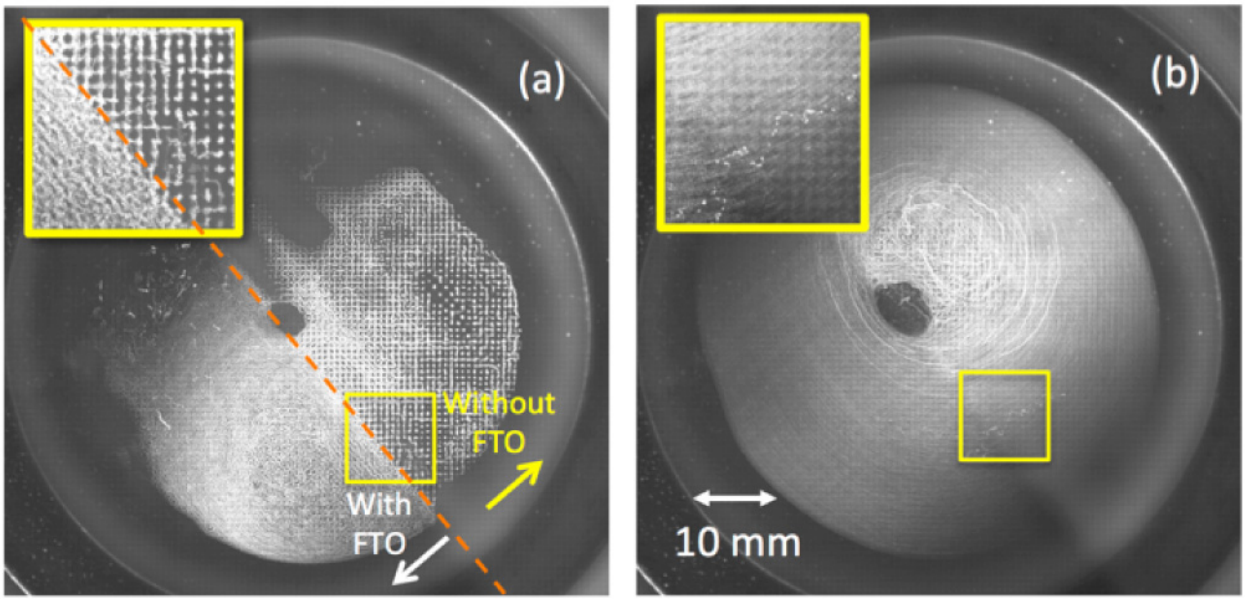

Figure 2-4 Dusty plasma of 2 μm diameter particles with FTO coated glass placed on one half of the titanium mesh. For both cases $B = 1.5$ T. (a) $P = 128$ mTorr. The figure shows how the FTO coating on the glass appears to short out the imposed, ordered structure on the side that it cover. (b) $P = 167$ mTorr. At higher pressures the imposed, ordered structure becomes washed out and are free to circulate regardless of the presence of the FTO coated glass. From Thomas, et al., Phys. Plasmas 22, 030701 (2015), Fig. 4.

the mesh. Though a clear boundary can be seen between the two regions, as in Figure 2-4. The paper concludes by postulating that these imposed structures are likely the result of a plasma sheath structure around the conducting mesh which is extended into the plasma due to the strong magnetic field. The reasoning behind this is that when examining the length scales related to plasma magnetization, discussed previously in Section 1.2, it would seem unlikely that particles within the plasma should be able to carry information about the grid through the plasma to the dust.

At the operating conditions in these experiments the ions would have a mean free path of $\lambda_{mfp,i} \sim 0.6$ mm and the electrons $\lambda_{mfp,e} \sim 8$ mm. The distance from the mesh to the dust particles would have been roughly 30 to 40 mm which would mean that the plasma particles would be likely to have had several collisions occur in that distance and any initial trajectory they were

following would be lost. This is what leads the authors to suggest that there is this extended sheath structure from the wire mesh which interacts with the strong magnetic field and carries the information and shape of the mesh deep into the plasma. When combined with the observation that the imposed, ordered structures are suppressed with increasing neutral pressure, which increases the number of collisions with neutral atoms, it is quite apparent that the degree of magnetization within the plasma plays a very important role in how these structures are formed.

This work will follow through on several aspects of these original ideas. Using sums of images to understand the organization of the dust particles and how confined the dust particles are to the imposed, ordered structures. This technique will be applied extensively in Chapter 3. The development of plasma sheaths around conducting elements within a plasma will also be discussed later in this chapter. How these sheaths play a role in the confinement of dust particles will be examined in Chapter 5.

A follow up study of the imposed structures focused on the spatial properties of the dust particles and on observations of a quasi-discrete "hopping" motion of the particles as they moved within the grid pattern. [43] Argon plasmas were generated at a fixed neutral pressure of 135 ± 3 mTorr (18 ± 0.2 Pa) using the same cc-rf within a narrow power range of 1.6 – 2.0 W. The magnetic field was the primary experimental parameter and varied from 1.25 – 2.5 T. These experiments also utilized a new "dual" wire mesh configuration. Within a custom designed and built mesh holder one half was 24 × 24 brass mesh with a 0.0142" (0.36 mm) wire diameter and 0.0421" (1.07 mm) center-to-center spacing, and the other half 30 × 30 aluminum mesh with a wire diameter of 0.011" (0.28 mm) and center-to-center spacing of 0.033" (0.85 mm).

This study focused on three aspects of the imposed, ordered structures: the spatial ordering of the particles, the velocities and velocity distributions of both trapped and drifting particles, and

the development of a basic understanding of the electric fields and potential structure present. The first of these, examining the spatial structure of the dusty cloud, again utilized the sums of sets of video frames to reveal the patterned structure of the mesh. Taking intensity profiles of selected regions within the image sums shows that the distance between peaks matches closely the spacing of the wires in the two meshes. They also show that biasing the grid either positive or negative relative ground can affect the flow of particles. At positive bias the particles more easily rotate under the influence of an ion $\vec{E} \times \vec{B}$ drift, and at negative bias the particles are more likely to be trapped in individual wells, with the cloud becoming more degraded.

The next sections focused on the particle dynamics of both trapped and flowing particles. For trapped particles, the particle positions were tracked within the video frames and velocity measurements, made from the instantaneous displacements, were found for multiple particles over a range of magnetic fields. For each magnetic field case a histogram of the velocity measurements for multiple particles was produced and fit with a Gaussian profile. A comparison of the distribution widths across the different magnetic fields found that they were approximately equal. Several particles which were found to "hop" from one trapping location to another were also identified. Using similar methods as before, the average particle velocities were calculated. A preliminary analysis of the motion was carried out to determine the effective electric potential in between two trapping locations. Using the relation:

$$\Delta K_j = \frac{1}{2} m_d \langle v_{dj} \rangle^2 - \frac{1}{2} m_d \langle v_{dj-1} \rangle^2 = -q_d \left(\phi_j - \phi_{j-1} \right) \tag{2-1}$$

where j is a measurement at time t, $j-1$ is a measurement at time $t - \Delta t$, m_d is the dust grain mass, v_{dj} is the dust grain velocity, and ϕ_j is the effective electric potential. The results of this

analysis show a very consistent shape of the effective electric potential which increases in strength with magnetic field. Examples of these measurements are shown in Figure 2-5.

Understanding the spatial ordering of the particles within the imposed ordered structures will be the core focus of Chapter 3. By using the image sums and measurements of the particle positions a set of parameters is developed to characterize under what conditions the structures are present and their degree of influence on the dust grains. Later, in Section 5.3 particle image velocimetry (PIV) techniques are used to measure average velocities of the cloud. This allows for the velocity profiles to be examined across the cloud, instead of just a few particles at a time, to find measurements of the larger confining potentials.

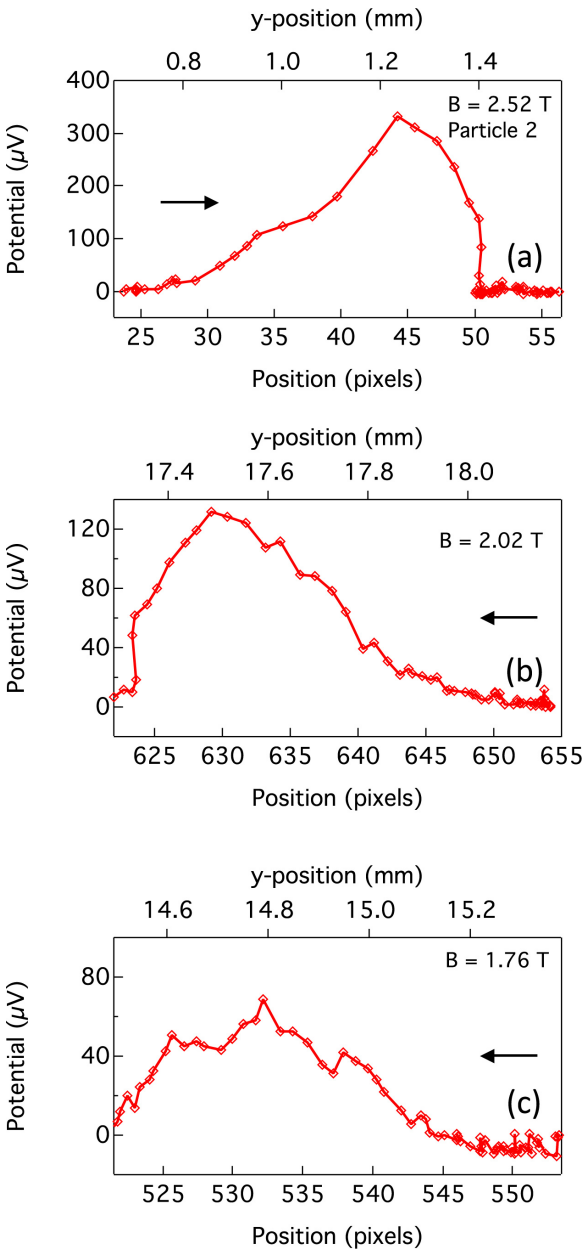

Figure 2-5 Plots of the effective potential measured from the motion of the particles at various magnetic fields. (a) $B = 2.52$ T; (b) $B = 2.02$ T; (c) $B = 1.76$ T. The arrow in each figure indicates the direction of particle movement. Notice how as the magnetic field increases the effective potential increases as well. From Thomas, et al., Phys. Plasmas 22, 113708 (2015), Fig. 9.

2.3 Plasma Diagnostic Systems

This section will detail the various diagnostics that were used to collect data during experiments. The first type of hardware discussed is the different scientific cameras used to record images and videos of dust particles within the plasma. The second will be the two different types of probe diagnostics used to measure plasma properties: a double Langmuir probe is used to measure the electron temperature and density, and a custom designed pair of ring probes is used to measure electric fields. Both probes were constructed as part of this research project.

2.3.1 Cameras and Lenses

The most common way to take measurements of dusty plasmas is to record videos of dust particles that have been illuminated by a laser sheet. The experiments discussed in this dissertation made use of two different model cameras. The first camera is a PointGrey, model Flea3 USB 3.0 13Y3M-C. This is a 1.3 MP CMOS camera with a resolution of 1280 × 1024 pixels, capable of recording at 150 fps at full resolution. The second camera is a Ximea model xiQ MQ042MG-CM camera. This is a 4.2 MP CMOS camera with a resolution of 2048 × 2048 pixels, capable of recording at 90 fps at full resolution.

Different experiments require different fields of view, so a few different lenses were used to record data. For the experiments discussed in Chapter 3, a 105mm (f/2.8) Nikon MicroNikkor lens was used. These experiments required a larger viewing area and so used a lens with a shorter focal length to capture the full area through the top window. The second lens used for the experiments discussed in Chapter 5 was a 200 mm (f/4.0) Nikon MicroNikkor. For those experiments only a small region of the vacuum chamber was of interest, combined with higher magnetic field necessitating placing the cameras further away, which led to the use of the longer

Figure 2-6 Image of Nikon 200 mm lens and Ximea camera.

focal length lens. An image of the Ximea camera connected to the 200mm lens using a C- to F-mount adapter can be seen in Figure 2-6.

2.3.2 Double Probe

One of the two plasma probe devices used in the experiments discussed in Chapter 4 was a double Langmuir probe (DLP). This probe differs from the typical single Langmuir probe (SLP) in that it has two conducting tips which are electrically biased relative to the other, instead of a single probe tip which is electrically biased relative to the chamber ground. [45,46] A variable voltage is applied between the two probe tips and the current through the circuit is measured, as is shown in the idealized illustration in Figure 2-7. The benefit to this design is that the DLP makes measurements of the plasma that are limited to the ion saturation current collected on each probe. Because of this, a DLP minimizes the electrical perturbation of the plasma during a voltage sweep.

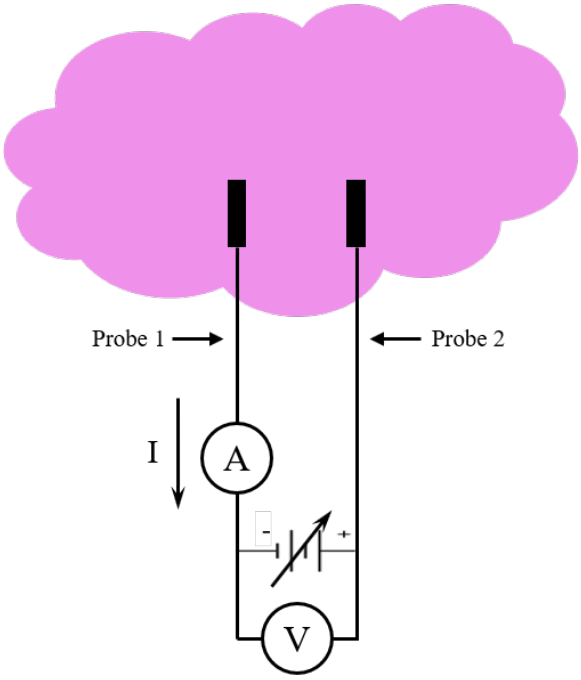

Figure 2-7 Idealized double Langmuir probe circuit. A variable voltage source is applied between two probe tips within a plasma. The current between the two tips is measured with an ammeter.

The probe used in these experiments was constructed from two tips of tungsten wire. The probe tips are each 0.5 mm (0.02”) in diameter, 2.5 mm (0.10”) long, and spaced 2 mm (0.08”) apart. The tungsten wires are fed through a ceramic tube with an outer diameter of 3.8 mm (0.15”). A picture of the probe tips is shown in Figure 2-8. The tungsten wire was fed through a ceramic shaft, which was then held in place by an aluminum vacuum feed through. The probe was moved through the chamber a distance of 15 cm (5.9”) using a Velmex stepper motor, in 0.1 cm (0.04”) increments. At each position a current-voltage (IV) trace was taken. Probe traces were made with a Keithley 2400 sourcemeter unit (SMU), with MiniCircuit low pass filters used to filter out any RF signal above 1.9 MHz.

The double Langmuir probe is useful because it allows for both electron temperature and density to be easily found from a characteristic current-voltage (I-V) trace. If the two probe tips are identical, the ideal characteristic trace takes the form:

$$I = I_{si} \tanh\left(\frac{eV}{2T_e}\right) \tag{2-2}$$

where I is the current collected, I_{si} is the ion saturation current, e is the electron charge, V is the voltage difference between the two tips, and T_e is the electron temperature. Modification to Equation 2-2 can be made to account for geometric and plasma sheath effects such that

$$I(V) = a_0(V - a_1) + a_2 \tanh\left(\frac{V - a_1}{a_3}\right) + a_4 \tag{2-3}$$

where a_0 is the slope of the ion saturation region resulting from sheath effects, a_1 is the voltage offset, a_2 is the ion saturation current, a_3 is the slope of the trace about zero volts ($dI/dV_{V=0}$), and a_4 is the current offset. A typical double probe trace and the modified hyperbolic tangent fit are

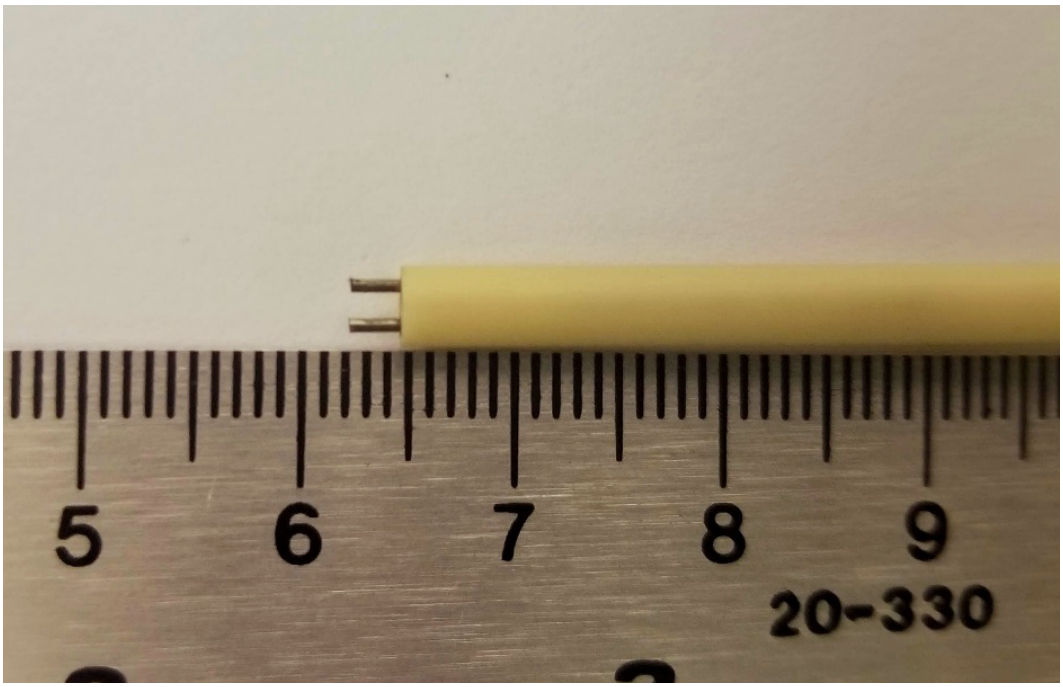

Figure 2-8 Image of the double Langmuir probe. The probe tips consist of tungsten wire of length 2.5 mm (0.10") and 0.5 mm (0.02") diameter, spaced 2 mm (0.08") apart. The ceramic shaft has an outer diameter of 3.8 mm (0.15").

shown in Figure 2-9 The electron temperature (T_e) and electron density (n_e) is calculated from the fit parameters using:

$$T_e = \frac{a_3}{2} \tag{2-4}$$

$$n_e = \frac{a_2}{eA\sqrt{\frac{eT_e}{m_i}}} \tag{2-5}$$

where A is the probe area given in m^2. [47,48] The error for the electron temperature and density are calculated as

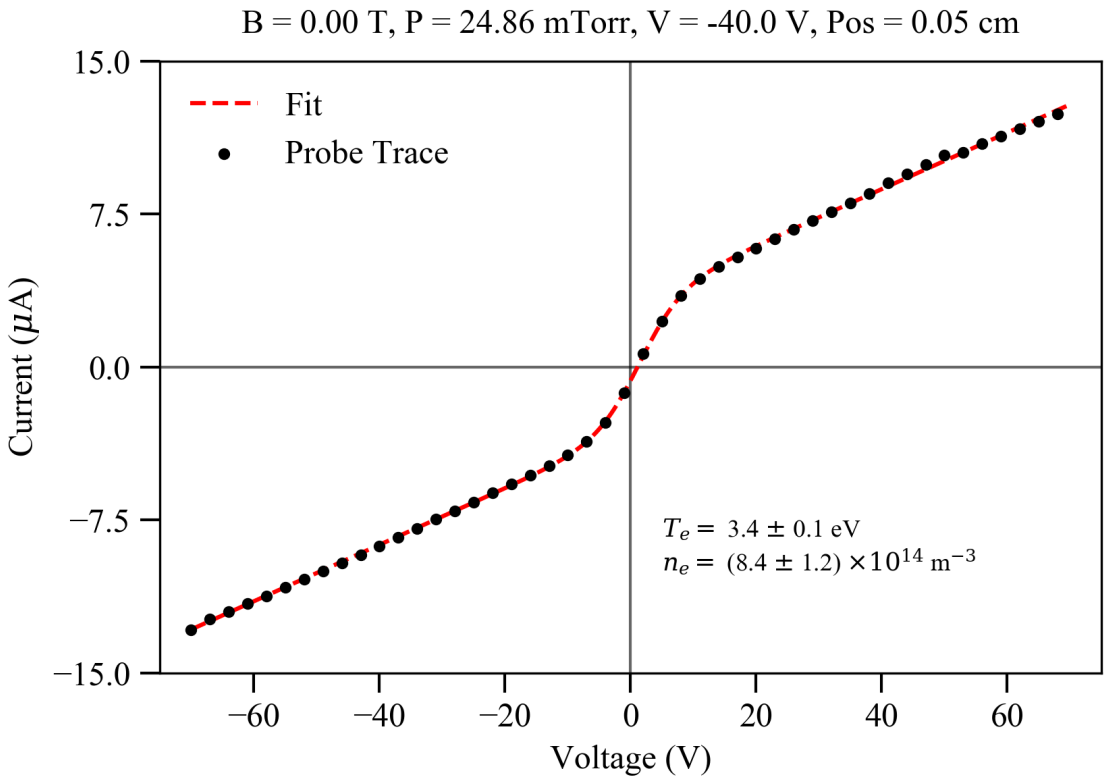

Figure 2-9 A typical double Langmuir probe trace is shown as black points. The fit to the data is shown in red. The fit produces results of an electron temperature of 3.4 eV and an electron density of 8.4 × 10^{14} m^{-3}.

$$\delta T_e = \sqrt{\frac{\delta a_3}{2}} \tag{2-6}$$

$$\delta n_e = n_e \sqrt{\left(\frac{\delta a_2}{a_2}\right)^2 + \left(\frac{\delta T_e}{2T_e}\right)^2 + \left(\frac{\delta A}{A}\right)^2} \tag{2-7}$$

where δa_2 and δa_3 come from the square root of the diagonal of the covariance matrix. In the example shown in Figure 2-9, the plasma has an electron temperature of $T_e = 3.4 \pm 0.1$ eV and an electron density of $n_e = (8.4 \pm 1.2) \times 10^{14}$ m^{-3}. Fits are determined using the "curve_fit" function from the "optimize" library in the SciPy Python package. This function uses a non-linear least squares algorithm to fit the function in Equation 2-3.

2.3.3 Ring Probe

The other type of probe that will be used in experiments discussed in Chapter 4 is a new probe design that will be referred to as a ring probe (RP). The intent of this probe is to allow for more direct measurements of the electric field within the plasma.

In an initial approach to measure the electric field, a pair of electrically floating, spatially separated, cylindrical Langmuir probe tips, 0.5 mm (0.02") in diameter, were used. However, in the strong magnetic field, the directed motion of the ions/electrons along the magnetic field lines appeared to strongly impact the floating potential measurements, as the design of the probe caused one of the probe tips to be "shadowed" and was unable to collect a comparable amount of current compared to the other probe tip. An alternative probe design, in which a pair of ring-shaped probes was developed in order to measure the floating potential while circumventing the "shadowing" issue.

This new probe is comprised of two stainless steel rings wrapped around a 3D printed probe head, which was designed with channels which allow an electrical connection to be fed through to multiple rings at multiple places along the head, shown in Figure 2-10. Each of the probe heads is electrically floating within the plasma, meaning that it develops some electrical potential on the surface through the collection of ions and electrons within the plasma; an electrical bias is not externally applied.

The 3D printed head is made of a photocurable polyacrylate and printed on a stereolithography (SLA) style 3D printer. A schematic of this probe head is shown in Figure 2-11. The head is 4.76 mm (0.1875”) in diameter and 25.4 mm (1”) in length, the base of the head has an OD of 6.35 mm (0.25”) and an ID of 4.76 mm (0.1875”). The design and print of the probe

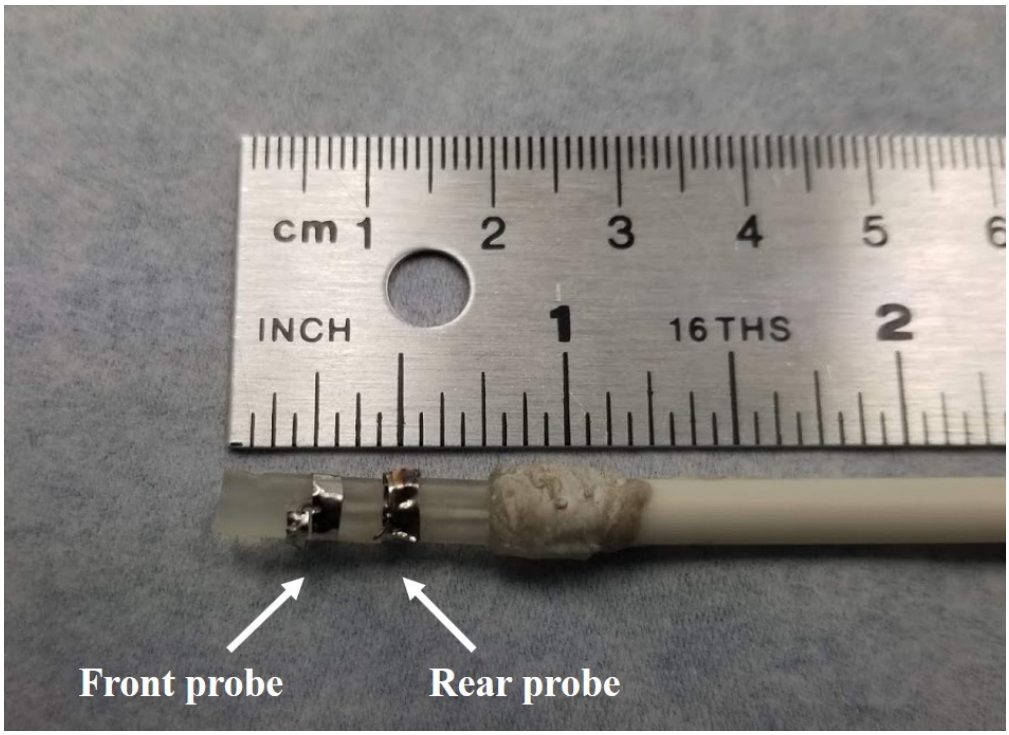

Figure 2-10 Ring probes and 3D printed probe head. The probe head is made of a 3D printed photocured polyacrylate, 25.4 mm (1”) in length with a 4.76 mm (0.1875”) diameter. The probe tips are stainless steel sheet metal 4.76 mm (0.1875”) wide and have a center-to-center spacing of 5.55 mm (0.22”).

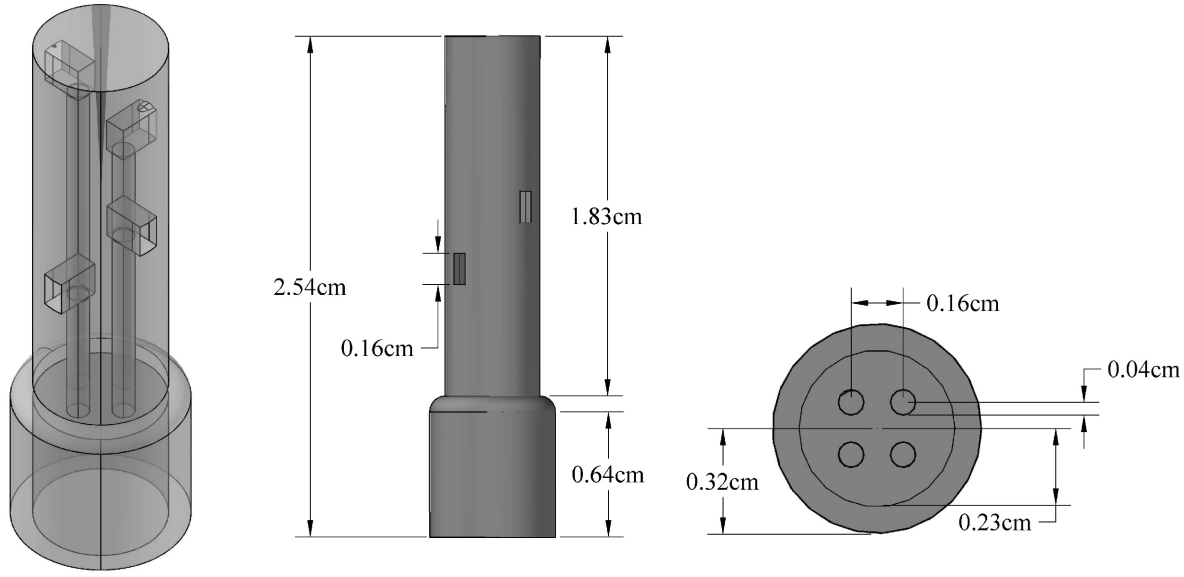

(a) X-ray view (b) Side view (c) Bottom view

Figure 2-11 Schematic drawing of the 3D printed probe head. Multiple views are shown including (a) an x-ray view illustrating the channel structures which allow wires to be run through the interior of the probe head, (b) a side view, and (c) a bottom view.

head intended to allow for several rings at various points along the head, but this proved more challenging than anticipated during the build phase and so only the minimum required two rings were built into the finished probe. The two ring probe tips are made by cutting stainless steel sheet stock into 2.4 mm (0.1") wide strips, wrapping them around the probe head, and spot welding to stainless steel wire that had been fed through the probe head. The gap between the rings is 3.18 mm (0.125") and the center to center spacing is 5.55 mm (0.22"). The probe head is then bonded to a ceramic shaft to complete the probe. The completed probe can be seen in Figure 2-10.

To measure the floating potential each voltage signal is first passed through a voltage divider. This basic voltage divider circuit consists of a 1 MΩ and a 100 kΩ resistor. The resistances were not matched though, and the front and rear probes were reduced by a factor of 10.91 and 10.87, respectively. The voltage is then measured using a National Instruments Data Acquisition

(DAQ) card Model SCB-68a. Each voltage measurement was made at a sampling rate of 50 kHz and 5000 samples were collected for each measurement; i.e.., a total sample time of $\Delta t = 0.1$ s. The ring probe was then incrementally stepped 15 cm (5.9") through the vacuum chamber with a step size of 0.1 cm (0.04"), waiting 0.25 seconds between each step to allow the floating potential to settle.

An example of the measurements made by these probes is shown in Figure 2-12(a). Although there is some noise to the signal the measurements made by each ring are easily distinguished from one another. In this example, under the experimental conditions of $B = 0.0$ T, $P = 25.29$ mTorr (3.37 Pa), the probes are beneath an electrode with a positive bias of $V = +40$ V applied to it, resulting in the positive floating potentials seen here. At each position an average floating potential is calculated. Figure 2-12(b) shows the two probe signals plotted as a function of position in a region about the center of the chamber at the same experimental conditions as Figure 2-12(a).

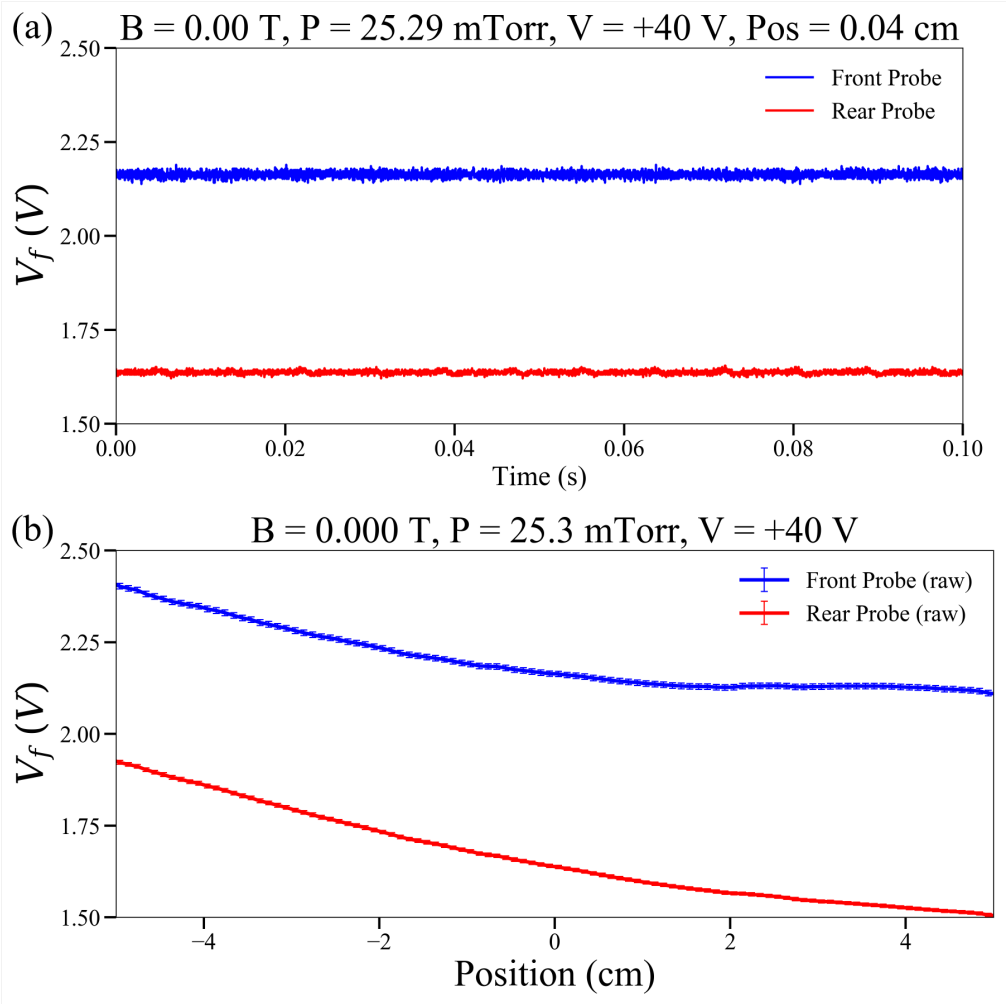

Figure 2-12 (a) Floating potential measurements made by the ring probe from the front probe is shown in blue, and the rear probe is shown in red. This position is directly beneath the "waffle" electrode with a bias of $V = 40$ V. The magnetic field was $B = 0.0$ T and the neutral pressure was $P = 25.29$ mTorr (3.37 Pa). (b) Floating potential profiles across the center of the chamber for the (a) front probe shown in blue and the (b) rear probe shown in red.

2.4 Experimental Configurations

This section outlines the various configurations and setups which were used for the experiments performed for this work. These outlines will detail the arrangement of various pieces of experimental hardware in and around the MDPX vacuum vessel. Discussion of the experimental parameters used in each configuration will be given in the appropriate chapters detailing those experiments.

2.4.1 Experiments with Conducting Mesh

The first configuration shown will be applicable to experiments discussed in Chapter 3, in which a fine conducting mesh is used to produce the imposed, ordered structures. This is the same type of mesh used by Thomas, et al. [43] This was a deliberate choice because a key criterion for these studies was to operate at similar conditions as the original experiments which examined the imposed, ordered structures. The conducting mesh was a size 30 × 30 aluminum wire cloth. The wires that comprised the mesh have a diameter of 0.28 mm (0.011”) and center-to-center spacing of 0.85 mm (0.033”). A 10.1 × 10.1 cm (4” × 4”) square piece of this mesh was inserted into the upper electrode to cover the through-hole.

With the current operating spacing of the MDPX electrodes at 11 cm (4.33”) a method to easily adjust the gap between where the dust resides in the chamber and the mesh in the upper electrode was needed. To more closely match previously reported operating conditions for the gridding experiments [27], which used a gap of 6.2 cm (2.4”), a conducting stand was designed. A schematic of this stand is shown in Figure 2-13, while a picture of the stand inside the chamber is shown in Figure 2-14. A schematic drawing of this configuration is shown in Figure 2-15. This stand consists of a 14.6 cm (5.75”) diameter, 1.4 cm (0.55”) thick, aluminum disk supported by three 5.1 cm (2”) tall aluminum posts. The stand was placed in the center of the vacuum chamber

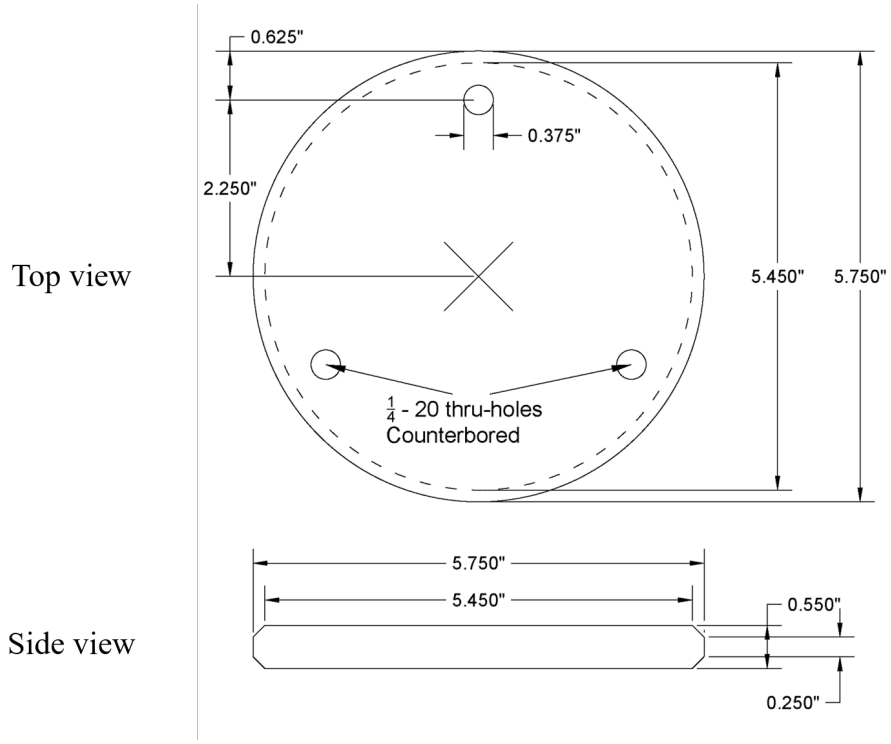

Figure 2-13 Schematic drawing of the stand used for the experiments with the conducting mesh. The stand was supported by 2" (5.1 cm) posts mounted beneath the 1/4-20 size (0.375”/0.95 cm OD) through-holes.

in the indent of the lower electrode so that the final spacing between the top of the stand and the wire mesh in the upper electrode was 4.85 cm (1.9”). A copper gasket of 6.2 cm (2.4”) outer diameter and 5.1 cm (2”) inner diameter was placed at the center of the stand to help provide confinement to the dust particles.

Dust is introduced into the plasma via a dust shaker, a small metal container with a fine mesh on the end, through one of the side windows. The dust shaker could be pushed into the chamber to create a dust cloud and then pulled back to the chamber edge in order to prevent disruption of other data collection. To visualize the dust particles in the experiment a 500 mW, 532 nm green laser beam is passed through a cylindrical lens to create a broad laser sheet which illuminates the dust particles in a thin layer. Videos of the dust particles were recorded using both the Point Grey and Ximea cameras using only the 105 mm Nikon lenses. The cameras were placed

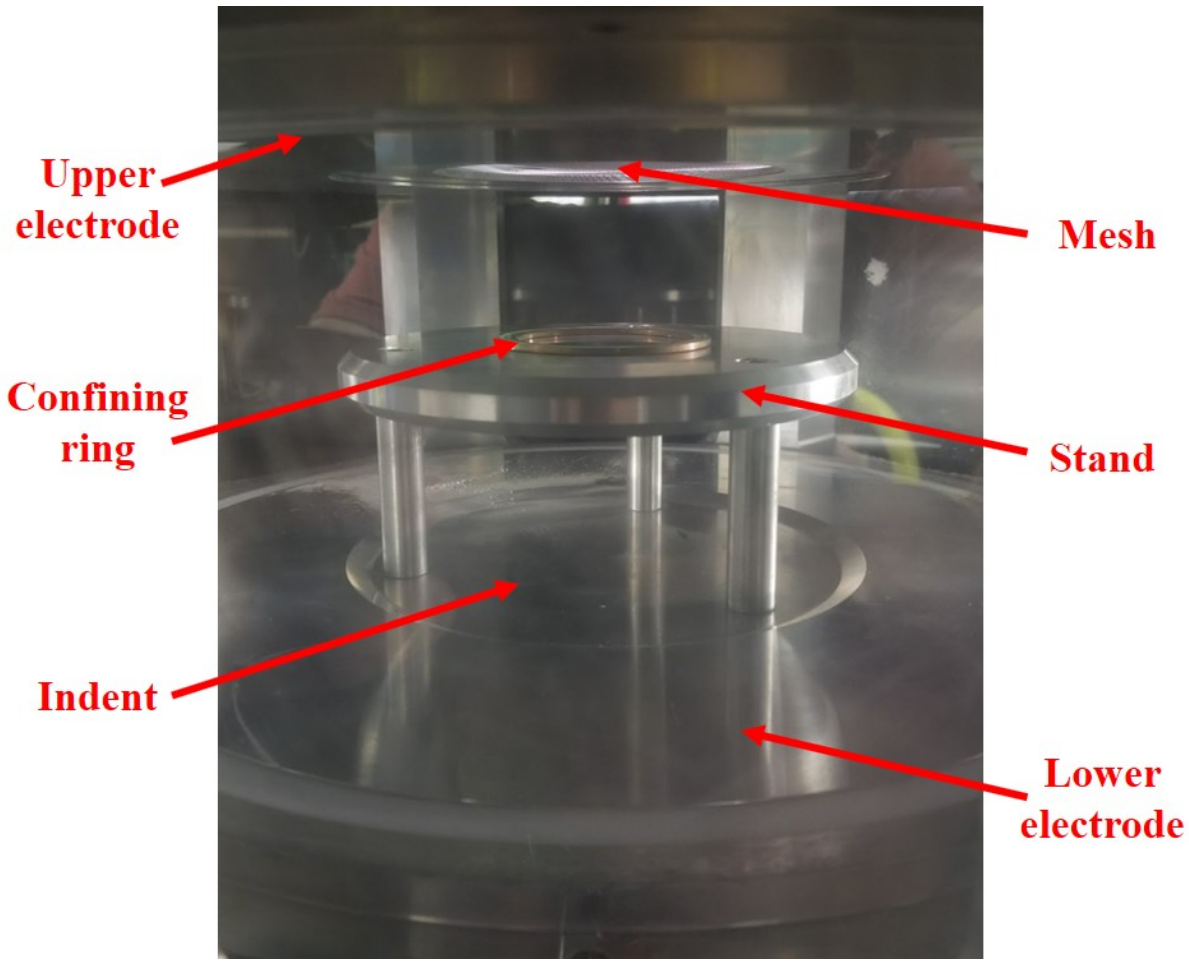

Figure 2-14 Conducting stand positioned in the center of the MPDX vacuum chamber. The gasket used to confine the dust particles can be seen on top.

above the magnet looking down through the bore, along the magnetic axis, to image the dust clouds through the hole in the top electrode.

2.4.2 Experiments with Large Grid Electrode

The second configuration outlined in this subsection will apply to experiments discussed in Chapter 4 and Chapter 5. Instead of a conducting wire mesh a large grid-like, or "waffle" shaped, electrode is used to create imposed, ordered structures and confine dust. Because the wires in the conducting mesh are small enough that plasma probes beneath the grid would be large compared to the wire dimension, it is not possible to resolve the plasma conditions beneath individual wires.

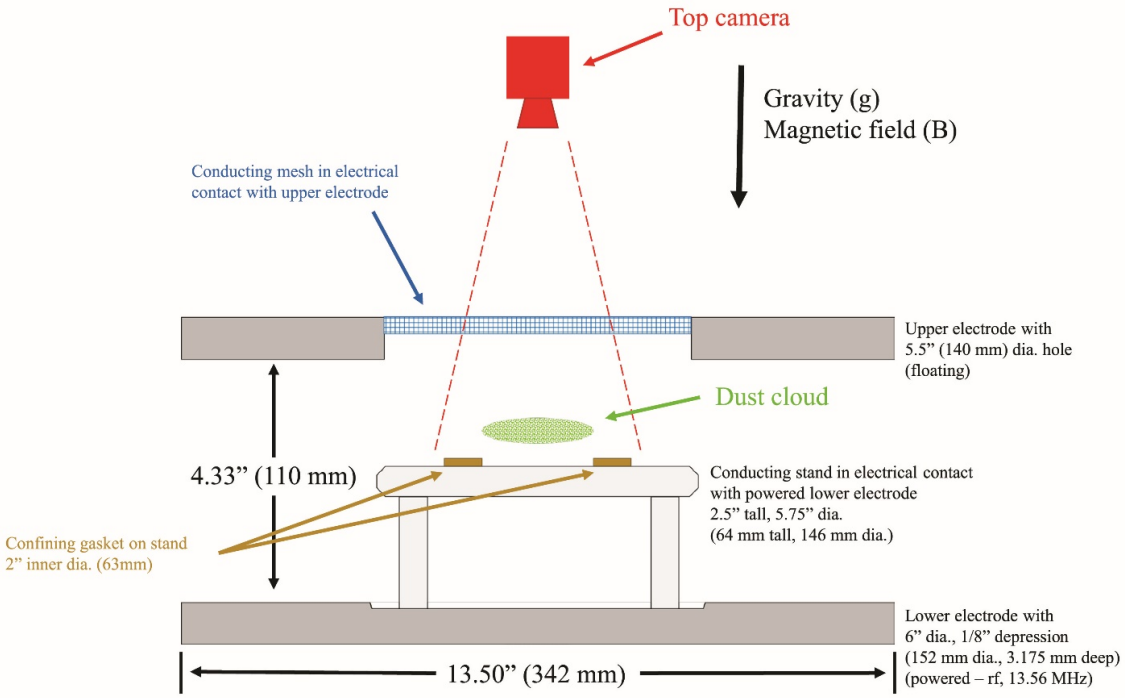

Figure 2-15 Schematic of the MDPX experimental chamber which includes the stand and electrode configuration. The dust cloud floats roughly 10 mm above the stand or ~40 mm below the conducting mesh. The magnetic field and gravity both point in a parallel downward direction as shown in the figure.

The so-called "waffle" electrode was designed so that diagnostics within the plasma, such as the ring probe and double probe, could take spatially resolved measurements beneath the grid (Chapter 4). The electrode is also large enough that the trapping location of the dust can be easily observed while the dynamics of the dust cloud are still observable from the top and side of the chamber (Chapter 5).

The "waffle" electrode, shown schematically in Figure 2-16, is a 0.64 cm (0.252") thick aluminum square of 7.2 cm (2.835") on each side with six 1.6 × 1.8 cm (0.63" × 0.71") rectangular holes giving the electrode its "waffle" design. The electrode was placed into the center of the vacuum chamber on an aluminum rod within a ceramic tube and an "s"-shaped arm which placed

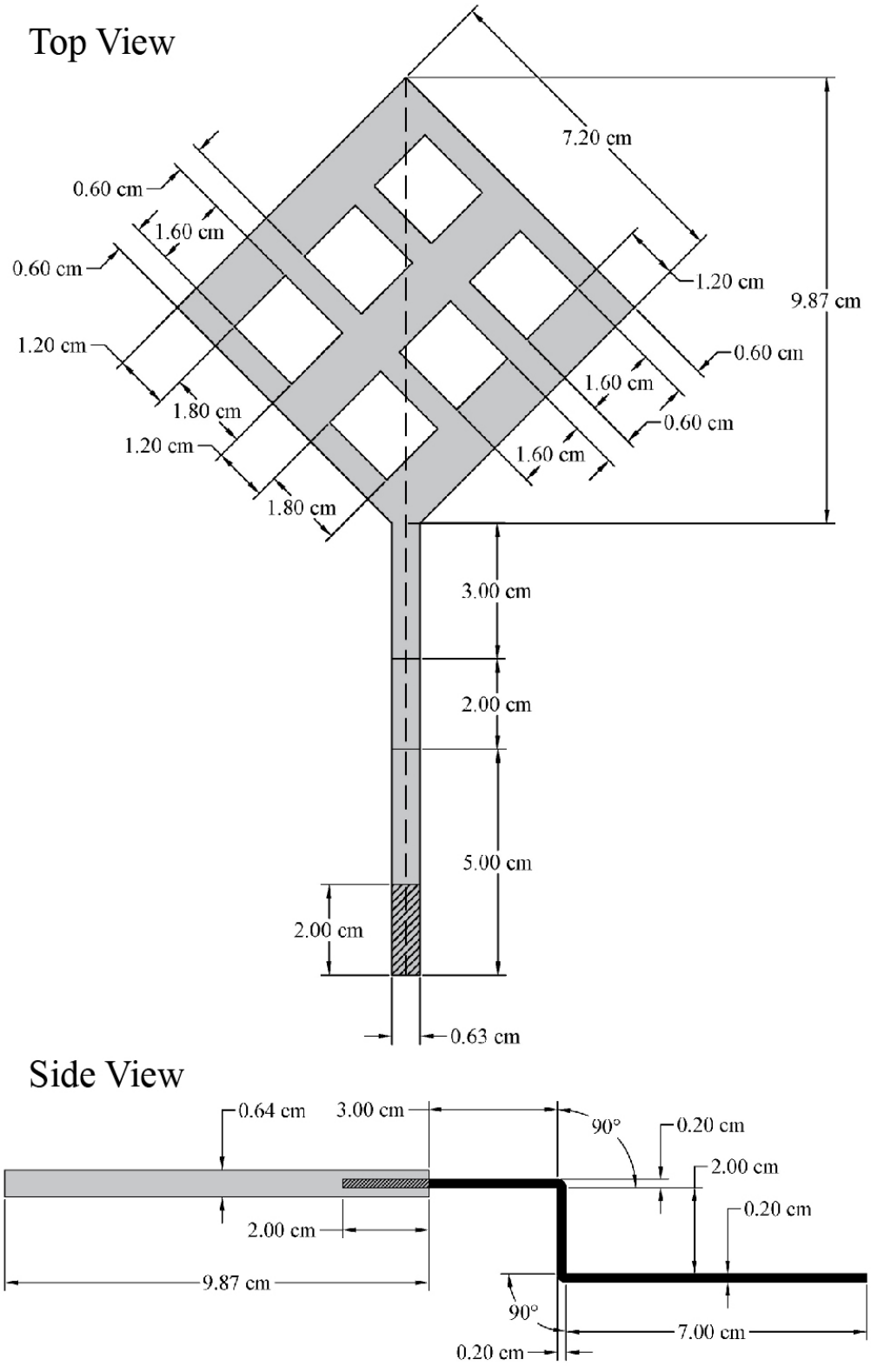

Figure 2-16 Top and side schematics of grid-like "waffle" electrode.

the electrode 8.25 cm (3.25”) above the bottom electrode. An electrical bias was applied to the electrode using either a KEPCO BOP 100-2ML model bipolar operation amplifier or a Keithley 2400 sourcemeter unit (SMU). The through-hole in the top electrode was completely covered with a square of FTO coated glass with the non-conducting side facing downward to mimic the non-conducting boundary above the conducting mesh described in Section 2.4.1.

A drawing of the experimental configuration can be seen in Figure 2-17. Images of the interior of the vacuum vessel can be found in Figure 2-18. The same dust shaker used in the experiments described in Section 2.4.1 is also used for these experiments. When dust particles were being used in this configuration they were confined to the center of the chamber below the “waffle” electrode with a 4-1/2” CF Flange copper gasket of 8.23 cm (3.24”) outer diameter and 6.38 cm (2.51”) inner diameter. Dust clouds were levitated between 0.5-1.5 cm (0.2-0.6”) above the lower electrode, 6.75-7.75 cm (2.4-3”) below the “waffle” electrode. Particles were illuminated by a red laser, oriented to make a vertical sheet of laser light to illuminate a vertical plane of particles to be viewed from the side of the chamber perpendicular to the magnetic axis. Dust particles were recorded from the side using a Ximea model camera and Nikon 200mm lens.

Both the double Langmuir probe and the ring probe were used in this configuration. Probes were affixed to a Velmex BiSlide linear translation stage which allowed them to be incrementally stepped through the vacuum chamber to take spatially resolved measurements. When extended into the center of the chamber the double probe was 2.2 cm (0.88”) below the “waffle” electrode, and the ring probe was 2.9 cm (1.13”) below the “waffle” electrode.

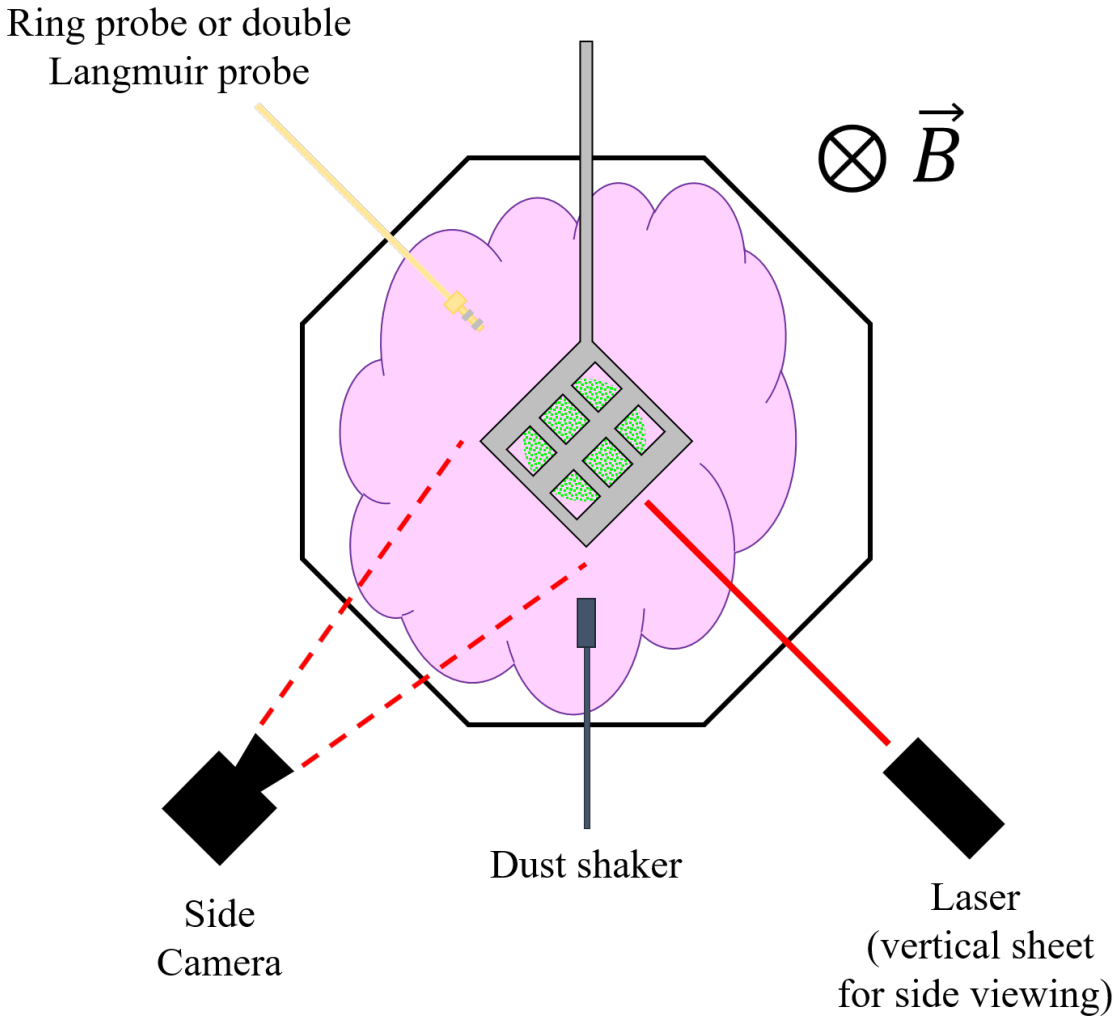

Figure 2-17 Cartoon of the grid electrode experimental configuration as it was set up in the MDPX vacuum vessel.

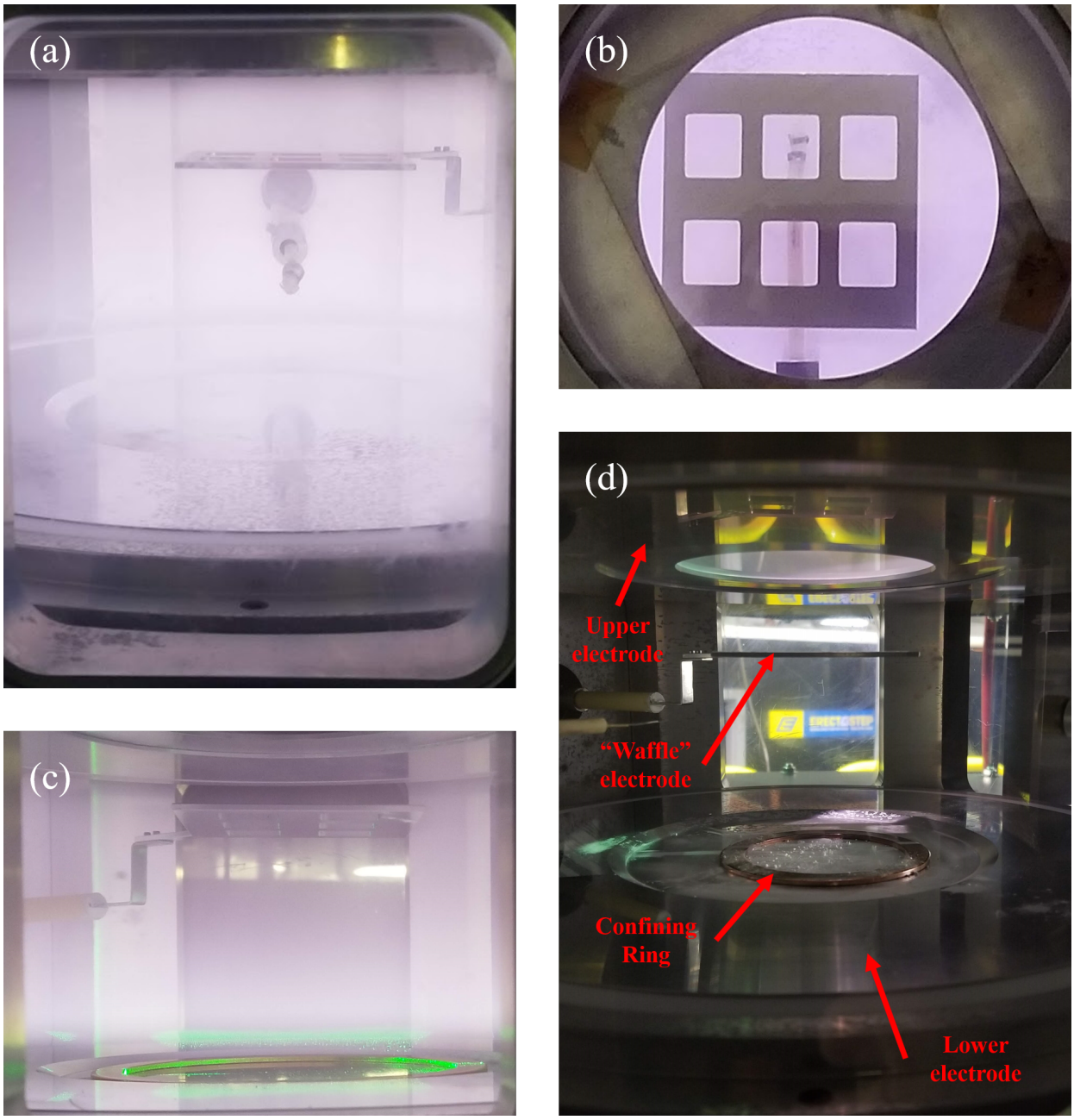

Figure 2-18 Interior of the MDPX vacuum vessel with the "waffle" electrode. (a) Looking through the plasma at the ring probes as they move through the chamber. (b) Ring probes from the top passing underneath the "waffle" electrode, measuring the electric fields in the holes of the electrode. (c) A dust cloud levitates in the chamber below the electrode at $B = 0$ T. (d) After the experiments remnants of the dust clouds which have settled onto the bottom electrode.

Chapter 3 Characterization of Imposed, Ordered Structures

The work presented in this chapter focuses on the development of robust analytic methods to characterize the formation of these structures within the plasma. As discussed in Section 2.2 previous authors have made progress in understanding the particle behavior in the imposed, ordered structures and to use them to reveal the background potential structure. Here the primary challenge will be to determine how to systematically quantify how the particles are organized within the experiment. While it is possible to use a single image to make an instantaneous measurement of the particle orientation in the experiment, that single image is insufficient to reveal the full complexity of the particle dynamics that occurs in the formation of these imposed, ordered structures.

This is illustrated by the images in Figure 3-1. In this image, a dust cloud made of 2 μm diameter silica microspheres is suspended in an argon plasma generated at 40 mTorr (5.33 Pa) with 5 W of rf power at a magnetic field of $B = 1.2$ T. Figure 3-1(a) and Figure 3-1(b) both come from the same, single video frame but highlighting two different regions of the dust cloud. For this single frame the two regions appear quite similar, both have dust grains arranged in a square lattice. However, when examining these two regions over a sum of 600 video frames the particles show different behavior. In Figure 3-1(c), the sum of images shows that the particles remain relatively fixed in space. By contrast, in Figure 3-1(d), the flowing motion of the particles is observed and resembles the overall square pattern. Methods for examining these imposed ordered structures must then be capable of considering the confinement and organization of particles both on small timescales (single frames) and long timescales (image sums over several seconds).

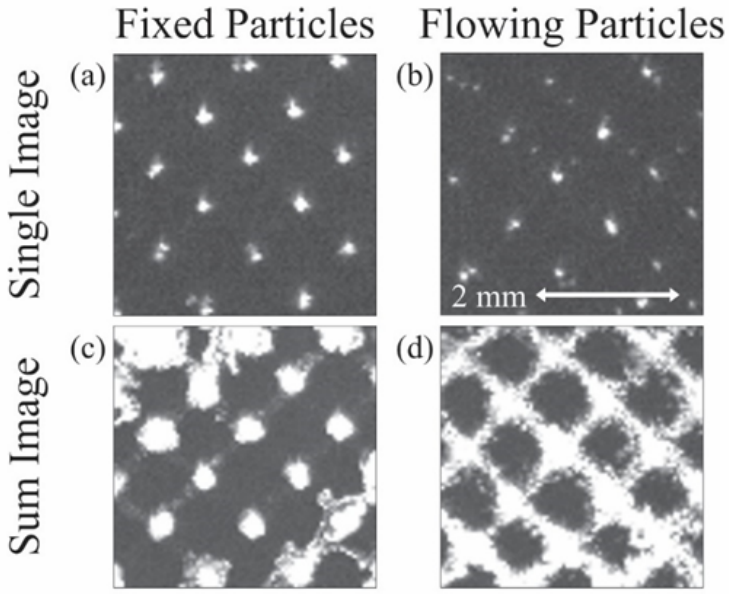

Figure 3-1 An example of the gridding phenomenon at B = 1.22 T and P = 40 mTorr. The first two images (a) and (b) show two different regions of the dust cloud in a single frame which exhibit the grid structure and qualitatively very similar. When the full data set is summed up the two regions (c) and (d) show different behavior though with (c) having fixed particles which do not flow and (d) where particles flow through the grid structure indicated by streaking. From Hall, et al., Phys. Plasmas 25, 103702 (2018), Fig. 1.

In a paper written by the author of this dissertation, Hall, et al, PoP (2018) [49], a two-parameter method was developed that enabled the characterization of both the spatial ordering and the flowing motion of particles that are suspended in the imposed, ordered patterns. This paper presented a method of identifying the particles, creating a 4-fold local bond ordering map, quantifying the flowing motion in terms of light intensity, then converting the result into a two-dimensional space that uses a Hall-parameter type ordering. This chapter of the dissertation incorporates the work that was published in that paper.

Section 3.1 will discuss the detailed experimental parameters which were used as well as a calibration scheme for comparing images made with two different cameras. The details of the experimental configuration were given previously in Section 2.4.1. Section 3.2 will discuss the

experimental measurements which were made and the data processing methods which were used. This section will also show the development of the two parameters which will be used to quantify the degree to which particles are influenced by the imposed, ordered structures. Section 3.3 will contain the primary results and discussion, showing how the developed parameters correlate to several different types of particle motion which were observed.

3.1 Experimental Parameters

This section provides the operating parameters for experiments performed with the conducting wire mesh. The details of the configuration of the experimental hardware was outlined in Section 2.3.1. An argon plasma was produced in the MDPX vacuum chamber by applying a 13.56 MHz radio frequency signal to the bottom electrode while the top electrode was grounded. Plasmas were created at a rf power of 5 W with 1 ± 0.2 W of reflected rf power.

The primary experimental parameters were: neutral gas pressure which ranged between 40 – 160 mTorr (5.33 – 21.33 Pa) and magnetic field which ranged between 0.49 – 1.46 T. These two parameters were chosen as the primary experimental conditions to vary as each of the plasma length scales discussed in Section 1.2 depend on just one of the two. The Larmor radius, r_L, is only a function of the magnetic field through the gyrofrequency, and the mean free path, λ_{mfp}, is only a function of neutral pressure through the neutral density and ideal gas law. The combination of these two parameters, i.e. the Hall parameter, h, which depends on both the magnetic field and pressure will also be shown to play an important role in determining the presence of the imposed, ordered structures.

The dust particles used in this experiment were silica microspheres which had a diameter of 2 ± 0.2 microns. The dust particles were illuminated using a 500 mW, 532 nm laser and recorded using either the PointGrey or Ximea camera described in Section 2.2.2. The PointGrey

camera was used for magnetic fields between B = 0.49 – 1.22 T and the Ximea was used at B = 1.46 T. The camera was changed due to the high magnetic fields interfering with the electronics of the PointGrey camera, causing data communication issues between the camera and the computer. Both cameras used the 105 Nikon lens and recorded in greyscale at either 120 fps (PointGrey) or 80 fps (Ximea). The spatial resolution of the PointGrey camera was 45.5 microns per pixel, and the spatial resolution of the Ximea camera was 35.8 microns per pixel. A calibration was made to compensate for the lower light levels collected with the Ximea camera.

To perform this calibration a short video was recorded with each of the cameras of the same basic scene. The same 105 mm focal length lens was used for each camera, and the lens aperture was maintained between the videos. The videos consisted of 100 frames each which were then averaged together to allow for outside fluctuations in the light levels. Those average images can be seen in Figure 3-2. Since the images taken with the Ximea camera tended to be darker, and the sample of the total data taken was smaller with the Ximea, it will be the dependent variable that is transformed through the calibration. The next step in creating the calibration was to take the

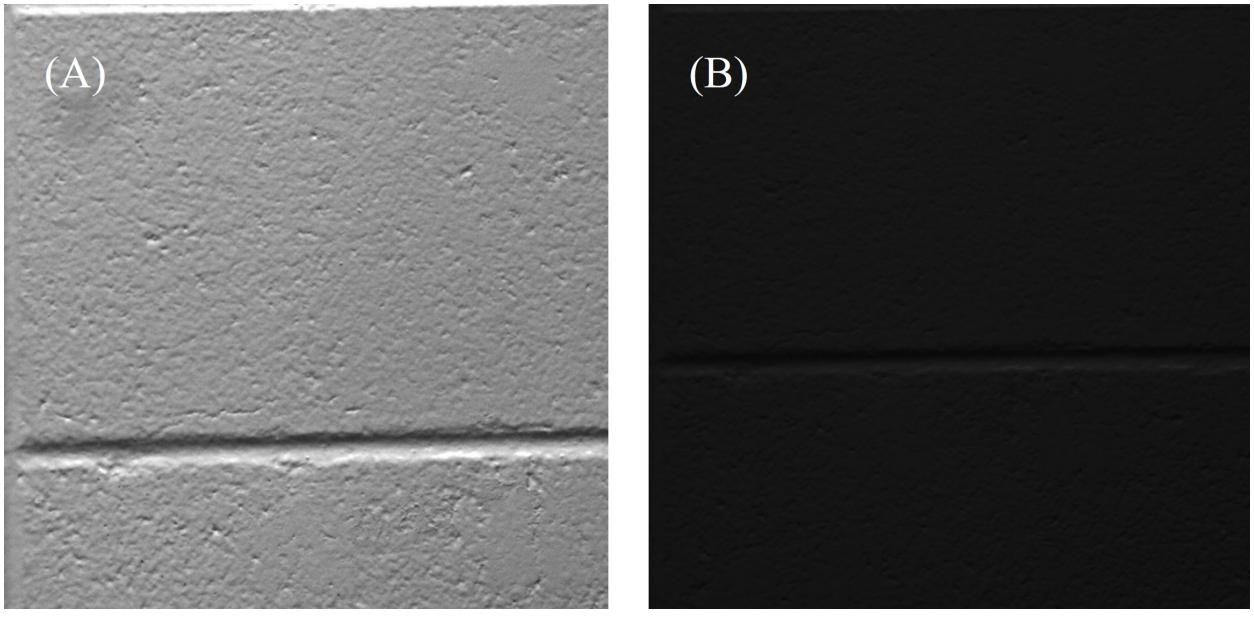

Figure 3-2 Average images from the (a) PointGrey and (b) Ximea cameras.

ratio of the PointGrey average image to the Ximea average image. A scatter plot is made of these average ratios to the pixel values of the Ximea average image. This scatter plot is then fit using a least square fit to a power law equation of the form:

$$f(x) = Ax^k \tag{3-1}$$

where A is the amplitude of the fit and k is the exponent. The parameters found were $A = 93.239$ and $k = -0.851$. The scatter plot and exponential fit are shown in Figure 3-3. When processing the Ximea images the pixel values were multiplied by this calibration factor, f, so that the calibrated pixels took the form

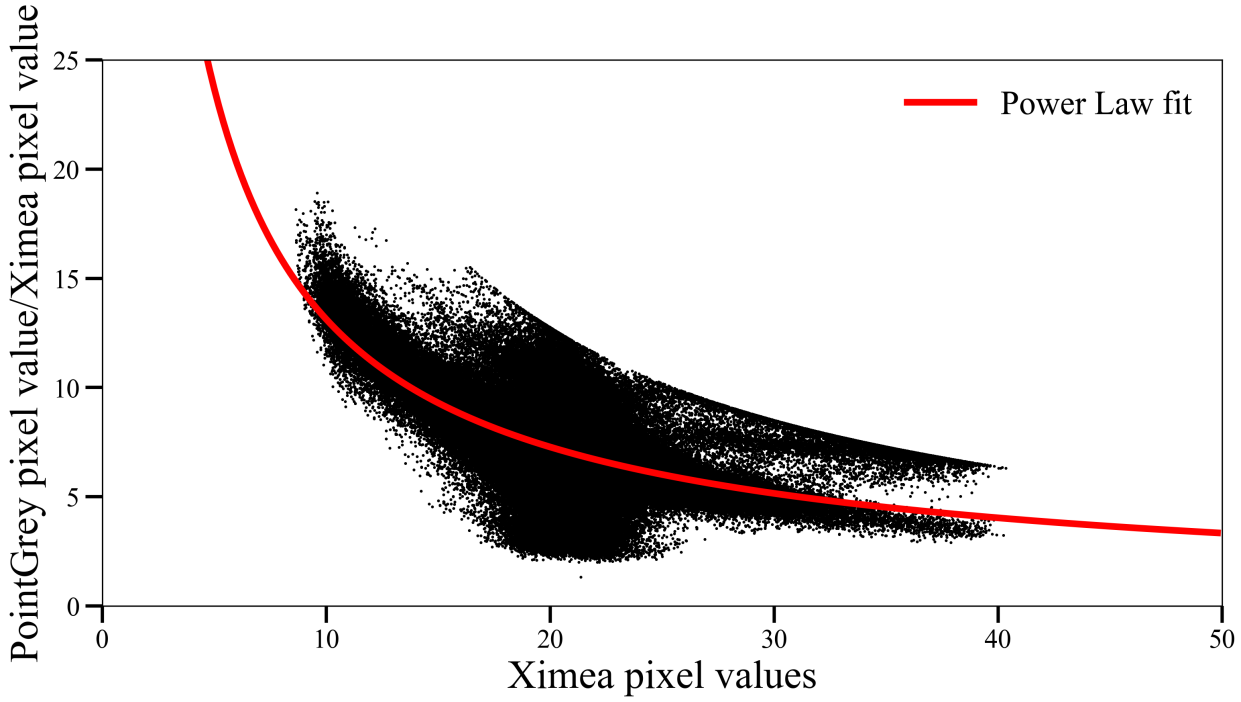

Figure 3-3 Calibration fit for comparing the Ximea and PointGrey image data. Pixel ratios of the PointGrey values to the Ximea values versus the raw Ximea pixel values are shown as black points. The power law fit is the red line.

$$Image = Ax^{1+k} \tag{3-2}$$

This final transformed image is what is used for comparing the pixel intensities between the Ximea and PointGrey data sets.

For the experiments discussed here, the ion length scales will be the primary focus. This is because the ion-neutral mean free path, λ_{mfp}^{in}, and ion Larmor diameter, d_L, twice the Larmor radius, r_L, will be comparable to the wire diameter of the conducting mesh, w; i.e., on the order of a few hundred microns. The electrons, by comparison, have Larmor diameters of only a few microns, and neutral mean free paths on the order a millimeter, meaning that their plasma length scales are either too small or too large to be meaningfully compared to the conducting mesh. The calculated ion length scales and their ratios to the wire diameter of the conducting mesh are given in Table 1. These experiments will also make use of the modified Hall parameter h' to combine the dependence on magnetic field and neutral gas pressure into a single unitless parameter which

Table 1 A list of experimental parameters, calculated ion-neutral mean free path lengths, λ_{mfp}^{in}, ion Larmor diameters, d_l, and the ratios of these quantities to the diameter of the wire in the wire mesh, w. The ion temperature is assumed to be $T_i = 300$ K for these calculations. The wire diameter is $w = 280$ μm.

B (T)	d_l (μm)	d_l/w	P (mTorr/Pa)	λ_{mfp}^{in} (μm)	λ_{mfp}^{in}/w
0.49	676.71	2.42	40/5.33	237.64	0.85
0.61	543.59	1.95	60/8.00	158.43	0.57
0.73	454.23	1.63	80/10.66	118.82	0.43
0.97	341.85	1.22	100/13.33	95.06	0.34
1.22	271.79	0.97	120/16.00	79.21	0.28
1.46	227.12	0.81	160/21.33	59.41	0.21

describes the magnetization of the ions. For the experiments presented here a maximum modified ion Hall parameter of $h'_{max} = 0.333$ was observed in the $B = 1.46$ T, $P = 40$ mTorr case.

3.2 Experimental Observations and Data Processing

This section details the experimental measurements that were made and the methods through which the data was processed. It will also describe the development and application of the two parameters which describe the particles confinement to the imposed ordered structures. The first of these parameters uses image sums and the average pixel intensity within a region of interest (ROI) to parameterize the global confinement of the dust particles. The second is a parameter called the local bond order parameter Ψ which will be used to quantify the particles organization relative to one another.

The initial step of the analysis was to create maximum intensity images from sets of 600 video frames for each set of experimental conditions. These maximum intensity images, as seen in Figure 3-4, highlight the transport of the particles through the background plasma for the span of several seconds. Three types of particle transport were identified. The first is *uncorrelated motion* to the conducting mesh structure as illustrated in Figure 3-4(a), (b), and (c). This motion is referred to as uncorrelated as there is no apparent effect from the imposed, ordered structures present. The second type of particle motion is an *ordered flow* that follows the pattern of the square mesh, as shown in Figure 3-4(d) and (e). These cases clearly show the presence of the imposed, ordered structures, where flowing particles trace out the pattern of the conducting mesh, but do not show the presence of particles trapped at fixed points within the imposed, ordered structure. The third type of particle motion shows the presence of many *trapped particles* in the grid structure which oscillate about fixed points, as highlighted in the boxed region in Figure 3-4(f).

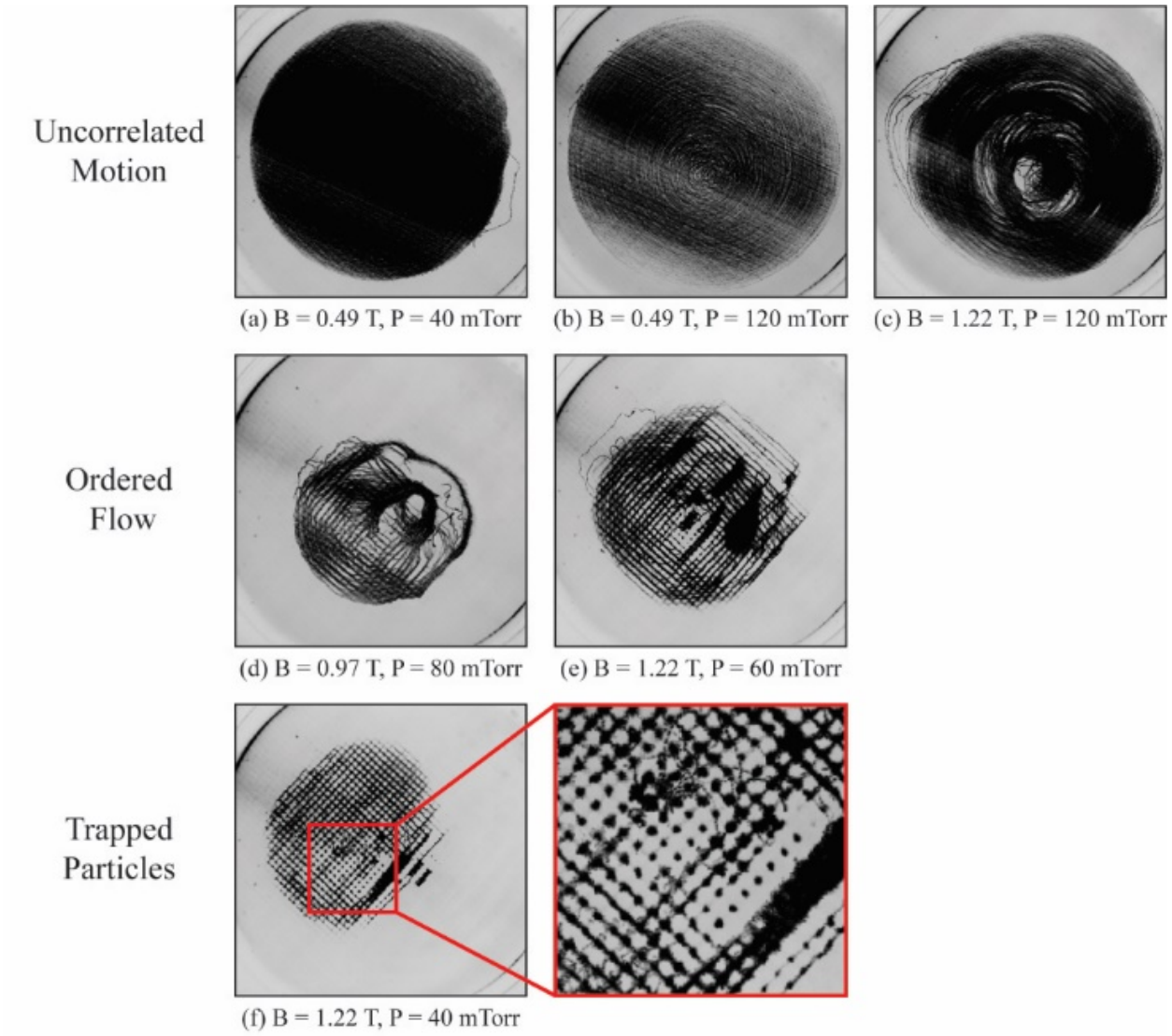

Figure 3-4 Inverted maximum intensity images at various magnetic fields and neutral gas pressures. (a) and (b) For low magnetic fields no gridding, or particle confinement, occurs, though an increased neutral pressure in (b) leads to slower rotation of the cloud and a less dense maximum intensity image. (c) At high magnetic fields, and high neutral pressure, the motion of the cloud is observed to be uncorrelated to the grid structure. (d) and (e) Higher magnetic fields and medium neutral pressure lead to ordered flows of the dust particles through the confining structure of the conducting mesh. (f) The presence of single particles which are confined to single points within the grid are observed at very high magnetic fields and low pressure. From Hall, et al., Phys. Plasmas 25, 103702 (2018), Fig. 3.

For each maximum intensity image, a region of interest (ROI) was identified. The process for determining this ROI is highlighted in Figure 3-5. To determine the ROI, the image was first convolved with a Gaussian kernel which blurs each maximum image sum. This kernel uses a sampling region of 11 × 11 pixels and has a standard deviation, σ, of 21 pixels. An additional median filter was then applied, again with a 11 × 11 sampling region. An example of this blurred image is seen in Figure 3-5 (a).

A binary threshold was then applied to the image. Image sets made with the PointGrey camera used a threshold value of 120, and the image sets made with the Ximea camera used a threshold value of 40. In each case pixels with an intensity below this threshold value were set to 0, and pixels with an intensity equal to or greater than the value were set to 255. A set of contours within the thresholded image were then located using the OpenCV *findContours* command. The largest contour was identified, and the minimum enclosing circle was found for that contour. The

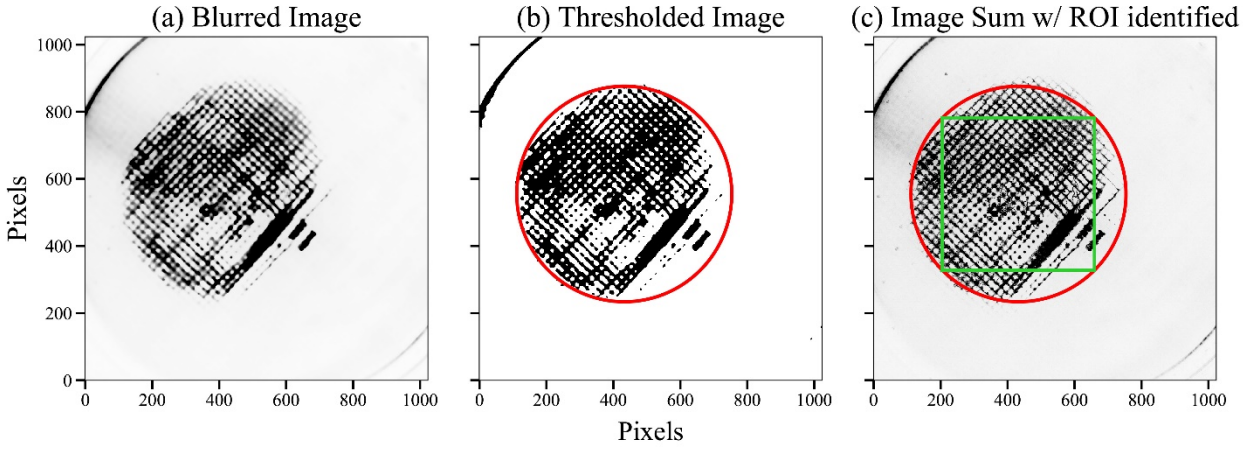

Figure 3-5 (a) Blurred image: When determining the region of interest (ROI), the maximum pixel intensity images are first blurred using Gaussian and median filters. (b) Thresholded image: The images are then thresholded and a minimum enclosing circle is drawn around the largest continuous contour in the image, as shown in red. (c) Maximum intensity image with ROI: A square inscribed within the minimum enclosing circle is found and defined as the ROI, shown in green. From Hall, et al., Phys. Plasmas 25, 103702 (2018), Fig. 4.

ROI was then defined as a square which fits within this minimum enclosing circle. These steps are shown in Figure 3-5(b) and (c).

Within this ROI an average pixel intensity I_{avg} was calculated for the maximum intensity image. Taking the ratio of I_{avg} to the maximum possible pixel intensity for an 8-bit greyscale image, $I_{max} = 255$, will give a measurement of the dust clouds confinement to the imposed, ordered structure over several seconds. For conditions in which a particle cloud was free to flow and rotate in the chamber, as in Figure 3-4(a) – (c), this ratio is near unity. When particles were confined to the imposed, ordered structure, as in Figure 3-4(d) – (f), the maximum intensity image had significant gaps and spaces between the paths through which particles could flow through the plasma, resulting in a reduced intensity ratio. This means that lower intensity ratios could be used as an average measurement of the global confinement to the imposed, ordered structures over long time scales.

While the average intensity ratio provided a measurement of large-scale confinement of the entire cloud over several seconds, it did not provide information on the particle scale organization within individual frames. To determine the particle scale measurements the local bond order parameter Ψ_α was used. For a given particle n, Ψ_α is defined as

$$\Psi_\alpha(n) = \frac{1}{N}\left|\sum_{j=1}^{N} e^{i\alpha\theta_{nj}}\right| \tag{3-3}$$

where α is the expected number of nearest neighbors, N is the measured number of nearest neighbors, and θ_{nj} is the angle of the bond between the n^{th} and j^{th} particles with respect to the x-axis.

The local bond order parameter was originally introduced as Ψ_6 to describe the ordering and melting of two-dimensional crystalline systems. [50] This parameter has been used to describe the structure and phase of various colloidal and dusty plasma systems due to their two-dimensional hexatic nature. [11,51–54] For these experiments a new form of the local bond order parameter will be used, Ψ_4, which will be more appropriate for examining these particles oriented under the square wire mesh. Particles with high values of Ψ_4 ($\Psi_4 \cong 1$) would be those particles which are oriented with angles of nearly ninety degrees between nearest neighbors. A cartoon illustrating the appropriate geometry for both Ψ_6 and Ψ_4 is shown in Figure 3-6.

Values of Ψ_4 were found by first identifying particle locations using the Python particle tracking toolkit TrackPy. [55] A minimum particle spacing of 9 pixels was chosen and measurements of the particle centers were made. A Delaunay triangulation was then found within the ROI for each video frame at a given set of experimental conditions. This Delaunay triangulation was formed by connecting a group of three points so that a circle drawn through each of the points

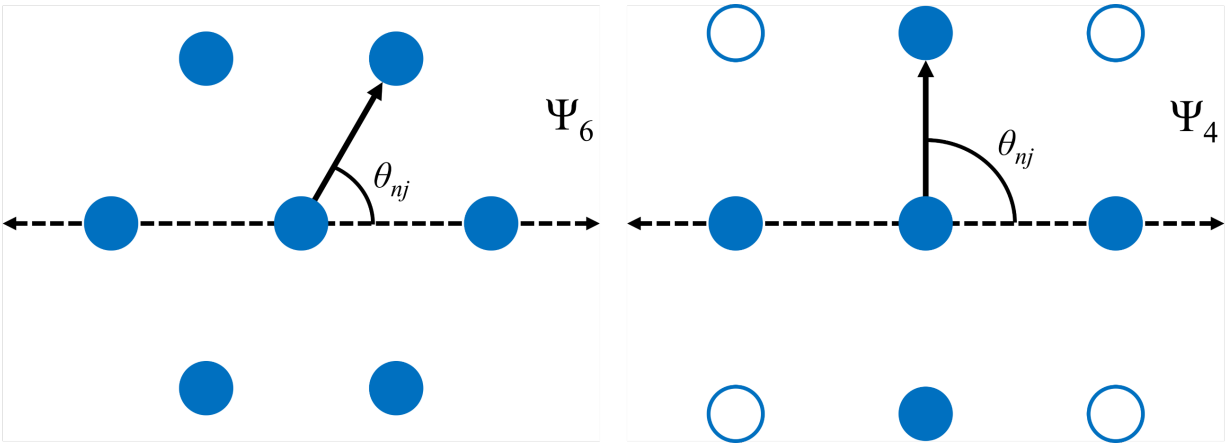

Figure 3-6 On the left is a cartoon demonstrating how Ψ_6 is appropriate for particles arranged in a hexagonal pattern such as those found in plasma crystals. On the right is an example of Ψ_4 which is introduced to more accurately quantify particles which are oriented in a square lattice like those observed in the presence of imposed, ordered structures.

does not contain any other points of the larger set. A histogram of the lengths of the connections found in the Delaunay triangulation, which are the distances between nearest neighbor pairs, was taken over all frames, as shown in Figure 3-7. Only four of the six examples previously given in Figure 3-4 were examined, to illustrate a more consistent set of magnetic fields and pressures. The histogram was then fit with a Gaussian distribution. Pairs of particles which were outside a set of bounds, determined as the points at which the Gaussian fit deviated from the histogram more than 10%, were excluded. This was done to remove pairs which were artificially too close due to being out of plane particles, as well as pairs of particles on the diagonals of the square structure.

Once correct pairs of nearest neighbors were identified, values of Ψ_4 could be calculated for each particle. To do so the difference between the x and y coordinates were taken and constructed into a complex vector of the form

$$v_{nj} = (x_j - x_n) + (y_j - y_n)i. \tag{3-4}$$

This allowed for the angle relative to the x-axis of the complex vector to be calculated using the NumPy function *angle* which could more efficiently find the angle θ_{nj} necessary for Equation 3-4. Once each of these angles was calculated the sum of the complex exponents was taken resulting in a final Ψ for the central particle. Both Ψ_6 and Ψ_4 were calculated using this method and a comparison of the differences between each of those results will be discussed later in Section 3.3.

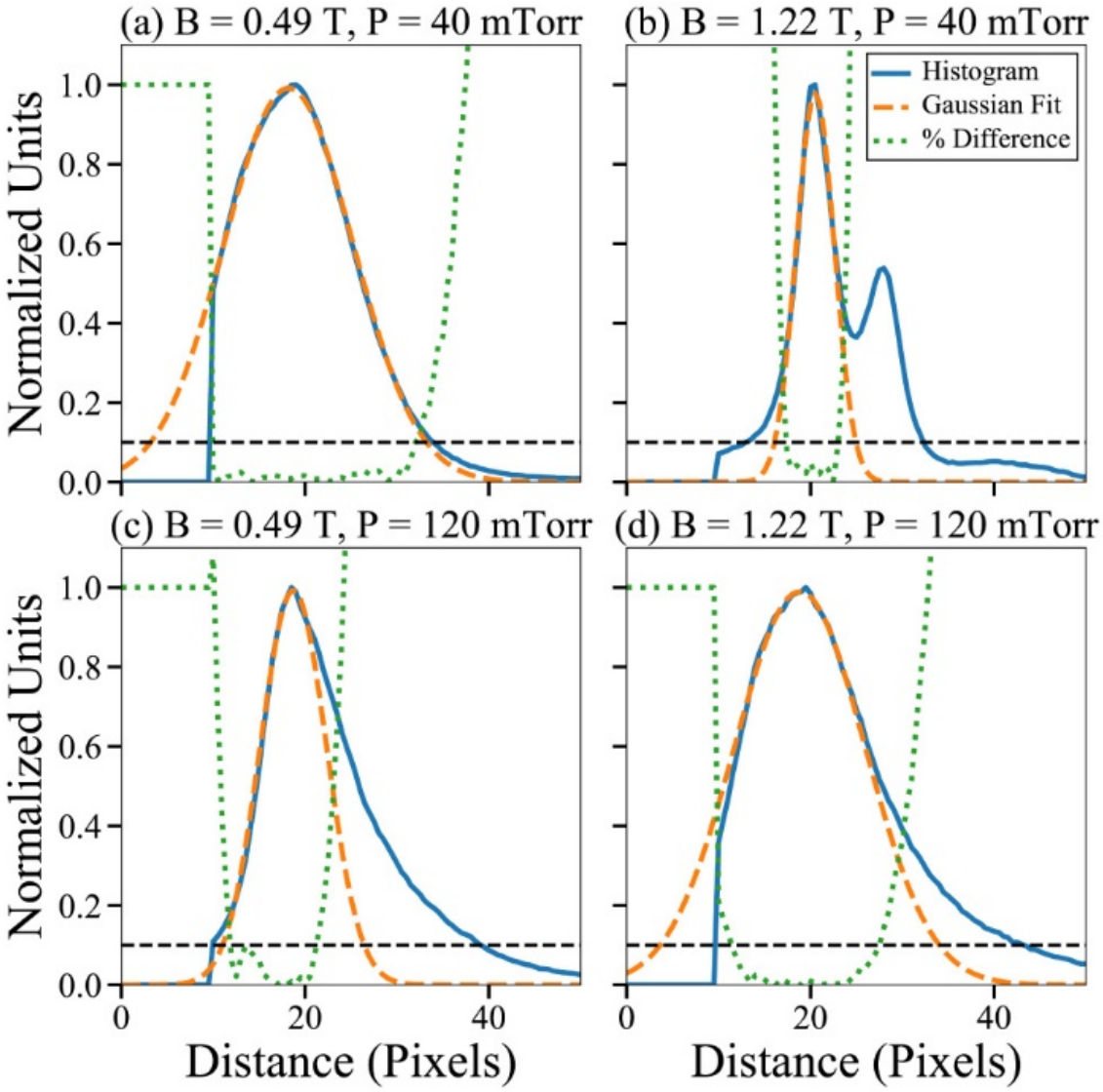

Figure 3-7 Histograms of distances between nearest neighbors, the solid blue curves, at the same set of magnetic fields and neutral pressures as in Figure 3-4(a)-(c) and (f). Gaussian fits of the histograms are given as dashed orange lines and the percent difference between the histogram and Gaussian fit is given as a dotted green line. The dashed black line shown at 0.1 is used for determining bounds of distances to nearest neighbors. From Hall, et al., Phys. Plasmas 25, 103702 (2018), Fig. 5.

Once the Ψ values were calculated it was helpful to examine the range of values of Ψ within the region of interest (ROI). Since the primary interest was in values of Ψ_4 as an indicator of particles following the imposed, ordered structures, only plots of Ψ_4 will be shown for these examples. Only those cases for which histograms were shown previously were examined. These figures illustrate the organization of the particles by marking the particle locations and coloring them according to that particles individual value of Ψ_4. This allows for the ordering of the particles to be easily identified.

For the cases which showed little or no gridding, and which exhibited *uncorrelated motion*, the values of Ψ_4 appear quite low throughout the ROI, as in Figure 3-8 (a), 3–8(c), and 3–8(d). Take for example the base of $B = 0.49\ \mathrm{T}, P = 40\ \mathrm{mTorr}$ in Figure 3-8 (a). This case shows particles scattered randomly through the ROI and those particles have very low values of Ψ_4 throughout, indicated by the dominance of blue and light green colored particles. Even in those other cases Figure 3-8 (c) and (d), which appear to have some particles with higher Ψ_4 values, these particles are a small percentage and over the whole data set do not necessarily maintain those high values.

Cases with high amounts of apparent gridding, which exhibited *trapped particles*, have a much higher value of Ψ_4 throughout the ROI, like that shown in Figure 3-8 (b). This result indicates that a high instantaneous value of Ψ_4 throughout a single image frame would mean that the particles are strongly fixed to a square pattern within that frame. Following from that, a data set which had a high average value of Ψ_4 over all its frames would mean that not only are the particles highly organized but they remain rigidly fixed over significant time scales. It is then possible to use the average Ψ_4 for the data set as a means to parameterize the degree to which particles are organized to the imposed, ordered structure on short time scales (single video frames) and small

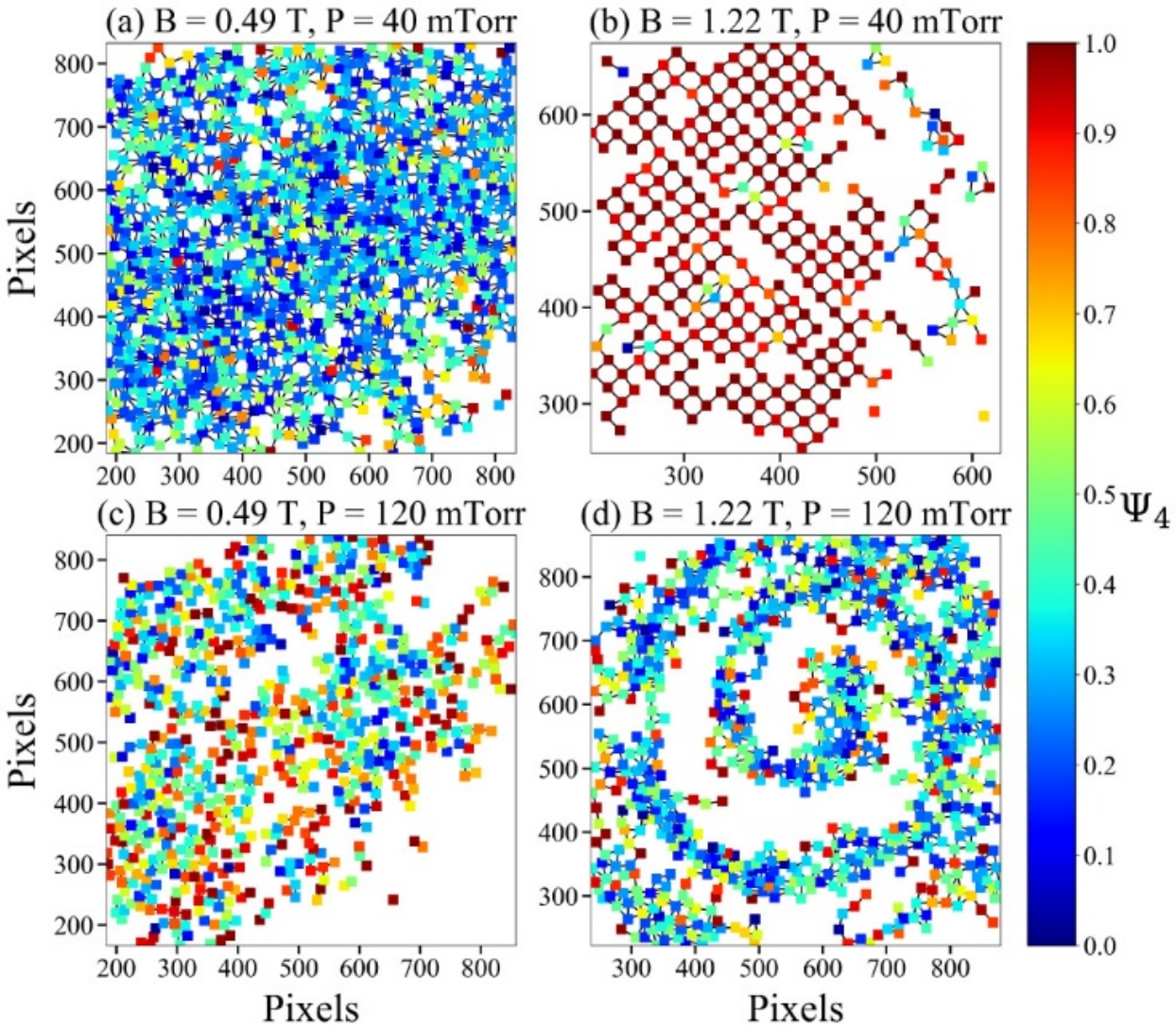

Figure 3-8 Plots of particle locations colored by Ψ_4 values in ROIs. (a) and (c) Experiments at low magnetic field have very little order and are arranged sporadically as indicated by the overall low values of Ψ_4. (b) At high magnetic field and low neutral pressure, particles on average have very high Ψ_4 due to the strong confinement to the imposed, ordered structure. (d) At high magnetic fields and high neutral pressure, a reduction in the value of Ψ_4 throughout the ROI is observed, corresponding to the increased level of flow from Figure 3-4 (d). Also apparent is the presence of plasma filamentation in the swirl pattern of the cloud. From Hall, et al., Phys. Plasmas 25, 103702 (2018), Fig. 6.

spatial scales (inter-particle distances).

These parameters, describing the bulk of the dust cloud's confinement over long time periods, the intensity ratio $\frac{I_{avg}}{I_{max}}$, as well as the average organization of the dust cloud on the particle scale, Ψ_4, were then combined to examine the degree to which the imposed, ordered structures are present. This is done in Figure 3-9(a) and Figure 3-10(a). Here the value of Ψ_4 for each case represents the average Ψ_4 over all video frames. Plots of the data as a function of the intensity ratio $\frac{I_{avg}}{I_{max}}$ versus Ψ_6 in Figure 3-9(b) and Figure 3-10(b) are also provided. This is done to allow for a comparison to the more typical form of Ψ.

The data sets can be examined in two ways. First, in terms of the ratios of the ion-neutral mean free path to the wire diameter λ/w, where the subscripts for the mean free path have been dropped for simplification, and the Larmor diameter to the wire diameter d_l/w, as shown in Figure 3-9. Plotting the data in this way allows for a representation of both of our primary experimental parameters, neutral pressure and magnetic field, each separate from the other. Second, the data can be plotted as a function of the modified ion Hall parameter h_i', which combines both magnetic field and neutral pressure into a single parameter, given in Figure 3-10. Both methods offer different insight into understanding this plasma phenomenon. More discussion on these figures will be provided in Section 3.3.

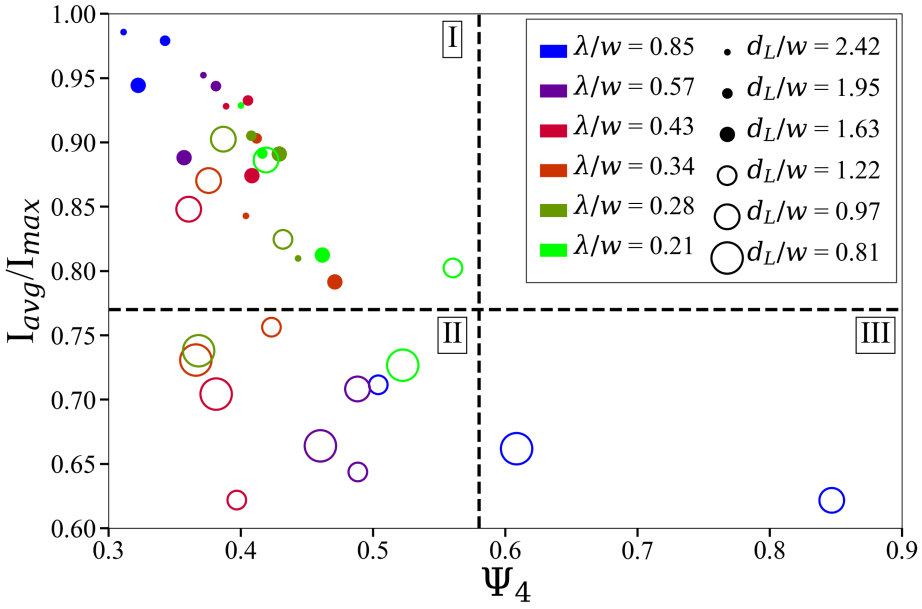

(a)

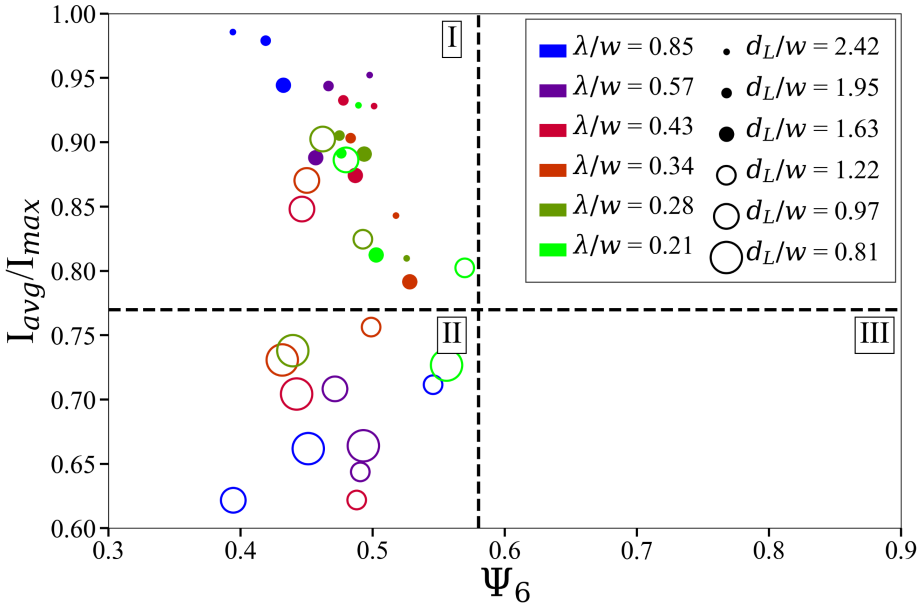

(b)

Figure 3-9 (a) Intensity ratio versus average Ψ_4. (b) Intensity ratio versus average Ψ_6. In both plots increasing size in circle radius indicates increasing magnetic field or decreasing ratio of the ion Larmor diameter to wire width. Open circles are those cases with $B \geq 0.97$ T. Blue cases are those with low neutral pressure (40-60 mTorr, 5.33-8.0 Pa), reds with mid-value pressures (80-100 mTorr, 10.67-13.33 Pa), and greens high neutral pressures (120-160 mTorr, 16.0-21.33 Pa). From Hall, et al., Phys. Plasmas 25, 103702 (2018), Fig. 7.

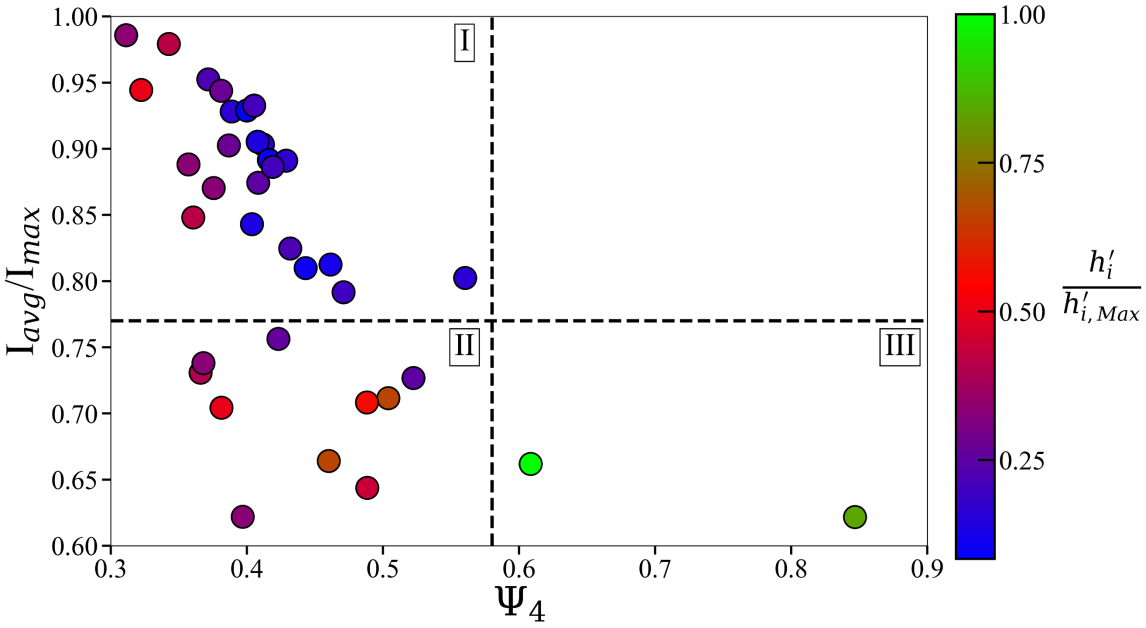

(a)

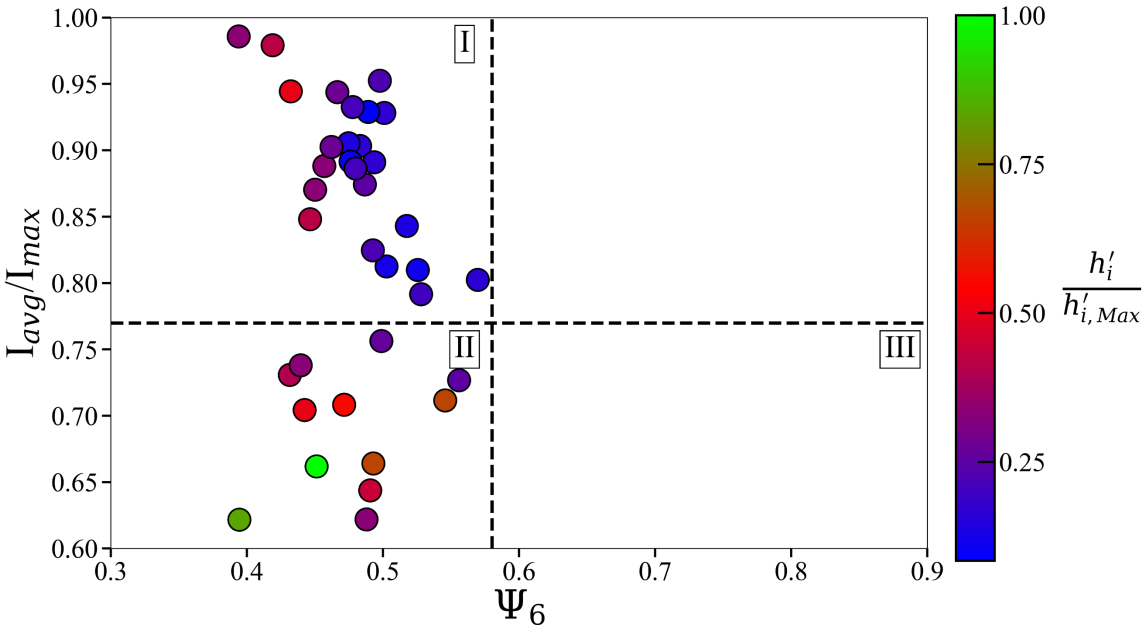

(b)

Figure 3-10 (a) Intensity ratio versus average Ψ_4. (b) Intensity ratio versus average Ψ_6. Here though the circles are colored according to their ratio to the maximum observed modified Hall parameter $h'_{max} = 0.333$. From Hall, et al., Phys. Plasmas 25, 103702 (2018), Fig. 7.

3.3 Results and Discussion

This section discusses the results of Section 3.2. The central idea of this discussion will focus on examining the results in Figure 3-9 and Figure 3-10, in the context of the various types of particle transport presented in Figure 3-4. It will be shown how the parameters of average pixel intensity ratio, $\frac{I_{avg}}{I_{max}}$, and local bond order parameter, Ψ, allow for the quantification of the degree of presence of the imposed, ordered structures.

Within the plots of Figure 3-9 and Figure 3-10 the data has been divided into three separate regions. These regions each correspond to one of the three different types of previously identified particle transport. The separation of these regions was chosen based on certain observations in the data. The separation on the *x*-axis was chosen to be at $\Psi = 0.58$ as there were no data sets which had an average Ψ_6 value higher than this cutoff. The separation on the *y*-axis was chosen to be at $\frac{I_{avg}}{I_{max}} = 0.77$ as the low magnetic field cases ($B < 0.75$ T, $\frac{d_l}{w} > 1.5$) all reside above this value.

Region I consists of data sets which exhibit *uncorrelated motion* with respect to the conducting grid where they are free to flow and circulate in the experiment, as was shown in Figure 3-4(a) – (c). Overall these cases have high intensity ratios and low average values of Ψ_4. Within Figure 3-9(a) this region contains all the low magnetic field cases ($d_l/w = 1.63 - 2.42$). It is observed that for these cases there is a definite trend within Figure 3-9(a) for the intensity ratio to decrease and the average Ψ_4 to increase as pressure increases, or where λ/w decreases This is indicated by the marker size increasing as the markers color changes from blue in the upper left corner of Region I to collections of reds and greens in the bottom right corner. As the pressure is increased the dust clouds are slowed by the greater number of neutral collisions and the flow of particles does not circulate through as large an area, thus reducing the intensity ratio throughout

the region of interest. This same effect is observed in Figure 3-10(a) as well, as the values of $\frac{h_i'}{h_{max}}$ decrease with decreasing intensity ratios. Indicating that the higher pressures cause a decrease in the modified ion Hall parameter due to its inverse dependence on the ion-neutral mean free path, which scales linearly with neutral pressure. While some points in this region do have slightly higher values of $\frac{h_i'}{h_{max}} \sim 0.5$, these same points in Figure 3-9(a) are those points at the lowest magnetic fields and neutral pressures. So, while the value of $\frac{h_i'}{h_{max}}$ for these cases may appear closer to those in Region II, this is more to do with the much lower neutral pressure.

Even though the parameter of Ψ_4 was introduced as a means of examining the particle organization to the square patterned mesh, the Ψ_6 parameter is used to examine the data through the lens of the classical crystalline packing. These results are shown in Figure 3-9(b) and Figure 3-10(b). Since the pixel intensity within the ROI is not affected by the interparticle organization, it is only a measure of the global ordering to the imposed, ordered structures, data that trends with average intensity does not change when comparing the Ψ_6 results to the Ψ_4. Within Figure 3-9(b) the data sets do not vary as much according to Ψ_6 and are clustered together more in the horizontal direction. For those data sets in Region I observe that particles also trend towards slightly higher values of Ψ_6 with increasing pressure. Overall though there is not much change for these sets aside from the slight increase in overall values of Ψ_6 over Ψ_4 and the reduction in range from the lowest Ψ value to the highest.

The second type of motion, confined, *ordered flow*, is observed predominately by cases present in Region II of Figure 3-9 and Figure 3-10. The decreased intensity ratios in this region are indicative of the confined flow developing which drastically reduces the total area through which the cloud can circulate. However, the low average values of Ψ_4 still suggest that while the

particles are confined to this grid structure, they are still free to flow freely and are not very rigidly organized. The examples of ordered flow from Figure 3-4(d) and (e) are found in this region.

The presence of plasma filaments [56–58] also begins to occur for experiments with these parameters, which can disrupt the flow structure. In at least one case, found in Figure 3-4(d) ($\frac{d_l}{w} = 1.22$, $\frac{\lambda}{w} = 0.43$), the occurrence of these secondary structures in the plasma can lead to erratic behavior of select regions of the cloud, causing an artificial decrease in the intensity ratio. Therefore, it is important to consider the average behavior of cases within this region over the behavior of individual data points.

In Figure 3-9(a), points within Region II are those experimental cases at the very highest magnetic fields, whose ion Larmor diameters are roughly on the order, or less than, the wire diameter $\left(\frac{d_l}{w} = 0.81 - 1.22\right)$. This fact also points to the possibility of some critical magnetic field necessary for the imposed, ordered structures to be observed. This result suggests that as the ion gyrodiameter approaches the diameter of the wire, combined with a higher degree of magnetization, the ions could potentially be constrained to only flow between the bottom electrode and the conducting mesh. This could also be interpreted as the ion gyromotion becoming smaller than the plasma sheath around the wire. This could be the critical condition which causes the ions to be unable to escape the sheath boundary around the wire and stay tied to the shape of the mesh. This would then lead to an imbalance of the ion and electron populations in the holes compared to beneath the wires, thus creating the trapping potential for the dust.

These cases in Region II show reduced values of the average intensity ratio indicating that the structure of the mesh is beginning to reveal itself over long time scales in the maximum sum images. The low values of Ψ_4 though tell us that while over those long time scales the mesh is becoming apparent, the particles have not yet begun to experience a trapping potential at the single

particle scale. The particles are still free to flow but they are constrained to only follow the paths imposed by the grid.

Within Figure 3-10(a) it is observed that the data sets which are in Region II are those that have an increased modified Hall parameter. Several of these cases have $\frac{h_i'}{h_{max}} > 0.5$, with some near $\frac{h_i'}{h_{max}} = 0.75$. This would be the equivalent classical Hall parameter of $h = 1.5$, just above the typical criteria for considering the ions to be magnetized. Other cases have significantly lower values of $\frac{h_i'}{h_{max}} \sim 0.25$. But when compared to Figure 3-9(a) it is noted that these are those points which are at the highest magnetic fields ($d_l/w = 0.81$). Even though these plasmas have a much higher pressure ($\lambda/w = 0.21 - 0.57$) the magnetic fields are sufficiently strong enough to produce the imposed, ordered structures.

At the very highest magnetic fields, and lowest neutral pressures, a significant number of particles within the dust cloud become confined to discrete points within the imposed, ordered structure. Cases in which *trapped particles* were observed are categorized as Region III within Figure 3-9 and Figure 3-10. These are cases where the imposed, ordered structure is strongly present, as would be suggested by a low intensity ratio, and high average Ψ_4. It is also observed that these are cases at, or near, the highest value of the modified ion Hall parameter observed in this experiment.

One notable observation from this region, in Figure 3-9(a), is an apparent reversal at high magnetic fields of the trend observed in Region I. At these high magnetic fields, the intensity ratio tends to increase, while the average Ψ_4 decreases, eventually resulting in a transition from Region III to Region I. This transition is especially apparent for those cases at B = 1.22 T ($d_l/w = 0.97$) which do not significantly pass through Region II, of the $d_l/w = 0.97$ cases on the one at $\lambda/w =$

0.28 falls into Region II, instead transitioning almost directly from Region III to Region I. However, at the highest magnetic field, B = 1.46 T ($d_l/w = 0.81$), there is only a transition from Region III to Region II. This means that it is likely that at this magnetic field these experiments did not reach sufficiently high neutral pressure to decrease the ion magnetization such that there would be a transition back into Region I. This would indicate that a much higher magnetic field is necessary for strong, fixed confinement, but that once the magnetization has decreased sufficiently, the dust cloud returns to its *uncorrelated motion*.

Also, of note is that the cases present in Region III are those which have a Larmor diameter at or less than the wire diameter. These cases at $d_l/w = 0.97$ and 0.81 also provide support that the ion dynamics must be comparable to the size of the wire, or the sheath around the wire, which would only be slightly larger.

When the data in Regions II and III is examined using the Ψ_6 parameter some interesting results are seen as well. First, is that those cases which were in Region III in Figure 3-9(a) and Figure 3-10(a), having the highest values of Ψ_4, are now the cases with the lowest values of Ψ_6. The fact that there are no cases data sets in Region III for these plots is unremarkable, as we chose the boundaries based on the cutoff determined by Ψ_6. That those cases which were very aligned to the square mesh now have such low Ψ_6 values tells us that they are decidedly *not* hexatic, and that the Ψ_4 parameter is a good parameter for quantifying the alignment to the conducting mesh and imposed, ordered structures.

In general, the observations and results appear to be in good agreement with the initial observations of the imposed, ordered structures. Two parameters, $\frac{I_{avg}}{I_{max}}$ and Ψ_4, which provide a good method of quantifying the presence of the imposed, ordered structures are introduced. These parameters allow for a representation of the development of the imposed, ordered structures as a

function of both magnetic field and neutral gas pressure which was consistent with the initial observations. As well, measurements of the intensity ratio and average Ψ_4, combined with the measurement of the modified ion Hall parameter, show an apparent correlation to the ion magnetization within the experiment. Or in other words, that as the ions within the plasma become more bound to the magnetic field lines, and once the ion gyro-orbit becomes comparable to the size of the wires within the conducting structure present, a confining potential develops which can affect the dust cloud dynamics. These measurements also show a transition between the various types of observed transport of particles within the dust cloud.

While these measurements do provide a method to quantify under what conditions the imposed, ordered structures begin to appear they only use the dust to show that the structures exist and their relative strength. To properly understand the imposed, ordered structures measurements of the background plasma need to be conducted. Since the wire mesh is so small it is difficult to probe the plasma beneath it. Because of the scale size of the system, an important outstanding question remains, are the dust particle trapped in the holes between the mesh or are they trapped beneath the wires. A related question is how the overall pattern of the wire mesh becomes mapped onto the plasma so that the particles appear to follow that spatial structure.

In order to circumvent this issue a new experimental configuration will be examined in the following chapters which will make of a large grid-like electrode designed to mimic the conditions observed here with the conducting mesh, only larger so that plasma diagnostics can be conducted.

Chapter 4 Plasma Probe Measurements

The wire mesh has up to now been a simple, yet robust experimental system. It is easily implemented into the experimental hardware while providing a consistently observable result. The small size of the wires in the mesh allowed for imaging through the hole in the top electrode while maintaining a uniform conducting surface. This resulted in creating imposed, ordered structures small enough for discrete particle trapping. However, while the mesh size allowed for experimental conditions favorable for creating novel dust dynamics, it created some difficulties for implementing other plasma diagnostics. The wires in the mesh are typically ~200 μm in diameter with 2-3 times that length of space between the wires. This means that even a small single Langmuir probe of 1 mm in diameter and 1-3 mm in length would be sampling an area of plasma beneath multiple wires within the mesh and would not be able to spatially resolve characteristics beneath the mesh.

Since a diagnostic could not be built small enough for the wire mesh a larger grid-like electrode was developed instead. This new electrode, which was detailed in Section 2.4.2 and shown in Figure 2-16, is large enough that plasma probe diagnostics can be built small enough to spatially resolve the plasma conditions beneath the electrode. It also has the added benefit of allowing for multiple "wire" thicknesses depending of the direction that is sampled beneath the electrode. This chapter will describe the measurements and results of those probe diagnostics.

Section 4.1 will describe measurements of the electron temperature and density made with the double Langmuir probe described in Section 2.3.2. These measurements will then be followed in Section 4.2 by calculations of effective electric potentials determined by applying Poisson's

equation to the measured electron densities. Measurements of the electric field made with the ring probes, which were introduced in Section 2.3.3, will then be described in Section 4.3. Finally, Section 4.4 will provide a description of effective electric potentials which are calculated from the electric field measurements.

4.1 Measurements of the Electron Temperature and Density

This section will provide details of measurements produced from the double Langmuir probe described in Section 2.3.2. Measurements of both electron temperature and density will be presented. Profiles of the electron density will also be used to calculate electric potential profiles by solving Poisson's equation.

The double Langmuir probe measurements were performed in the primary MDPX vacuum chamber in the configuration laid out in Section 2.4.2. The top-down schematic of the vacuum chamber is shown in Figure 4-1. Argon plasmas were generated using radio frequency (rf) heating at 13.56 MHz and an input power of 5 W. The electrodes were configured in a capacitively coupled configuration, with the bottom electrode being powered with rf and the top electrode electrically floating. For these experiments the T&C Power Conversion Inc. Model AG 0313 power supply was used for plasma generation. Neutral gas pressures of 25, 50, and 75 mTorr (3.33, 6.66, and 10 Pa) were used. The calculated magnetic field in the experiment ranged from $B = 0 - 3$ T. These measurements were conducted alongside experiments where dust particles were present. These particles were 8 ± 0.8 μm silica microspheres levitating 1-2 cm (0.4-0.8") above the bottom electrode, or 4-5 cm (1.6-2") below the path that the probe sampled.

Double probe measurements were taken beneath the "waffle" electrode shown in Figure 4-1. The probe consisted of two tungsten wires 0.5 mm (0.02") in diameter, 2.5 mm (0.10") long, and spaced 2 mm (0.08") apart. Data was taken over a range of 15 cm (5.9") across the plasma

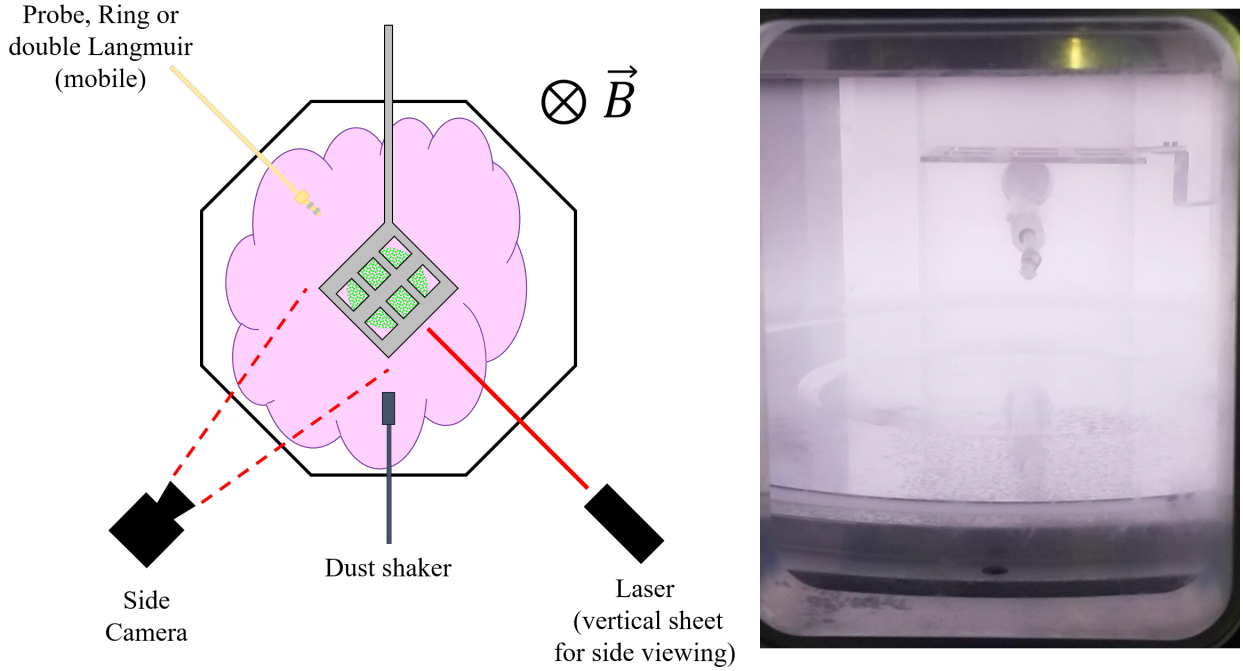

Figure 4-1 (Left) Top-down schematic of the MDPX vacuum chamber. (Right) Interior image of the vacuum chamber with "waffle" electrode and probe present. In both images the ring probe is shown, which could be replaced with the double Langmuir probe in the same configuration.

volume in 0.1 cm (0.04)" steps. The probe was scanned across the chamber beneath the center pair of holes in the electrode, where the conducting sections of the electrode are 1.2 cm (0.47") wide, and the holes are 1.8 cm (0.71") wide. Two different dc biases were applied to the "waffle" electrode at $V = \pm 40$ V. The position of the probe relative to the "waffle" electrode is determined by the methods detailed in Appendix B.1 and controlled by a LabView program included in Appendix C.1 where the probe sweep was performed by an additional LabView program shown in Appendix C.2.

Measurements of the electron temperature and density were determined from current-voltage traces (IV traces) performed at each position across the plasma volume. These measurements were calculated from the IV traces according to the process detailed in Section 2.3.2. A typical double Langmuir IV trace, when there is no magnetic field present, can be seen in

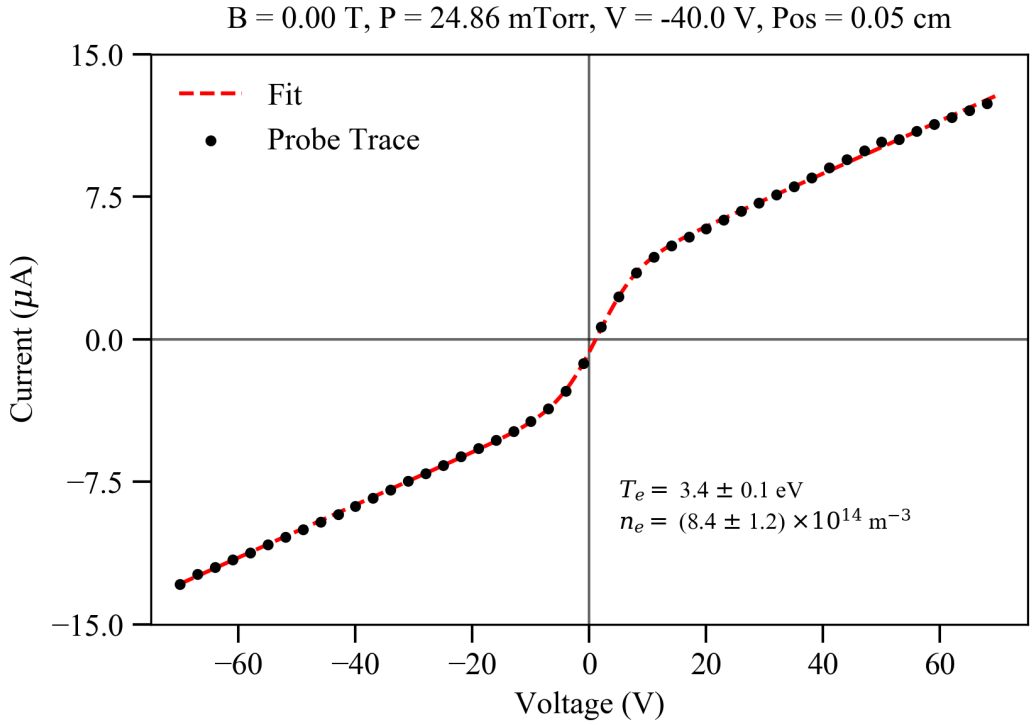

Figure 4-2 A typical double Langmuir probe trace is shown as black points. The fit to the data is shown in red. The fit produces results of an electron thermal energy of 3.4 eV and an electron density of $8.4 \times 10^{14}\ m^{-3}$.

Figure 4-2, which is taken from the example in Section 2.3.2. Here an electron temperature of 3.4 ± 0.1 eV, and an electron density of $(8.4 \pm 1.2) \times 10^{14}$ m^{-3} is measured at a position near the center of the chamber.

When magnetic fields are introduced though things can become more complicated. Probe diagnostics can oftentimes become unreliable, and the measurements made with them do not behave in a way which allows for the usual analysis. In the past, probe measurements made with both single Langmuir probes and triple Langmuir probes have been attempted in the MDPX laboratory, each with different limitations at high magnetic fields. Single Langmuir probes would often reach an electron saturation which was far below the expected regime, and triple probes, as a result of their design, are difficult to orient so that "shadowing" effects do not occur along the magnetic field lines. By using a double Langmuir probe though the current which is drawn by

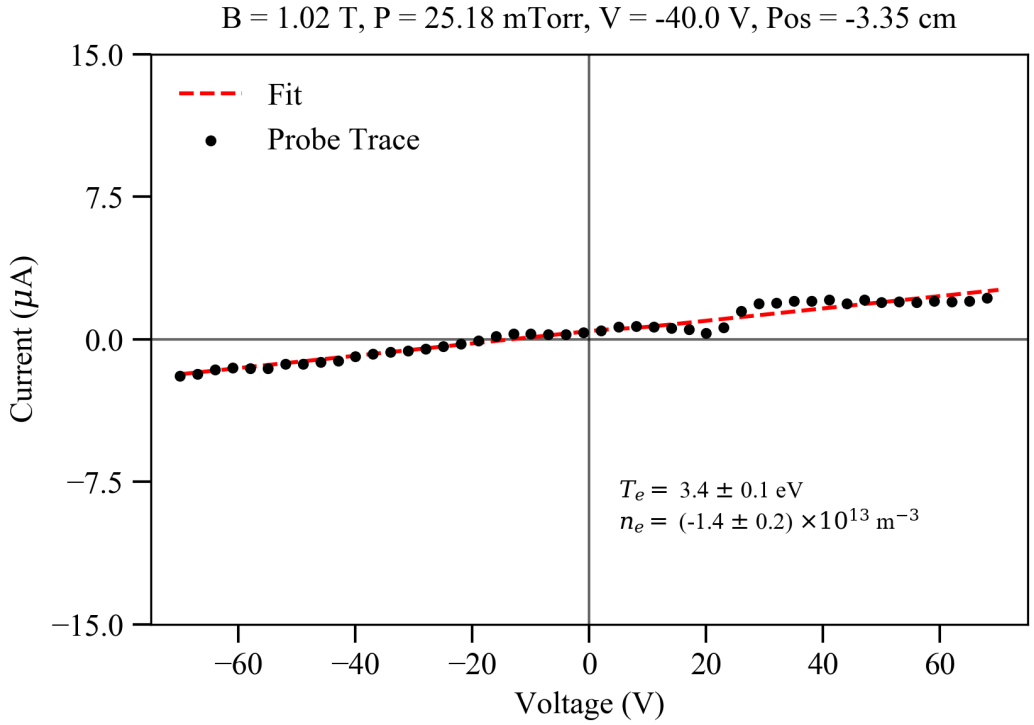

Figure 4-3 An IV trace made at high magnetic field. The fit of the IV trace produces a nonphysical electron density of $(-1.4 \pm 0.2) \times 10^{13}$ m^{-3}.

either probe tip is determined by the ion saturation current, and the probe tips are able to be oriented such that the line connecting the two tips is perpendicular to the magnetic axis. These two factors allow for the double Langmuir probe to behave more reliably than the other types of probe diagnostics in the high magnetic fields. This is not to say that the probe never has issues at those higher magnetic fields.

Take for example the IV trace shown in Figure 4-3. Here the magnetic field was quite high, $B = 1.02$ T, with a pressure of 25 mTorr (3.33 Pa) and potential bias on the electrode of -40 V, at a position of -3.35 cm relative to the center of the chamber. The saturation current that the probe measured was greatly reduced compared to the case with no magnetic field, almost an order of magnitude less, though this was not uncommon among all the data sets as the magnetic field increased. The IV trace was also not symmetric around the origin, making it difficult for the fitting

functions to find a proper set of parameters. In this example the electron temperature was fixed at its $B = 0.0$ T value but its electron density was determined to be $(-1.4 \pm 0.2) \times 10^{13}$ m^{-3}. This negative density is unphysical but is simply a result of the poor fit.

Fortunately, this is only an example of one case at which the fit did not return results which are reasonable and many of the points during these measurements were able to be fit, and electron densities extracted. To account for those cases which did not work a set of conditions were applied when fitting the IV trace at each position within a given set of experimental conditions. The first was that if a program error was returned when calling the curve fitting function then the IV trace at that position would be skipped. Then, if one of three rules was found to be broken for the density calculation then no measurement would be recorded at that position. These rules were (1) that the parameter be greater than or equal to zero, (2) that the error from the covariance matrix be greater than or equal to zero, and (3) that the ratio of the error to the parameter must be less than 50%. By applying these rules, profiles of the electron temperature and density were produced.

Examples of these profiles are given in Figure 4-4. The data points on these profiles show the original data, which was not removed according to the previously stated rules, as black squares. Electron temperatures were determined from the $B = 0.0$ T data. The results from those measurements were then used as inputs for all $B > 0.0$ T measurements for each corresponding neutral gas pressure and "waffle" electrode bias. Error bars show the calculated error from the covariant matrix resulting from the least squares fit. The red line is the fit of the data. The electron temperature data is fit with a binomial function to show its general trend. The electron density data is fit using an interpolating function to account for the gaps in the data which result from the checks put in place. This interpolation was performed by the "PchipInterpolator" function from the Python SciPy library. The function uses a monotonic cubic interpolation according to the Fritsch-Carlson

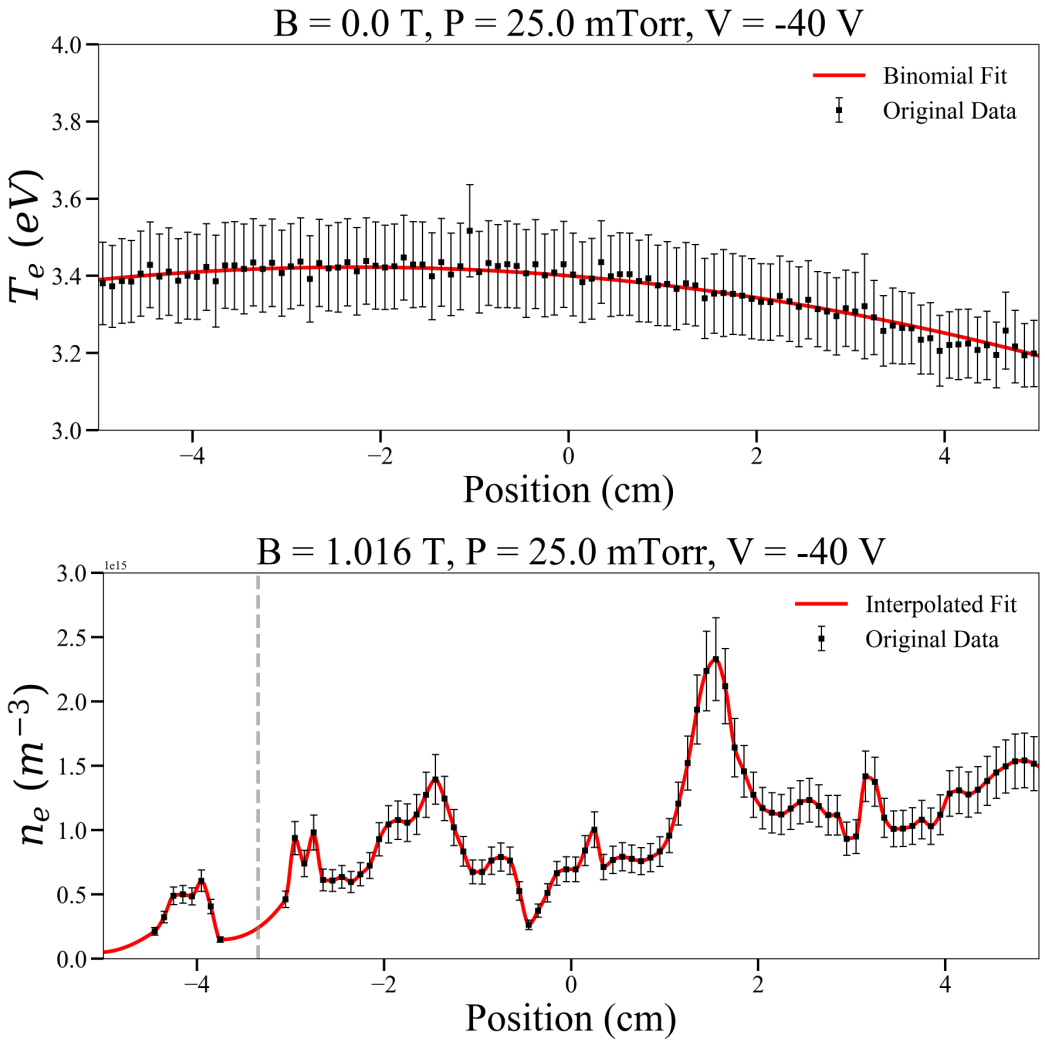

Figure 4-4 Electron temperature and density profiles at $B = 1.02$ T, $P = 25$ mTorr, $V = -40$ V. The original data is shown as black squares. For the electron density the red line is the interpolated fit using PCHIP interpolation. The vertical grey dashed like shows the position of the example given in Figure 4-3. Several fits around this position were not able to be fit and so the profile relies on the interpolation instead.

method. [59] This method of interpolation helped to preserve the order of the system, ensuring that the fit did not overshoot the data in the gaps. Other interpolation schemes, such as a cubic spline interpolation, would often predict too large of jumps in the data, producing fits to temperature or density profiles which would be negative and thus unphysical.

As was mentioned previously, the electron temperatures were only determined for the $B = 0.0$ T data sets. These electron temperature profiles were then assumed to remain constant for the data sets where $B > 0.0$ T. The electron temperature profiles for the various neutral gas pressures and "waffle" electrode biases are given in Figure 4-5. The temperature profiles typically ranged between 3.0-3.5 eV and each followed a relatively smooth binomial function as illustrated by the red lines in the plots. The temperatures measured for a "waffle" electrode bias of -40 V and at neutral pressures of 50 and 75 mTorr (6.67 and 10 Pa) show a greater variance as a function of position as well as larger errors.

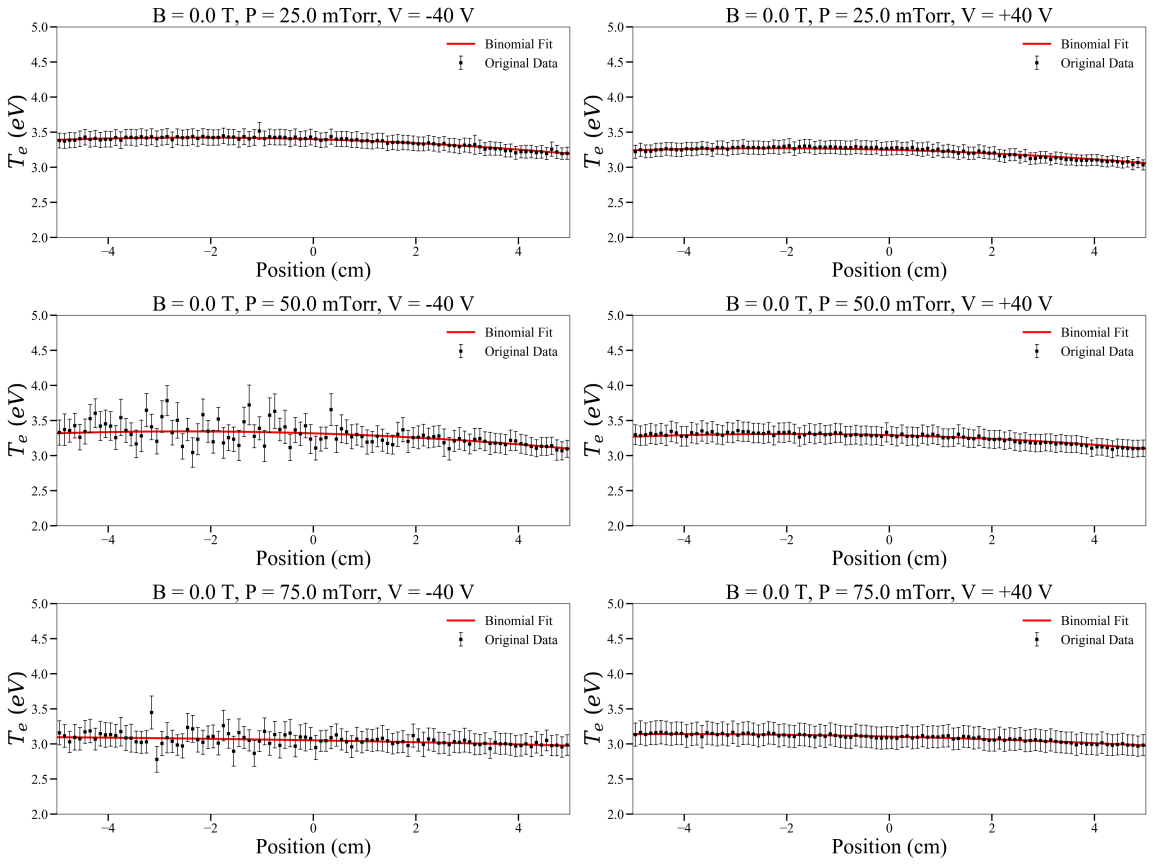

Figure 4-5 Electron temperature profiles for $B = 0.0$ T. Electron temperatures determined from fits of the Current-Voltage (I-V) traces are given as black squares with appropriate error bars. The red line represents a best fit to a binomial function to illustrate the general trend of the data.

Once the density profiles were determined at each set of experimental conditions, they were accumulated to observe trends as a function of neutral pressure and magnetic field. These contour plots are shown in Figure 4-6. These plots show the electron density plotted as a two-dimensional contour plot with magnetic field in Tesla on the horizontal axis, and the chamber position relative to the "waffle" electrode on the vertical axis. The position and span of the conducting sections of the electrode are shown as grey bars going across the contour plot. Each of the columns shows data for the different electrode biases, with the -40 V data in the left column, and the +40 V data in the right column. Rows show the neutral pressure changing from 25 to 75 mTorr going from top to bottom. The data within these contour plots is colored on a log scale though from a range of $10^{14} - 10^{16}$ m^{-3}.

In the left column, at an electrode bias of -40 V, deficiencies in the density can be seen near the electrode edges at 25 mTorr. These reduced densities are on the order of 10^{14} m^{-3} compared to near the center of the holes which are on the order of 10^{15} m^{-3}, or higher. The most obvious decrease in density seems to appear between 2 – 2.5 T, the same magnetic field range that the warm areas began to appear in the temperature plots. This same phenomenon can also be seen at 50 and 75 mTorr (6.67 and 10 Pa). As the magnetic field increases the overall density of the plasma tends to decrease, except for small regions within the electrode holes. This decrease appears somewhat suddenly for each of these cases, but at different magnetic fields. At 50 mTorr (6.67 Pa) the change occurs at around 1 T and at 75 mTorr the density is seen to decrease around 0.75 T.

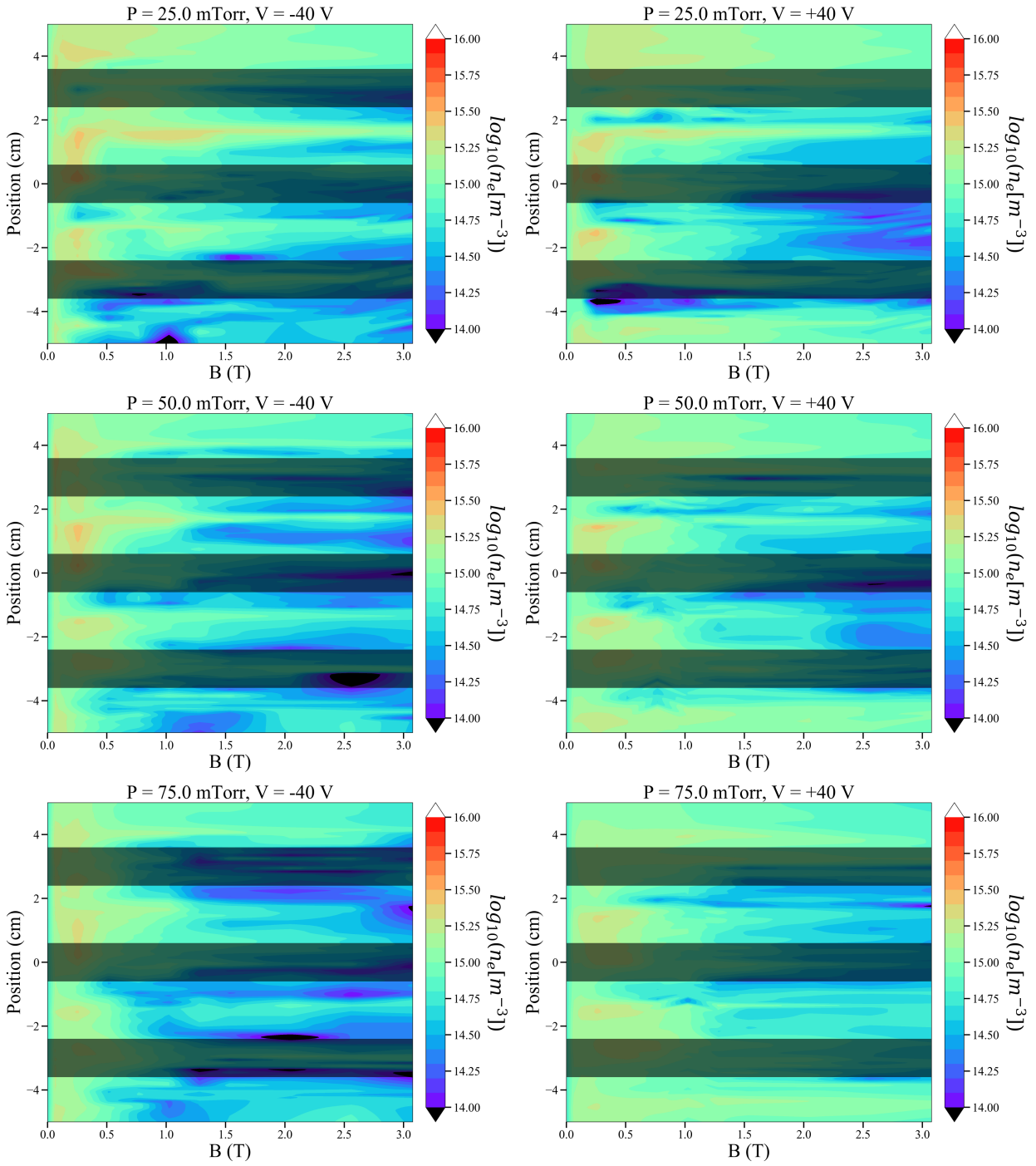

Figure 4-6 Two-dimensional log contour plots of the electron density as a function of magnetic field on the horizontal axis, and position on the vertical axis. Plots are colored based on the log value of the electron density. The horizontal bands indicate the position of the "waffle" electrode.

When the electrode bias is at +40 V, similar results are seen. For a neutral pressure of 25 mTorr (3.33 Pa), a buildup of charge near the center of the holes is still observed. Additionally, a much more obvious region of high densities develops beneath the electrodes conducting bands. This may be because the positively biased electrode is attractive to electrons and can more easily maintain the electron buildup in these spaces. As the pressure increases, the bands of high density are still observed at 50 mTorr. Very clear high-density areas can be seen both in the holes and beneath the conducting bands. These bands are not as evident in the 75 mTorr data. While there is some density variation it is not nearly as pronounced as the data at lower neutral pressures. For both the 50 and 75 mTorr data, the sudden decrease in density occurs at around 1.5 T.

Overall, the density does seem to respond to the magnetic field. It develops regions of both increased and decreased density relative to when there is no magnetic field present. The behavior of the density may also be similar to the behavior of plasma filaments, areas in which the plasma density builds up with increasing magnetic field. These filaments present themselves as patterned structures within the plasma which can change pattern with magnetic field and neutral pressure. [56–58,60] When observed as just the plasma glow, there is also a much brighter glow within the holes of the electrode. The brightness of the plasma is often associated with higher electron densities recombining with the ions. This picture is consistent then in that the higher electron densities were detected in the regions which had a brighter plasma glow.

When examining the relative error of the electron density, $\delta n_e/n_e$, shown as contour plots in Figure 4-7, it can be seen that the relative error is mostly uniform as a function of position and magnetic field. The relative error for all neutral gas pressures and “waffle” electrode biases typically ranges between 13-14%. In the cases of the 50 and 75 mTorr (6.67 and 10 Pa) neutral pressures at a “waffle” electrode bias of -40 V, it can be seen that the relative error does show

some increase to around 16%. This is most likely due to the increased relative temperature error under these conditions. This was seen previously in Figure 4-5 for the same cases in which the electron temperature profiles were more irregular. Overall these relative error profiles show that when evaluating the electron density with a fixed electron temperature profile at high magnetic fields the results are consistent.

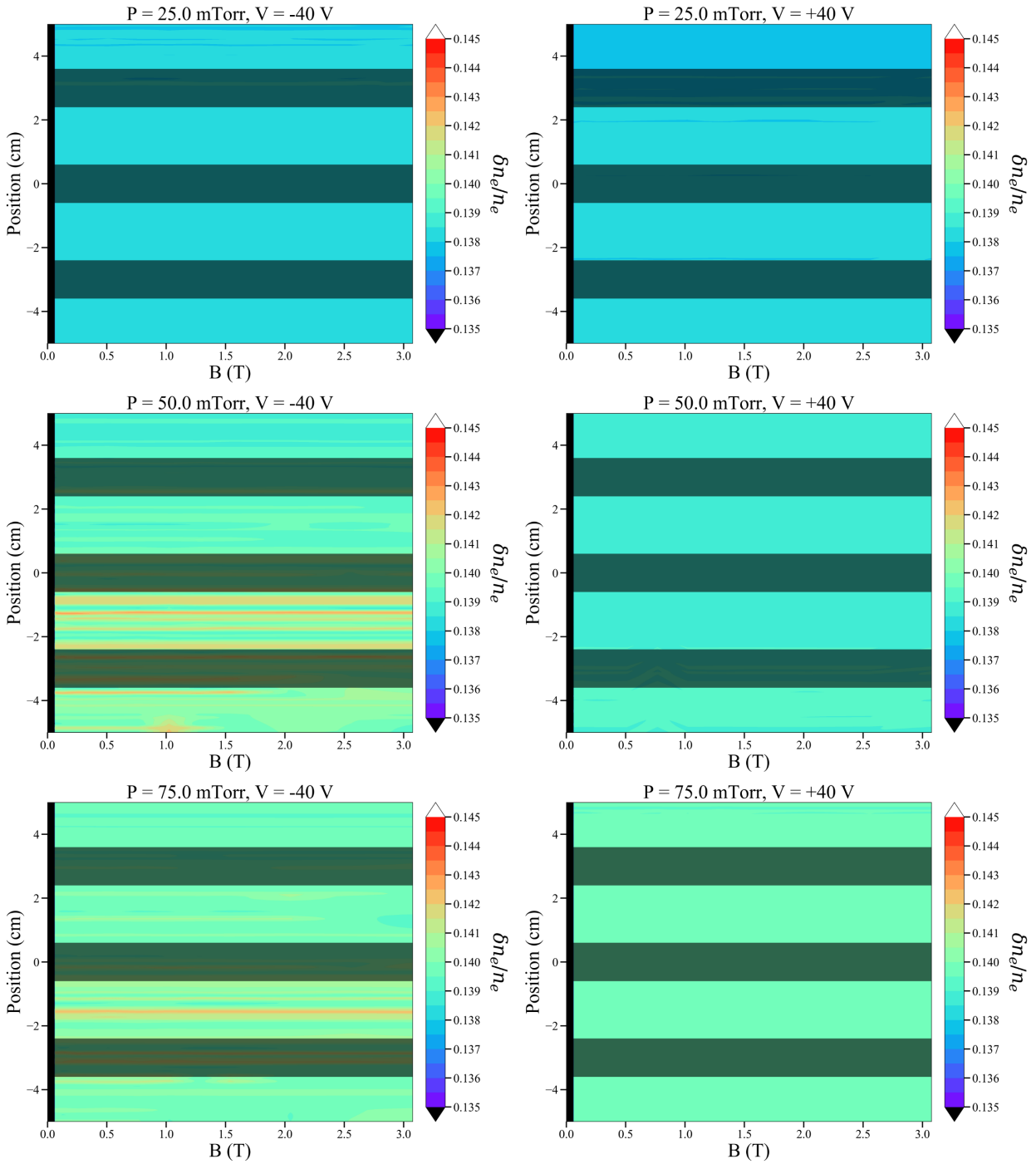

Figure 4-7 Relative error of the electron density measured by the double Langmuir probe.

4.2 Effective Electric Potential Using Poisson's Equation

This section will present a method by which effective electric potentials are calculated from the electron density measurements in the previous section. This is done by determining a profile for the background ion density and then performing a double integral over the net charge density. A discussion of the effective electric potentials and their dependence on the parameters of magnetic field, neutral pressure, and electrode bias is then provided.

Once the electrons densities were determined they could be used to calculate an effective electric potential beneath the "waffle" electrode. This was be done by applying Poisson's equation:

$$\nabla^2\phi = -\frac{\rho}{\epsilon_0} \tag{4-2}$$

where ϕ is the electric potential, ρ is the charge density, and ϵ_0 is the permittivity of free space. For the data presented here, the densities are only in the *x*-direction and so Poisson's equation is more properly written as:

$$\frac{\partial^2\phi(x)}{\partial x^2} = -\frac{\rho}{\epsilon_0} \tag{4-3}$$

Within a plasma the total charge density is considered to be equal to zero over the whole plasma to maintain quasi-neutrality between the electrons and ions. [4,25] In reality small variations in the density can lead to electric fields and electric potentials within the plasma. The charge density can then be defined as:

$$\rho = e(n_i - n_e) \tag{4-3}$$

where n_i and n_e are the ion and electron number densities, respectively. Because the double probe does not directly measure the ion density, another approach for approximating the ion density must be applied.

The question then is what type of profile should be chosen for the ions. Often, when there are no high magnetic fields present, it is possible to assume that the ion density is constant across the plasma. In these scenarios this is not unreasonable to do, as the ions move slowly compared to the electrons, satisfying the condition that the electron population decreases much faster than the ion population near the edges in order to develop a sheath. In this scenario though, in the presence of high magnetic fields, the situation is more complicated. The electrons, and to some extent the ions also, are strongly tied to the magnetic field lines, and not able to diffuse towards the wall. It does not appear unreasonable then that the ion density profile should differ significantly from the electron density profile in the presence of a magnetic field. The reasoning behind this is that the ion density should roughly follow the electron density to maintain quasi-neutrality throughout the plasma. An ion density profile determined from the electron density should serve an adequate choice for solving Poisson's equation.

To determine this ion density profile, a high-order polynomial fit of the electron density was found. This smooth fit of the electron density provided a general profile of the density while allowing for small differences between the measured density and the smooth profile. Linear profiles for the ion density, or low-order polynomial fits did not allow for these small differences. They primarily resulted in profiles which were determined by the ion profile, instead of the combination of the two densities. Examples of these fits are shown in Figure 4-8. This figure shows two density profiles at 1.02 T (blue) and 2.05 T (red), for a neutral pressure of 25, 50, and 75 mTorr (3.33, 6.67, and 10 Pa), all at an electrode bias of -40 V. These profiles are fitted with a 13^{th} order

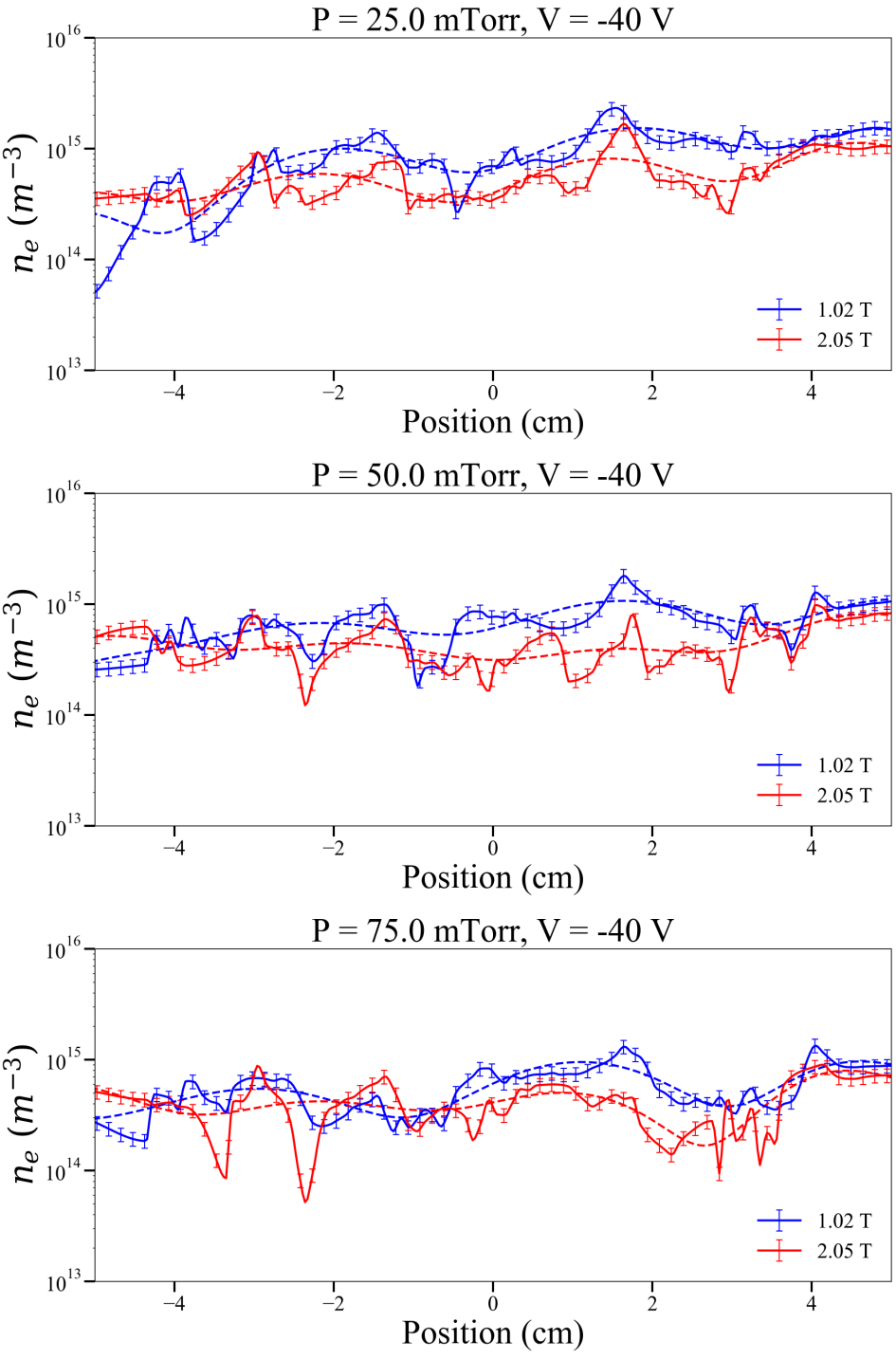

Figure 4-8 Electron density profiles at 25, 50, and 75 mTorr (3.33, 6.67, and 10 Pa) of neutral gas pressure and -40 electrode bias. Two magnetic fields are shown; 1.02 T (Blue) and 2.05 T (Red). The solid lines are the measured density profiles, and the dashed lines are polynomial fits which are used to represent the ion density.

polynomial on the range $x_{min} = -8$ cm to $x_{max} = 6$ cm. Using the density profile and fit, the effective electric potential could then be calculated by integrating Poisson's equation in the form:

$$\phi(x) = -\iint_{x_{min}}^{x_{max}} \frac{e\big(n_0(x) - n_e(x)\big)}{\epsilon_0} dx^2 \tag{4-4}$$

where n_0 is the density fit. After the first integral was performed the average effective "electric field" is subtracted away, before the final integral was carried out. The electric potential error was not included due to the double integral causing its growth to exceed the scope of the electric potential as the error was propagated.

These effective potentials are then plotted versus position. The first set of these potentials is shown in Figure 4-9. In this figure the effective potentials are shown as a function of neutral pressure across the columns, 25 mTorr on the left increasing to 75 mTorr on the right, and magnetic field down the rows. This figure is continued on the following page, so that magnetic fields from 0.0 – 0.77 T are shown in the first part, and magnetic fields from 1.02 – 3.08 T are shown in the continuation. Both pages represent data at an electrode bias of -40 V.

At 25 mTorr the potential is quite low when there is no magnetic field. Compared to the data sets where magnetic field is present this potential effectively flat across the plasma and does not show a significant potential with which negatively charged dust particles might be confined. As the magnetic field increases the effective potential also begins to develop beneath the "waffle" electrode. This potential develops positive peaks beneath the holes of the electrode, seen between the dark vertical bands which represent the conducting bands of the electrode. These peaks begin to appear with even a small amount of magnetic field ($B = 0.06$ T) and grow as the field increases. The importance of positive peaks within then potential is that these are location which would be electrically confining to negatively charged dust particles within the plasma. With slightly higher

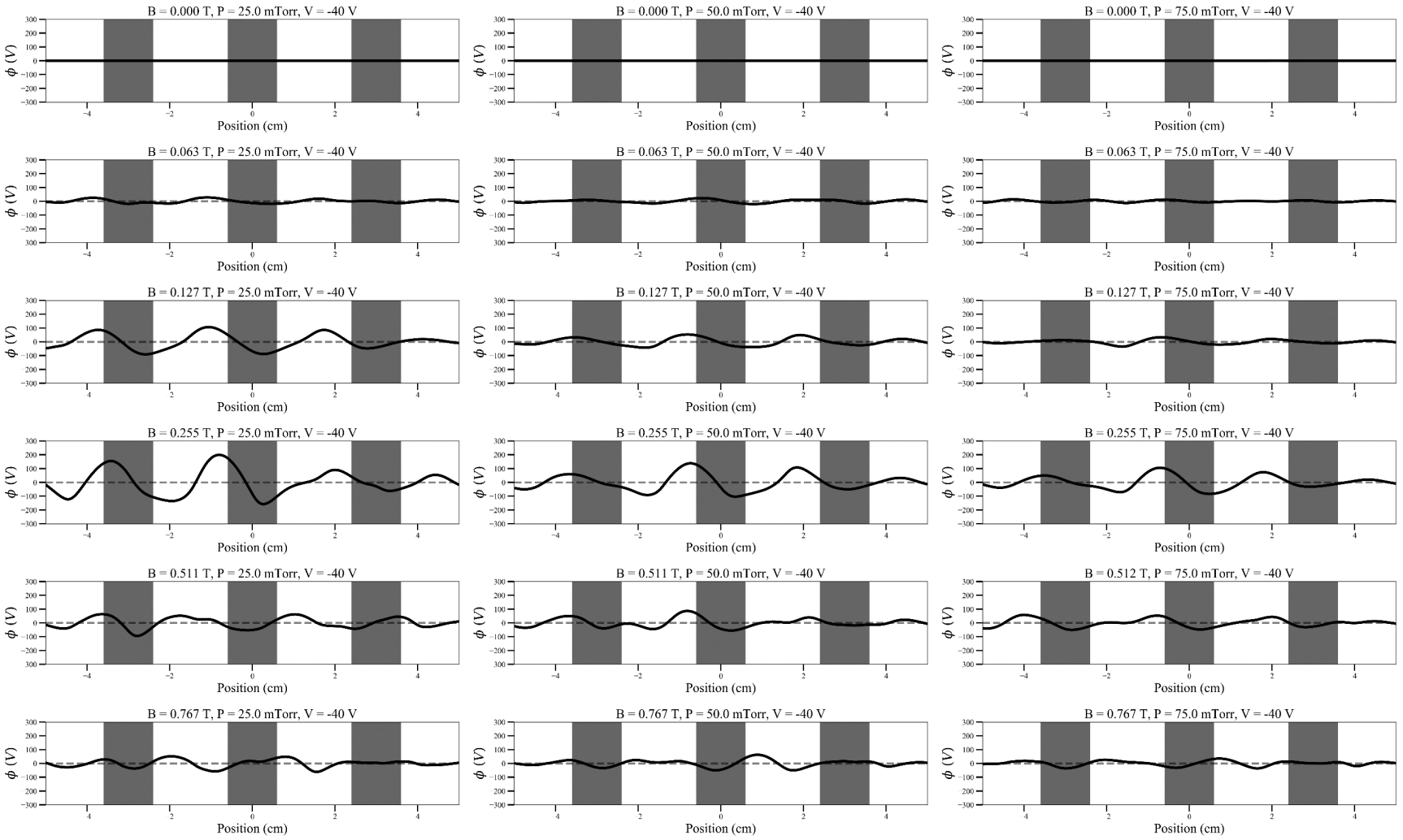

Figure 4-9 Effective electric potential profiles for an electrode bias of -40 V. Columns show profiles for increasing neutral pressure from left to right (25 - 75 mTorr). Rows show increasing magnetic field strength (0.0 - 0.767 T).

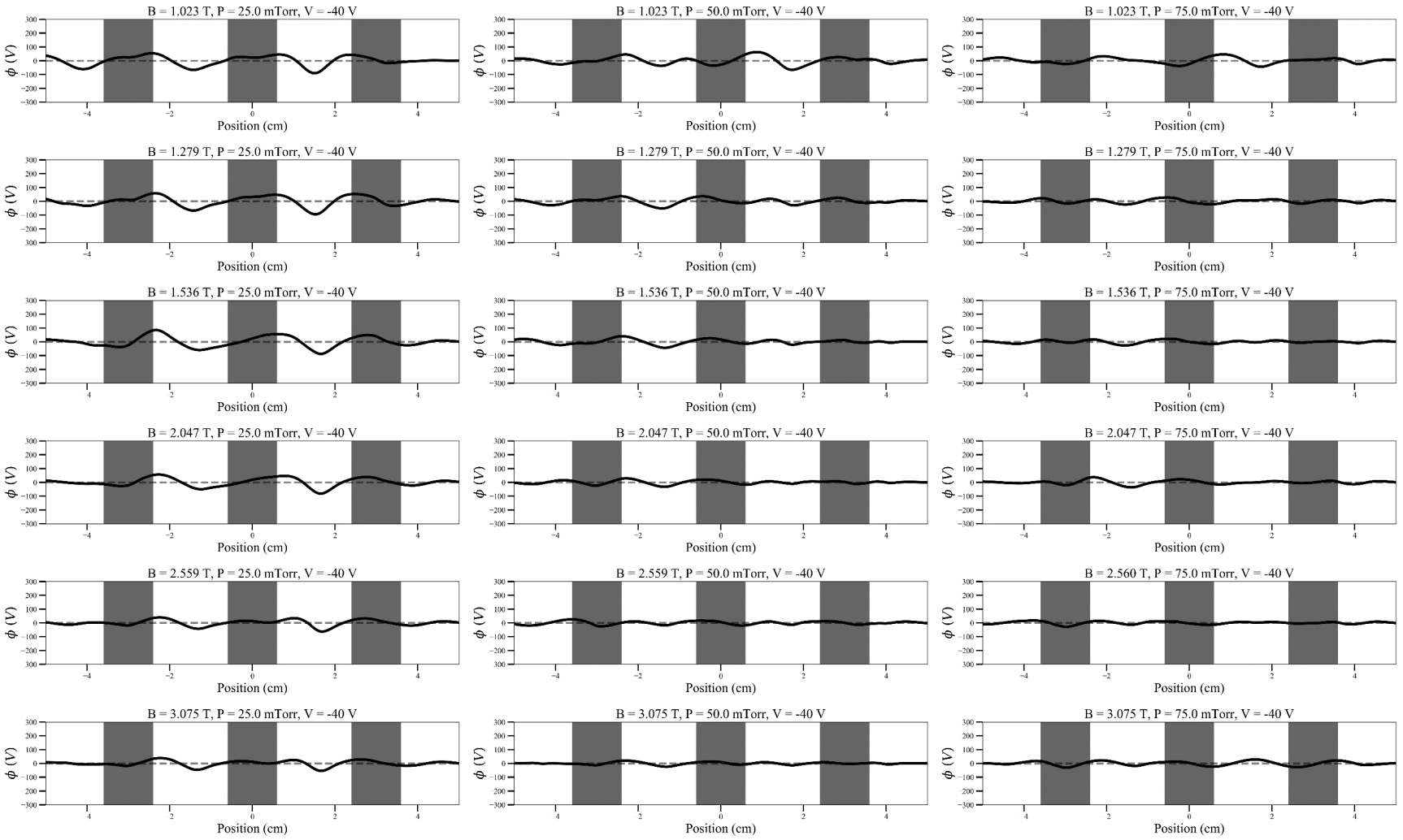

Continuation of Figure 4-8 Effective electric potential profiles for an electrode bias of -40 V. Columns show profiles for increasing neutral pressure from left to right (25 - 75 mTorr). Rows show increasing magnetic field strength (1.02 – 3.08 T).

magnetic field the potentials appear to decrease in strength slightly between 0.51 T and 1.02 T, though the same peak structure is still apparent. Beginning at 1.28 T the potential structure begins to change somewhat. More observable at 2.05 T and higher, the potential shows two peaks within the holes instead of the single peak at lower magnetic fields, with two small peaks beneath each hole at 3.08 T.

In the middle column, at 50 mTorr, a similar set of trends is observed. When no magnetic field is present the potential is effectively flat. As the magnetic field increases, the magnitude of the potential increases as well, developing positive potential peaks within the electrode holes. These peaks can be seen between 0.13 T and 0.51 T, though the potentials do not have the same strength as at 25 mTorr. Above 0.51 T to a magnetic field strength of 1.28 T, these potential structures become less apparent, with their peaks shifting away from the holes to underneath the conducting bands. This is also roughly the range that the potential in the 25 mTorr case decreased in strength. At the highest magnetic fields, 1.54 – 3.08 T, the potential becomes significantly reduced, with some small peak structures still observable. The potential appears to show multiple small peaks beneath the holes, just as in the 25 mTorr data. At 3.08 T, the potential has a low, broad positive region within the holes, which may be several small peaks which are not able to be individually resolved.

At the highest pressure, 75 mTorr (10 Pa) in the right most column, the same behavior as at 50 mTorr (6.67 Pa) is observed. No significant potential at $B = 0.0$ T, and a slowly developing potential structure with magnetic field. These potentials do show peaks at similar positions to the 25 and 50 mTorr (3.33 and 6.67 Pa) data, but with a lower potential than either. The sharp reduction in potential strength seen at 50 mTorr and 1.54 T is observed here a lower magnetic field, occurring around 1.02 T. At the highest magnetic field only, a small peak is observed beneath the hole,

compared to the multiple peaks seen at lower pressures. These reductions in the potential with neutral pressure appear consistent with the picture of the imposed, ordered structures beneath the wire mesh whereas the neutral pressure increased at a given magnetic field, the confining potential structure was also decreased or even washed out.

In Figure 4-10 effective potential profiles for the electrode bias of +40 V are shown. These plots laid out like those in Figure 4-9, with three columns at 25, 50, and 75 mTorr, and rows at increasing magnetic fields from 0.0 – 3.08 T across two pages. In the first column, at 25 mTorr, in the absence of a magnetic field the potential profile is effectively flat. Once the magnetic field has been turned on though, a potential structure does begin to develop. From 0.06 – 0.51 T the structure shows singular positive peaks beneath the holes of the electrode, which is consistent with the -40 V data. Beginning at 0.77 T, the potential shows the development of the two-peak structure beneath the right hole, with a diminished singular peak on the left. This two-peak structure appears earlier than at -40 V, which needed field near 1.54 T before developing similar structures. By 1.54 T the +40 V data does show two peaks beneath both the left and right holes. This structure appears to continue up to higher magnetic field, but with the strength of the effective potential becoming considerably reduced.

At 50 mTorr the potential is also flat when no magnetic field is present and develops structure as it increases. A single-peak structure appears beneath both holes up to a magnetic field of 0.77 T. While these structures appear similar to the 25 mTorr case they are slightly weaker in strength. At 1.02 T the two-peak structure is apparent beneath the right hole but not the left. For higher magnetic fields the effective potential becomes quite weak. There may be some evidence of a positive potential peaks near the electrode edges at 2.56 or 3.08 T, but these structures are quite small.

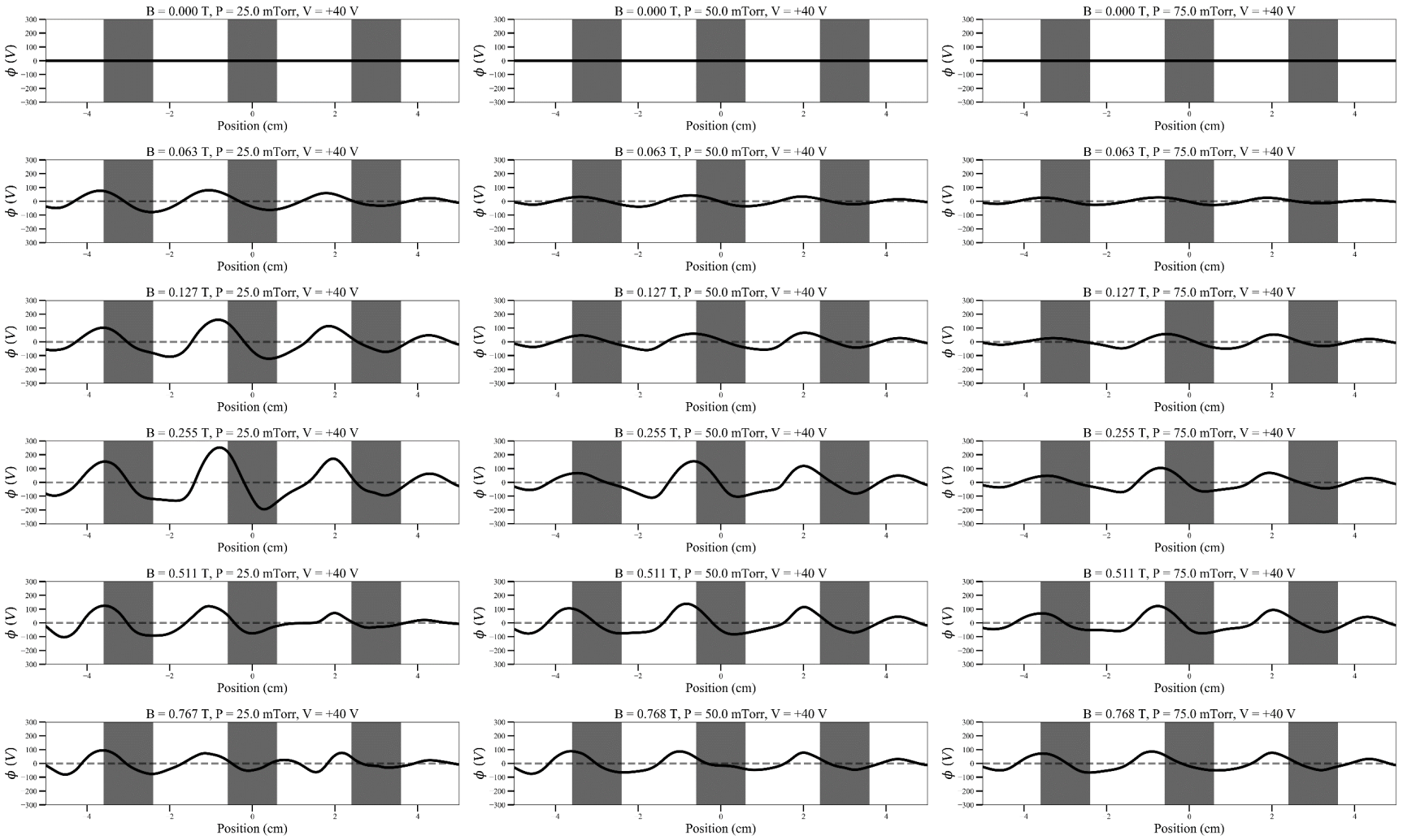

Figure 4-10 Effective electric potential profiles for an electrode bias of +40 V. Columns show profiles for increasing neutral pressure from left to right (25 - 75 mTorr). Rows show increasing magnetic field strength (0.0 - 0.767 T).

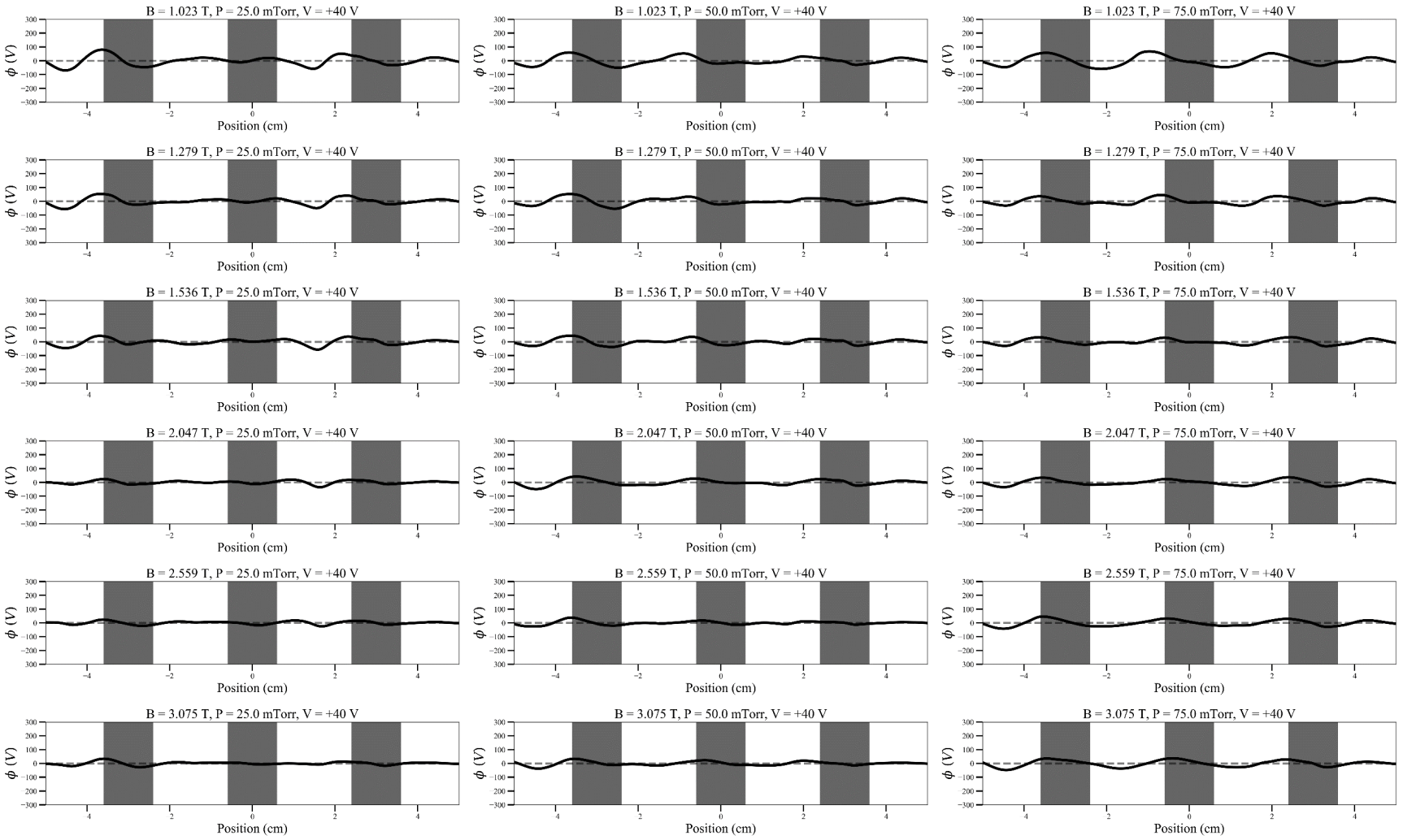

Continuation of Figure 4-9 Effective electric potential profiles for an electrode bias of +40 V. Columns show profiles for increasing neutral pressure from left to right (25 - 75 mTorr). Rows show increasing magnetic field strength (1.02 – 3.08 T).

In the left column, the 75 mTorr (6.67 Pa) data shows a flat potential at $B = 0.0$ T. As the magnetic field increases single positive peaks begin to appear from 0.06 to 1.02 T. The structures seen in this data are qualitatively similar to the 25 and 50 mTorr (3.33 and 6.67 Pa) data and shows the same trend as the -40 V bias where the strength of the effective potential decreases with the neutral pressure. At 1.54 T a two-peak structure is observed beneath the left hole. These structures appear much earlier overall for the +40 V electrode bias, and this structure is not observed at all for the 75 mTorr (6.67 Pa) data at -40 V.

Using a double Langmuir probe, measurements of the electron temperature and density are taken in a magnetized low-temperature plasma. Structures in the temperature and density are shown to develop at high magnetic fields. The densities are then integrated according to Poisson's equation to calculate effective electric potentials within the plasma. These effective electrical potentials, which have a form that would confine negatively charged dust particles, within the plasma are observed at a range of neutral pressures and electrode biases. These potentials are shown to increase in strength with increasing magnetic field and develop new patterns at the highest magnetic fields. Measurements suggest that the dust particles would be confined to areas near the center of the holes of the "waffle" electrode at lower magnetic fields. When new patterns emerge at high magnetic fields, $B = 1.54 - 3.08$ T, the locations of particle confinement would be closer to the edges of the electrode, with multiple confining locations beneath each hole.

4.3 Measurements of the Electric Field

This section will report the measurements made by the ring probes introduced in Section 2.3.3 and the process by which these measurements are used to calculate effective electric fields across the plasma. Initially, profiles of the plasma floating potential at multiple points through the plasma are found. These profiles are then used to calculate electric fields beneath the "waffle"

electrode. A background electric field is determined and then subtracted away. The resulting electric fields are then presented for various magnetic fields, neutral pressures, electrode biases.

Ring probe measurements were taken beneath the “waffle” electrode with the probe scanning between the “waffle” electrode’s different conducting band thicknesses. Figure 4-11 shows these two dimensions highlighted on the “waffle” electrode schematic, as well as the path and direction which the probe scans for either dimension. For these experiments a DC bias was placed on the “waffle” electrode at six different values ± 20, ±40, and ±60 V. Although no dust

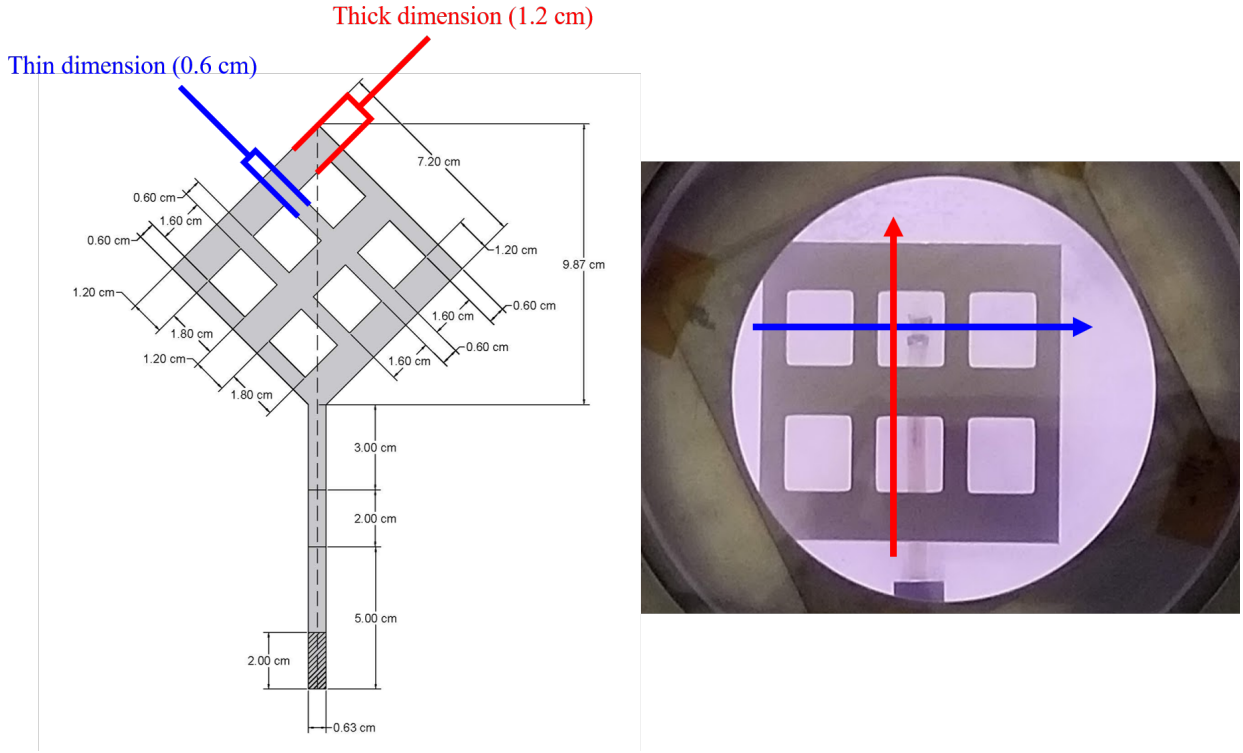

Figure 4-11 Defining the "thick" and "thin “dimensions of the “waffle” electrode. The “thick” dimension has conducting bands with a 1.2 cm width and is the primary dimension used. The “thin” dimension has conducting bands 0.6 cm wide. On the right is shown the path beneath the electrode that the ring probe takes for either probe dimension, with the “thick” dimension shown in red, and the path for the “thin” dimension shown in blue.

particles were present in the plasma while collecting data with the ring probe, the 4-1/2" CF Flange gasket was placed in the chamber on the bottom electrode for consistency.

For these experiments the MDPX vacuum chamber was configured according to the description in Section. 2.4.2. Measurements of the electric field are made under the same experimental conditions of pressure, magnetic field, and rf power as the double probe measurements. For the experiments performed at an electrode bias of ±20 V or ±60 V, the RF-VII, Model RF-3-XIII, power supply was used for generating the plasma. For data collected at an electrode bias of ±40 V the T&C Power Conversion Inc., Model AG 0313, power supply was used for plasma generation.

The reason why two different rf networks were used for the different data sets is the data sets were collected at different times. The ±20 V and ±60 V experiments were initially carried out in early 2019 as an independent experiment to examine the electric fields beneath the "waffle" electrode. Later that year, in the summer of 2019, the rf network systems were upgraded to the T&C Power Conversion Inc. system. The double Langmuir probe measurements (Section 4.1) and dust cloud observations (Chapter 5) were carried out after this upgrade. In order to allow for some comparison between the different experiments, a set of measurements with the ring probe was made for electrode biases of ±40 V and a neutral pressure of 25 mTorr. Magnetic field conditions were kept the same.

The ring probe was designed and built to measure the electric fields beneath the grid electrode. This probe, which was described in detail in Section 2.3.3, consists of two strips of stainless steel around a tip of 3D printed material, electrically connected through the tip to vacuum feedthroughs. These tips are offset in the *x*-direction by some amount, *dx*, and each tip is allowed to remain at its local floating potential, V_f. This floating potential was measured at a sampling rate

of 50 kHz over a time interval of 0.1 s. The probes were moved through the plasma on a stepper motor over a range of 15 cm (5.9”) through the plasma at a step interval of 0.1 cm (0.04”) along a line 2.9 cm (1.13”) below the “waffle” electrode. This process was controlled by a LabView program provided in Appendix C.3. The position of the probe relative to the “waffle” electrode was determined by the methods detailed in Appendix B.2. The electric field, E_x,E along the probe axis, at the location between the rings was then calculated as

$$E_x = -\frac{V_{f1} - V_{f2}}{dx}. \tag{4-5}$$

In order for the floating potentials to be used to calculate the electric fields they must first be processed. A series of plots showing the results of initial steps of this processing are presented in Figure 4-12. The floating potential signals are processed by first averaging the measured signal at each position. This process is then repeated at each unique position giving a plot of the floating potential versus position for each probe tip. The floating potential profiles were then smoothed by computing a moving average. This average was taken by convolving the data points with a one-dimensional array $\boldsymbol{A}$, which is a length-N array of ones $\boldsymbol{I}_N$ divided by N, of the form:

$$\boldsymbol{A} = \frac{\boldsymbol{I}_N}{N} = \frac{1}{N}(1 \quad 1 \quad \cdots \quad 1) \tag{4-6}$$

where $N = 11$.

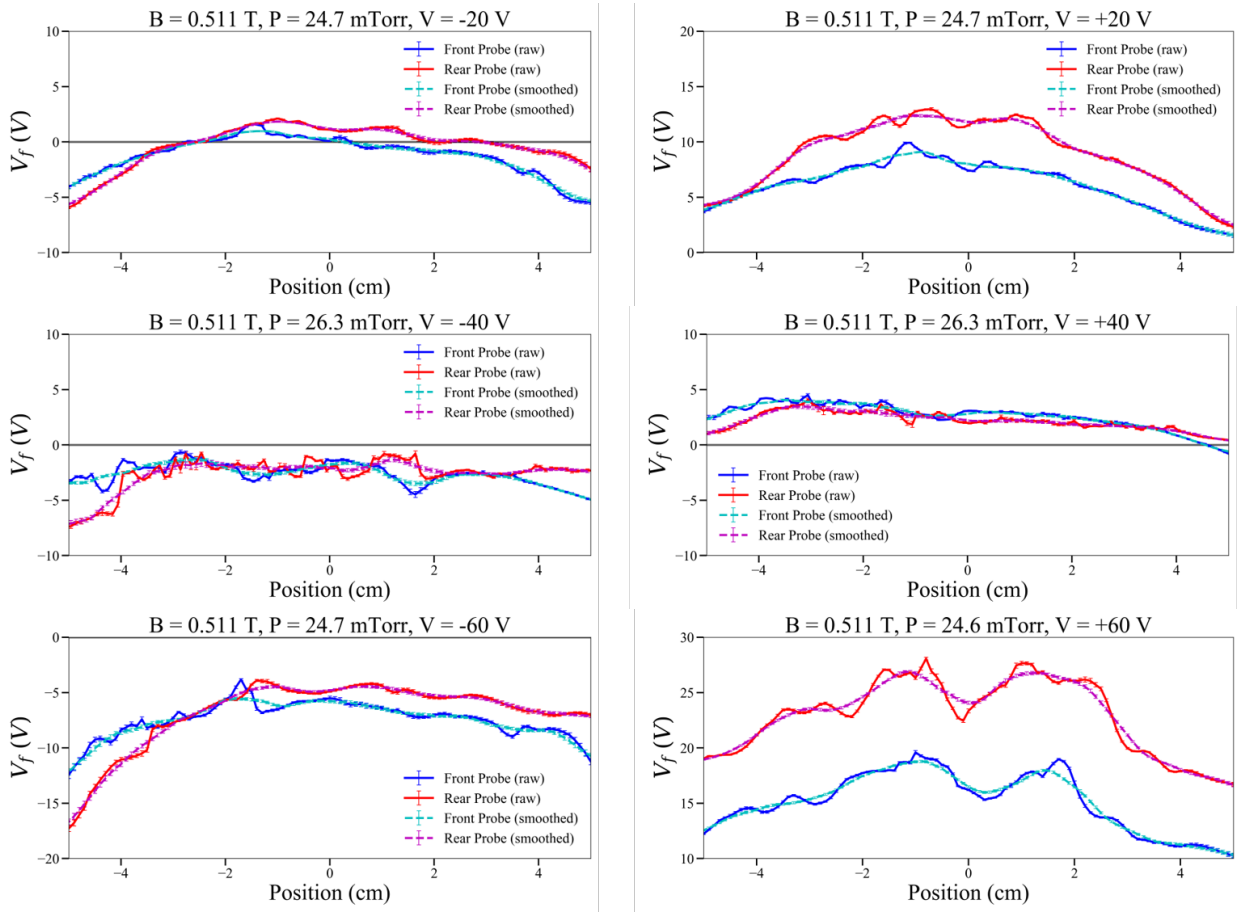

Figure 4-12 Floating potential profiles at a B =0.51 T and P = 25 mTorr. Electrode biases between -60 V to +60 V are shown. Measurements made with front probe are shown in blue, and with the rear probe are shown in red. Dashed lines represent the smoothed data used to determine the electric fields, with cyan being smoothed front probe data, and magenta being smoothed rear probe data.

Once this smoothing was performed, the potential difference was taken, and an electric field was calculated according to Equation 4-5. In order to examine the finer electric field structure which may be confining the dust particles, it was necessary to remove the background electric fields. Some examples of this process are shown in Figure 4-13. To determine a form for the background electric field a cubic function was fit to the calculated electric field over the range of $x = -5.0$ cm to $x = +5.0$ cm. By choosing a cubic function, the background potential has odd parity. This allows for the function to take opposite signs far away from the center position, and

also follows logically from the supposition that the background potential is qualitatively symmetric about some central point and would exhibit even parity. Once the fit parameters were calculated, the background electric field was subtracted away from the calculated electric field. The resultant field, hereafter simply referred to as the effective electric field, is what will be used in the remainder of this section.

These electric fields are then grouped together by pressure and electrode potential and plotted as two-dimensional contour plots where the horizontal axis is the magnetic field, and the

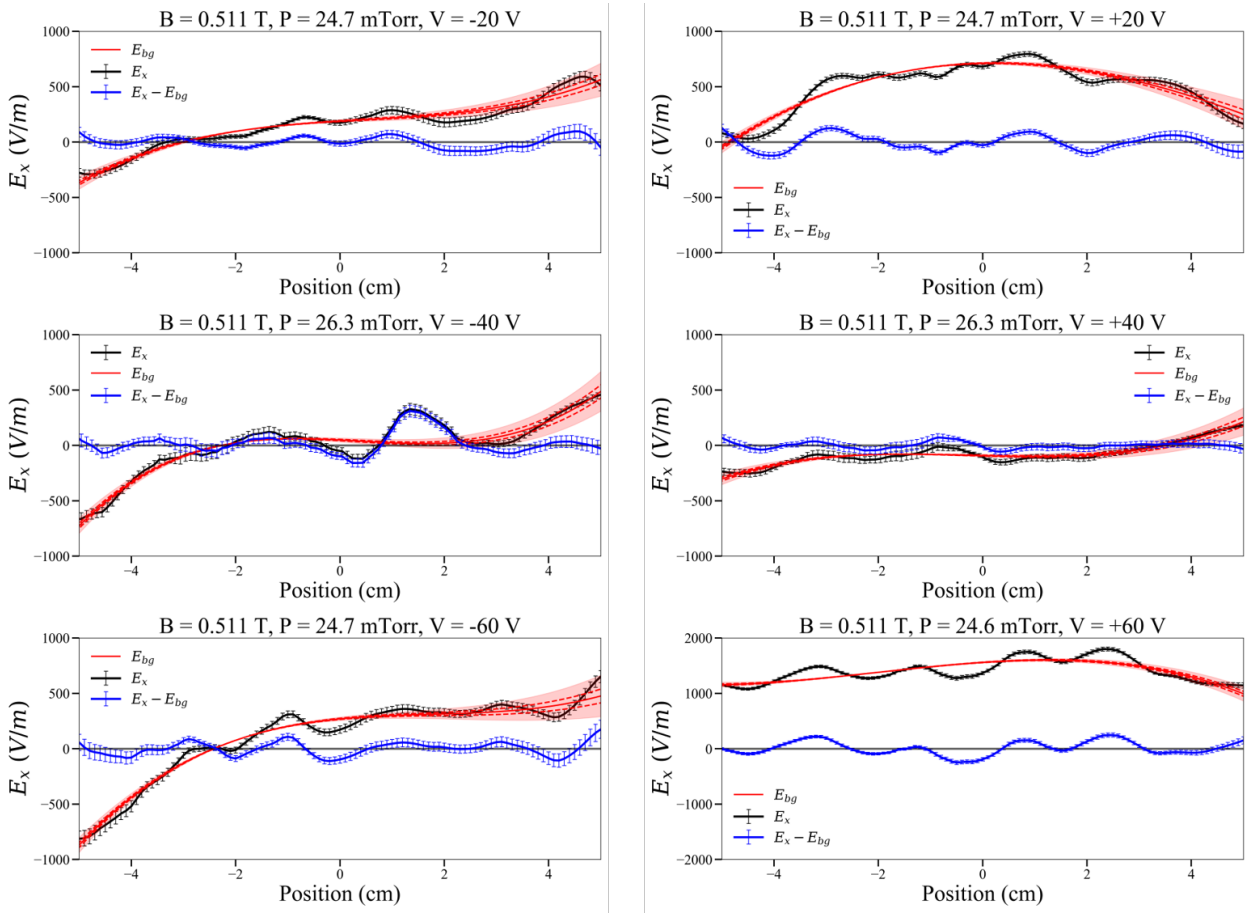

Figure 4-13 Plots of the calculated effective electric fields for B = 0.51 T, P = 25 mTorr. Electrode biases between -60 V to +60 V are shown. The calculated electric fields, E_x, are shown as solid black lines. The cubic fits, E_{bg}, are shown as solid red lines with ±1σ intervals as red dashed lines and the ±3σ interval as the shaded red area. The resulting background electric field, $E_x - E_{bg}$, is shown as the solid blue line.

vertical axis is the position relative to the center of the electrode. Several of these contour plots are shown in Figure 4-14. The contour plots are colored either red or blue to denote the direction of the electric field along the probe axis, either positive or negative respectively. The extent of the color range is determined by the maximum of the electric field magnitude over the range of $x = -5.0$ cm to $x = +5.0$ cm, rounded up to the nearest factor of ten. This is done to allow for the maximum amount of contrast within each electric field contour plot. The dark grey bars spanning the plot in the horizontal direction represent the location of the conducting bands of the grid electrode.

One of the most important features in these figures is regions of white between areas of red and blue. These areas are important because they indicate where the electric field in the *x*-direction is zero, or in other words, where *the direction of the electric field reverses direction*. This means that at a position where the electric field changes direction, a charged particle experiences no electric force in the horizontal *x*-direction and is in an equilibrium state. It is presumed that the ion drag forces will have a negligible contribution at these locations because the ions will also experience opposing force, only in the opposite directions as the dust. An additional assumption of a negligible neutral drag in the horizontal direction is made, as the neutral drag depends on the dust velocity relative to the neutral particles which should go to zero at an equilibrium point.

These equilibrium states can represent either a stable or unstable equilibrium. For a negatively charged particle, such as the dust microparticles present in experiments conducted in the MDPX vacuum chamber, locations at which the electric field, and electric forces, are directed away from each other, would provide a stable equilibrium where the dust feels no net force in the *x*-direction and the dust can group together as clouds within the plasma. This can be seen in the contour plots where the electric field gradient goes from negative (blue) to positive (red) with

increasing position in the vertical direction. Unstable equilibrium positions, where the dust is repelled away from, are found where the electric field goes from positive (red) to negative (blue) with increasing position in the vertical direction.

The first set of these effective electric field contours is shown in Figure 4-14. This figure contains effective electric field contours for the data sets at a neutral pressure of 25 mTorr and electrode biases of ±20 V, ±40 V, and ±60 V. For plots in the first row, the cases of ±20 V, these areas of electric field reversal are observed both beneath the "waffle" electrodes conducting bands and the holes of the electrode. At low magnetic fields, $B \leq 1.5$ T, an unstable equilibrium is seen in the top hole. This unstable region, where the electric field goes from positive to negative with increasing position, eventually dissipates at higher magnetic field and changes into a stable region at the highest magnetic fields. Interestingly this change appears as opposite effects between the two plots. For the -20 V case the region of positive electric field shifts upward toward the top conducting band, developing a region of negative electric field below it; and the +20 V case has the region of negative electric field shifting down, developing a region of positive potential above it. The result in the two cases is the same. A region of stable equilibrium, where the electric field goes from negative to positive with increasing position, develops at the center of the hole for $B \geq 2.0$ T, but could indicate that the process or mechanism by which these structures develop has a dependence on the bias applied to the conducting surface. Beneath the bottom hole, an unstable equilibrium if found for both cases which either continues to high magnetic fields (-20 V bias) or becomes a region of positive electric field only (+20 V bias). In either case no position of stable equilibrium is found beneath the lower half of the electrode at high magnetic fields.

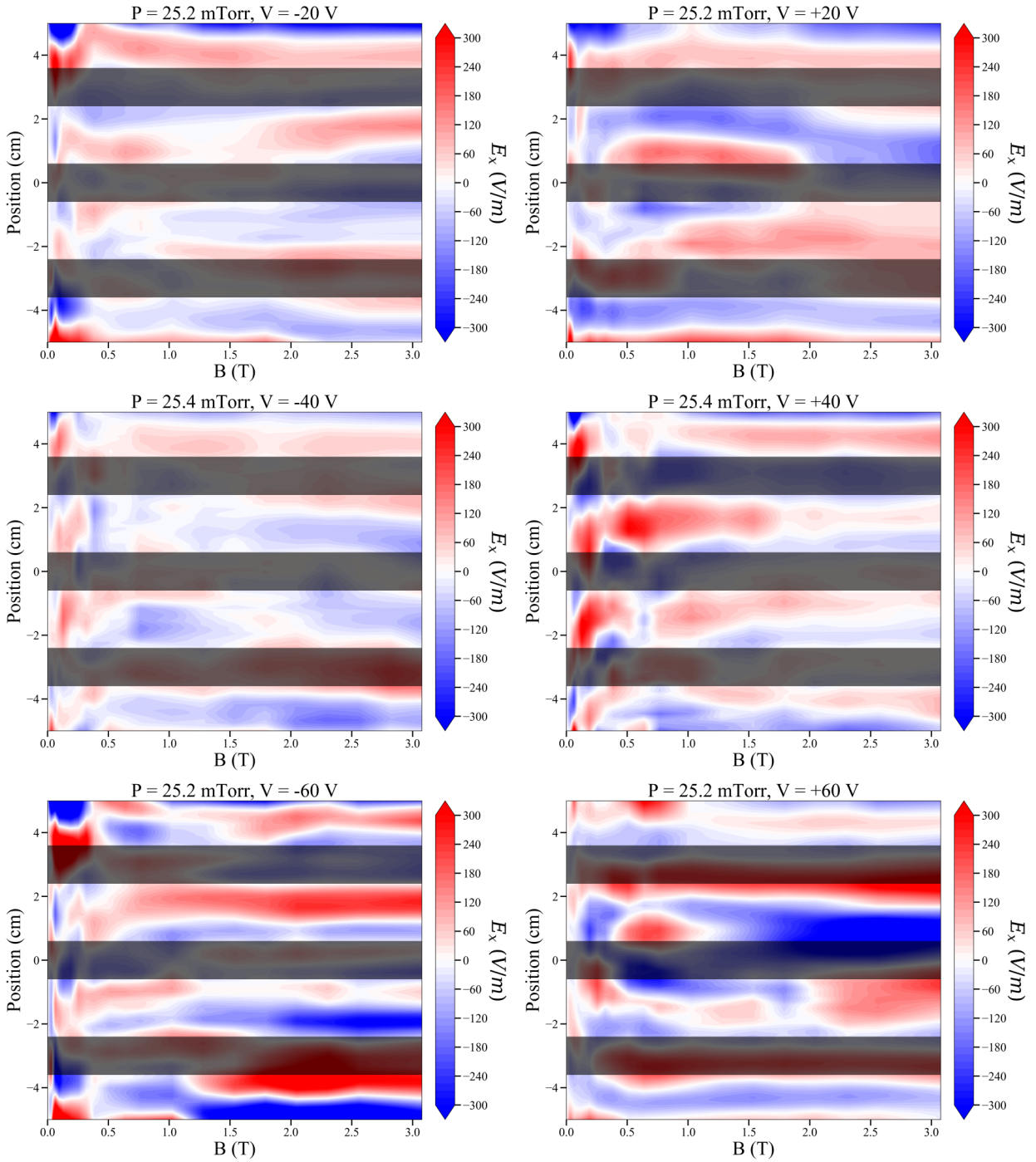

Figure 4-14 Contour plots of effective electric field as a function of chamber position and magnetic field for a neutral pressure of 25 mTorr and variety of electrode biases. The dark gray bars overlaid on the contour plots show the location of the conducting bands of the electrode. Plots are colored red for regions of positive (+ x-direction) electric field and blue for negative (-x-direction) electric field.

For the ±40 V and ±60 V electrode biases, these locations of stable equilibrium are also found beneath the holes of the "waffle" electrode. These electric field structures appear most prominently beneath the top hole of the electrode. Beneath the bottom hole, stable equilibriums are observed at low magnetic fields, $B \leq 1.0$ T, for both the -40 and -60 V biases, though these equilibriums disperse at magnetic fields beyond 1.0 T. For the +40 V and +60 V cases the structure beneath the bottom hole still appears stable, but neither has electric fields with as high a magnitude as beneath the top hole.

The next two figures, Figure 4-15 and Figure 4-16, contain effective electric field contours for neutral pressures of 50 and 75 mTorr (6.67 and 10 Pa) respectively. Electrode biases of ±20 V and ±60 V are presented in both figures. The results for these two neutral pressures are quite similar and so will discussed jointly. For the ±20 V electrode bias in the first row, the measurements show unstable equilibrium at the center of both holes for the -20 V case, and at the center of just the top hole for the +20 V case. Stable equilibrium can be found instead below the conducting bands. This is consistent with the observation made for the neutral pressure of 25 mTorr (3.33 Pa) at low magnetic fields. However, the electric fields at these two pressures retain the unstable equilibrium in the holes even at high magnetic fields, and do not show the same shift in the equilibrium position as the 25 mTorr (3.33 Pa) case.

The ±60 V electrode biases, bottom row, also appear consistent with the 25 mTorr (3.33 Pa) data within the top half of the contours. Stable equilibrium can be found at high magnetic fields beneath the top hole and at each of the electrode biases. The -60 V data also shows stable equilibrium at high magnetic fields beneath the lower hole for each of the two pressures, which is consistent with the measurements at 25 mTorr. The +60 V each show regions of positive electric

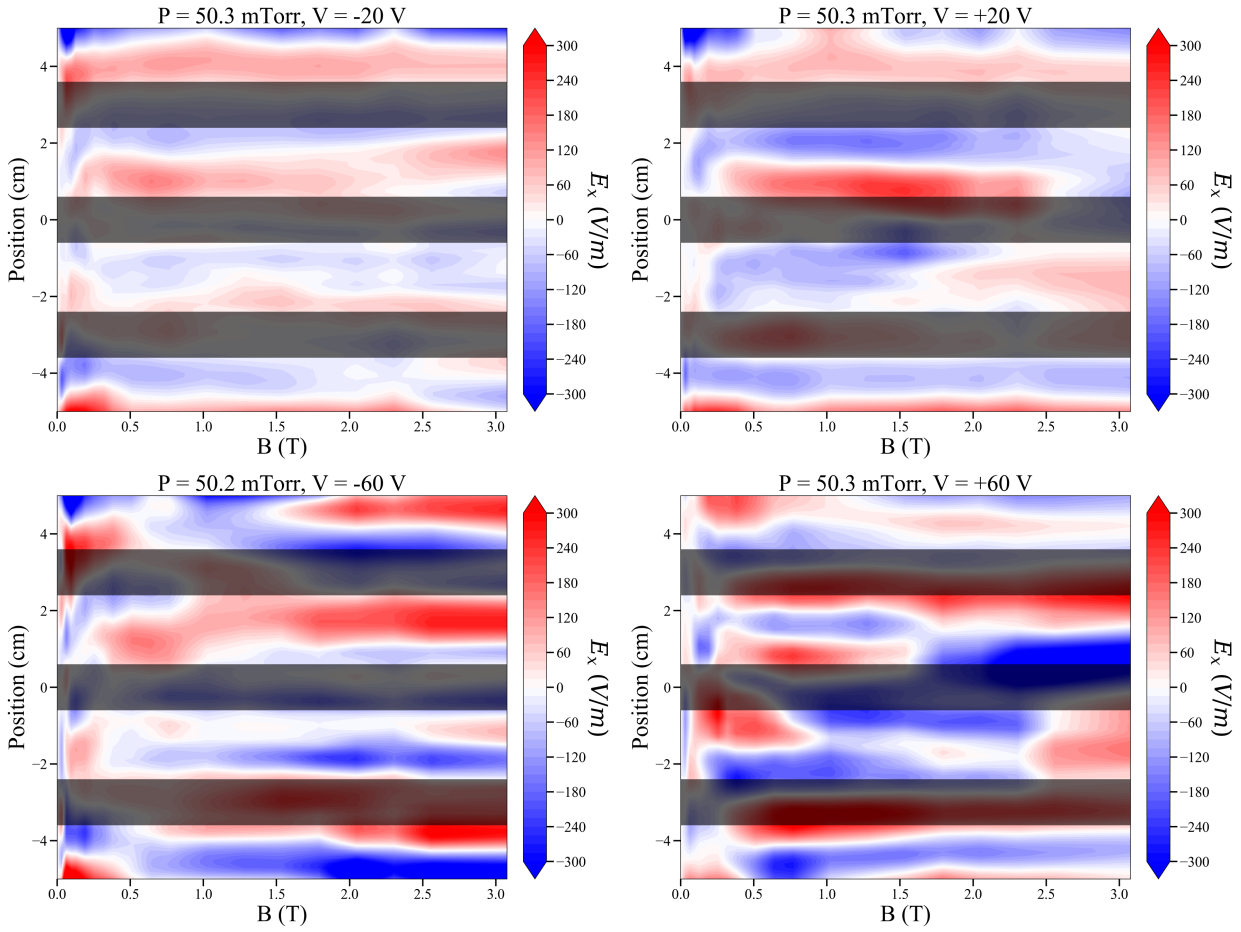

Figure 4-15 Contour plots of effective electric field as a function of chamber position and magnetic field for a neutral pressure of 50 mTorr and variety of electrode biases.

fields within that same region, which also appear at 25 mTorr. Overall, each of the four electrode biases appear qualitatively similar between the three neutral pressures.

The ring probe is also capable of measuring effective electric fields for other size dimensions of the "waffle" electrode. Figure 4-17 shows a set of effective electric field contour plots which were taken in the direction of the "thin" electrode dimension for a neutral pressure of 25 mTorr, and electrode biases of ±20 V and ±60 V. At ±20 V, unstable equilibriums are observed beneath the top hole at high magnetic fields, and beneath the lower hole at magnetic fields below 1.5 T. In the bottom row, stable equilibriums are found beneath each of the three holes for the -60

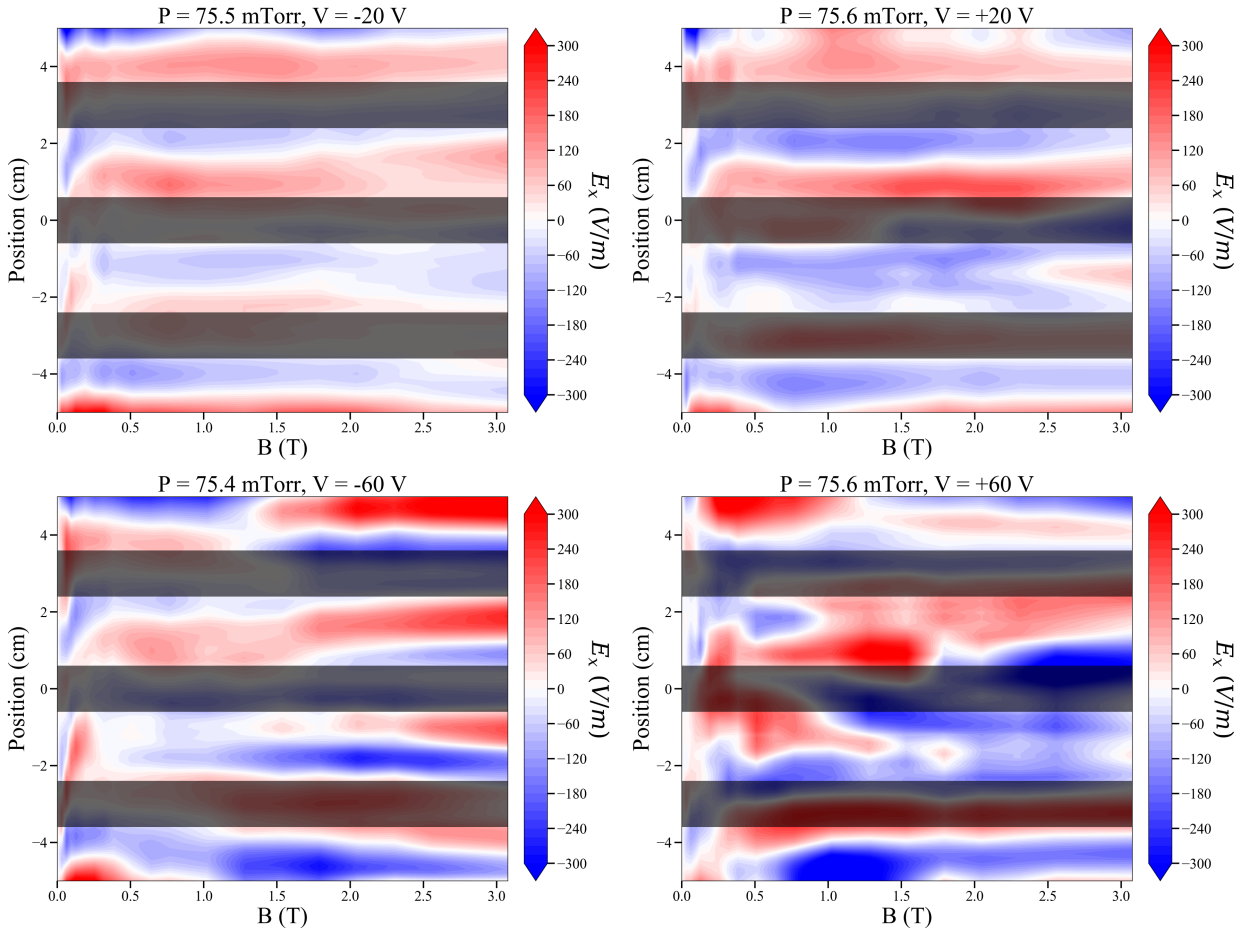

Figure 4-16 Contour plots of effective electric field as a function of chamber position and magnetic field for a neutral pressure of 75 mTorr and variety of electrode biases.

V bias, and beneath the top hole for the +60 V bias. These observations show effective electric field structures which correspond to the different electrode dimension and are qualitatively self-consistent with observations made with the "thick" electrode dimension for comparable pressure and bias conditions.

The fact that these measurements show consistent trends over a range of magnetic fields, neutral pressures, and electrode biases, should provide credible support for the robustness of the analysis methods. It also shows that the measurements and analysis methods presented for the ring probe are able to resolve these effective electric fields for a variety of proportions of the conductor

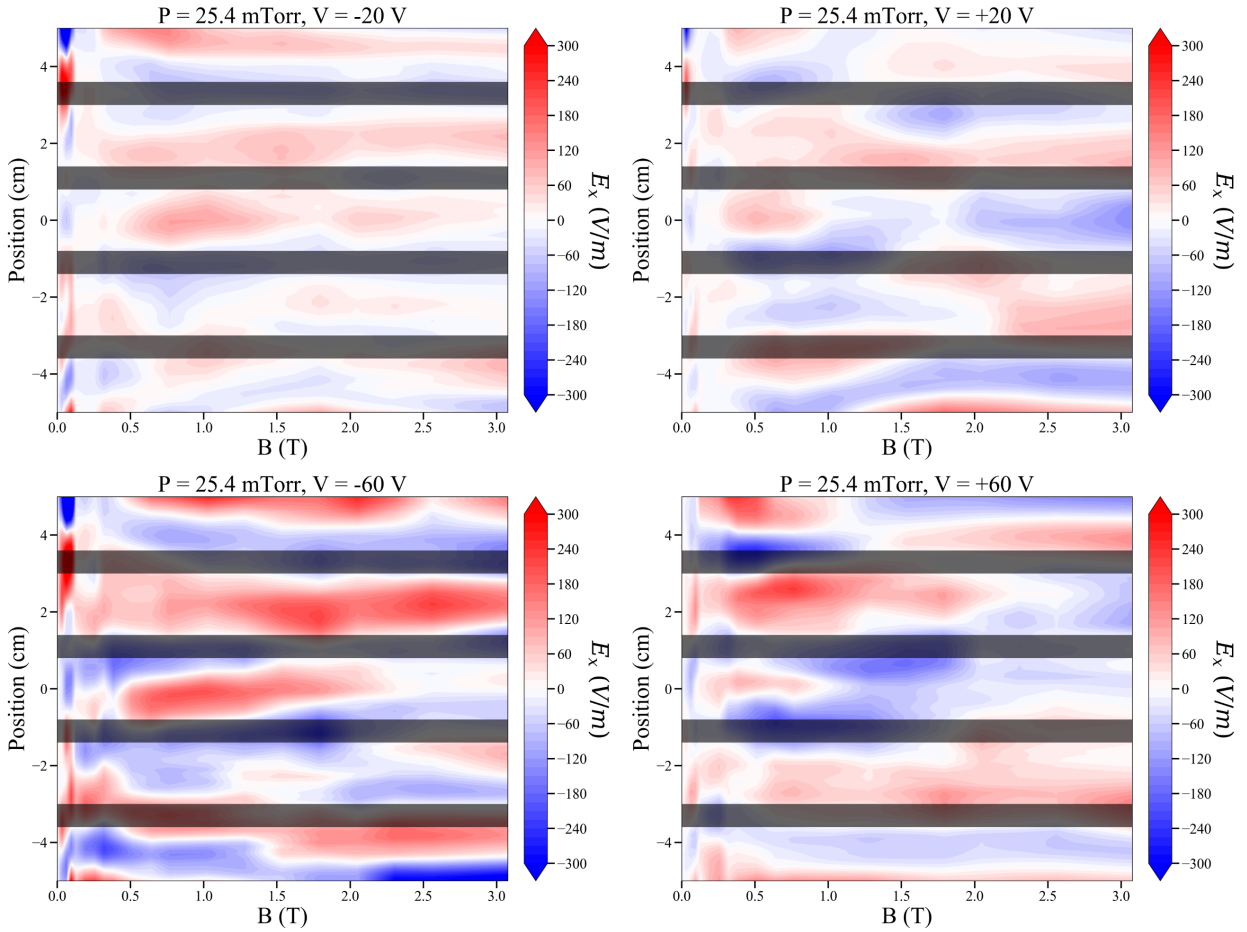

Figure 4-17 Contour plots of effective electric field beneath the "thin" dimension as a function of chamber position and magnetic field for a neutral pressure of 25 mTorr and variety of electrode biases.

which produces the plasma structures. While there are unknown factors which may affect the floating potential measurements, such as the probes own sheath dynamics or interactions between the probes themselves, the measurements themselves are self-consistent in their behavior. In their present state as a diagnostic, the ring probes show some ability to detect effective electric field structures which could influence negatively charged dust particles in a manner which is compatible with the observations of the imposed, ordered structures.

4.4 Effective Electric Potentials from Electric Fields

The purpose of this section will be to present a method for finding effective electric potential profiles using the electric field results from the previous section. These potentials are calculated by integrating the effective electric potential as a function of position. The resulting effective electric potentials are then discussed.

In the previous section it was mentioned that the electric fields field measurements had been made in plasmas generated by different rf networks. Only electric fields measured at a neutral pressure of 25 mTorr, and with "waffle" electrode biases of ±40 V were taken in a plasma generated by the same rf network as the double probe measurements presented previously in Section 4.1, and the dust particle measurements presented later in Chapter 5. Because of this the calculations and analysis of effective electric potentials in this section will be limited to those data sets. The purpose of this choice is to reduce the number of external factors which need to be considered when comparing the various effective electric potential results.

To calculate the effective electric potentials, ϕ, the integral of the electric field, $\vec{E}$, must be taken in the form:

$$\boldsymbol{\phi} = -\int \vec{\boldsymbol{E}} \cdot \boldsymbol{d}\vec{\boldsymbol{x}} \tag{4-7}$$

For the measurements and calculations discussed in this work, the effective electric fields are one-dimensional, in the *x*-direction. So, the integral equation can be reduced to:

$$\boldsymbol{\phi}(\boldsymbol{x}) = -\int_{\boldsymbol{x_{min}}}^{\boldsymbol{x_{max}}} \boldsymbol{E_x}(\boldsymbol{x})\boldsymbol{dx} \tag{4-8}$$

This integral was carried out computationally by the trapezoidal rule for numerical integration within the electric field error being propagated through. Once the integral is performed, the average value of the effective potential is subtracted away.

The first set of the calculated effective electric potentials is shown in Figure 4-18 which contains effective potentials for a neutral pressure of 25 mTorr and electrode bias of -40 V. This figure is split across two pages, with the first part comprised of effective potentials which range from 0.0 T to 0.77 T, and the second part comprised of magnetic fields from 1.02 T to 3.08 T. When there is no magnetic field present the effective potential is quite flat with apparent structure. As the magnetic field increases, an increase in the calculated effective potential is observed. For very low magnetic fields, $B \leq 0.51$ T, no significant trends are observed. The effective electric fields in this range did fluctuate quite a bit with magnetic field, and so this result is not all to surprising. The potentials do show some evidence of positive effective potential peaks at 0.26 T on the right and 0.51 on the left, but because the measurements appear so ill behaved in this region it is difficult to trust those results.

As the magnetic field increases trends in the data begin to present themselves. Between 0.77 T and 1.54 T, a similar potential peak beneath the left hole, and low broad peak on the right, which extends both beneath the hole and the conducting bands is observed. The peak on the left slowly decreases with magnetic field, and is no longer observable at 1.54 T. The peak on the right appears just at the outer edge of the electrode at 0.77 T and gradually becomes broader towards the center of the right hole. At the highest magnetic fields, $B = 2.05 - 3.08$ T, these trends appear to continue. Beneath the left hole, the potential continues to decrease, developing a negatively peaked potential valley at the inner edge of the electrode on the left side. The low, broad potential

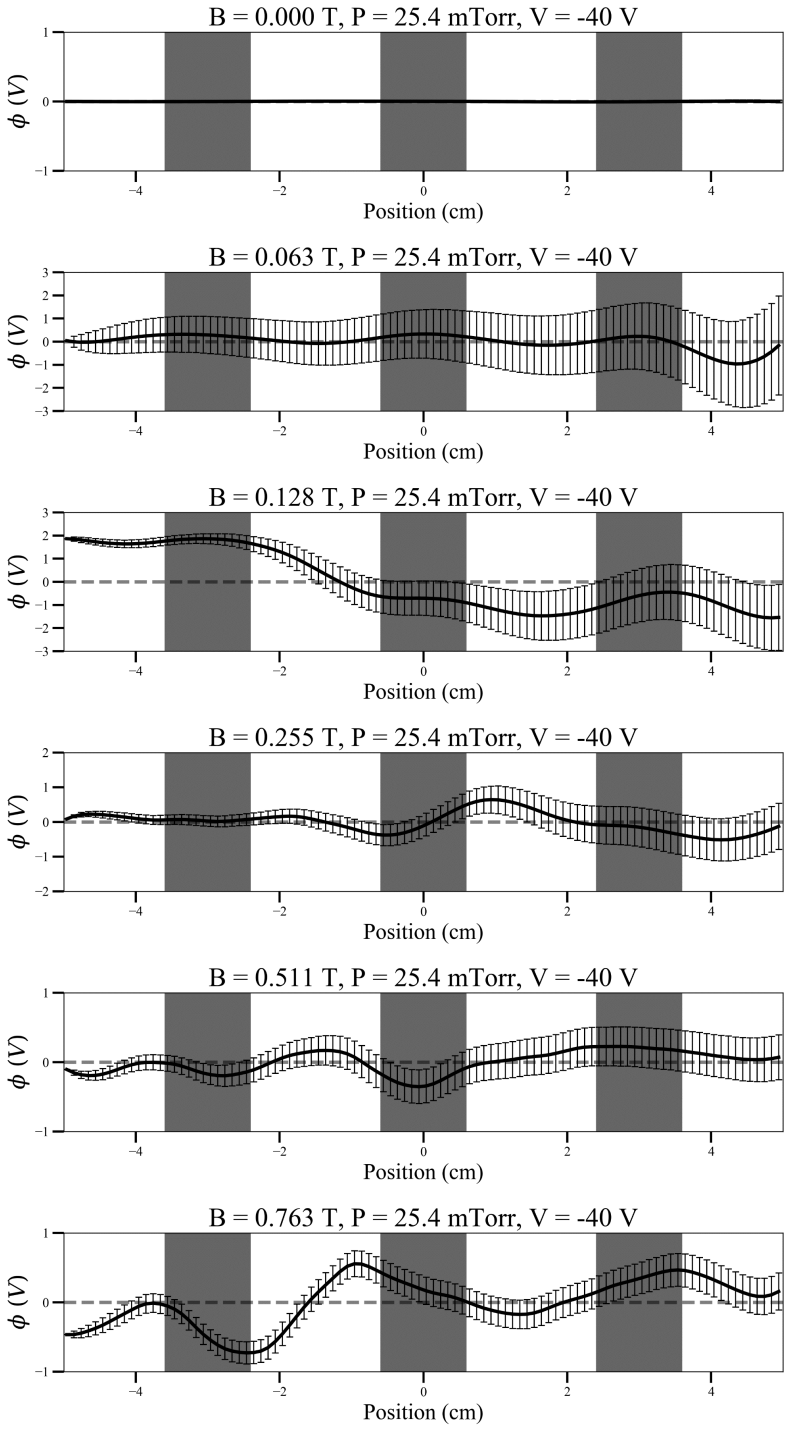

Figure 4-18 Effective electric potentials calculated from electric fields at a neutral pressure of 25 mTorr and electrode bias of -40 V. Magnetic fields range from 0.0 T to 0.77 T. The wide, vertical bars indicate the position of the "waffle" electrodes conducting bands.

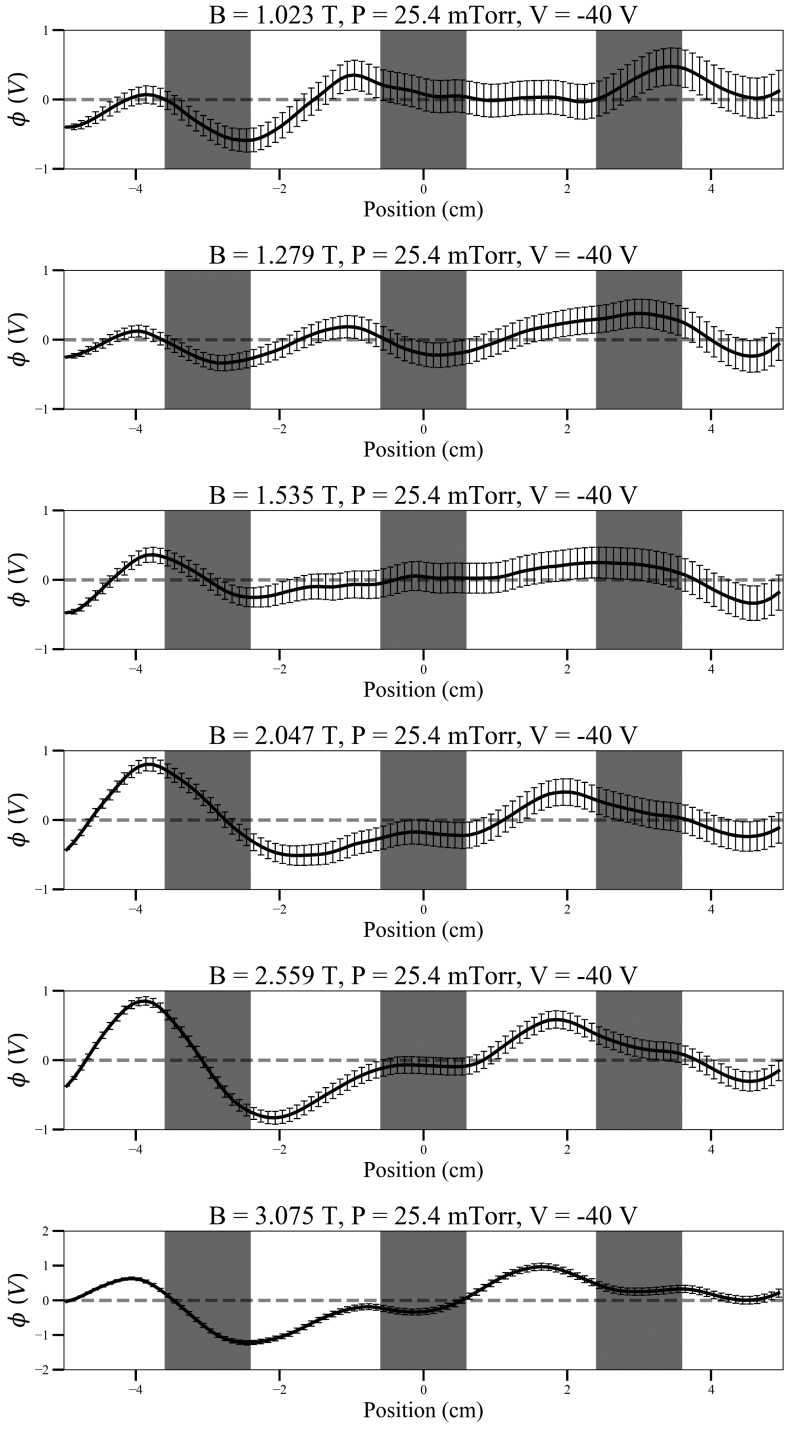

Continuation of Figure 4-17 Effective electric potentials calculated from electric fields at a neutral pressure of 25 mTorr and electrode bias of -40 V. Magnetic fields range from 1.02 T to 3.08 T.

on the right, becomes narrower, cresting beneath the right hole. This crest gradually becomes higher, and more centrally located beneath the hole at 3.08 T. Across all these magnetic fields, 0.77 – 3.08 T, another peak is also observed on the outer edge of the electrode on the left side. This peak gradually increases in strength over the entire magnetic range.

Figure 4-19 presents the effective electric potentials which were calculated from the electric fields at a neutral pressure of 25 mTorr and an electrode bias of +40 V. At $B = 0.0$ T, the potential is qualitatively uniform at a potential of zero volts, as was the case in the -40 V data. As the magnetic field increases various potential peaks and valleys can be seen. At low magnetic fields, $0.06 \leq B \leq 0.26$, three different peaks in the effective potential are found beneath the three conducting bands of the "waffle" electrode. Within this magnetic field range, those peaks gradually shift to the right in positive *x*-direction. From 0.51 T to 0.77 T, the middle of those three peaks increases in magnitude while the other two decrease, with the leftmost potential becoming fully negative.

The central peak diminishes in magnitude somewhat from 1.02 T to 1.28 T, while continuing to shift towards the center of the right hole. In this same range, the left potential peak reverses again, and appears as a small positive peak, comparable in magnitude to the peak beneath the right hole, just off center beneath the left hole. The peak on the far right remains just at the outer edge of the electrode and does not its magnitude with magnetic field in a significant way. At the highest magnetic fields, $B \geq 1.54$ T, the two peaks found beneath the holes roughly maintain their magnitude and do not shift their position in a significant way. While they do not demonstrate a very high potential, the profiles do maintain a structure which would be confining to negatively charged dust particles.

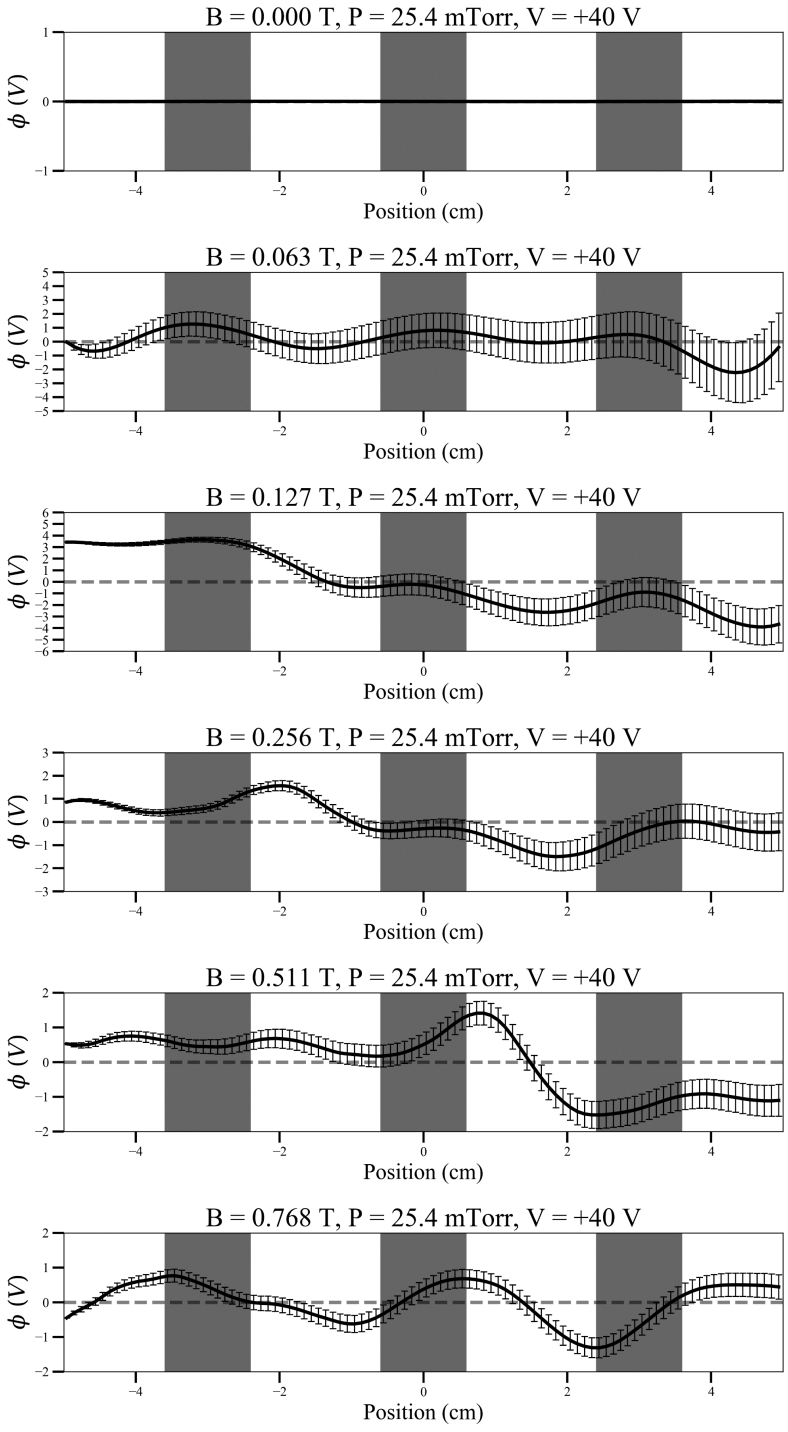

Figure 4-19 Effective electric potentials calculated from electric fields at a neutral pressure of 25 mTorr and electrode bias of +40 V. Magnetic fields range from 0.0 T to 0.77 T. The wide, vertical bars indicate the position of the "waffle" electrodes conducting bands.

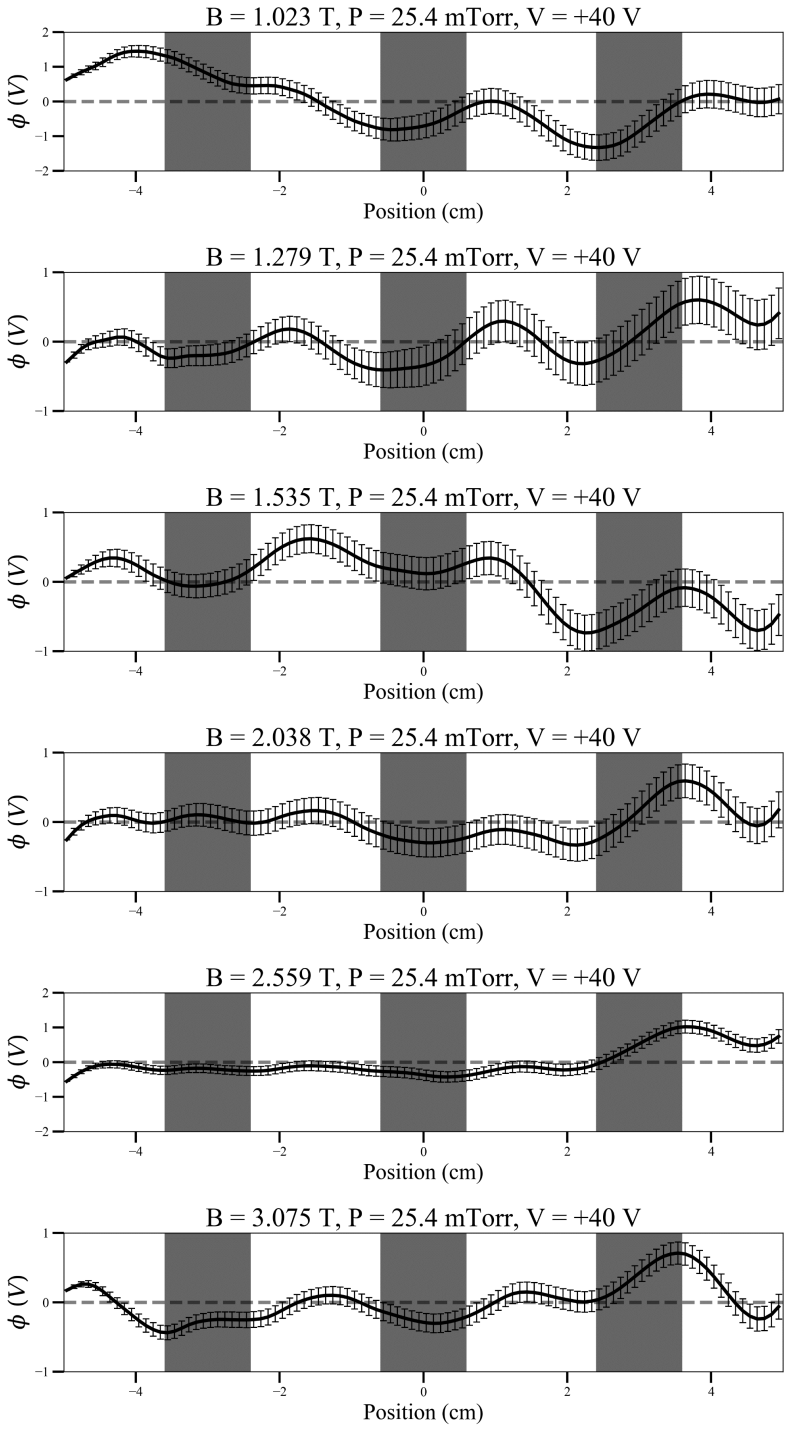

Continuation of Figure 4-18 Effective electric potentials calculated from electric fields at a neutral pressure of 25 mTorr and electrode bias of +40 V. Magnetic fields range from 1.02 T to 3.08 T.

Between these two data sets, at -40 V and +40 V, potential profiles, which would be attractive and confining to negatively charged dust particles, are observed for conditions at which imposed, ordered structures would be expected to occur based on previous experiments. The question at this stage in the analysis is then whether or not the effective potentials calculated from these electric fields are representative of the imposed, ordered phenomenon.

For both the double probe and the ring probe, measurements which show a dependence on the parameters of magnetic field, neutral pressure, and electrode bias are found. Robust methods for analyzing the measurements from plasma probes are present, with those methods able to produce results for effective electric potentials. It is strongly believed that these results show that plasma probe diagnostics can be made at these high magnetic fields and likely have a place alongside other non-invasive diagnostic measurements. These results are qualitatively consistent with the imposed, order structures, and will be compared to other estimates of the potential structure in Chapter 5.

When interpreting the data presented in this chapter, it has been assumed that the probes are behaving appropriately in the strong magnetic field. It is thought that the floating potentials measured by the ring probe, and that the ion saturation measured by the double probe are reasonably known. However, further modeling of the plasma is needed to fully interpret the probe especially at these high magnetic fields. It is recognized that several key pieces of information are missing for both probe diagnostics: the ion density for the double probe measurements, and the interaction between the sheaths of the ring probe.

The theories behind these probes do not include magnetic field effects and are thus inherently incomplete for the applications presented. But incomplete does not mean incompatible. The first step is that the probe theory needs to be revisited and reworked to incorporate high

magnetic fields. New computational models of low-temperature plasmas, such as those by Menati, et al., [58] will be invaluable in determining the underlying physics behind these magnetically enhanced plasma sheaths. Other non-invasive diagnostics, such as plasma spectroscopy [61,62] and laser induced fluorescence (LIF) [63–67], should be tools which provide supporting measurement of the plasma parameters. LIF, with its capability to measure ion velocity distributions, could be incredibly useful for understanding the evolution of the ion and electron velocity and energy distribution which are so critical to the probe theory. The results reported in this chapter should therefore be considered in the context of this discussion and considered as a first step towards the development of new probe applications in high magnetic field environments.

Chapter 5 Dust Behavior in the Presence of a Confining Electric Potential

In the previous chapter, effective potential structures beneath the "waffle" electrode were observed by independent measurements made using two different plasma probes. This chapter will present a third method for examining the effective potential structures within the plasma by using dust microparticles as diagnostic probes in the plasma. It is observed that the particles are confined to a space within the plasma which is beneath the holes of the "waffle" electrode, consistent with the predictions resulting from the observations in Chapter 4. The purpose of this chapter will be to describe the experimental methods used to observe dust particles confined beneath the "waffle" electrode, to present the results of the effective electric potentials made from those observations, and to discuss a qualitative comparison between the results obtained from the plasma probe methods and the dust observation method.

This chapter is divided into four parts. In Section 5.1 the experimental parameters are described. Section 5.2 then presents the methods by which the video recordings of the dust particles are processed so that plasma parameters can be determined from the resultant images. Section 5.3 discusses experimental observations and results from the video recordings using particle image velocimetry (PIV). These PIV methods are used to make measurements of the particle velocities. Using these velocities, the particles kinetic energies are calculated and used to determine an effective electric potential through the conservation of energy. Finally, Section 5.4 provides a summary and discussion of the primary results and how they fit into the broader context of the results made in earlier chapters.

5.1 Experimental Parameters

This section will provide a description of the experimental parameters for the experiments discussed in this chapter. These experiments examined the behavior of dust particles beneath the grid-like "waffle" electrode initially described in Section 2.4.2.

Experiments were performed in the primary MDPX vacuum vessel with the configuration described previously in Section 2.4.2. Argon plasmas are generated using capacitively-coupled radio frequency (cc-rf) electrodes at a frequency of 13.56 MHz and an input power of 5 W. The electrodes had a spacing of 11 cm (4.33"). The bottom electrode is powered, and the top electrode is electrically floating. The "waffle" electrode is inserted from one of the eight window ports and was 8.25 cm (3.25") above the bottom electrode.

Silica dust particles of 8 ± 0.8 μm diameter were introduced to the plasma via a dust shaker which could be pushed into the chamber when injecting particles and then pulled out to the side of the chamber when recording videos, so the cloud was not disturbed. These particles were confined to the center of the chamber using a 4-1/2" CF Flange copper gasket. Particles were illuminated using a red laser, spread out into a vertical laser sheet using a cylindrical lens.

Videos of the dust particles were recorded using a Ximea camera with a 200mm Nikon lens described in Section 2.3.1. The camera was positioned to view the particles from the side perpendicular to the magnetic axis and was outfitted with a red laser light filter. Videos were recorded at 90 fps with a 10ms exposure time. The resolution for video was 2048 × 800 pixels with a spatial resolution of 0.026924 mm/pixel for a viewing area of 55.1 × 21.5 mm. Recorded videos contained 500 frames (~5.6 seconds).

Experiments were conducted using argon gas at a range of background neutral pressures of 25 – 75 mTorr (3.33 – 10 Pa). The magnetic fields used ranged from 0 – 3 T. The "waffle"

electrode was powered with a DC bias at either ±40 V. A full list of these experimental parameters is provided in Table 2.

5.2 Image Processing

This section will describe the methods through which the videos of the dust were processed. All image processing was made using the *Fiji* software package and was fully automated. [68] The images processes in this way will be used to determine both particle locations and calculate average velocity vectors through particle image velocimetry (PIV). [69–73] Descriptions of those measurements will be provided in later sections.

To begin, the videos of the dust particles were imported into the *Fiji* software. The contrast of the videos was then enhanced using the "Enhance Contrast…" function which stretches the image histogram, only allowing 0.5% of pixels to become saturated, and then normalizing the histogram to a pixel range of 0-255 for the 8-bit images. Once this is complete, the "Z Project…" function is used to calculate an Average Intensity image of the video, which creates a new image using the average value at each pixel location. This Average Intensity image is then subtracted from the video frames using the "imageCalculator" processing tool in order to remove the

Table 2 List of parameters for dust experiments.

P (mTorr/Pa)	25/3.33	50/6.66	75/10			
B (T)	0.0	0.064	0.128	0.256	0.512	0.768
	1.024	1.280	1.536	2.048	2.560	3.075
V (V)	-40	+40				

background glow and produce images with more easily identifiable particles. Examples of these steps are shown in Figure 5-1.

Next, a mask was created which removes the remaining portion of the background image which did not contain particles. To do this a Max Intensity image was created using the same "Z Project…" function as before, but only now from the video frames which had the average pixel values subtracted out. This Max Intensity image was then filtered using the "Gaussian Blur…" function with a sigma of 2.0. The filtered image was thresholded with a range of 0-100 so that pixels which fell within this range were set to 0 and pixels outside this range were set to 255. This now binary image was turned into a mask using the "Create Mask" function. Using this mask, a selection was created, with the function "Create Selection", which automatically selected the largest region of black pixels, which in this situation would be the background around the dust particles. This selection was then transferred to the video frames "Restore Selection" function and all the pixels inside the selection were set to a value of 0 with the "Clear" function, which eliminated any extra background elements from the video frames. These processing steps are illustrated in Figure 5-2.

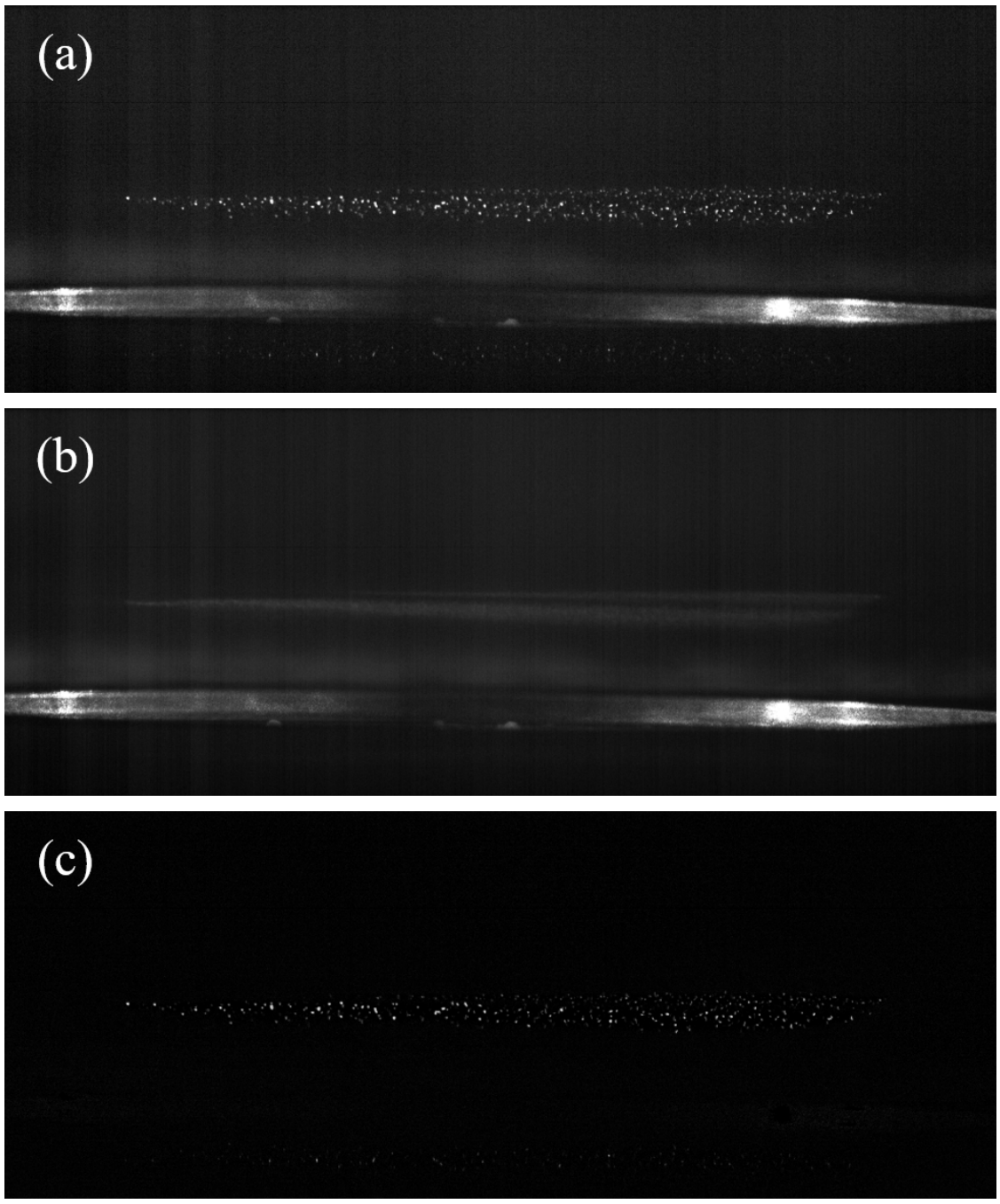

Figure 5-1 Examples of the initial processing steps. (a) Still image of the enhanced dust particles. (b) Average Intensity image made from the 500 video frames. (c) The same still image as (a) but with the Average Intensity image from (b) subtracted out. This creates a much more distinct image of the dust particles.

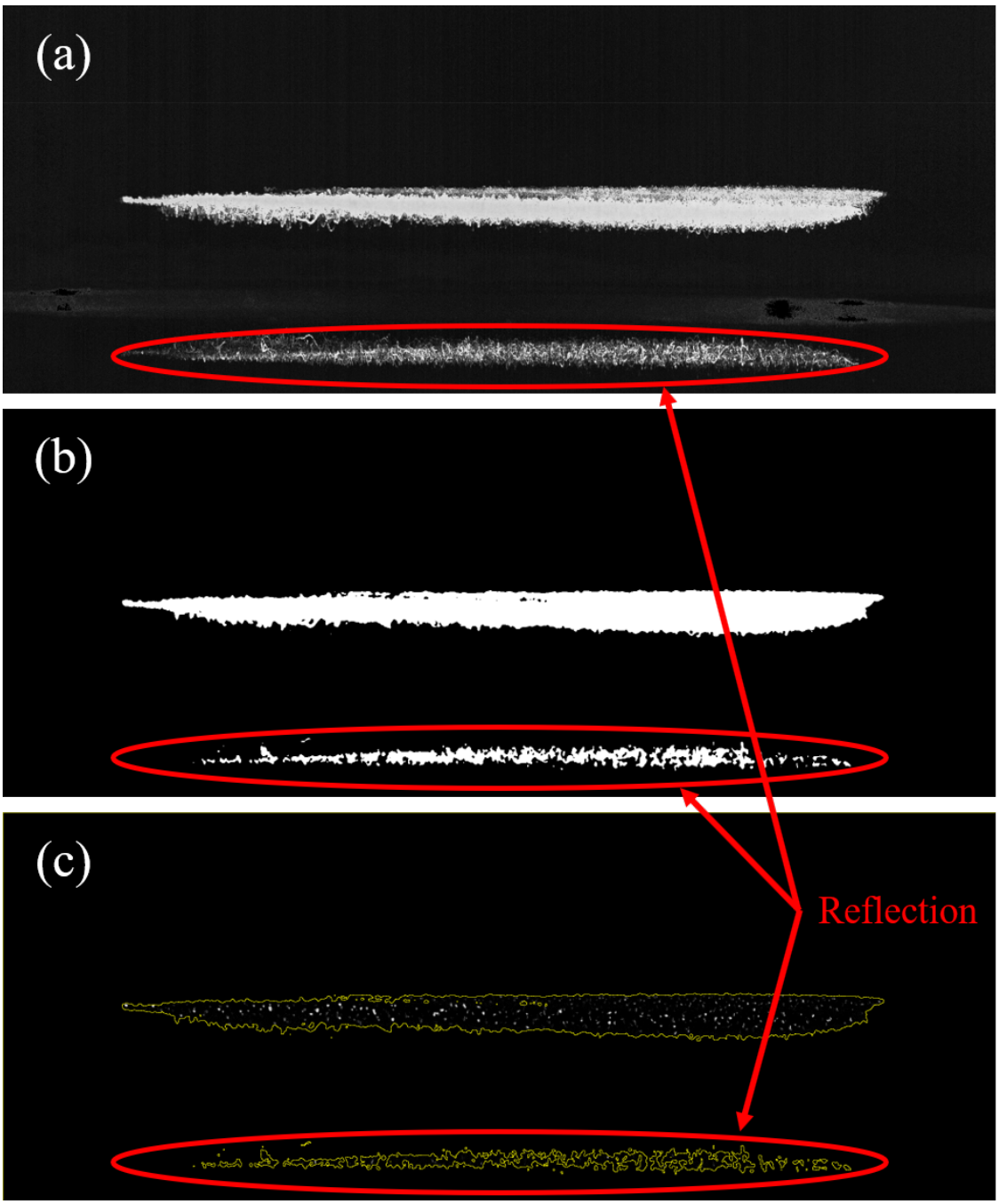

Figure 5-2 Examples of the masking process. (a) Max Intensity image created from the video frames after the Average Intensity was subtracted. (b) Mask image created from the Max intensity image after a blur filter and thresholding. (c) Final image of the particles after the background outside the yellow selection has been set to black. The remaining particles can be seen inside the yellow area. The red highlighted sections are reflections of the particles on the bottom electrode.

5.3 Determining Confining Potentials

This section will discuss the process through which measurements of the dust particle velocities are used to determine an electric potential which confines the dust particle. Initially velocities are found through the use of particle image velocimetry (PIV). Then, spatial velocity profiles are extracted from the PIV results and used to calculate an effective electric potential through the conservation of energy.

Particle velocities are found using the processed images which were created at the end of Section 5.2. These images were loaded into the PIV software from LaVision called *DaVis*. [74] Before the images can be used to calculate velocities, image pairs are created with consecutive pairs, i.e. (1+2), (2+3), (3+4), etc. Velocity vectors were then calculated using these image pairs. The PIV process was carried out using small interrogation windows which are moved throughout the image pairs to determine the average particle displacement within the interrogation window. For the PIV calculations carried out on the dust particle images, a square interrogation window with a size of 16 × 16 pixels was used, with a 75% overlap between the image pairs. Using this pair of interrogation windows from sequential frames, a cross-correlation was performed between two images to determine the average displacement of all the particles within that region. The average 2D pixel displacement was used to calculate the particle velocities. Once this processing was complete, a velocity vector field, like the example given in Figure 5-3, was produced for each image pair.

Once these pixel displacements have been determined for all data sets, they are then converted into velocities by multiplying the displacements by the spatial resolution in units of meters per pixel (0.026924 mm/pixel) and the frames per second (90 fps). Velocities whose location coordinates within the image which were outside some vertical bounds, below 4.04 mm

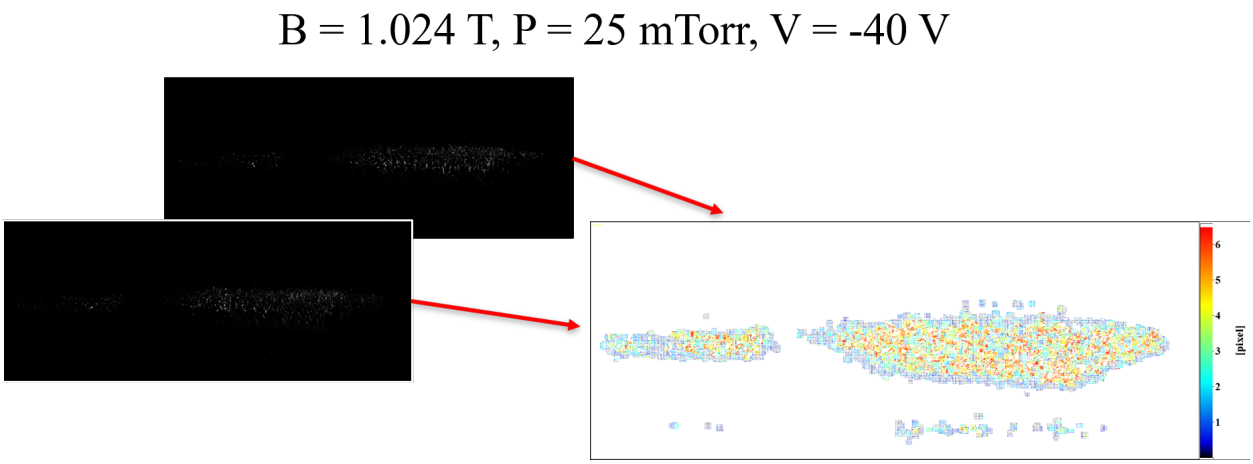

Figure 5-3 Example of PIV displacement vectors which are calculated from two consecutive video frames. The frames shown here were taken at B = 1.024 T, P = 25 mTorr, and an electrode bias of V = -40 V.

and above 16.15 mm, were removed as those regions fall outside the location of the dust cloud and are reflections or do not contain vectors with a non-zero value. Velocities within the vertical bounds which were identically zero were also removed as these represent displacements which are calculated in areas which did not contain any particles. Using the remaining valid velocities, a root mean square velocity was calculated at each spatial coordinate (i.e. interrogation cell) over the full 500-image sequence as:

$$v_{rms} = \sqrt{\frac{1}{n}\left(\left(v_{x1}^2 + v_{y1}^2\right) + \left(v_{x2}^2 + v_{y2}^2\right) + \cdots + \left(v_{xn}^2 + v_{yn}^2\right)\right)} \tag{5-1}$$

where n is the number of valid vectors at each spatial point.

By plotting the results of the v_{rms} calculations for each of the cases, various systematic changes become more apparent, the first set of which is shown in Figure 5-4. Within these plots the locations of the electrodes conducting bands are highlighted by the vertical grey bars. The location of the maximum v_{rms} within each plot is marked by a red x and a box 0.2 cm tall is

centered vertically according to that location. The purpose of this box will be to calculate an effective potential profile as will be discussed later in this section.

Figure 5-4 shows the first set of the v_{rms} results for an electrode bias of $V = -40$ V. This figure is organized into three columns representing the three neutral gas pressures which were used: $P = 25, 50, 75$ mTorr ($P = 3.33, 6.66, 10$ Pa) respectively. The rows display the data organized top to bottom by increasing magnetic field, $B = 0.0 - 3.08$ T. The first set of magnetic fields, $B = 0.0 - 0.77\,T$, is shown on one page, with the higher magnetic fields, $B = 1.02 - 3.08\,T$, continued on the following page.

Beginning with the first column, $P = 25$ mTorr (3.33 Pa), it is observed that when no magnetic field is present, $B = 0.0$ T, the cloud is fairly condensed vertically, and spread out horizontally beneath the electrode, with no preference for being positioned in the region of the electrodes conducting bands or holes. In the presence of magnetic field through, it is observed that the dust cloud separates into two bodies which are situated mainly beneath the holes of the "waffle" electrode. While the larger cloud on the right maintains its position in the center of the right hole of the electrode, the cloud on the left is observed to shift its equilibrium position from near the edge of the electrode to the center of the left hole as the magnetic field increases. It is believed that this observation may be due to the increasing confinement potential which develops in both holes due to the magnetic field. The organization and confinement seen here would suggest that the previously observed imposed ordered structures that are reported in Chapter 2 and Chapter 3 may be due to particles becoming trapped in the hole regions. The benefit of this experiment is that the large electrode now provides a method to observe the particle clouds on a macroscopic scale instead of individual particles.

As the magnetic field increases above 1 T several trends from the low magnetic field data continues and several new trends begin to appear. At 1.02 T the 25 mTorr case, in the left column, appears much the same as the last few rows from Figure 5-4. As the magnetic field increases though a new observation is made. Beginning at 1.28 T the center of the dust cloud on the right shows a decrease in the root mean square velocity near the center of the cloud, at the mid-point between the conducting bands. With further increasing magnetic field, 1.54 T and above, the cloud in this region fully separates into two clouds which sit just at the edges of the conducting bands. Starting at 2.05 T the left cloud also begins to become unstable and fragmented as the reduced number of confined particles makes it difficult to define a definite cloud boundary. Eventually, at 3.07 T magnetic field, the dust particles are still confined to the region beneath the hole, but they do not the appearance of a singular collective cloud. The few particles which are still confined at this high magnetic field also appear to be able to transition back towards the center of the hole.

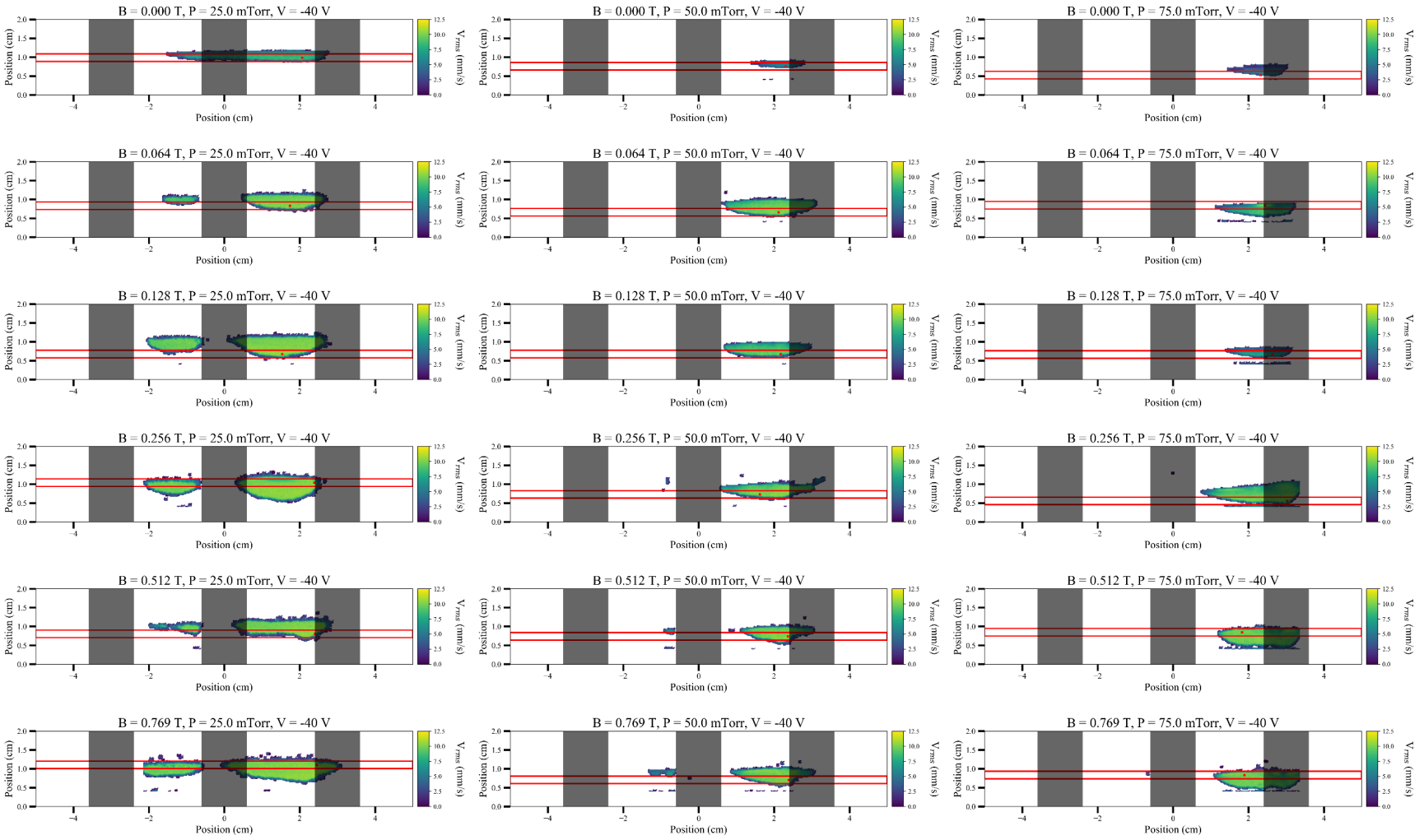

Figure 5-4 Root mean square velocities - Electrode Bias V = -40 V. Each of the three columns shows data at one of three pressures: 25, 50, or 75 mTorr. Each row shows increasing magnetic field from top to bottom (B = 0 – 0.77 T).

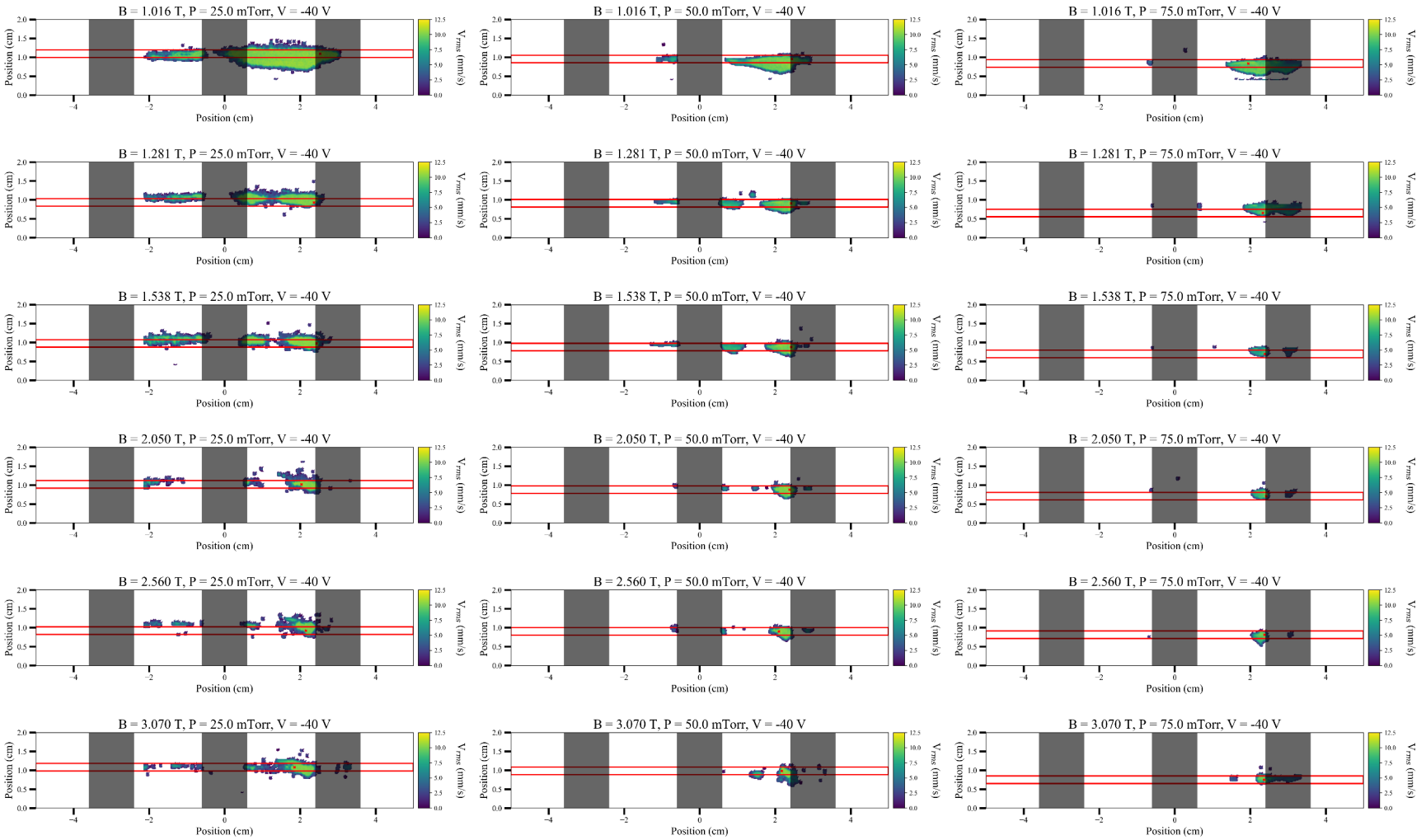

Continuation of Figure 5-4 Root mean square velocity - Electrode bias V = -40 V. Columns show data from one of three neutral pressures: 25, 50, or 75 mTorr. Continuing from the previous figure, rows display magnetic field strengths from top to bottom (B = 1.02 – 3.07 T).

Within Figure 5-4, two other neutral pressure conditions are also shown. At $P = 50$ mTorr (6.67 Pa), the cloud is observed to be much smaller than at $P = 25$ mTorr (3.33 Pa) at $B = 0.0$ T. This could be attributed to the fact that at the high neutral pressure the cloud is compressed due to a higher number of neutral collisions, also evident by the decreased v_{rms}. Looking down the $P = 50$ mTorr (6.67 Pa) column, it is also observed that the cloud becomes more energetic as the magnetic field increases. Also occurring as the magnetic field increases, this column also begins to develop a second smaller dust cloud confined beneath the left hole of the electrode, from $B = 0.26 - 0.77$ T. This second cloud is qualitatively consistent with the one observed at $P = 25$ mTorr (3.33 Pa), but the higher neutral pressure appears to reduce the confinement. The additional cloud is also smaller and has lower velocities than the lower pressure case, which matches the observations made for the $B = 0.0$ T scenario.

At higher magnetic fields similar trends to the 25 mTorr (3.33 Pa) case can observed in the 50 mTorr (6.67 Pa) data. The left most cloud, which began developing at around 0.51 T, continues to grow in size until 1.28 T. At this point the left cloud reaches its maximum size and the bifurcation of the confining potential begins to become the dominant component. As the edge confining potential develops the left cloud reduces in size, until disappearing altogether at 3.07 T. The bifurcation of the right dust cloud is also observed, just as it was 25 mTorr (3.33 Pa). This bifurcation appears in these data sets at the same magnetic field, 1.28 T, but is observed as a much more definitive split at this magnetic field. At higher magnetic fields, up to 2.56 T, it is again observed that the cloud reduces in size with the cloud positions becoming more focused near the edges of the conductor, with the cloud closer to the center of the electrode almost disappearing completely. At 3.07 T, however, there is a reemergence of a small cloud just near the center of the

hole, which may be related to the transition of particle back to the center of the hole at 25 mTorr (3.33 Pa).

When examining the third column, $P = 75$ mTorr (10 Pa), the effect of the increased neutral pressure causing a decrease in the size and energy of the cloud is continued. When looking down the rows of the column, the 75 mTorr (10 Pa) data never shows the development of a second cloud as the magnetic field increases, unlike the 25 mTorr and 50 mTorr (3.33, 6.67, 10 Pa) columns. At 75 mTorr (10 Pa), the cloud also appears to maintain its position relative to the "waffle" electrode, showing no significant evidence of a confining potential developing in the hole of the electrode; the cloud is only confined by the radial electric fields from the confining ring present in the experiment. The cloud under these conditions does appear to become more energetic though, and has an increased vertical range, as the magnetic field increases. This is likely due to the fact that, while the ions would not be considered magnetized at these conditions, they prefer to flow along magnetic axis and just provide a driving force for the increased vertical motion observed at each of the three neutral pressures.

At $P = 75$ mTorr (10 Pa), in the right most column, the cloud continues to reduce in size with increasing magnetic field. Any possible confining potential resulting from the imposed, ordered structures does not appear until around 1.56 T. At this magnetic field the cloud is reduced to a size which is comparable to the other neutral pressure cases, appearing to be confined to the inside edge of the electrode. This behavior continues as the magnetic field increases, until 3.07 T, where the cloud appears beneath the conducting band again.

When looking at this data set as a whole, the development of multiple modes of the imposed, ordered structure appear to develop as the magnetic field increases. When the magnetic field is present, but still low ($B < 1.28$ T), the first mode is characterized by an initial bifurcation

of the dust cloud, observed as confinement within the holes of the electrode. Speculation would suggest that the plasma sheath around the electrode has only just begun to extend into the plasma, providing a larger confining structure. There is supported somewhat by the observations from Chapter 4 in which effective potentials are presented which would be confining to the negatively charged dust particles. Those measurements are made several centimeters above the vertical location of the dust particles and would observe those potentials developing at lower magnetic fields, when the sheath structure has not extended into the plasma as far.

As the magnetic field increases $(1.28\ \mathrm{T} \leq B < 3.07\ \mathrm{T})$ a new mode develops in the background plasma in which multiple trapping regions become apparent in the holes of the electrode. These smaller potentials are more focused near the edges of the conducting bands and can be attributed to a sharper edge to the plasma sheath around the electrode, which extends even further into the plasma. Finally, a third mode is observed at the highest magnetic field, $B = 3.07$ T. In this mode the confining potential structures near the edges have reduced in size even further, allowing for a third confining potential in the center to develop. In the 25 mTorr case, the particles still have high enough velocities that they are possibly able to move between these multiple potentials, but at 50 mTorr the central potential can be clearly seen on the right.

The development of these modes, especially the third confining potential at $B = 3.07$ T, is very reminiscent of the plasma filamentation phenomenon discussed previously in Chapter 3 and Chapter 4. The fact that these trapping potentials appear to change in similar manner, lends support to the idea that the imposed, ordered structure phenomenon and the plasma filamentation phenomenon are a result of similar, if not the same, underlying physical process.

The data sets which were performed at an electrode bias of $V = +40$ V are shown in Figure 5-5. The root mean square velocities are plotted in the same way as for the -40 V data, with each

figure containing three columns corresponding to the three neutral pressures, 25, 50, and 75 mTorr (3.33, 6.67, and 10 Pa), and each figure representing a different range of magnetic fields. When examining the 25 mTorr (3.33 Pa) data in Figure 5-5, the dust cloud behaves very much like the 25 mTorr data at -40V. When there is no magnetic field, the cloud does not have much vertical range and is extended horizontally beneath the grid electrode under both the conducting bands and the holes. In the presence of the magnetic field, the dust cloud separates into two clouds which are centered beneath the holes of the electrode. The cloud also increases its vertical extent and overall v_{rms} in the bulk of the cloud.

As the magnetic field increases further ($B \geq 1.02$ T) the behavior of the dust cloud begins to exhibit different behavior from its -40 V counterpart. The dust cloud does not appear to show the same development of the different modes in the imposed, ordered structures. When looking at the dust cloud beneath the right hole at $B = 1.28$ T, the vertical extent of the cloud does decrease at the center of the hole, but the cloud does not fully bifurcate as the magnetic field continues to increase. At very high magnetic fields, $B \geq 2.56$ T, the cloud does become unstable, which may indicate that the plasma is in the process of changing modes. It is most likely that the pressure here is too low for the neutral gas atoms to stabilize the particles and make confinement possible.

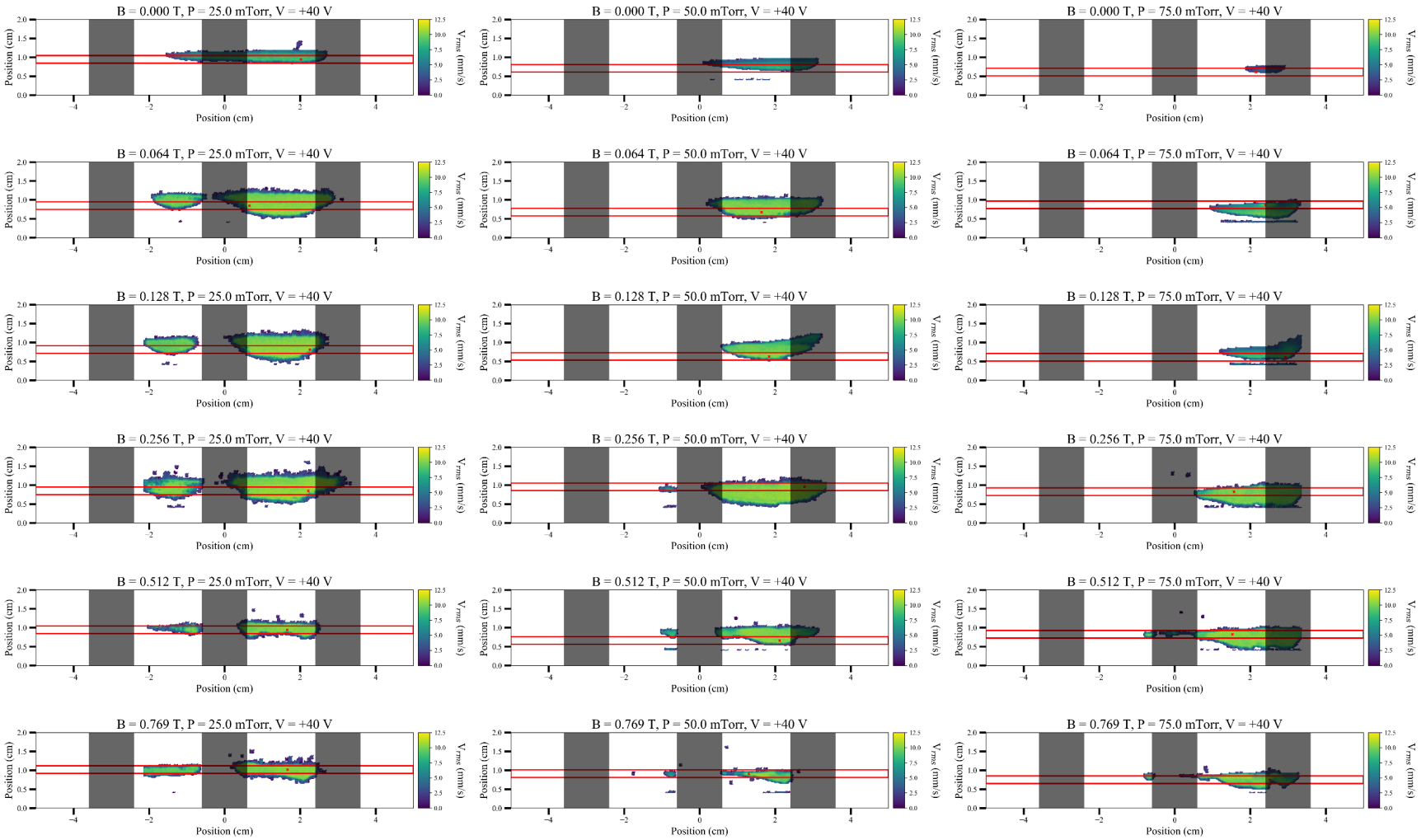

Figure 5-5 Root mean square velocities- Electrode Bias V = +40 V. Each of the three columns shows data at one of three pressures: 25, 50, or 75 mTorr. Each row shows increasing magnetic field from top to bottom (B = 0 – 0.77 T).

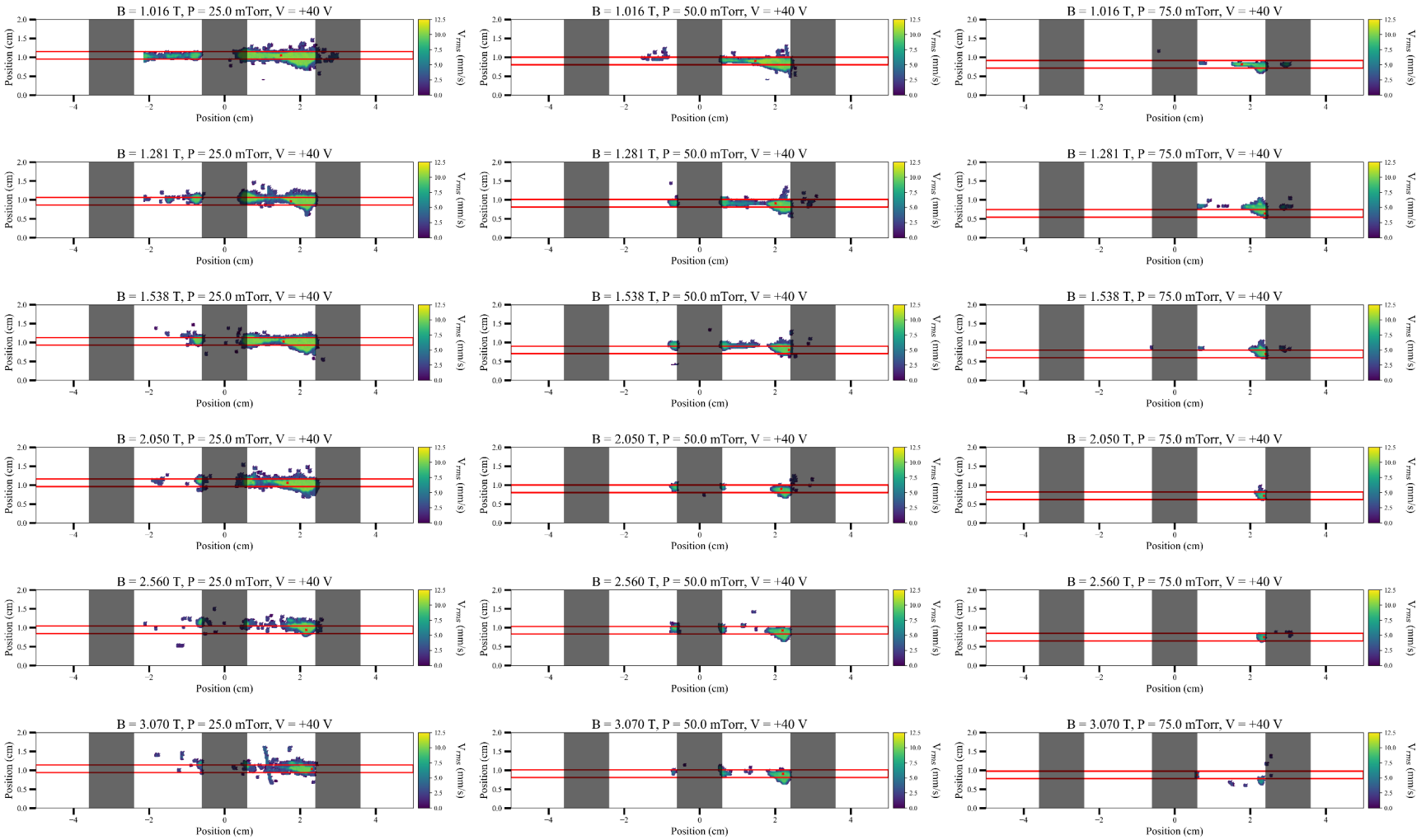

Continuation of Figure 5-5 Root mean square velocities- Electrode bias V = +40 V. Columns show data from one of three neutral pressures: 25, 50, or 75 mTorr. Continuing from the previous figure, rows display magnetic field strengths from top to bottom (B = 1.02 – 3.07 T).

At 50 mTorr (6.67 Pa) the +40 V data continues to behave very similarly to the -40 V data at low magnetic fields. It is initially a small thin cloud when there is no magnetic field, developing a much larger vertical extent and higher root mean square velocities as the magnetic field increases. A small cloud also develops and becomes trapped beneath the left hole, like in the -40 V data. This trend continues up to $B = 1.02\text{T}$ in the continuation of Figure 5-5. At $B = 1.28$ T, the cloud becomes unstable, much like in the 25 mTorr (3.33 Pa), +40 V data set, as the next mode of the imposed, ordered structure develops. Unlike the 25 mTorr case, this second mode is observable at 50 mTorr (6.67 Pa). Between 1.54 T and 2.56 T, there are multiple clouds observed, one on the left and two on the right, that appear relatively stable near the edges of the electrode. Finally, at $B = 3.07$ T, the plasma is found to be able to support multiple clouds beneath the right most hole, indicating that the third imposed, ordered structure mode is present.

The last column at +40 V, the $P = 75$ mTorr (10 Pa) data on the right, also continues similar behavior to the -40 V data up through $B = 0.26$ T. There is a small dust cloud in the absence of the magnetic field, and when the field is present the cloud shows no indication of shifting its position towards the center of the electrode hole. Even so, the dust particles within the cloud develop show an overall increased v_{rms}, and a larger vertical extent. Beginning at 0.26 T, a much larger fraction of the cloud is positioned beneath the hole, and at 0.51 T a small cloud near the inner edge of the left hole is observed, meaning that the imposed, ordered structure does begin to appear much earlier at +40 V than it did at -40 V, appearing the field was above 1.02 T. This structure is not sustained for very high magnetic fields. The cloud is already observed to have diminished in size at 1.02 T, though there may be some presence of the second mode. Smaller clouds can be seen at 75 mTorr (10 Pa) near the edges of the hole up through 1.54 T. Above this,

$B = 2.05 - 3.07$ T, the plasma is too unstable to support a larger cloud and only a few particles are observed to be trapped near the edges of the electrode.

Overall, the two data sets of the electrode bias at $V = -40$ V and $V = +40$ V, share many similarities. The development of at least two different imposed, ordered structure modes with increasing magnetic field are observed, and possibly a third at very high magnetic fields. These modes do not always develop at the same conditions though, with new modes developing at lower magnetic fields for the +40 V data. The locations of the dust particles at both electrode biases is also consistent with the particle locations which were predicted from the results in Chapter 4.

As was mentioned previously, each of the v_{rms} plots in the last several figures contain a red box, 0.2 cm tall, which is centered vertically at the position of the maximum v_{rms}. Within this box the root mean square velocities will be averaged in the vertical *y*-direction to produce one-dimensional v_{rms} profiles. These profiles can then be used to calculate an effective electric potential by applying the conservation of energy:

$$\frac{1}{2} m_d v_{rms}(x)^2 = \frac{1}{2} m_d v_0^2 - q_d \phi(x) \tag{5-2}$$

where m_d is the dust mass, v_0 is the maximum root mean square velocity, q_d is the dust charge, and ϕ is the electric potential. This equation can then be rearranged to the form:

$$\phi(x) = \frac{1}{2} \frac{m_d}{q_d} (v_0^2 - v_{rms}(x)^2) \tag{5-3}$$

from which the electric potential will be calculated. For the 8 ± 0.8 μm diameter silica particles used in this experiment $m_d \cong (5.9 \pm 1.0) \times 10^{-13}$ kg based on a density of silica of 2200 kg/m^3. For the purposes of these calculations it is assumed that the OML estimate of the particle charge,

which was detailed in Section 1.1, will remain relatively constant with increasing magnetic field as the electron temperature is also assumed to be constant at higher magnetic fields. It is believed that this is a reasonable assumption since the particles remain levitated within the plasma under all conditions from $B = 0.0 - 3.07$ T. The dust charge for each data set is determined using the electron temperature for the $B = 0.0$ T case for a given combination of neutral pressure and electrode bias. The resulting average dust charge number, Z_d, for these combinations are used in the determination of the effective electric potential and are provided in Table 3.

Additionally, when estimating the effective potential, it has been assumed that the dust particles are trapped by an electrostatic well and that the depth of the well will be determined by the average kinetic energy of the particles. It is acknowledged that this calculation does not include neutral drag or ion drag effects. The ion drag, in particular, does not have a well-defined mathematical form in a magnetized plasma and continues to be a subject of discussion within the field. The neutral drag, as a dissipative force, could lead to an increase in the value of the effective potential, but it would do so for all cases considered here. Therefore, the resulting calculations of the effective potential should be considered qualitatively as a means to provide insight into how the particles may become trapped in the plasma.

Table 3 Table of average number of electron charges, Zd, on the dust grains calculated from the measured electron temperatures at $B = 0.0$ T.

	25 mTorr	50 mTorr	75 mTorr
-40 V	21,510 ± 2,400	21,140 ± 2,660	19,970 ± 2,540
+40 V	20,720 ± 2,260	20,900 ± 2,450	20,140 ± 2,520

Figure 5-6 shows the effective electric potentials for an electrode bias of -40V calculated from the v_{rms} plots in Figure 5-4. At a glance each of the columns shows behaves consistently with the analysis on the v_{rms} plots. When no magnetic field is present, the 25 mTorr (3.33 Pa) data shows a broad potential which extends beneath both the conducting bands and holes of the "waffle" electrode. As the magnetic field increases the relative strength of the potential also increases. From $B = 0.06$ T to 1.02 T, the electric potential increases slightly overall, and the potential profile broadens with increasing magnetic field. Additionally, a second peak beneath the hole on the left also develops and increases with magnetic field. As the profile broadens, the peak potential stays relatively uniform, with the profiles taking on plateau appearance. This results in slopes on the edges of the potential becoming sharper with the magnetic field. These steep slopes are reminiscent of the formation of a sheath-like potential near the boundaries of an electrode.

For the low magnetic field data at 25 mTorr (3.33 Pa), one case does not appear to fully follow this trend, the 0.51 T case. When examining this same data set in Figure 5-4, it should be noted where the region which is used to determine the profile is taken from. The peak v_{rms} is located in a small pocket of the cloud which sits lower than the overall center of the cloud. This causes the profile region to sample velocities which are on the bottom edge of the cloud instead of through the center, resulting in a decreasing average v_{rms} profile, and thus a decreased effective potential profile. Had the profile region been slightly higher, the same plateau effect would likely have been found.

At higher magnetic fields, $B \geq 1.28$ T, the potential profile begins to develop two potentials which are located closer to the inner edges of the electrode hole. These peaks show similarly steep slopes beneath the conducting sections of the electrode, but also at the center of the hole. For the highest magnetic fields, $B = 2.56 - 3.07$ T, only a single confining peak is observed.

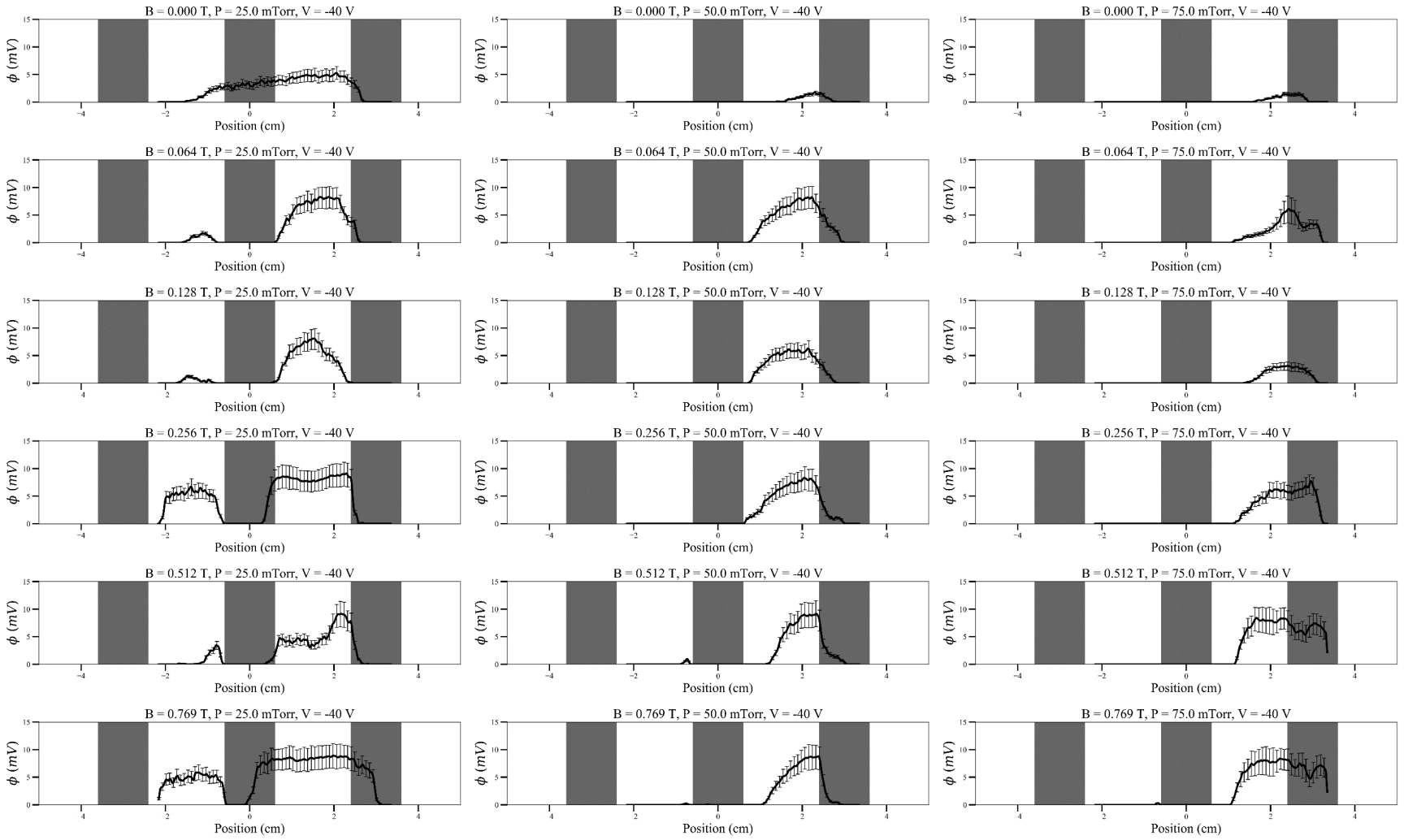

Figure 5-6 Series of plots of the effective electric potential calculated from the v_{rms} plots in Figure 5-4. Electrode bias $V = -40$ V. Columns are those data sets at 25, 50, and 75 mTorr (left to right). Rows show increasing magnetic fields from $B = 0.0$ T to $B = 0.77$ T.

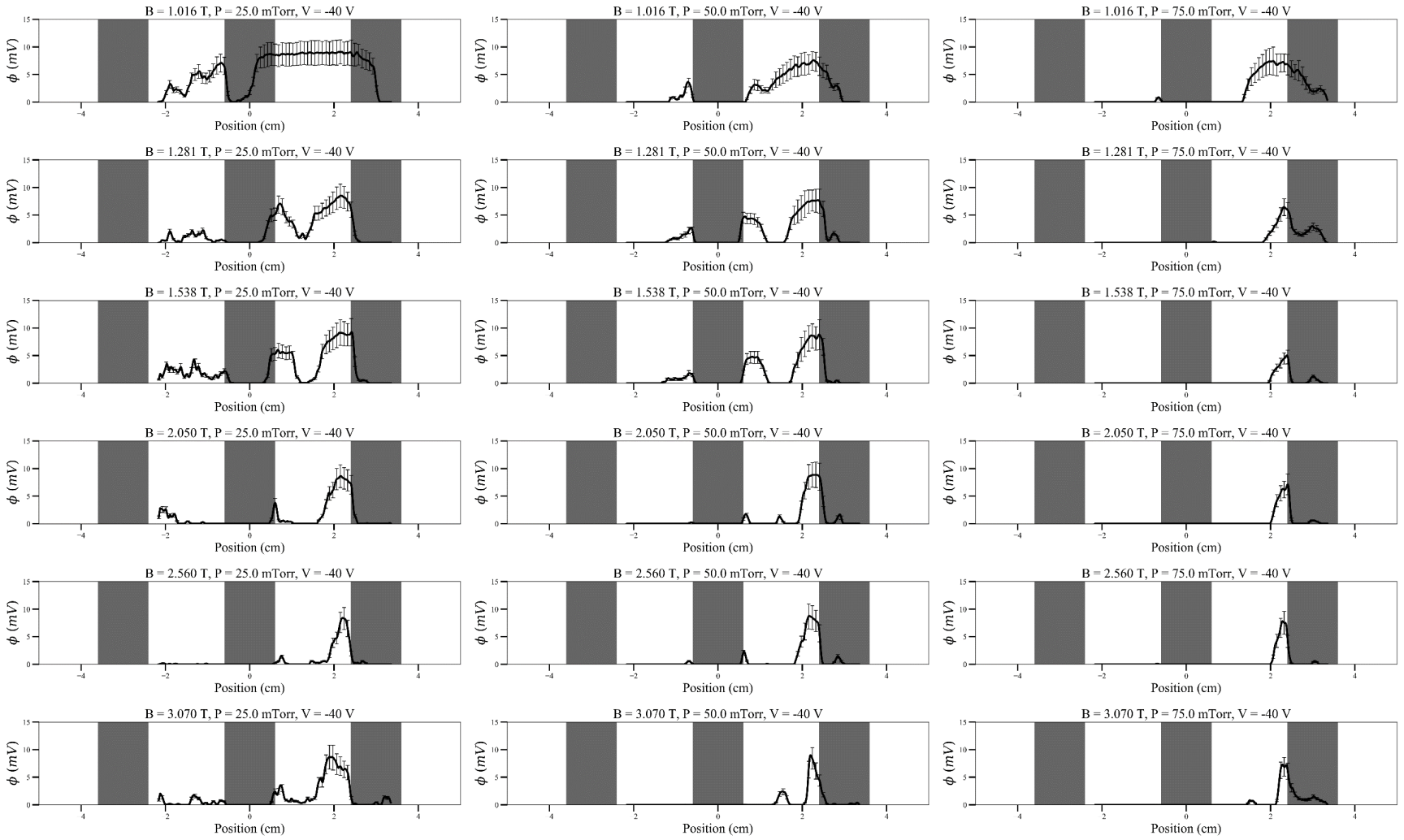

Continuation of Figure 5-6 Series of plots of the effective electric potential calculated from the v_{rms} plots in Figure 5-4. Electrode bias $V = -40$ V. Columns are those data sets at 25, 50, and 75 mTorr (left to right). Rows continue from the previous figure, showing increasing magnetic fields from $B = 1.016$ T to $B = 3.07$ T.

For all the potential profiles though the maximum effective potential is rather alike, ranging between 8.5 – 9.5 mV.

For the data at 50 mTorr (6.67 Pa), a similar situation is found. The effective potential at 0.0 T is negligible. As the magnetic field increases the potential at the boundary between the hole and the electrode becomes increasingly steeper as well. The left side of the potential peak has a gentler slope which slowly extend further into the hole at higher magnetic field. The peak of the potential does not move far from its position just inside the hole though. This may indicate that the central region has become more attractive to the dust particles, but the background confinement from the bottom electrode sheath and confining ring is still dominant. At 1.28 T the mode change of the imposed, ordered structure is observed though. Here the two potential peaks are found just inside the hole on the right. For higher magnetic fields, $B \geq 2.05$ T, only a single peak in observed though, resulting primarily from the poor capability to confine dust particles at these fields in general. At 3.07 T, a small peak is observed at the center of the hole, which may be a result of the changing modes of the imposed, order structure discussed previously. The data at 50 mTorr (6.67 Pa) also showed a slightly lower range of peak effective potential compared to the 25 mTorr data (3.33 Pa), which fluctuated from 6.1 – 9.2 mV, not including the 0.0 T case which had a peak potential of only 1.7 mV.

In the rightmost column the 75 mTorr (10 Pa) data behaves similarly to the 50 mTorr (6.67 Pa) data at low magnetic fields. At 0.0 T the potential appears as a small singular peak, where the peak potential increases as the magnetic field also increases. The potential strength does not grow quite as quickly as the 50 mTorr (6.67 Pa) data though. Unlike the central column, the 75 mTorr (10 Pa) data does not show evidence of its central peak shifting towards the center of the hole. The cloud maintains its position relative to the grid, with just the potential increasing; a behavior which

continues through a magnetic field of 1.02 T. This potential increase is only associated with an increasing v_{rms} within the cloud. This would suggest that there are two different effects occurring across the data set. The first is the confining structure which concentrates the dust clouds beneath the holes. The second is the increase in particle velocities, mostly observed in the vertical direction along the magnetic axis, which contributes primarily to the strength of the potential. Speculation would suggest that this may be caused by an increased momentum transfer from the ions as their preference to flow along the magnetic field increases. So, at low magnetic fields, the 75 mTorr (10 Pa) data shows that the background plasma effects which are producing higher particle velocities are present but without the indicators of particle confinement.

At higher magnetic fields, 1.28 and 1.54 T, the potential decreases in magnitude and appears to show signs of decreasing its width as well, becoming more focused near the inner edge of the electrode. This change is fully observed at $B \geq 2.05$ T, where the potential has only one localized confining peak at the edge. This means that even at the low pressures, a strong enough magnetitic field can still produce the confining potentials associated with the imposed, ordered structures. The potential strength of the 75 mTorr (10 Pa) data was lowest at $B = 0.0$ T, with a peak potential of 1.5 mV. It was at its highest at 0.51 and 0.77 T with a peak of 8.4 mV. Otherwise the peak potential ranged from 3.1 – 7.8 mV, which is consistent with the observation that the overall strength of the potential decreases as the neutral pressure increases.

Potential profiles are also calculated for the data at an electrode bias of +40 V. These results are shown in Figure 5-7 and its continuation on the following page. Beginning with the 25 mTorr (3.33 Pa) data in left column, a similar broad potential profile can be seen like the one in the -40 V data. Once the magnetic field is present though the data shows a much more drastic response. The potential develops a plateau appearance almost immediately beneath the hole on the right,

with another clear peak beneath the left hole. The potential beneath the right hole remains at a relatively stable maximum plateau value, with the sloped edges beneath the conducting bands of the electrode becoming increasingly steeper from 0.06 T to 0.77 T. This would suggest that the same sheath potential that was apparent near the inner edges of the electrode at -40 V is also present here. The effect is much stronger though when the positive bias is applied to the electrode.

Beginning at around 1.02 T, the potential which had developed on the left side of the electrode has become degraded, and the potential on the right shows evidence of a small depression near the center. This continues through 1.54 and 2.05 T, with the left potential becoming quite narrow and limited to the inner edge of the electrode, decreasing in strength with increasing magnetic field. The depression on the right becomes more prominent, but does not fully separate the potential into two distinct plateaus as was observed for similar conditions at -40 V. It may be that the particles here maintained high enough velocities to overcome the potential barrier between the two halves and flow between the two confining regions. At the highest magnetic fields, 2.56 and 3.07 T, the potential on the left has completely vanished as it was no longer possible to maintaining a dust cloud in that location. The potential on the right becomes much narrower and is limited to more or less to a single peak just inside the inner edge of the electrode. For the data at 25 mTorr, the potential is at its lowest at 0.0 T with peak at 5.6 mV. Between 0.06 and 1.54 the potential maintains consistently high peak between 9.0 to 10.2 mV, a higher range than at -40 V, and decreases slightly beginning at 2.05 T to a peak of 7.9 mV at 3.07 T.

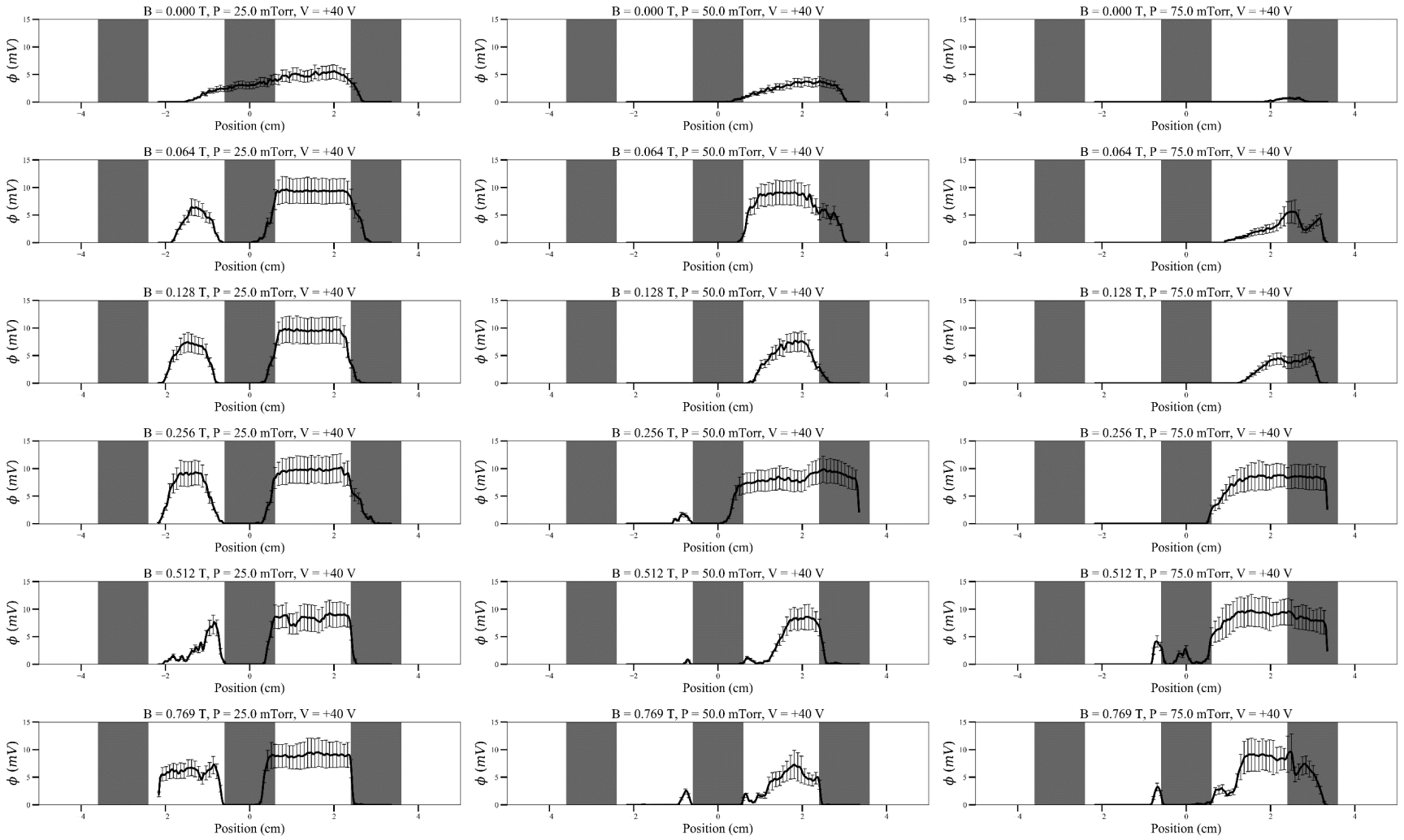

Figure 5-7 Series of plots of the effective electric potential calculated from the v_{rms} plots in Figure 5-5. Electrode bias $V = +40$ V. Columns are those data sets at 25, 50, and 75 mTorr (left to right). Rows show increasing magnetic fields from $B = 0.0$ T to $B = 0.77$ T.

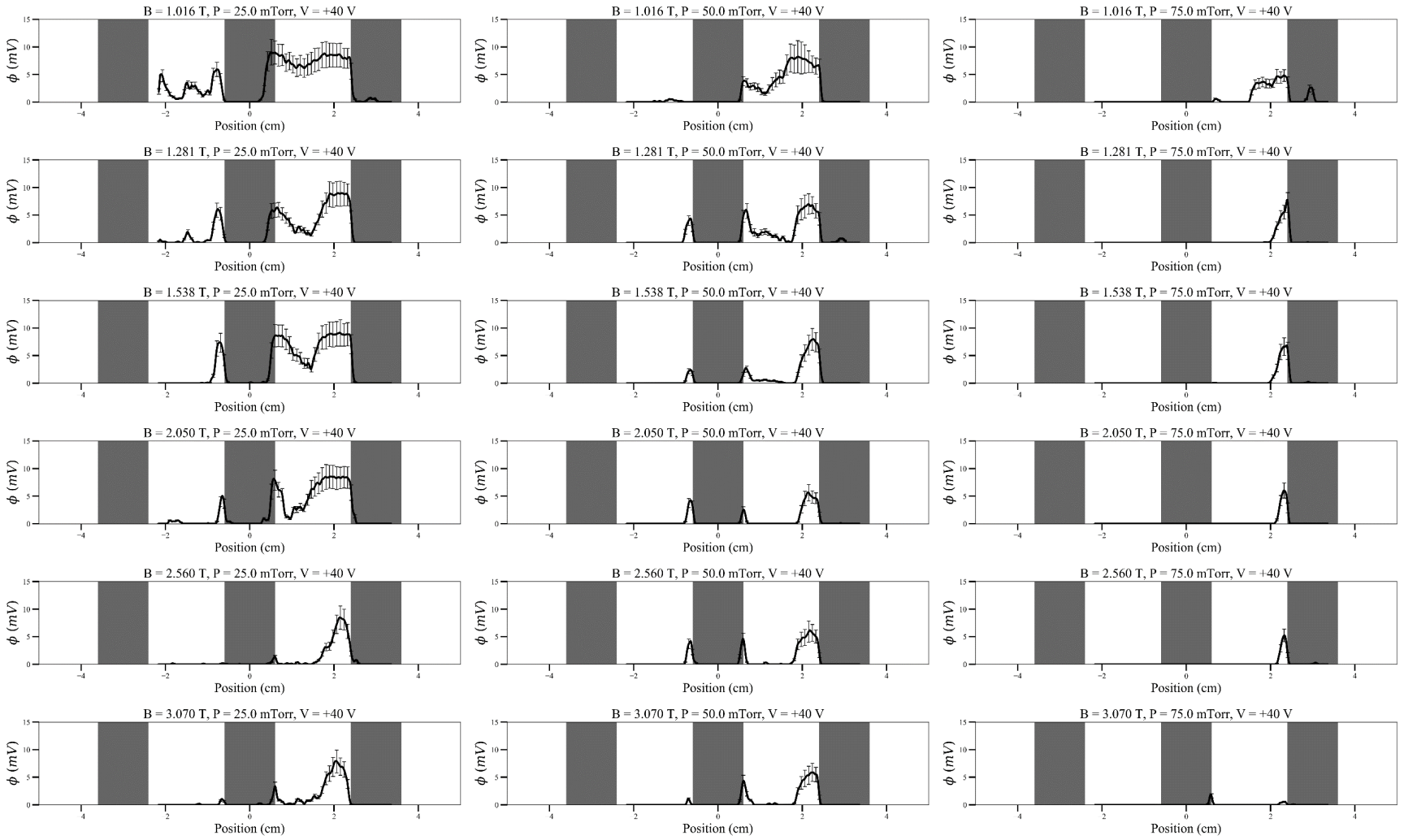

Continuation of Figure 5-7 Series of plots of the effective electric potential calculated from the v_{rms} plots in Figure 5-5. Electrode bias $V = +40$ V. Columns are those data sets at 25, 50, and 75 mTorr (left to right). Rows continue from the previous figure, showing increasing magnetic fields from $B = 1.016$ T to $B = 3.07$ T.

Continuing with the 50 mTorr data, a higher, broader potential profile is found at an electrode bias of +40 V than was the case when that bias was -40 V The peak potential increases some with magnetic field, and the potential profile is shown to become broader was well. A slight decrease in the profile width is seen going from 0.06 T to 0.13 T, but when the plots of v_{rms} are examined in Figure 5-5, it is found that the sampling region is located towards the lower portion of the dust cloud which is narrower. This same effect is also seen for the 0.51 T case. Much like the 25 mTorr data, these low magnetic field cases show an increasingly steeper slope on the edges of the potential profile when extend beneath the conducting bands. Between 0.77 and 1.02 T the potential structure is observed to deteriorate slightly.

At higher magnetic fields, $B \geq 1.28$ T, the potential has transitioned to a two peak structure much in the same way that the 25 mTorr data did. Here though, the two peaks are located slightly further apart and have a slightly lower peak potential. At 1.28 T, a third peak at the inner edge of the left hole has also developed. As the magnetic field increases to 3.07 T, these peaks maintain their separation and decrease in magnitude. The lowest peak potential of 3.8 mV occurs at 0.0 T for the 50 mTorr data, much like at -40 V, but this peak is much higher. The potential has its highest peaks between 0.06 T and 0.26 T, ranging from 7.7 – 9.9 mV. These peaks occur over a smaller range than the 25 mTorr data, but are higher than the comparable case at -40 V. The peak potential trends downward with increasing magnetic field, only ranging from 5.7 – 6.2 mV for magnetic fields between 2.05 – 3.07 T, which is lower than at -40 V.

Finally, at 75 mTorr in rightmost column, the potential at $B = 0.0$ T appears very similar to the potential at -40 V. Here a sudden potential increase still occurs at 0.06 T, and continues to increase through 0.77 T. This rise in the peak potential occurs much slower for the 75 mTorr data than for either of the lower pressure data sets though. The potential also exhibits the plateau

shaping as the lower pressures between the magnetic fields of 0.26 T to 0.77 T. However, the slopes of the potential on the edges, beneath the conducting bands, are not as steep in this magnetic field range. The potential is observed to extend into the right hole much further than when the electrode bias was at -40 V, which is consistent with the effect of the imposed, ordered structures being stronger at for the positive bias.

As the magnetic field continues to increase the peak potential begins to decrease. At 1.02 T, the peak potential drops by roughly half, and becomes narrower. From 1.28 T to 2.56 T the potential is only observed as a singular narrow peak at the inner edge of the right hole. These peaks are both narrower and lower than the peaks at 25 or 50 mTorr (3.33 or 6.67 Pa), and no secondary peaks are observed at any magnetic field. Eventually the peak disappears completely at 3.07 T. The smallest potential peaks, 0.8 mV and 1.9 mV, occur at the extremes of the magnetic field range, 0.0 T and 3.07 T respectively. The peak potential increases with magnetic field to a range of 8.8 – 9.8 mV with the magnetic field range of 0.26 – 0.77 T. Beyond these field strengths the peak potential trends downward between 0.77 – 2.56 T, over a range of 7.8 – 5.2 mV. Like the 25 and 50 mTorr (3.33 and 6.67 Pa) cases, this range is lower than the comparable case at -40 V.

Through this analysis a method for determining effective electric potentials through observations of dust particle dynamics has been presented. These effective potentials are shown to be confining to negatively charged dust particles, with the capacity of those potentials to confine dust particles changing with neutral pressure, magnetic field, and bias potential on the “waffle” electrode. Among all cases the potentials show a decreased magnitude as the neutral pressure changes. With magnetic field, the effective potentials develop various confining profiles with multiple modes of confinement presenting themselves at higher and higher magnetic fields. For the two electrode biases, the negative bias, -40 V, exhibits slightly smaller peak potentials on

average across the various other parameters. However, these peak potentials are more consistent than for the +40 V bias, which exhibits a larger swing between the peak potentials at low magnetic fields to high magnetic fields.

5.4 Discussion of Potential Profiles

The goal of this section will be to discuss a comparison between the primary results of the previous section, the effective potential profiles calculated from the PIV vector measurements, with the primary results of Chapter 4, effective electric potential profiles calculated from measurements of the electron density and measurements of the electric field. Through an examination of these effective electric potentials, which were determined through three independent methods, new insights into the development of the imposed, ordered structures.

A common set of plasma conditions was only recorded for a neutral pressure of 25 mTorr, and so all data presented in this section will be at that pressure. Data sets were recorded for "waffle" electrode biases of -40 V and +40 V. Experiments were also performed for a common set of magnetic fields which ranged from $B = 0.0 - 3.07$ T.

The three different types of diagnostic schemes which are under examination, the double probe, the ring probe, and dust velocities, were each performed at different vertical positions relative to the "waffle" electrode. The double probe and ring probe were much closer to the "waffle" electrode, as they were stepped through the plasma along an axis which was very near to the vertical center of the plasma generating electrodes. The double probe was 2.2 cm (0.88") below the "waffle" electrode, and the ring probe was 2.9 cm (1.13") below the "waffle" electrode. Dust clouds levitated between 0.5-1.5 cm (0.2-0.6") above the lower electrode putting them 6.8-7.8 cm (2.4-3") below the "waffle" electrode. Because the various methods for determining these effective

electric potentials produced results which varied over several orders of magnitude, the effective potentials will be normalized within the comparison plots. The normalization will be determined by the maximum of the absolute value of the effective potential within the range of $x = -5$ cm to $x = 5$ cm. Maximum potential values which were used for normalization are provided in Table 4 and Table 5 for electrode bias values of -40 V and +40 V respectively.

Special attention should also be drawn to the fact that each of the methodologies which were used to determine the effective electric potentials has an unknown factor associated with it. These factors were systematically worked around in order to determine the effective potentials. Calculations performed on the double Langmuir probe measurements did not have a true

Table 4 Values of the maximum electric potential magnitudes for an electrode bias of -40 V. These potential values are used for data normalization within the plots of Figure 5-8.

	Double Probe (V)	Ring Probe (V)	Dust (mV)
0.00 T	0.39	0.01	5.29
0.06 T	27.72	0.97	8.27
0.13 T	106.75	1.86	8.10
0.26 T	199.15	0.64	9.11
0.51 T	94.75	0.35	9.15
0.77 T	61.46	0.73	8.91
1.02 T	90.51	0.59	9.11
1.28 T	94.45	0.38	8.52
1.54 T	88.31	0.47	9.28
2.05 T	82.01	0.80	8.64
2.56 T	63.16	0.85	8.39
3.07 T	54.25	1.22	8.65

knowledge of the ion density within the plasma, and so had to use fits of the electron densities as an approximation. The ring probe similarly had to determine background electric fields. Also, neither of those probe diagnostics account for the modified sheath dynamics which occur at high magnetic fields. Finally, the dust particles have an unknown charge. While the particles must be charged to levitate in the plasma, the charging process is known to be drastically modified by the magnetic fields, and so the OML calculated values which were used are likely much higher than they truly are. [27] With these facts in mind, the comparison presented here is a qualitative one only.

Table 5 Values of the maximum electric potential magnitudes for an electrode bias of +40 V. These potential values are used for data normalization within the plots of Figure 5-8.

	Double Probe (V)	Ring Probe (V)	Dust (mV)
0.00 T	0.41	0.00	5.62
0.06 T	80.01	2.24	9.66
0.13 T	159.97	3.90	9.81
0.26 T	252.40	1.57	10.22
0.51 T	124.35	1.52	9.23
0.77 T	94.80	1.31	9.54
1.02 T	79.68	1.45	9.05
1.28 T	57.12	0.60	9.00
1.54 T	56.84	0.74	9.14
2.05 T	35.66	0.59	8.57
2.56 T	25.03	1.02	8.47
3.07 T	33.86	0.71	7.94

The first set of plots showing a comparison of the effective potential profiles is shown in Figure 5-8, continued over two pages. This figure presents the effective electric potentials for an electrode bias of -40 V, and a magnetic field range of $B = 0.0 - 3.07$ T. When no magnetic field is present the data does not show any strong correlation, but none of the three methods showed evidence of any ordered structure when being analyzed previously in this dissertation. As the magnetic fields increases, certain correlations can be found. The effective electric potentials show several peaks whose central positions line up with each other. These correlations appear at many of the electric fields and between various combinations of the three methods. The double probe and dust methods show the greatest number of these shared peak positions. Corresponding peaks between the dust velocity method and the double probe method are found beneath the center of the right hole at 0.06 – 0.51 T, and beneath the left hole from 0.06 – 1.02 T and 2.05 T. At high magnetic fields the two methods even show evidence of a multiple peak structure with peaks at the inner edge of the right hole from 1.54 – 3.07 T.

The ring probe method results are also found to correspond between these other two cases. The ring probe and double probe measurements correlate nicely beneath the right hole at 0.51 – 1.02 T and 2.56 – 3.07 T, and beneath the left hole at 1.02 T and 3.07 T. Additionally, the ring probe and dust velocity measurements can be found to behave similarly beneath the left hole from 0.77 – 1.28 T, or beneath the right hole from 0.25 – 0.51 T and 1.28 – 3.07 T. Overall, there is strong indication that the structure observed in each of these effective potential profiles is the same structure present in the background plasma. It can also be shown that the correlation between the different experimental methods is not only limited to just the -40 V bias data.

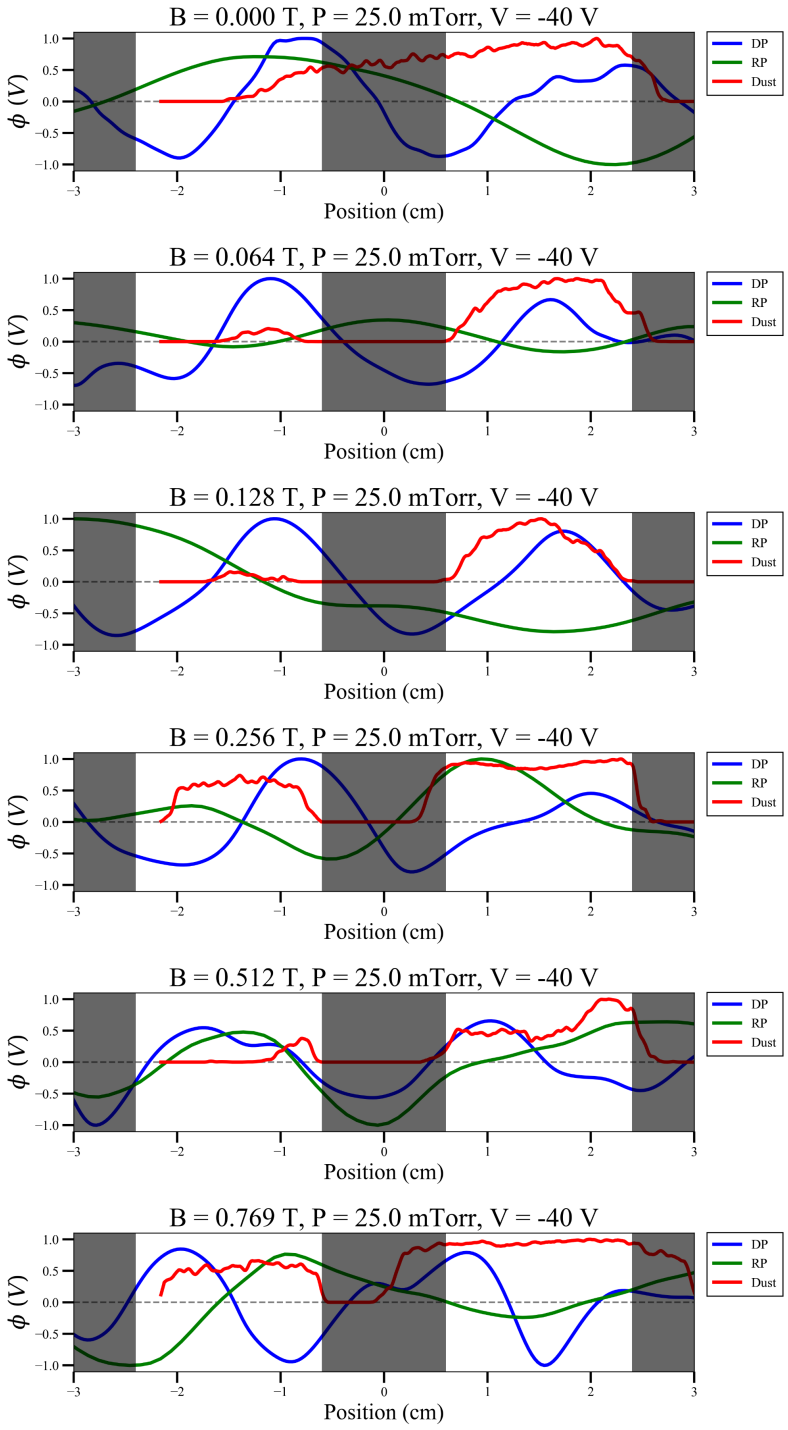

Figure 5-8 Normalized effective potentials at a neutral pressure of 25 mTorr and electrode bias of -40 V. Magnetic fields range from 0.0 T to 0.77 T. These effective potentials represent the results from measurements made by the double probe (Blue), ring probe (Red), and PIV (Red). Potentials are normalized to the maximum of the absolute value of the potential over the range $x = -5$ cm to $x = 5$ cm.

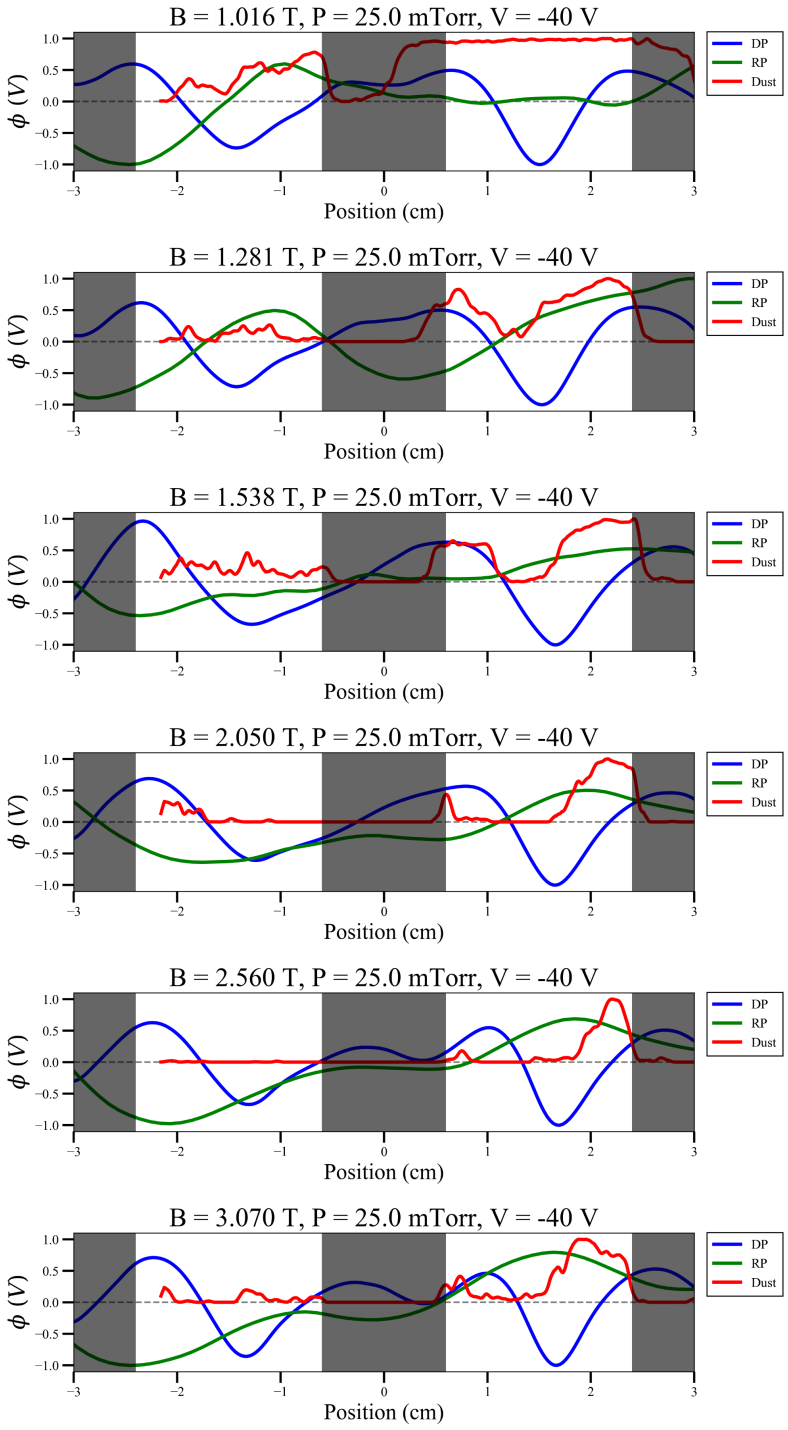

Continuation of Figure 5-8 Normalized effective potentials at a neutral pressure of 25 mTorr and electrode bias of -40 V. Magnetic fields range from 1.02 T to 3.07 T. These effective potentials represent the results from measurements made by the double probe (Blue), ring probe (Red), and PIV (Red). Potentials are normalized to the maximum of the absolute value of the potential over the range $x = -5$ cm to $x = 5$ cm.

The second set of effective electric potentials, which are at an electrode bias of +40 V, are presented in Figure 5-9. Much like the results at -40 V electrode, the effective electric potentials at +40 V present a high degree of correlation among the various experimental methods. Beneath the right hole, the double probe and the dust measurements appear strongly similar across all magnetic fields. Especially noteworthy is the development of the two-peak structure in each of these measurements at higher magnetic fields. Beginning at around 0.51 T peaks near the inner edges of the "waffle" electrode start to appear in the effective potential from the double probe method. This formation is later followed by the development of two peaks in the effective potential from the dust velocities at 1.02 T. Once the magnetic field has reached 1.28 T the two peaks are observed in each of the data sets simultaneously. This is strong evidence that the structure in the potential requires higher magnetic fields to penetrate deeper in the plasma. On the left side, the double probe and dust velocity methods are loosely correlated at lower magnetic fields where the two peaks have very near potential peak positions at 0.06 T which drift apart slightly before realigning at 0.512 T.

The ring probe and double probe results show the strongest correlation between the two data sets at high magnetic fields. From 0.77 – 2.56 T the structure of these two effective potential profiles develop in near unison, deviating only slightly in their peak potential positions at 1.54 T and 2.05 T. The ring probe and dust velocity measurements show a stronger correlation at this electrode bias than for the -40 V bias. Between 0.51 T to 1.54 T the two methods present potential profiles which align near the inner edge of the right hole. These two cases also appear quite closely correlated at 0.26 T. These measurements, combined with the observations and comparisons at -40 V, paint a clear picture that these experimental methods can detect an electric potential which behaves in a manner consistent with the imposed, ordered structure phenomenon.

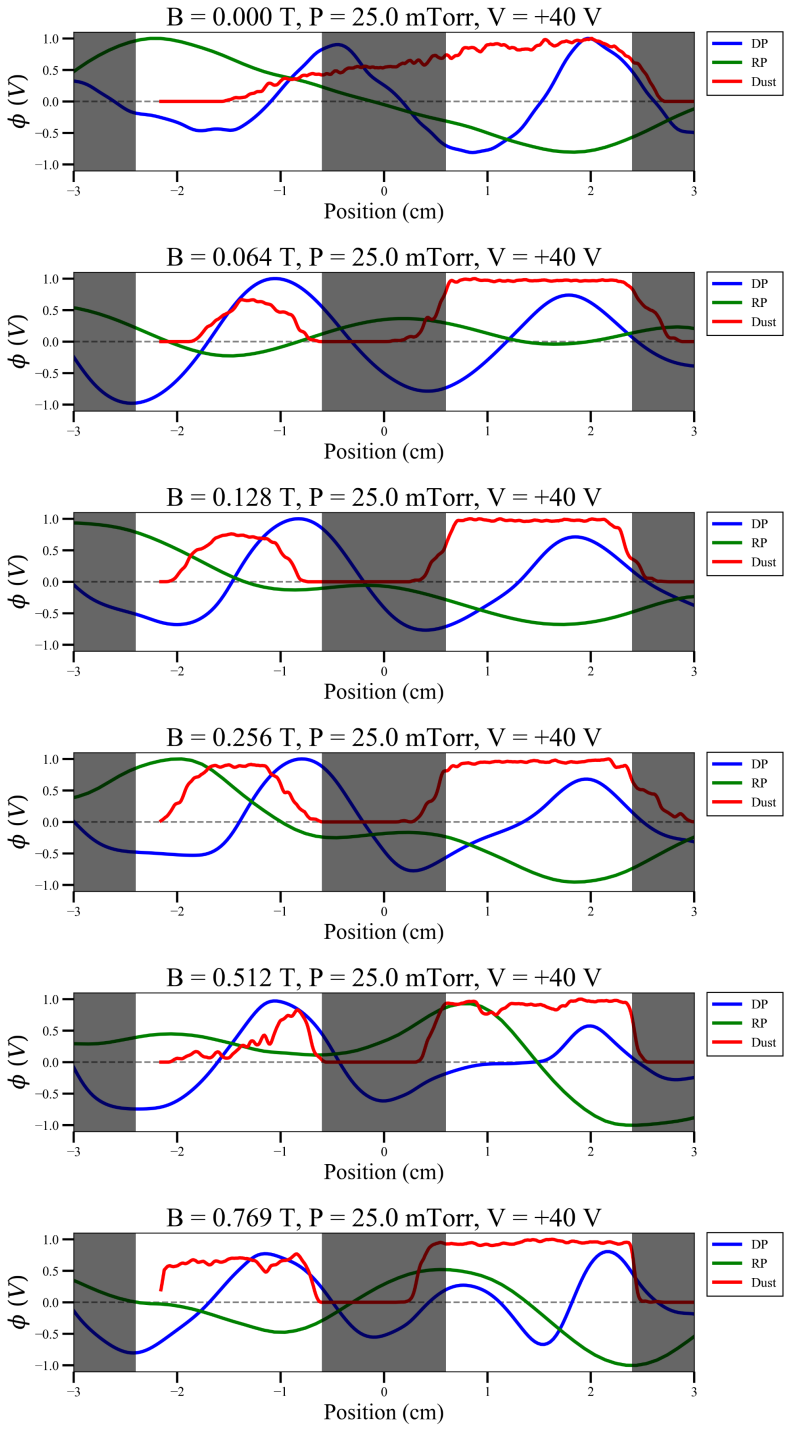

Figure 5-9 Normalized effective potentials at a neutral pressure of 25 mTorr and electrode bias of +40 V. Magnetic fields range from 0.0 T to 0.77 T. These effective potentials represent the results from measurements made by the double probe (Blue), ring probe (Re). Potentials are normalized to the maximum of the absolute value of the potential over the range $x = -5$ cm to $x = 5$ cm.

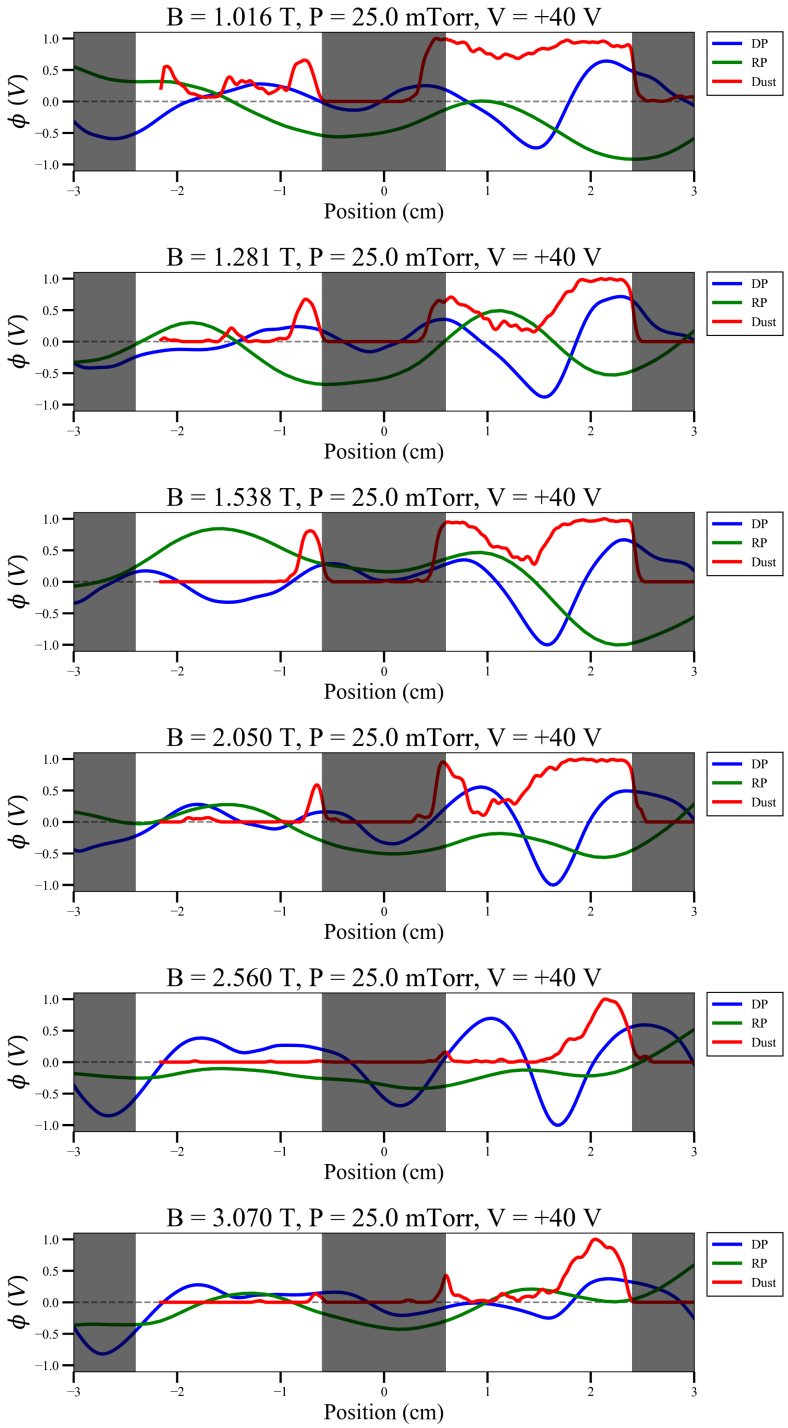

Continuation of Figure 5-9 Normalized effective potentials at a neutral pressure of 25 mTorr and electrode bias of +40 V. Magnetic fields range from 1.02 T to 3.07 T. These effective potentials represent the results from measurements made by the double probe (Blue), ring probe (Red), and PIV (Red). Potentials are normalized to the maximum of the absolute value of the potential over the range $x = -5$ cm to $x = 5$ cm.

While each of the three methods is limited in different ways, the results in this comparison suggest a relationship between the three effective electric potential determination methods. Each of the effective potentials present profiles which are primarily peaked at the center of the "waffle" electrode holes. These peaks become more centralized beneath the holes at higher magnetic fields, and the potentials calculated from dust observations and the double probe density measurements both begin to show evidence of a two peaked profile at the highest field strengths. The evidence of an ordered structure which confines dust particles to the center of the holes of the "waffle" electrode is quite apparent from these findings.

From these experimental results, answers to two of the most outstanding questions from previous publications are proposed. The first is whether the dust particles observed beneath the wire mesh in previous experiments are beneath the wires or beneath the holes. The results here show that they are beneath the holes, as the effective electric potentials in the hole regions of the "waffle" electrode are positively peaked and would be confining to negatively charged particles. Dust clouds are also observed to become and remain trapped in those regions at high magnetic fields. The second question is what is the physical mechanism which produces the confining structure. The results from each of the various methods would suggest that a magnetically modified plasma sheath which extends into the plasma along the magnetic axis is the primary phenomenon. The three methods show a similarly ordered structure at various vertical heights within the plasma, indicating that a potential from the electrode is being propagated down through the plasma.

The confidence in each of the methods for determining the effective electric potentials from the three methods should be addressed. The strongest case can be made for the potentials determined from the dust particles. Those measurements require no other interpretation than to examine the position of the dust particles and see that they are located beneath the holes of the

"waffle" electrode. Therefore, a potential which confines the dust to that region must be present, because that is where the dust is found. The potential found from the double Langmuir probe is believed to be the second most reliable method for determining the effective electric potential. The peaks in those electric potential results correspond to the results from dust observation in a majority of the cases. Using a double probe to determine the plasma densities is also a very well-established diagnostic within plasma physics and the results found here show modifications to the plasma density which would be consistent with the imposed, ordered structures. Finally, the results from the ring probe appear as the least consistent with the other two results. This diagnostic is the most recently developed and should be tested in more situations to determine is full effectiveness. Ultimately the dust observations most conclusively show that there is a confining potential beneath the holes of the "waffle" electrode.

Due to the various limitations of each of these experimental methods, this dissertation does not present these answers as the definitive solution to the imposed, ordered phenomenon only as strong indicators as to the underlying mechanisms which cause these structures to appear. The "waffle" electrode is still much larger than the wire mesh used in early experiments. Whether or not the imposed, ordered structures develop, and behave in a corresponding way when the structural source of the potential is much smaller is an open question. The wire mesh used in Section 2.2 and Chapter 3 have wires which are on the order of the Debye length in the plasma. In these situations, the sheaths around the mesh wires are likely to overlap and interact with each other under various conditions. These experiments only suggest these final answers about the imposed, ordered structures and serve as a basis for future experiments which may examine the ways in which the magnetically modified sheaths scale with changes in the shape and size of the conducting source of the structures.

Chapter 6 Conclusions and Future Work

At the beginning of this dissertation the goal of investigating the phenomenon called imposed, ordered structures was established. This was to be accomplished through an investigation into the plasma conditions at which the phenomenon occurs and to establish a set of experiments which would reveal the confining structure present in the background plasma. In this concluding chapter a discussion of how, and to what degree, these goals were met will be presented.

In Chapter 1 an introduction to several core dusty plasma principles which would be relevant to the experiments within the dissertation was given. This included derivations of the dust charging equations, defining the concept of plasma magnetization, and discussing plasma sheaths. In dusty plasmas, knowing the dust charge is incredibly important as the charge impacts nearly every aspect of the dusty plasma system. When plasmas are exposed to magnetic fields, the dynamics of charged particles within the plasma are modified by magnetic forces. These forces result in gyromotion where charged species rotating around magnetic field lines in a plane perpendicular to the magnetic field, with a frequency called the gyrofrequency. Charged species are also subject to collisions with neutral particles, which typically occur with some frequency called the collision frequency. Combining these two parameters allows for the definition of the Hall parameter which describes the charged species magnetization and whether collisional or magnetic dynamics dominate the particles motion. Finally, plasma sheaths were introduced. These sheaths are regions of strong electric fields at plasma boundaries close to the walls of the vacuum vessel and near the surface of other conducting elements within the plasma.

The next chapter presented a description of the experimental hardware and the experimental configurations which were used for experiments presented in later chapters. The primary experimental apparatus was the Magnetized Dusty Plasma Experiment (MDPX), a superconducting magnet capable of reaching fields of up to 4 T. One of the earliest discoveries on the MDPX was the observation of imposed, ordered structures. This phenomenon presents itself as a pattern formation within a cloud of dust microparticles in which the microparticles become aligned to the structure of a conducting element within the plasma. In the case of the original observations, this conducting element was a wire mesh. Several plasma diagnostic systems which would be used to further study these imposed, ordered structures were then described. These included cameras for observing dust particle, and two different plasma probe diagnostics: a double Langmuir probe for measuring electron temperatures and densities, and a ring probe for measuring electric fields in the plasma. The chapter then described two configurations of the MDPX vacuum chamber that would be used for performing experiments. The first of those configurations would be for experiments which used a wire mesh like that used in the original observation to investigate the experimental conditions at which the imposed, ordered structures were most present. The second configuration made use of a larger, “waffle”-shaped electrode. Using this electrode plasma probe diagnostics and dust particle observations were used to determine effective electric potentials within the plasma.

The experiments which examined the onset of the imposed, ordered structures were presented in Chapter 3. Within this chapter, two parameters, which provide a means of quantifying the presence of the imposed, ordered structures, are introduced. The first parameter used sums of images to determine an average pixel intensity within a region of interest, which allows for quantifying the degree of confinement over long time scales. The second parameter, the local bond

order parameter Ψ_4, was used to describe the inter-particle organization to a square lattice. These parameterization methods could then be used to describe the development of the imposed, ordered structures as a function of both magnetic field and neutral gas pressure which was consistent with the initial observations.

When measurements of the intensity ratio and average Ψ_4 were combined with measurements of a modified ion Hall parameter, a correlation to the ion magnetization within the experiment was found. This correlation showed that as ions within the plasma became more magnetized a confining potential develops which can affect the dust cloud dynamics. These measurements also made possible a qualitative description of the transition between the various types of observed transport of particles through the dust cloud.

While these measurements provided a method to quantify the conditions at which the imposed, ordered structures begin to appear they only use the dust to show that the structures exist and their relative strength. To properly understand this phenomenon experiments which examine the background plasma itself needed to be conducted. However, since the wire mesh is so small it is difficult to probe the plasma beneath it and so other means of investigating these plasma structures needed to be developed. Additionally, several important outstanding questions remain. First, are the dust particle trapped in the holes between the mesh or are they trapped beneath the wires? Second, how does the overall pattern of the wire mesh become mapped into the plasma so that the particles appear to follow that spatial structure?

To answer these questions a “waffle”-shaped electrode was designed to reproduce the imposed, ordered structures on a larger scale. This electrode is large enough for dust confinement to be observed, and to allow for plasma probe diagnostics to take spatially resolved measurement

s of the plasma beneath the electrode. Experiments performed with this “waffle” electrode were presented in Chapter 4 and Chapter 5.

In Chapter 4, measurements made with two different plasma probe diagnostics were presented. The first of those diagnostics was a double Langmuir probe. The double probed allowed for measurements of the electron temperature and density to be taken for various magnetic fields, neutral pressures, and dc biases on the “waffle” electrode. Using the electron density profiles, effective electric potentials were calculated using Poisson’s equation. The second diagnostic was a custom designed and built ring probe, which consisted of a pair of conducting rings used to measure the floating potential within the plasma. By taking the difference in the floating potentials measured by each of the two ring, effective electric fields were calculated and then integrated to produce another set of effective electric potentials. For both the double probe and the ring probe, measurements which showed a dependence on the parameters of magnetic field, neutral pressure, and electrode bias were found. Methods for analyzing the measurements from plasma probes were then presented, with those methods showing a reliable ability to produce results for effective electric potentials.

The final chapter presented measurements made by observing dust particle dynamics beneath the “waffle” electrode. In the presence of the magnetic field, the particles were observed to be confined to locations within the plasma which were directly below the holes of the “waffle” electrode. Using particle image velocimetry (PIV) techniques, the particle velocities were measured and used to calculate an effective electric potential by applying conservation of energy. The three independent methods for determining the confining electric potentials within the plasma, the double probe, the ring probe, and the dust velocities, were then qualitatively compared.

While each of the three methods was limited in different ways, the results in the comparison suggest a relationship between the three effective electric potential determination methods where each of the effective potential profiles were peaked near the center of the "waffle" electrode holes. From these experimental results, answers to the two outstanding questions from Chapter 3 are proposed. The first is whether the dust particles observed beneath the wire mesh are beneath the wires or beneath the holes. The second question is what is the physical mechanism which produces the confining structure. The comparison of the various methods suggests that a magnetically modified plasma sheath which extends into the plasma along the magnetic axis is the primary phenomenon. The three methods show a similarly ordered structure at various vertical heights within the plasma with the calculated effective electric potential decreasing in strength with increasing distance from the "waffle" electrode.

These results address the core goals of this dissertation laid out in the introduction to Chapter 1. The conditions at which the imposed, ordered structures was clearly addressed in Chapter 3 through the development of parameterization methods which enabled a quantitative analysis of the presence of the imposed, ordered structures within a dusty plasma. A correlation between these quantitative methods and the particle dynamics was also given. Several independent experiments also gave evidence that a magnetically modified plasma sheath around a conducting element within the plasma can produce potential structures within the plasma which are capable of confining dust particles.

While the experiments presented in this dissertation were capable of determining a set of results which satisfied the original goals, those experiments also revealed a number of limitations in the current understanding of these highly magnetized plasma systems. First, the need for new plasma probe theories which incorporate magnetic fields is severely needed. The magnetic fields

within a plasma are known to modify the dynamics of charged particles which is not accounted for when considering the flux of ions or electrons onto to probe surface. Neither does the probe theory account for modifications to the velocity or energy distributions of the particles at these high fields. A continued effort into computationally modeling the magnetic effects on low-temperature plasmas is also required. These models will help to motivate new experiments which will investigate these systems and provide context when interpreting results. One of the largest limitations within this dissertation was the drastically different scales which experiments were performed over. While those different dimensions were necessary for establishing this initial framework, experiments which examine the scaling behavior of the imposed, ordered structures should be a priority.

As the physical understanding of these structures is being investigated, new applications of the phenomenon should also be pursued. The ability of this phenomenon to produce consistent plasma structure cannot be understated. Structures within the plasma may be able to produce new etching patterns through this phenomenon. An example of this is shown in Figure 6-1. This image shows an example of plasma etching on a piece of glass which covered the hole in the top rf electrode where the imprint of the "waffle" electrode is clearly observed. The plasma structures may also have applications to other dusty plasma experiments. In experiments which used acetylene gas to grow carbon nanoparticles, the resulting particles were shown to be strongly influenced by the magnetic field. [75] By using patterned conductors within the plasma, the growth of these nanoparticles could be systematically modified the presence of imposed, ordered structures. Finally, low temperature plasmas have shown a clear ability to modify certain types of materials used in medical applications. [76,77] The electrospun materials in these works have been shown to increase their wettability with exposure to the same types of low-temperature plasmas

Figure 6-1 Results of plasma etching on glass square in the presence of the "waffle" electrode. The piece of glass was used to cover the hole in the top rf electrode within the MDPX vacuum chamber.

produced in MDPX. The application of patterned modification of these materials could be of interest to communities outside of plasma physics.

Ultimately imposed, ordered structures are still a new and exciting phenomenon in the field of low-temperature and dusty plasmas. The work presented here shows a clear indication that these structures are related to the development of magnetically modified plasma sheaths. It also reveals various limitations in the current ability of plasma probes to measure plasma parameters. These imposed, ordered structures reveal a host of new interesting physics, and offer several avenues for new experiments and applications.

References

[1] E. Thomas, B. Lynch, U. Konopka, R. L. Merlino, and M. Rosenberg, Phys. Plasmas **22**, 030701 (2015).

[2] P. K. Shukla, Phys. Plasmas **8**, 1791 (2001).

[3] A. Barkan, N. D'Angelo, and R. L. Merlino, Phys. Rev. Lett. **73**, 3093 (1994).

[4] A. Piel, *Plasma Physics* (Springer Berlin Heidelberg, Berlin, Heidelberg, 2010).

[5] P. K. Shukla and A. A. Mamun, *Introduction to Dusty Plasma Physics.* (Institute of Physics Publishing, 2002).

[6] H. Thomas, G. E. Morfill, V. Demmel, J. Goree, B. Feuerbacher, and D. Möhlmann, Phys. Rev. Lett. **73**, 652 (1994).

[7] J. H. Chu and I. Lin, Phys. Rev. Lett. **72**, 4009 (1994).

[8] S. Jaiswal, T. Hall, S. LeBlanc, R. Mukherjee, and E. Thomas, Phys. Plasmas **24**, (2017).

[9] L. Couëdel, V. Nosenko, A. V. Ivlev, S. K. Zhdanov, H. M. Thomas, and G. E. Morfill, Phys. Rev. Lett. **104**, 195001 (2010).

[10] L. Couëdel, S. Zhdanov, V. Nosenko, A. V. Ivlev, H. M. Thomas, and G. E. Morfill, Phys. Rev. E - Stat. Nonlinear, Soft Matter Phys. **89**, (2014).

[11] L. Couëdel, V. Nosenko, M. Rubin-Zuzic, S. Zhdanov, Y. Elskens, T. Hall, and A. V Ivlev, Phys. Rev. E **97**, 043206 (2018).

[12] O. Arp, D. Block, A. Piel, and A. Melzer, Phys. Rev. Lett. **93**, 165004 (2004).

[13] O. Arp, D. Block, M. Klindworth, and A. Piel, Phys. Plasmas **12**, 1 (2005).

[14] M. Bonitz, D. Block, O. Arp, V. Golubnychiy, H. Baumgartner, P. Ludwig, A. Piel, and A.

Filinov, Phys. Rev. Lett. **96**, 1 (2006).

[15] A. V. Ivlev, G. E. Morfill, H. M. Thomas, C. Räth, G. Joyce, P. Huber, R. Kompaneets, V. E. Fortov, A. M. Lipaev, V. I. Molotkov, T. Reiter, M. Turin, and P. Vinogradov, Phys. Rev. Lett. **100**, 095003 (2008).

[16] A. V. Ivlev, P. C. Brandt, G. E. Morfill, C. Rath, H. M. Thomas, G. Joyce, V. E. Fortov, A. M. Lipaev, V. I. Molotkov, and O. F. Petrov, IEEE Trans. Plasma Sci. **38**, 733 (2010).

[17] H. M. Thomas, G. E. Morfill, V. E. Fortov, A. V. Ivlev, V. I. Molotkov, A. M. Lipaev, T. Hagl, H. Rothermel, S. A. Khrapak, R. K. Suetterlin, M. Rubin-Zuzic, O. F. Petrov, V. I. Tokarev, and S. K. Krikalev, New J. Phys. **10**, 033036 (2008).

[18] A. V. Ivlev, M. H. Thoma, C. Räth, G. Joyce, and G. E. Morfill, Phys. Rev. Lett. **106**, 155001 (2011).

[19] M. Y. Pustylnik, M. A. Fink, V. Nosenko, T. Antonova, T. Hagl, H. M. Thomas, A. V. Zobnin, A. M. Lipaev, A. D. Usachev, V. I. Molotkov, O. F. Petrov, V. E. Fortov, C. Rau, C. Deysenroth, S. Albrecht, M. Kretschmer, M. H. Thoma, G. E. Morfill, R. Seurig, A. Stettner, V. A. Alyamovskaya, A. Orr, E. Kufner, E. G. Lavrenko, G. I. Padalka, E. O. Serova, A. M. Samokutyayev, and S. Christoforetti, Rev. Sci. Instrum. **87**, 093505 (2016).

[20] O. Ishihara and S. V. Vladimirov, Phys. Plasmas **4**, 69 (1997).

[21] D. Winske, IEEE Trans. Plasma Sci. **29**, 191 (2001).

[22] G. A. Hebner and M. E. Riley, Phys. Rev. E - Stat. Nonlinear, Soft Matter Phys. **69**, 1 (2004).

[23] P. K. Shukla and M. Salimullah, Phys. Plasmas **3**, 3858 (1996).

[24] M. Nambu, M. Salimullah, and R. Bingham, Phys. Rev. E - Stat. Nonlinear, Soft Matter Phys. **63**, 564031 (2001).

[25] F. F. Chen, *Introduction to Plasma Physics and Controlled Fusion* (Springer International Publishing, Cham, 2016).

[26] S. A. Khrapak, J. Plasma Phys. **79**, 1123 (2013).

[27] B. R. Lynch, Microparticle Dynamics in Strongly Magnetized Low Temperature Plasmas, Auburn University, 2017.

[28] K. U. Riemann, J. Phys. D. Appl. Phys. **24**, 493 (1991).

[29] M. A. Lieberman and A. J. Lichtenberg, *Principles of Plasma Discharges and Materials Processing* (John Wiley & Sons, Inc., Hoboken, NJ, USA, 2005).

[30] G. -H. Kim, N. Hershkowitz, D. A. Diebold, and M. -H. Cho, Phys. Plasmas **2**, 3222 (1995).

[31] N. Hershkowitz, Phys. Plasmas **12**, 055502 (2005).

[32] R. H. Cohen and D. D. Ryutov, Phys. Plasmas **2**, 2011 (1995).

[33] X. Zou, J.-Y. Liu, Y. Gong, Z.-X. Wang, Y. Liu, and X.-G. Wang, Vacuum **73**, 681 (2004).

[34] D. D. Tskhakaya, P. K. Shukla, B. Eliasson, and S. Kuhn, Phys. Plasmas **12**, 1 (2005).

[35] M. M. Hatami and B. Shokri, Phys. Plasmas **19**, 083510 (2012).

[36] M. M. Hatami, Phys. Plasmas **22**, 043510 (2015).

[37] J. E. Allen and J. T. Holgate, Nucl. Mater. Energy **12**, 999 (2017).

[38] Z. Jiang, Z. Wei, and J. X. Ma, Phys. Scr. **92**, 115601 (2017).

[39] E. Thomas, R. L. Merlino, and M. Rosenberg, IEEE Trans. Plasma Sci. **41**, 811 (2013).

[40] E. Thomas, U. Konopka, D. Artis, B. Lynch, S. Leblanc, S. Adams, R. L. Merlino, and M. Rosenberg, J. Plasma Phys. **81**, 345810206 (2015).

[41] M. Puttscher and A. Melzer, Phys. Plasmas **21**, 123704 (2014).

[42] T. H. Hall and E. Thomas, IEEE Trans. Plasma Sci. **44**, 463 (2016).

[43] E. Thomas, U. Konopka, B. Lynch, S. Adams, S. LeBlanc, R. L. Merlino, and M.

Rosenberg, Phys. Plasmas **22**, 113708 (2015).

[44] E. Thomas, J. Plasma Fusion Res. **93**, 1 (2017).

[45] E. O. Johnson and L. Malter, Phys. Rev. **80**, 58 (1950).

[46] F. F. Chen, Rev. Sci. Instrum. **35**, 1208 (1964).

[47] E. M. Tejero, Spontaneous Electromagnetic Emission from a Strongly Localized Plasma Flow, Auburn University, 2011.

[48] A. M. DuBois, Laboratory Investigation of the Dynamics of Shear Flows in a Plasma Boundary Layer, Auburn University, 2013.

[49] T. Hall, E. Thomas, K. Avinash, R. Merlino, and M. Rosenberg, Phys. Plasmas **25**, 103702 (2018).

[50] B. I. Halperin and D. R. Nelson, Phys. Rev. Lett. **41**, 121 (1978).

[51] H. Lowen, J. Phys. Condens. Matter **4**, 10105 (1992).

[52] H. M. Thomas and G. E. Morfill, Nature **379**, 806 (1996).

[53] J. Chakrabarti and H. Löwen, Phys. Rev. E **58**, 3400 (1998).

[54] X. Qi, Y. Chen, Y. Jin, and Y.-H. Yang, J. Korean Phys. Soc. **730000**, 2 (2006).

[55] D. Allan, T. Caswell, N. Keim, C. Van Der Wel, and trackpy: Trackpy v0.3.2. Zenodo. http://doi.org/10.5281/zenodo.60550, Zenodo (2016).

[56] M. Schwabe, U. Konopka, P. Bandyopadhyay, and G. E. Morfill, Phys. Rev. Lett. **106**, 215004 (2011).

[57] E. Thomas, U. Konopka, R. L. Merlino, and M. Rosenberg, Phys. Plasmas **23**, (2016).

[58] M. Menati, E. Thomas, and M. J. Kushner, Phys. Plasmas **26**, 063515 (2019).

[59] F. N. Fritsch and R. E. Carlson, SIAM J. Numer. Anal. **17**, 238 (1980).

[60] E. Thomas, B. Lynch, U. Konopka, M. Menati, S. Williams, R. L. Merlino, and M.

Rosenberg, Plasma Phys. Control. Fusion **62**, 014006 (2020).

[61] J. Boffard, R. Jung, C. Lin, L. Aneskavich, and A. Wendt, J. Phys. D. Appl. Phys. **45**, 45201 (2012).

[62] I. Arnold, An Investigation into the Role of Metastable States on Excited Populations of Weakly Ionized Argon Plasmas, with Applications for Optical Diagnostics., Auburn University, 2017.

[63] J. L. Kinsey, Annu. Rev. Phys. Chem. **28**, 349 (1977).

[64] L. Oksuz, M. A. Khedr, and N. Hershkowitz, Phys. Plasmas **8**, 1729 (2001).

[65] R. F. Boivin and E. E. Scime, Rev. Sci. Instrum. **74**, 4352 (2003).

[66] A. M. Keesee, E. E. Scime, and R. F. Boivin, Rev. Sci. Instrum. **75**, 4091 (2004).

[67] E. Scime, C. Biloiu, C. Compton, F. Doss, D. Venture, J. Heard, E. Choueiri, and R. Spektor, Rev. Sci. Instrum. **76**, 026107 (2005).

[68] J. Schindelin, I. Arganda-Carreras, E. Frise, V. Kaynig, M. Longair, T. Pietzsch, S. Preibisch, C. Rueden, S. Saalfeld, B. Schmid, J.-Y. Tinevez, D. J. White, V. Hartenstein, K. Eliceiri, P. Tomancak, and A. Cardona, Nat. Methods **9**, 676 (2012).

[69] R. Adrian and C. S. Yao, in *Unkn. Host Publ. Title*, edited by X. B. J. Reed, G. K. Patterson, and J. L. Zakin (Univ of Missouri-Rolla, 1984), pp. 170–186.

[70] R. J. Adrian, Appl. Opt. **23**, 1690 (1984).

[71] R. J. Adrian, Exp. Fluids **39**, 159 (2005).

[72] E. Thomas, J. D. Williams, and J. Silver, Phys. Plasmas **11**, L37 (2004).

[73] E. Thomas, Phys. Plasmas **6**, 2672 (1999).

[74] LaVision, Prod. Man. (2013).

[75] L. Couëdel, D. Artis, M. P. Khanal, C. Pardanaud, S. Coussan, S. LeBlanc, T. Hall, E. T.

Jr, U. Konopka, M. Park, and C. Arnas, Plasma Res. Express **1**, 015012 (2019).

[76] B. S. Tucker, P. A. Baker, K. G. Xu, Y. K. Vohra, and V. Thomas, J. Vac. Sci. Technol. A **36**, 04F404 (2018).

[77] K. VIG, K. Swain, T. Mlambo, P. Baker, B. Tucker, V. Thomas, and Y. K. Vohra, FASEB J. **33**, 603.3 (2019).

Appendix A Stability of the Plasma Sheath

This appendix provides the derivation of the stability criterion for the plasma sheath presented in Section 1.3. The final solution for the potential within the plasma sheath, which was derived in Section 1.3 is

$$\epsilon_0 \frac{d^2\phi}{dx^2} = e(n_e - n_i) = en_0 \left[\exp\left(\frac{e\phi}{k_B T_e}\right) - \left(1 - \frac{2e\phi}{m_i u_0^2}\right)^{-1/2} \right] \tag{A-1}$$

where ϵ_0 is the permittivity constant, e is the elementary charge, ϕ is the electric potential in the sheath, n_e and n_i are the electron and ion number densities, k_B is the Boltzmann constant, T_e is the electron temperature, m_i is the electron mass, and u_0 is the ion drift velocity with which they enter the sheath. This nonlinear solution is not always stable, though it is possible to calculate the stability criterion.

To do so let us first take a step back and examine the equation of motion for a point mass m in a classical potential $V(x)$.

$$m\frac{d^2x}{dt^2} = -\frac{dV}{dx} \tag{A-2}$$

The potential V here is what determines the trajectory of x. If the potential V has a minimum ($d^2V/dx^2 > 0$)or maximum $d^2V/dx^2 < 0$, then that is the location at which the trajectory of x is either stable or unstable. We can then apply this same line of thought to solving for the stability of the sheath. We will first rewrite Poisson's equation as

$$\frac{d^2\phi}{dx^2} = f(\phi) = -\frac{d\Psi}{d\phi} \tag{A-3}$$

In which the right-hand side of the equation is a function of the pseudopotential Ψ, also known as the classical potential or Sagdeev potential. This pseudopotential is mathematically equivalent to the mechanical potential *V(x)* in the mechanical problem. Now though we do not need to calculate the second derivative $d^2\Psi/d\phi^2$ to find the stability criterion, we only need to find the first derivative $-df(\phi)/dx$.

This function $f(\phi)$ is taken from Equation A-1 as:

$$f(\phi) = en_0\left[\exp\left(\frac{e\phi}{k_B T_e}\right) - \left(1 - \frac{2e\phi}{m_i u_0^2}\right)^{-1/2}\right] \tag{A-4}$$

which ultimately results in

$$-\frac{df}{d\phi}\bigg|_{\phi=0} = \frac{e}{k_B T_e} - \frac{e}{m_i u_0^2} \leq 0 \tag{A-5}$$

This result, called the *Bohm-criterion* after physicist David Bohm (1917 – 1992), can also be written as

$$u_0 \geq v_B = \left(\frac{k_B T_e}{m_i}\right)^{1/2} \tag{A-6}$$

This *Bohm velocity*, v_B, is identical to the ion sound speed and tells us that the speed of the ions at the sheath edge must be equal to or greater than the *Bohm velocity*. [4]

Appendix B Determining Probe Offsets

This appendix will describe the methods that were used to calculate the position of the double and ring probes relative to the "waffle" electrode. When collecting data with these devices, positions are recorded over the range of $x = 0$ cm to $x = x_{max}$, where $x_{max} = 5.9"$ (15 cm). The first section with probe the methods used for determining the offset position of the double Langmuir probe, and the second section will describe the methods for determining the position of the ring probe.

B.1 Double Probe Offset

To determine the position of the double Langmuir probe relative to the "waffle" electrode, images of the probe at several positions beneath the electrode were recorded such as the example image in Figure B-1 which shows the probe at a measured position of $x = 7.5$ cm. These images required that the full length of the two probe tips be visible beneath in the holes of the electrode. Using the *Fiji* software package four distance measurements were taken for each probe tip, eight in total, for each position image, which are highlighted in Figure B-1. These measurements provide the distances form the leading edge of each probe tip to the nearest and furthest edges of the center conducting band of the "waffle" electrode, as well as the leading edge of the ceramic rod to those same edges of the electrode. Because each of the eight distances recorded were taken by hand, in reality each of the measurements represents an average of three separate measurements for that distance.

By taking the average of those eight distances, the result is the distance from the central point of the two double probe tips to the central point of the "waffle" electrode, for that probe position. By plotting each of the distances, x, versus the probe probes measured position, y, the probes position when at the center of the "waffle" electrode can be determined as the y-intercept of a linear fit of the plotted data. The plotted data points, as well as the fit is shown in Figure B-2.

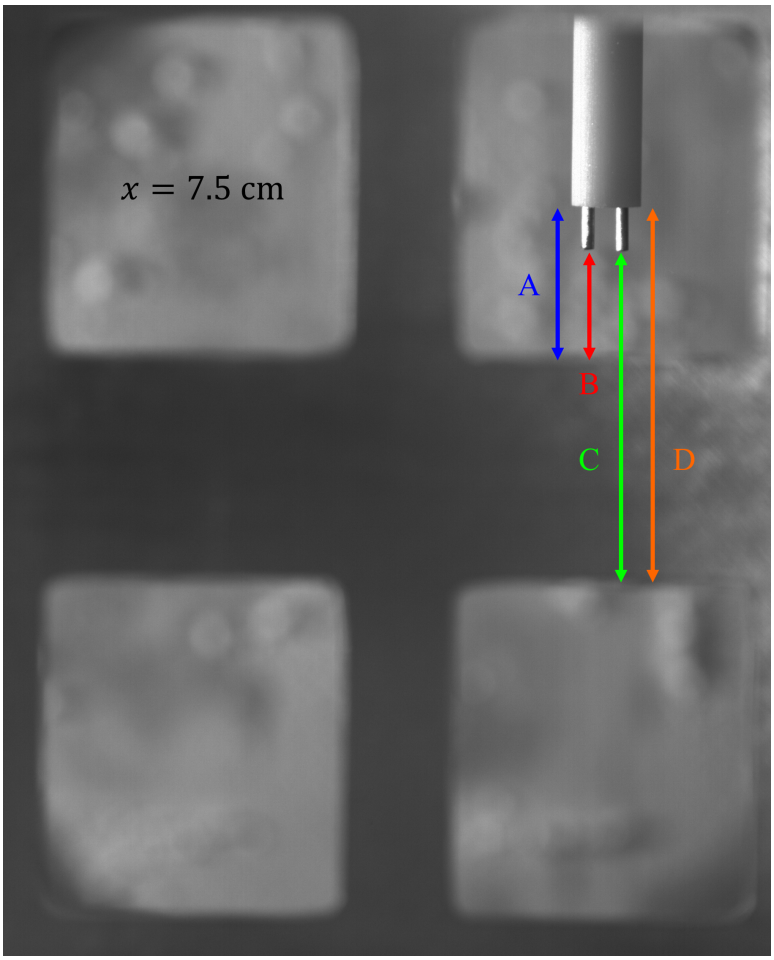

Figure B-1 The double Langmuir probe at a measured position of 7.5 cm. The four distances which were measured are shown: A – leading edge of ceramic rod to the near edge of the "waffle" electrode, B – leading edge of probe tip to near edge of electrode, C – leading edge of the probe tiop to the far edge of the electrode, D – leading edge of ceramic rod to the far edge of the electrode. Each of these four measurements were taken for the two probe tips, for eight measurements in total.

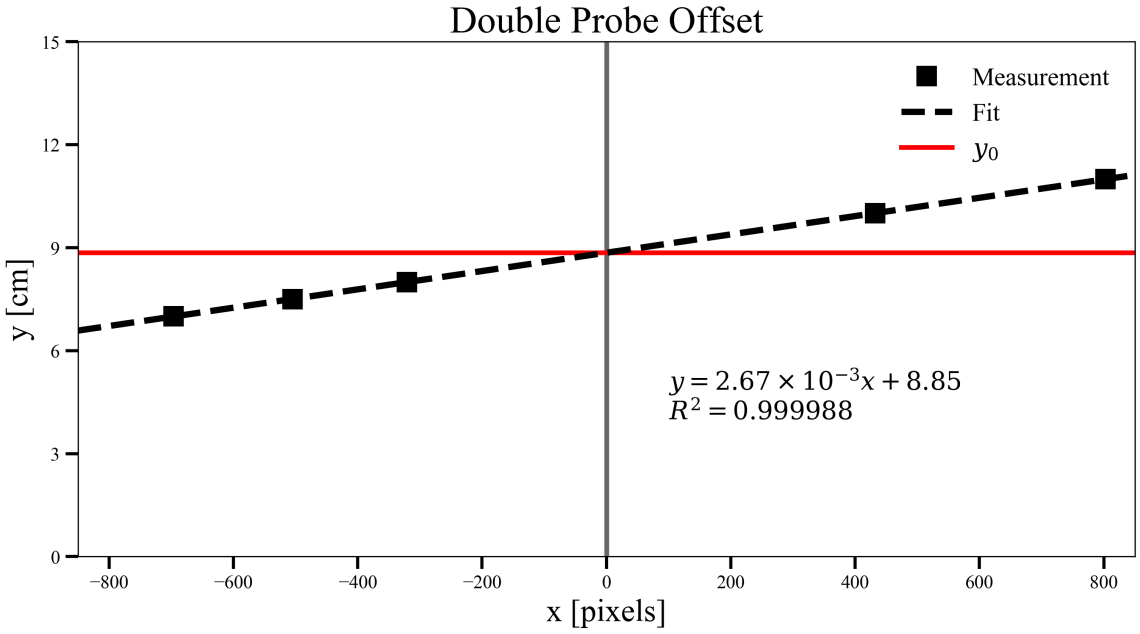

Figure B-2 Plot of double Langmuir probe position versus probe distance to center of "waffle" electrode. The *y*-intercept, shown as a horizontal red line, is used to define the double Langmuir probes position relative to the "waffle" electrode. A linear fit of the data is shown as a black dashed line.

The offset of the double Langmuir probe is found to be 8.85 cm, with its position on the vertical axis shown as a horizontal red line in the figure.

B.2 Ring Probe Offset

The details which are described here apply to each of the three sets of ring probe measurements. These are the measurements taken at an electrode bias of ±20 V and ±60 V for the "thick" dimension, the "thin" dimension measurements, and the measurements taken at an electrode bias of ±40 V beneath the "thick" dimension. To determine the position of the double Langmuir probe relative to the "waffle" electrode, images of the probe at several positions beneath the electrode were recorded such as the example image in Figure B-3 which shows the probe at a measured position of $x = 7.5$ cm.. These images required that both bands of the ring probe be visible beneath in the holes of the electrode. Using the *Fiji* software package four distance

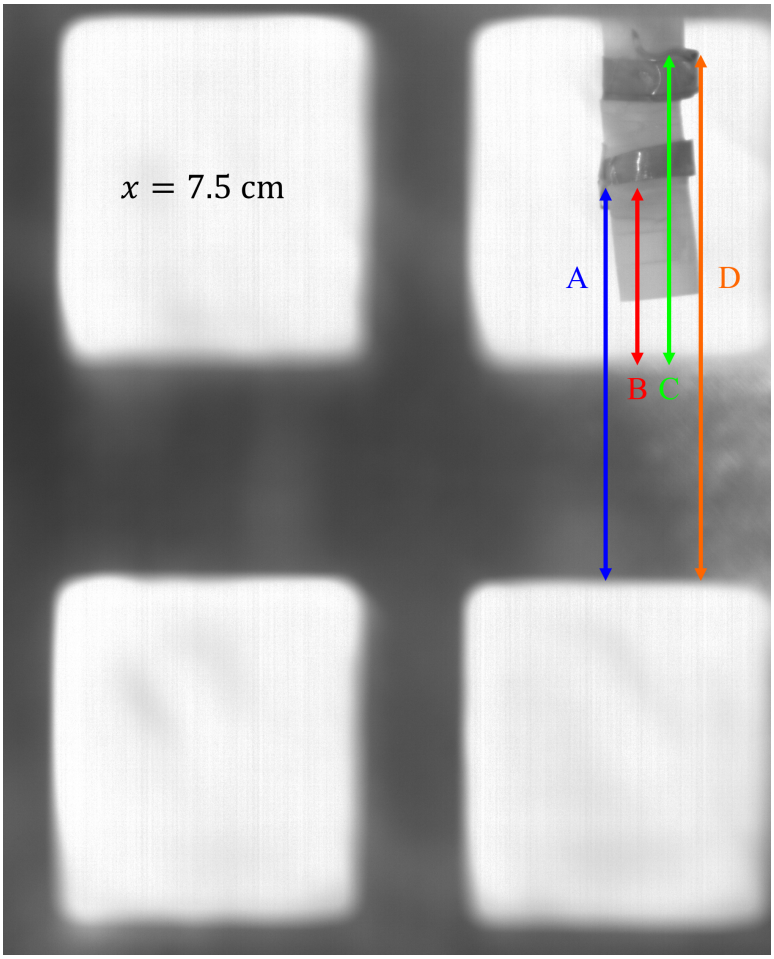

Figure B-3 The ring probe at a measured position of 7.5 cm. The four distances which were measured are shown: A – leading of the front probe to the far edge of the "waffle" electrode, B – leading edge of front probe to near edge of electrode, C – trailing edge of the rear probe to the near edge of the electrode, D – trailing edge of rear probe to the far edge of the electrode.

measurements were taken for the ring probe. For each position image. These measurements provide the distances form the leading edge of the front probe to the near and far edges of the "waffle" electrode, and the distances from the trailing edge of the rear probe to the near and far edges of the "waffle" electrode. Because each of the four distances recorded were taken by hand, in reality each of the measurements represents an average of five separate measurements for that distance.

By taking the average of those four distances, the result is the distance from the central point between the two probe rings to the central point of the "waffle" electrode, for that probe position. By plotting each of the distances, *x*, versus the probes measured position, *y*, the probes position when at the center of the "waffle" electrode can be determined as the *y*-intercept of a linear fit of the plotted data. The plotted data points for the ±40 V bias measurements, as well as the fit, is shown in Figure B-4. The offset of the ring probe is found to be 8.85 cm, with its position on the vertical axis shown as a horizontal red line in the figure.

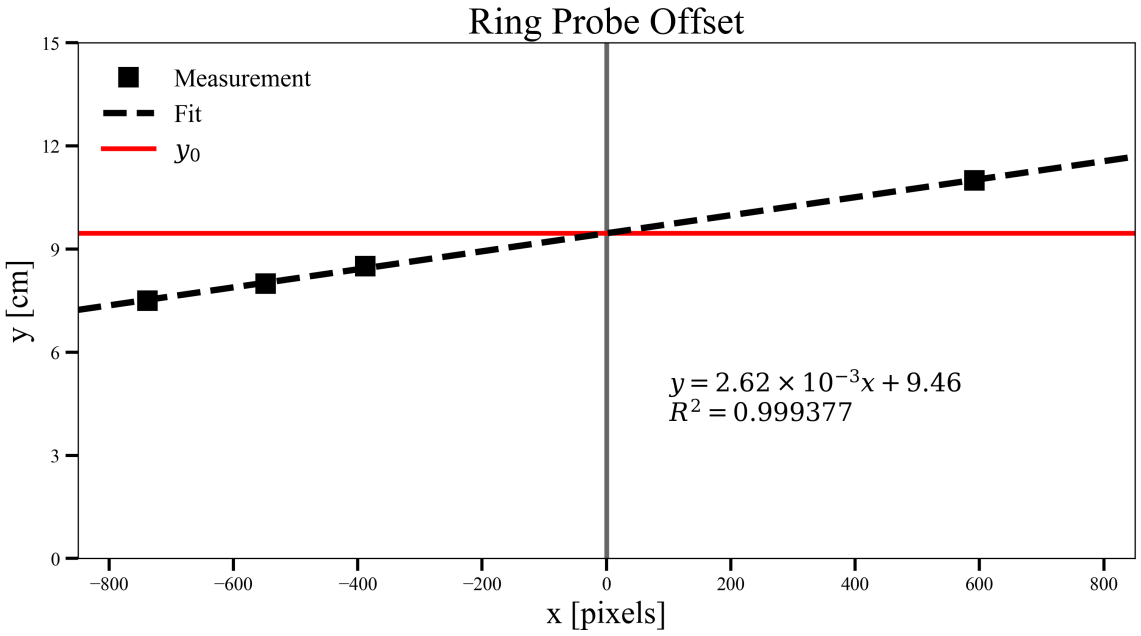

Figure B-4 Plot of ring probe position versus probe distance to center of "waffle" electrode. The *y*-intercept, shown as a horizontal red line, is used to define the double Langmuir probes position relative to the "waffle" electrode. A linear fit of the data is shown as a black dashed line.

Appendix C LabView Codes

C.1 Double Langmuir Probe VI

Front Panel

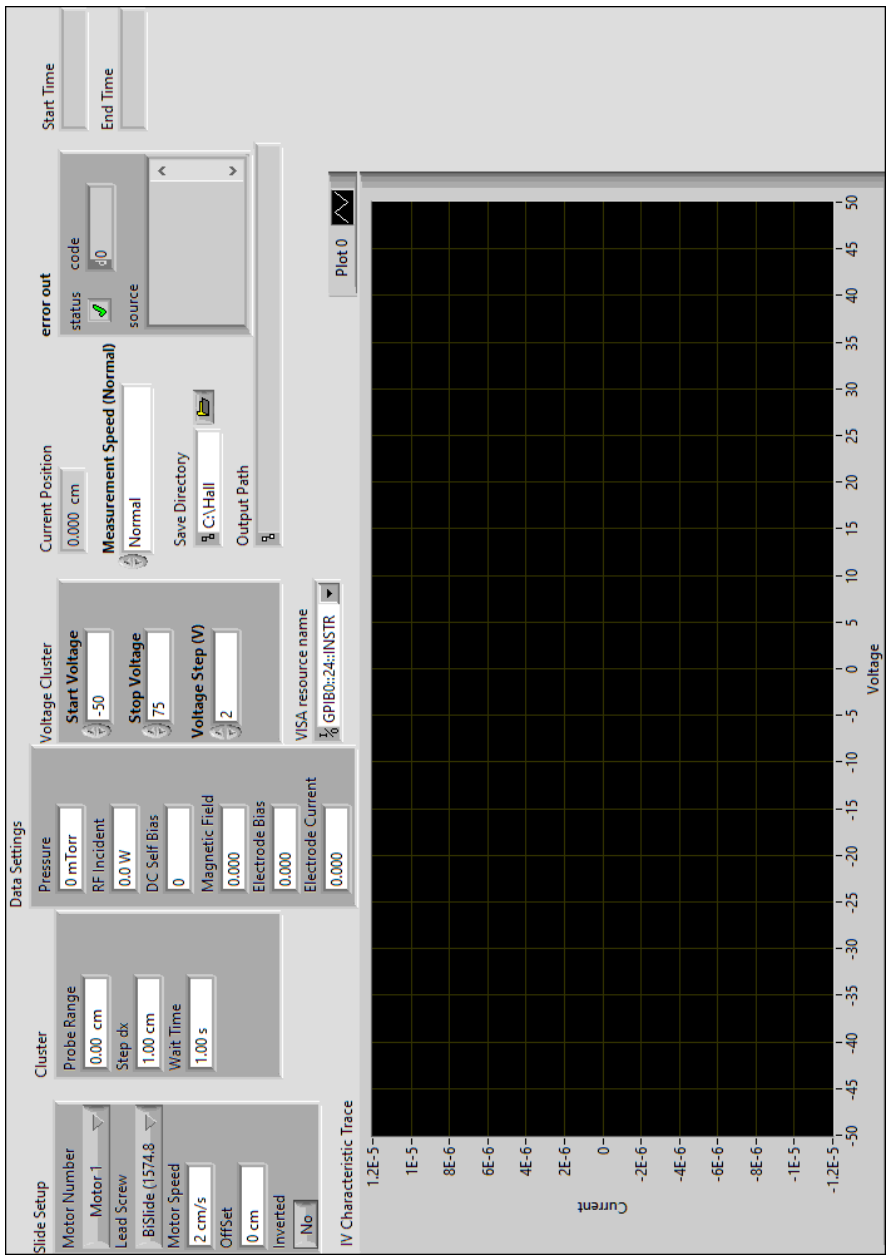

Block Diagram

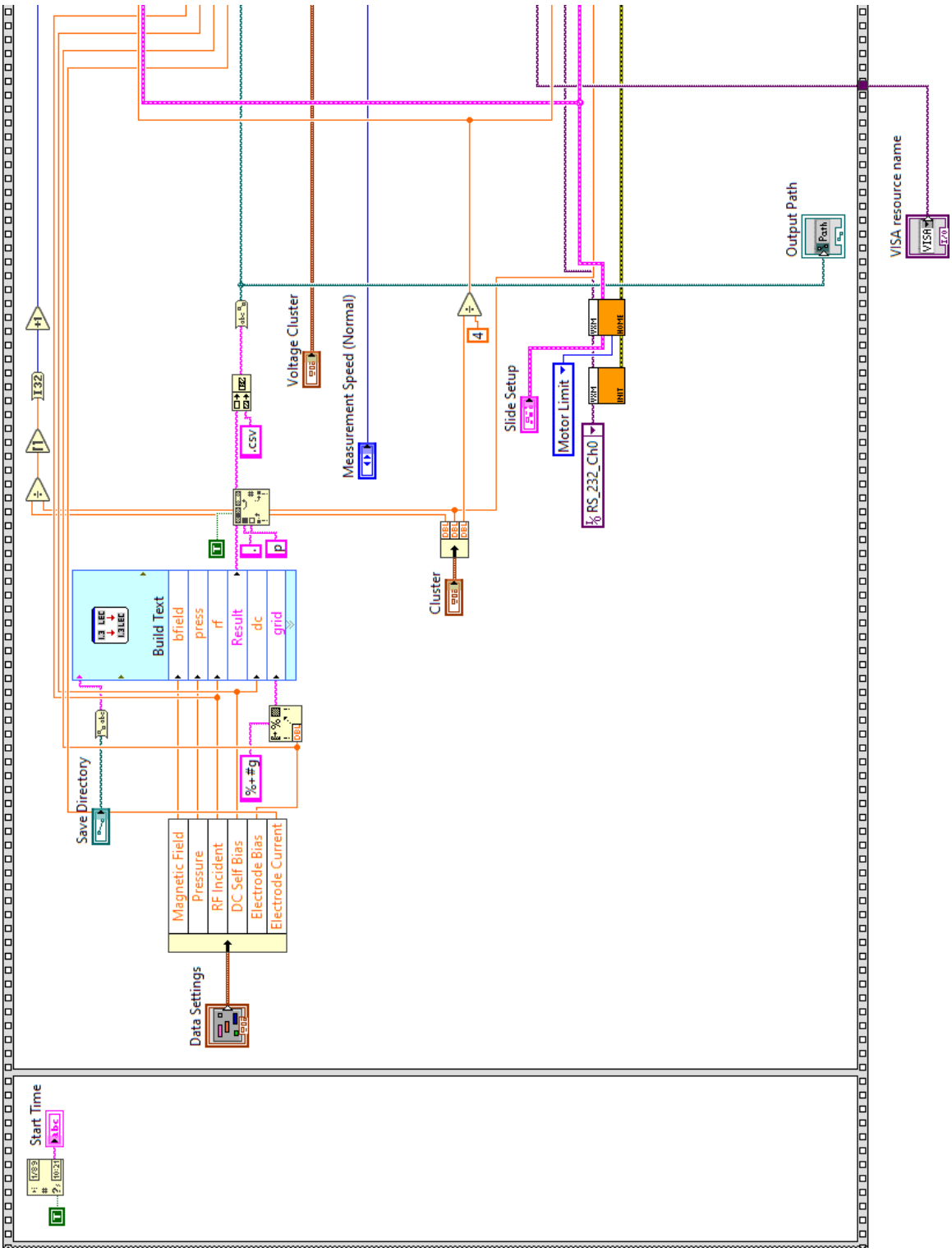

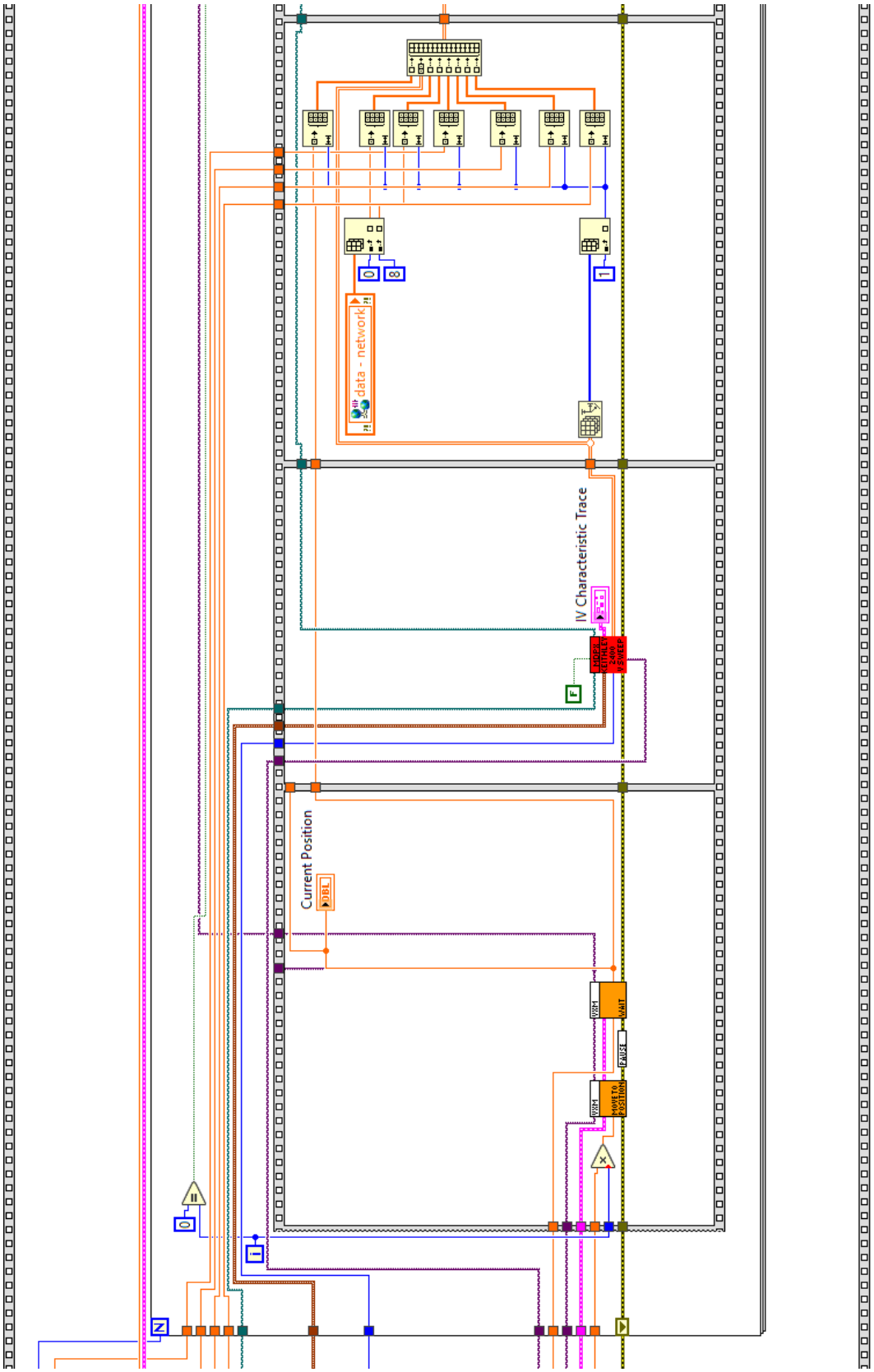
data - network
IV Characteristic Trace
Current Position
DBL
WAIT
PAUSE
MOVE TO POSITION

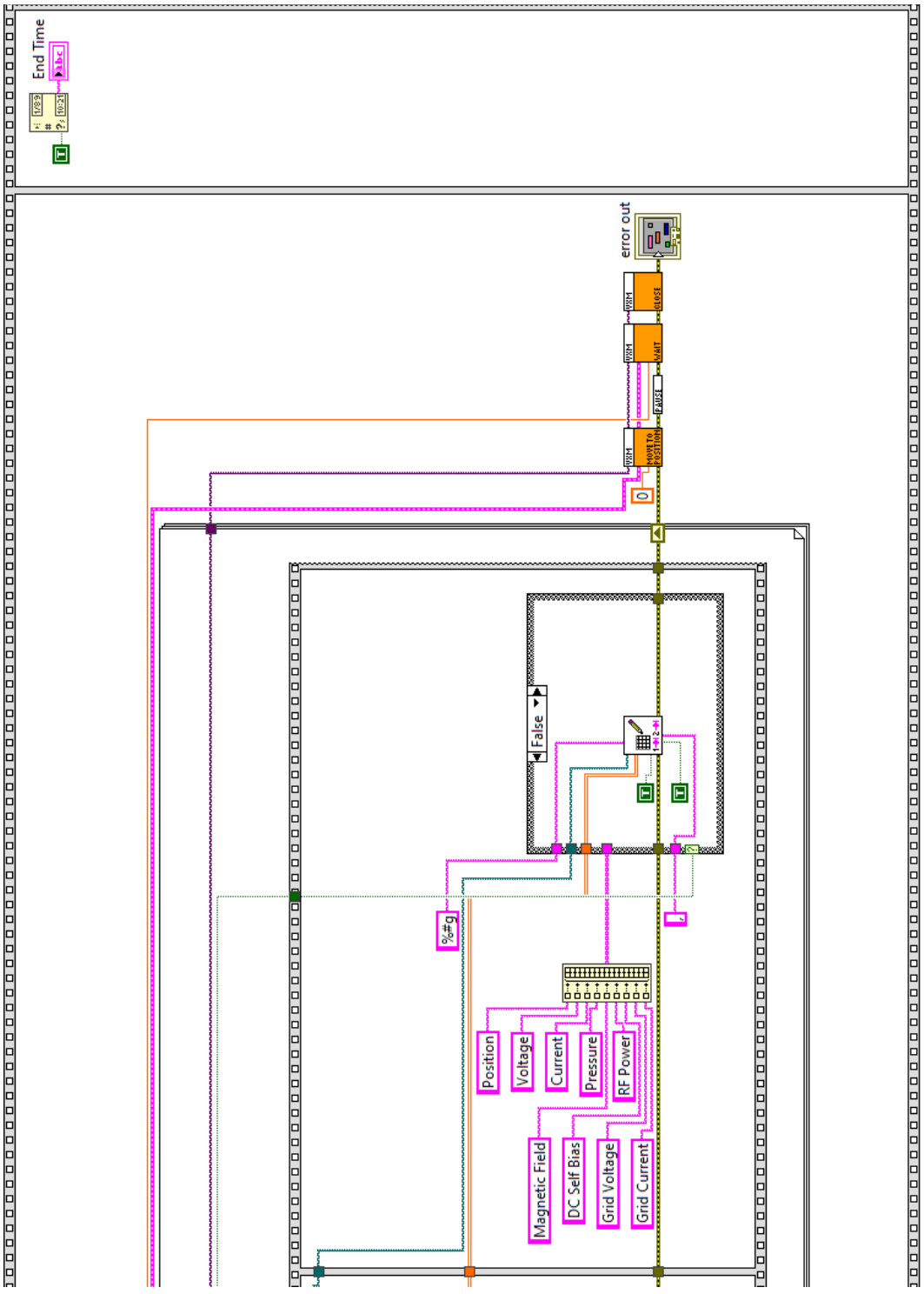
End Time
error out
WORM
CLOSE
WORM
WAIT
WORM
MOVE TO POSITION
PAUSE
0
False
%#g
Position
Voltage
Current
Pressure
RF Power
Magnetic Field
DC Self Bias
Grid Voltage
Grid Current

C.2 Keithley 2400 Probe Sweep VI

Front Panel

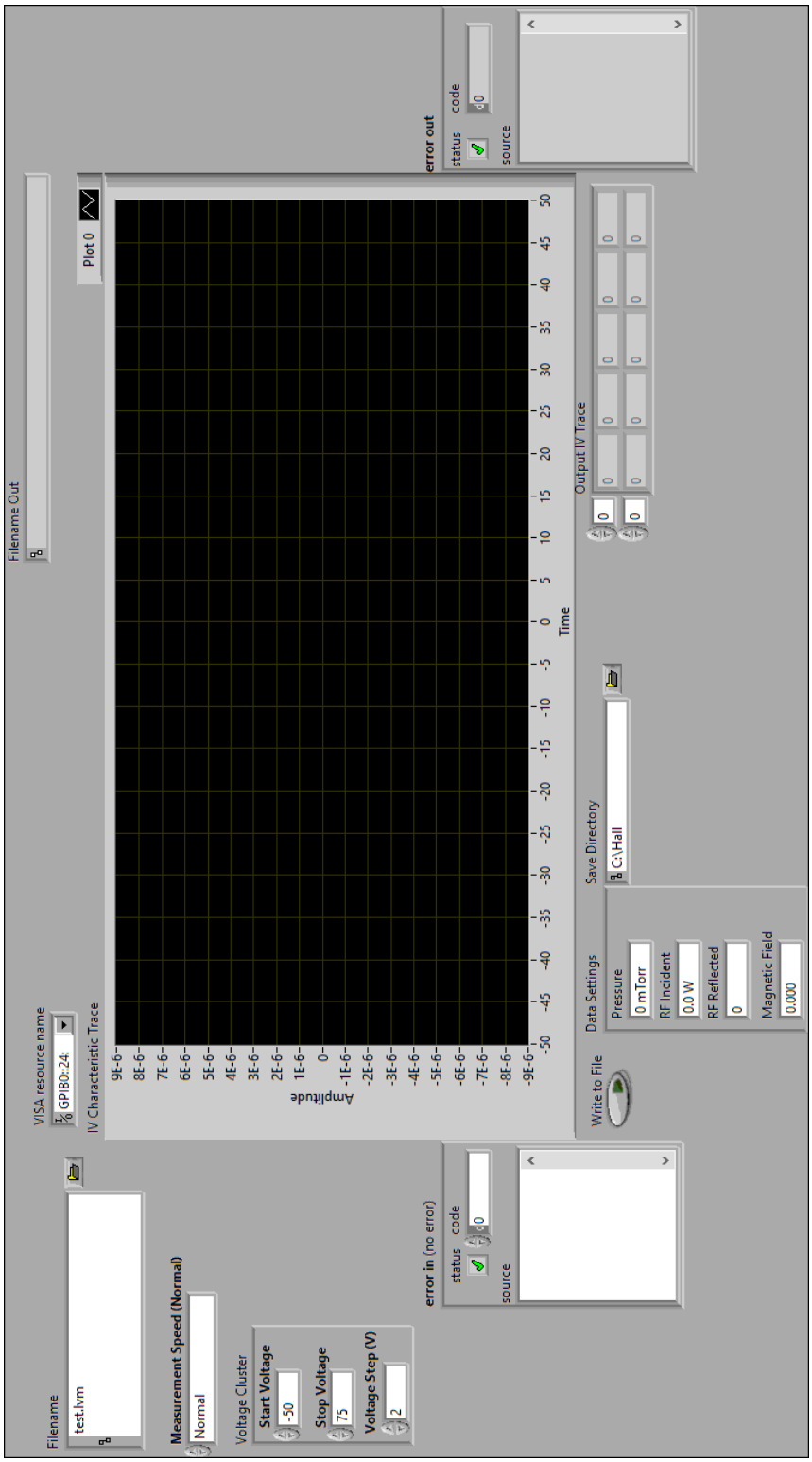

Block Diagram

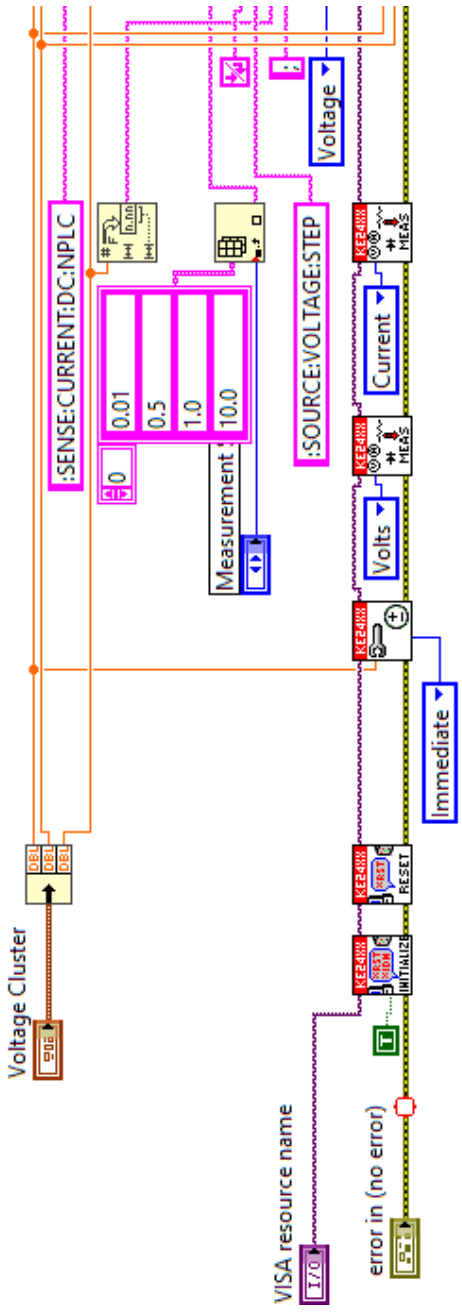

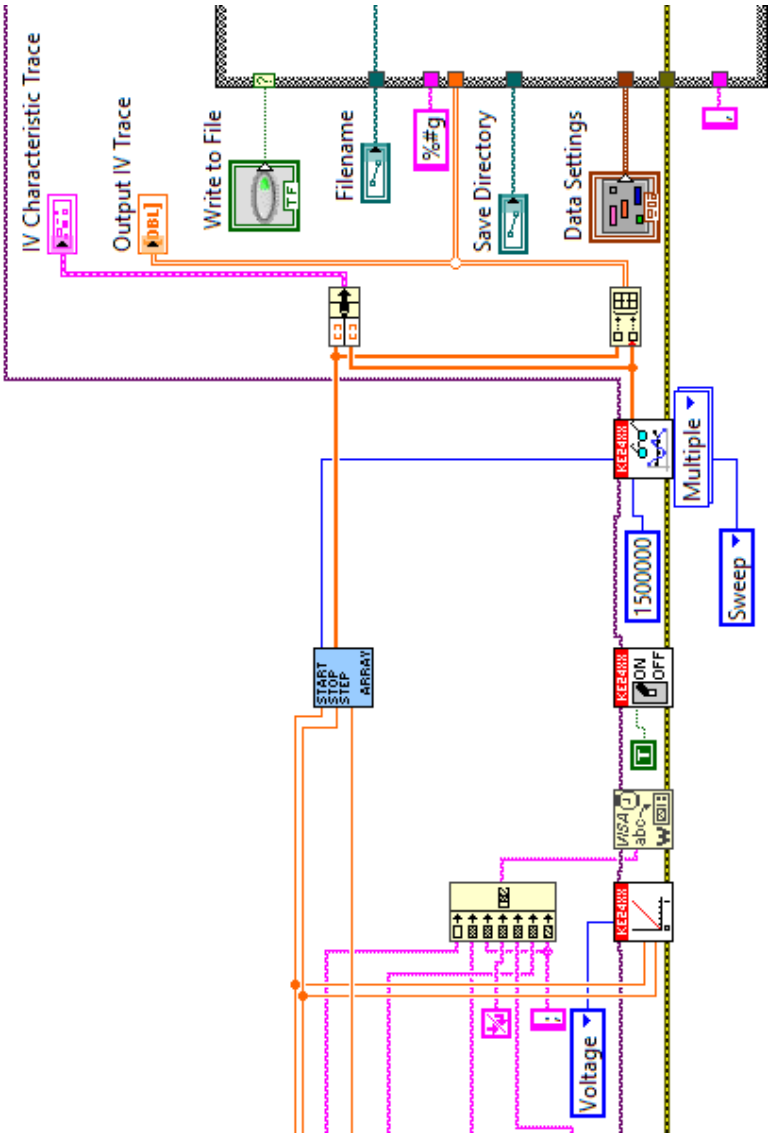
IV Characteristic Trace
Output IV Trace
Write to File
Filename
%#g
Save Directory
Data Settings
Multiple
1500000
Sweep
START
STOP
STEP
ARRAY
ON
OFF
Voltage

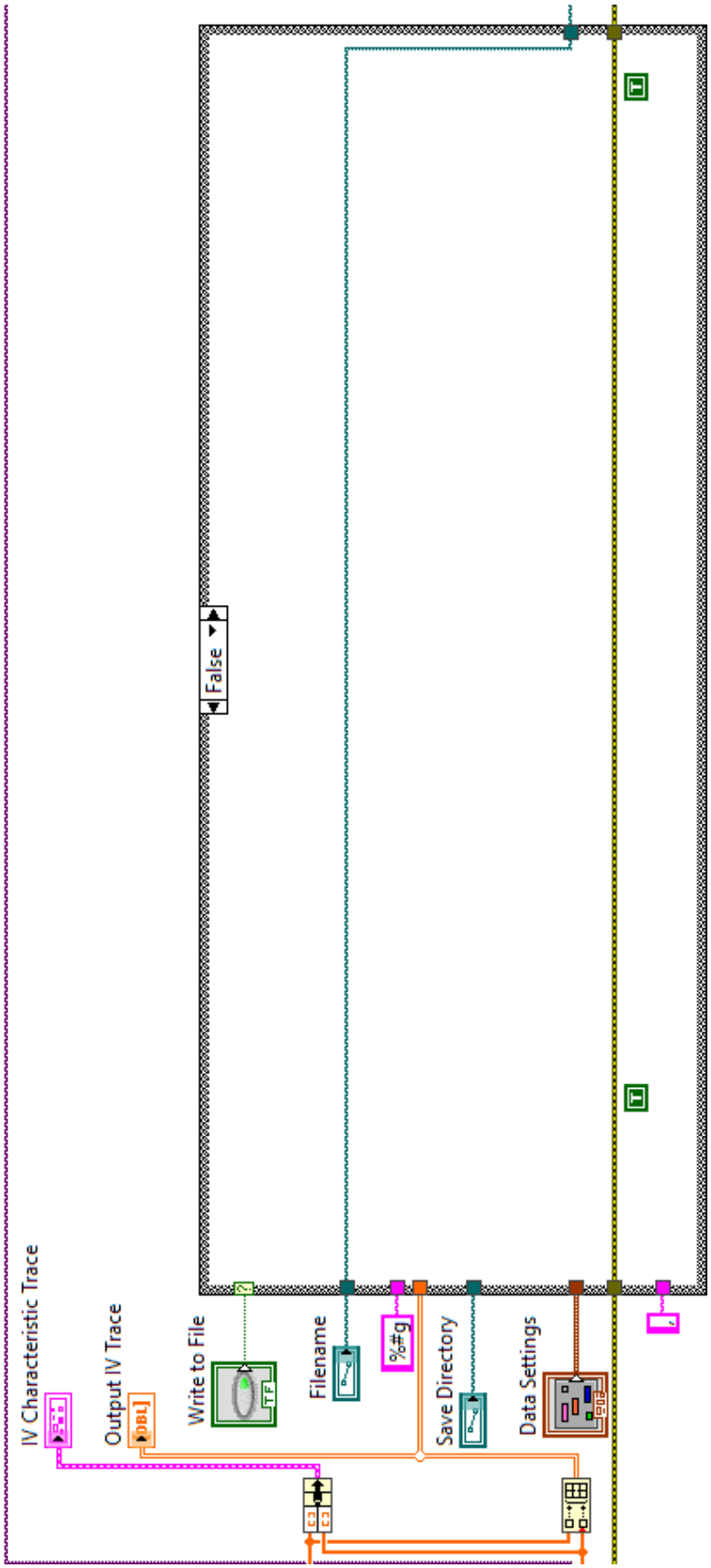
IV Characteristic Trace
Output IV Trace
DBL
Write to File
TF
Filename
%#g
Save Directory
Data Settings
False

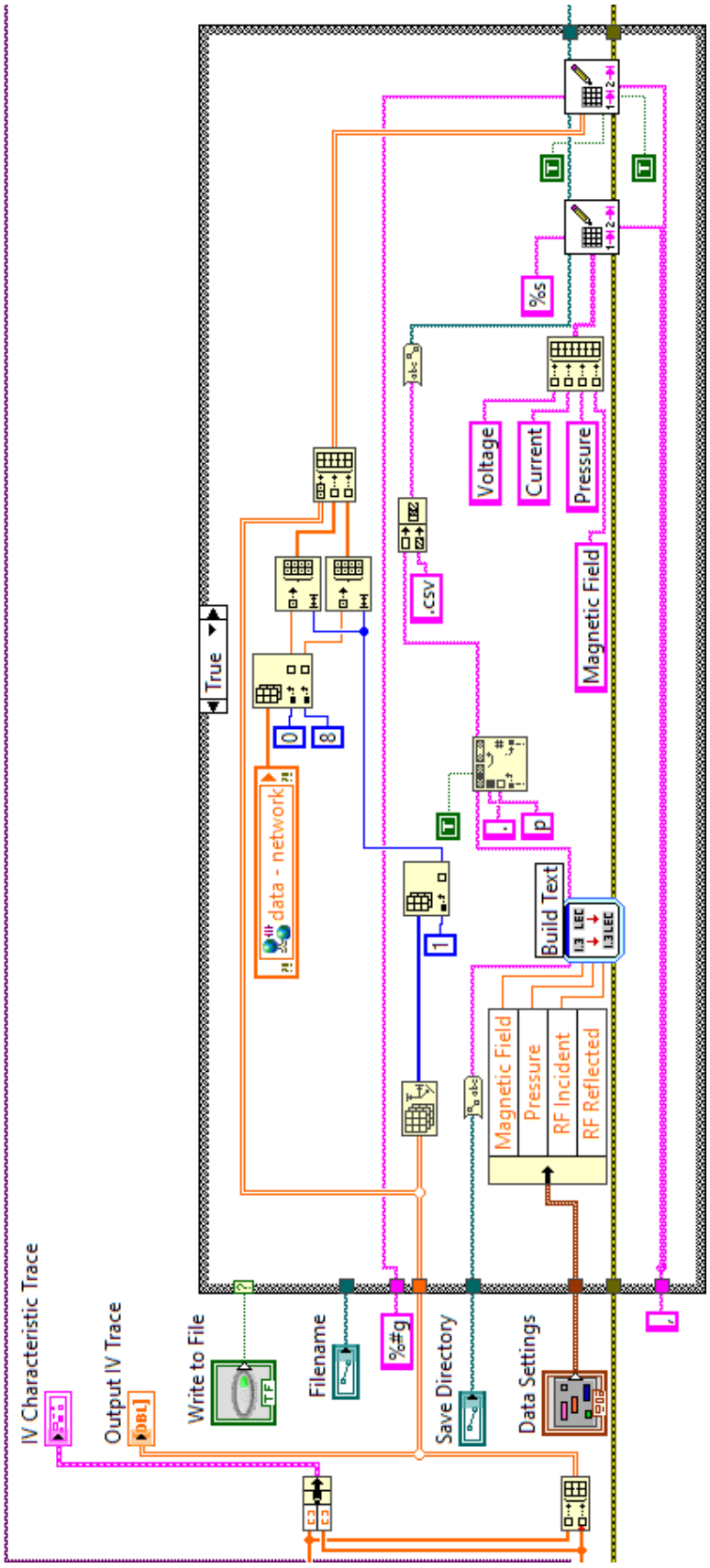
IV Characteristic Trace
Output IV Trace
Write to File
Filename
%#g
Save Directory
Data Settings
True
data - network
.csv
%s
Voltage
Current
Pressure
Magnetic Field
Build Text
Magnetic Field
Pressure
RF Incident
RF Reflected

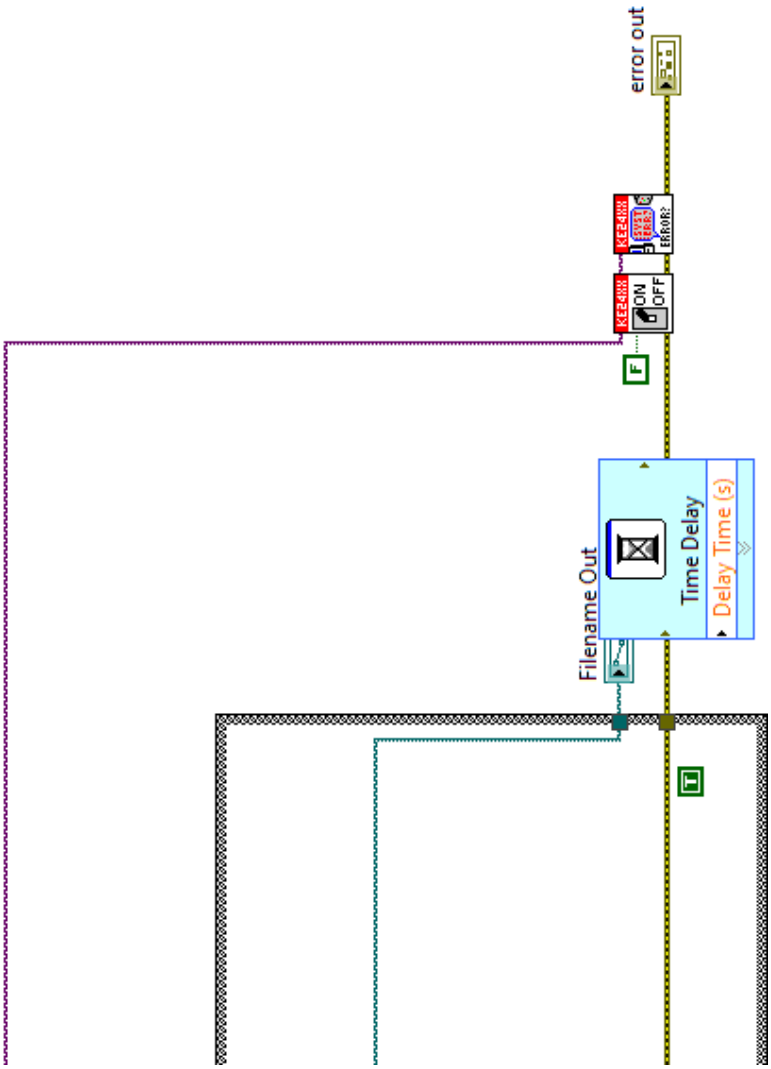
error out
ON
OFF
F
Time Delay
Delay Time (s)
Filename Out
T

C.3 Ring Probe VI

Front Panel

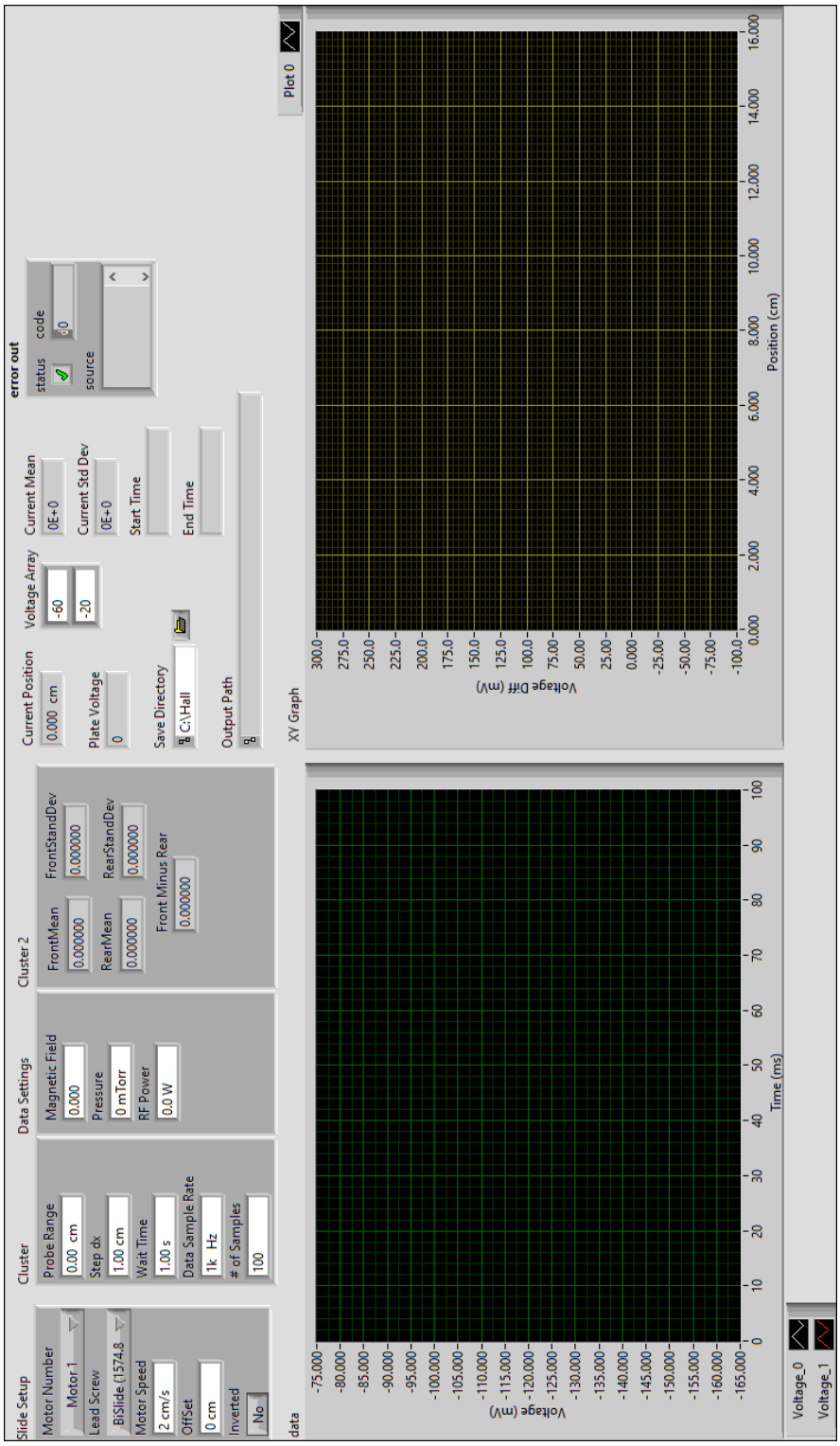

Block Diagram

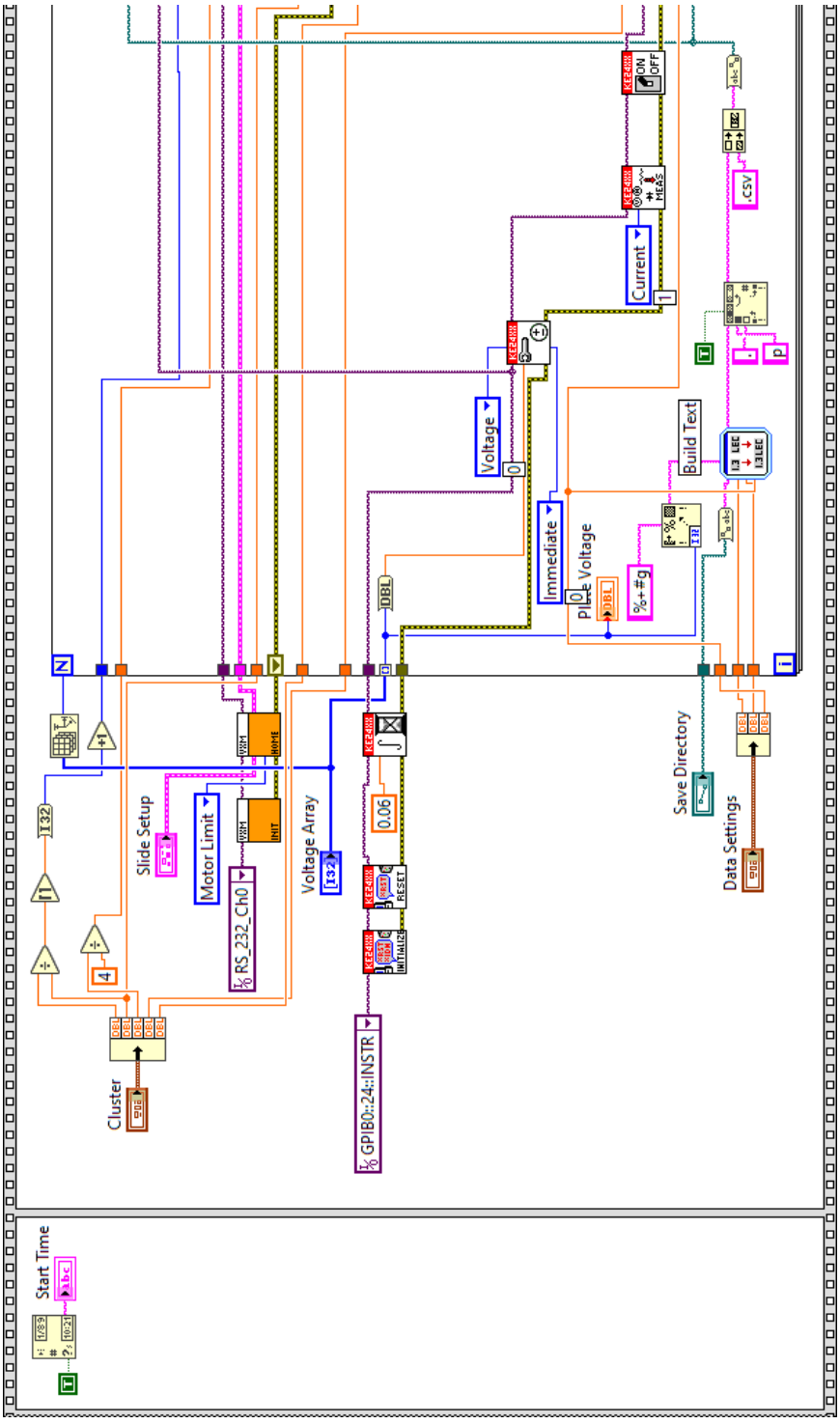

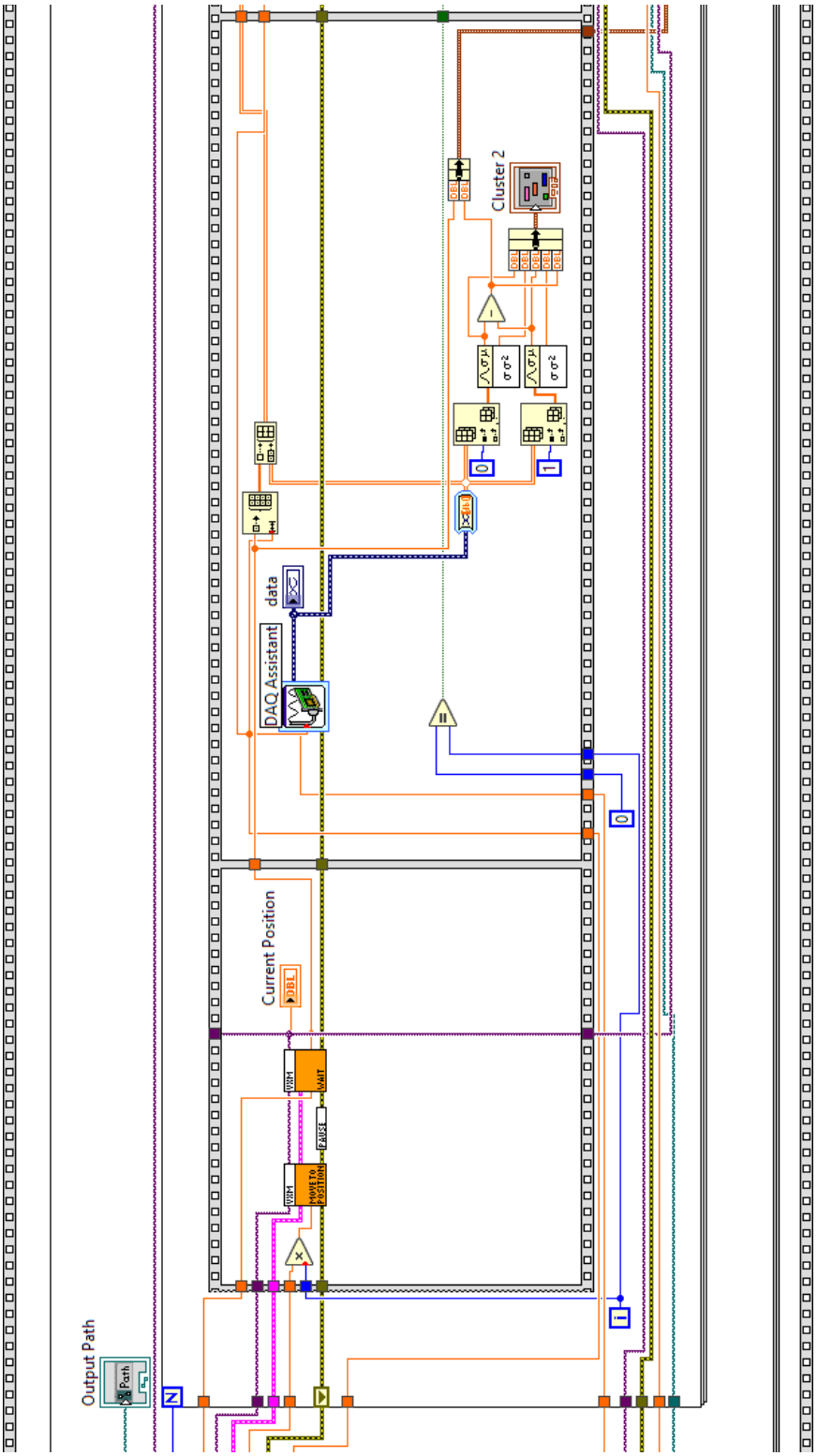
Output Path
Path
Current Position
DBL
data
DAQ Assistant
Cluster 2
DBL
WAIT
PAUSE
MOVE TO POSITION

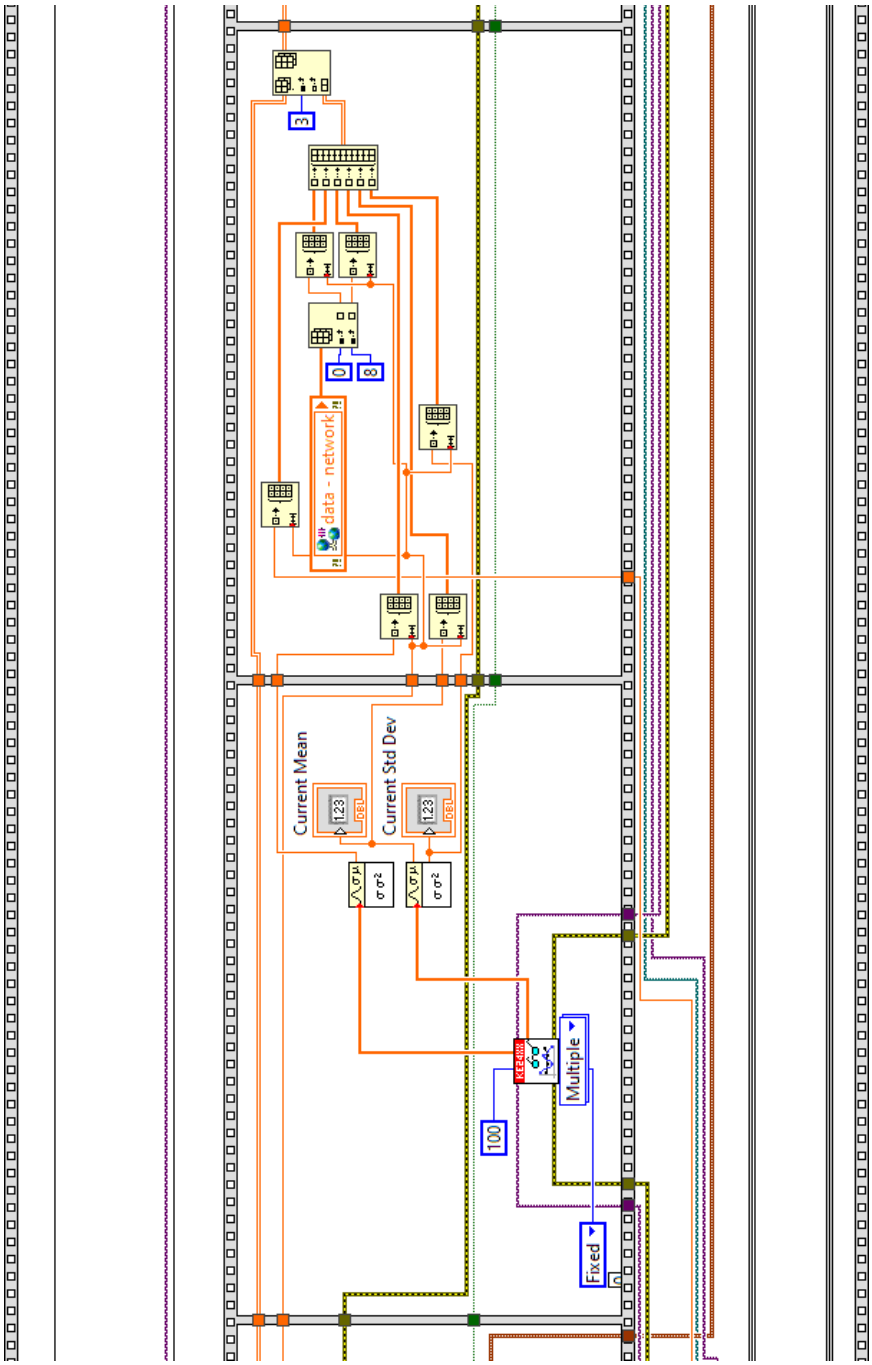
data - network
Current Mean
Current Std Dev
Multiple
Fixed
100

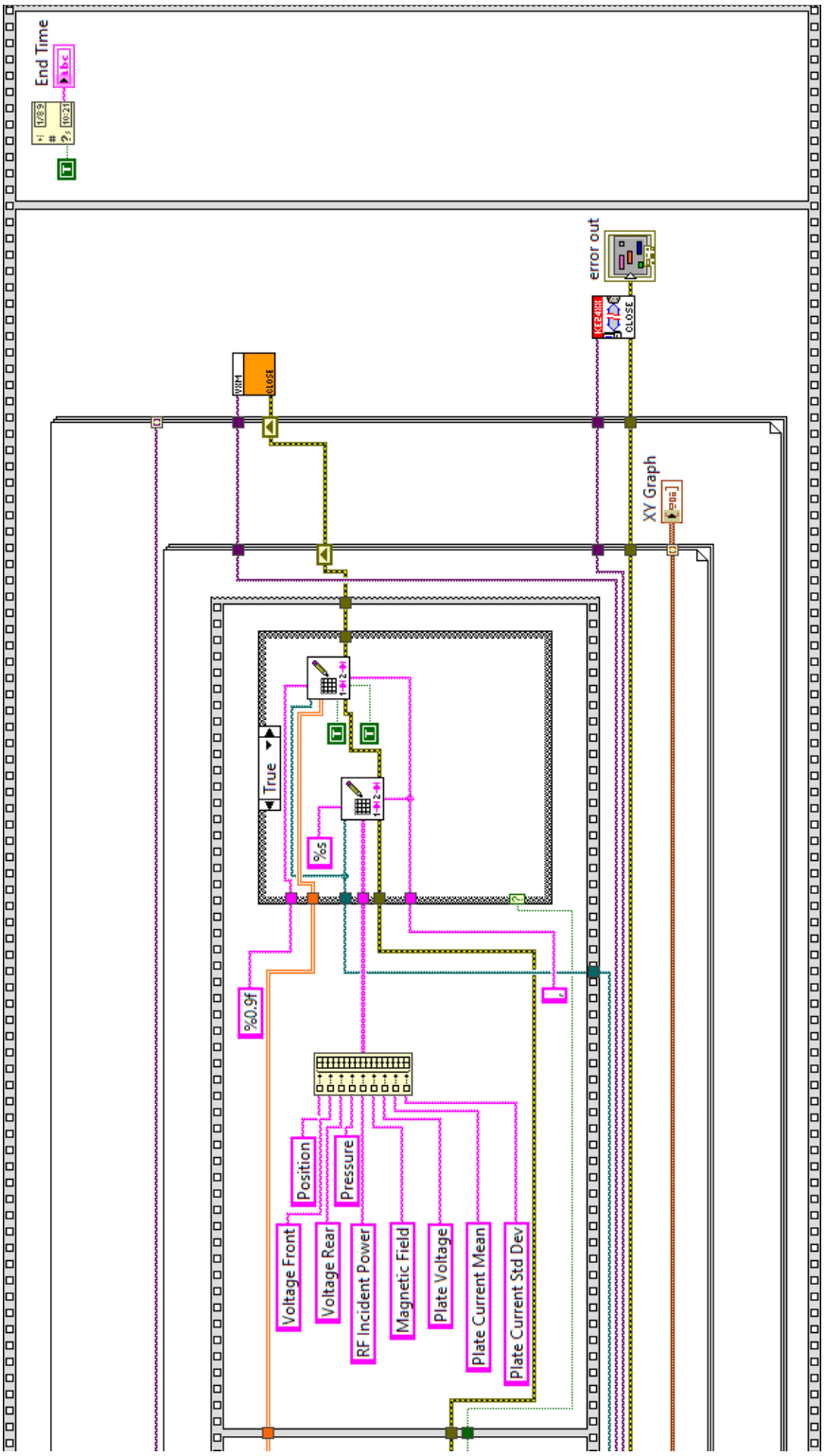
End Time
error out
XY Graph
True
%s
%0.9f
Voltage Front
Voltage Rear
RF Incident Power
Magnetic Field
Plate Voltage
Plate Current Mean
Plate Current Std Dev
Pressure
Position